

# Quantum Dot Optomechanics with Surface Acoustic Waves

Dissertation  
zur Erlangung des akademischen Grades  
Dr. rer. nat.

Eingereicht an der  
Mathematisch Naturwissenschaftlich Technischen Fakultät  
der Universität Augsburg

von

Matthias Weiß

Augsburg, Januar 2020



Erstgutachter: Prof. Dr. Hubert Krenner  
Zweitgutachter: Prof. Dr. Manfred Albrecht  
Drittgutachter: Prof. Dr. Kai Mueller

Datum der mündlichen Prüfung: 8. Juli 2020

# Abstract

Semiconductor quantum dots (QD) are considered to be an essential part of future quantum technologies due to their superior performance as an efficient source of single and indistinguishable photons. Such single photons are necessary to transport quantum information over large distances via established fibre optic networks. A fundamental requirement for these single photon sources is the possibility to precisely tune and modulate their emission energy. Due to the solid-state nature of semiconductor quantum dots, this is possible through the use of the deformation potential coupling. The main focus of this work is the control and manipulation of the optical properties of single quantum dots via the deformation potential induced by surface acoustic waves (SAW). These are mechanical waves that propagate along the surface of a crystal and can easily be excited electrically by interdigital transducers on piezoelectric substrates.

First, the modulation of the quantum dot transition energy by surface acoustic waves is studied closely by analysing the photoluminescence signal of a dynamically strained quantum dot. Different experimental measurement techniques, that allow for different deep insights into the underlying processes, are introduced and the corresponding measurement data is shown.

Next, the concept of frequency chirped transducers is presented. The design of these transducers allows them to excite surface acoustic waves over broad frequency bands rather than only at discrete frequencies. This capability is demonstrated by monitoring the optomechanical response of a single quantum dot over a broad range of surface acoustic wave frequencies. Furthermore, the properties of frequency chirped transducers are exploited to phase-lock the frequency of a surface acoustic wave to the repetition rate of a pulsed laser source and thus allowing for the realisation of stroboscopic SAW spectroscopy.

In order to obtain single photons of superior quality concerning coherence and indistinguishability, resonant optical excitation is employed. Of particular interest is the optical resonance fluorescence signal of a quantum dot dynamically strained by a surface acoustic wave. In this regime, the formation of discrete phononic sidebands can be observed in the emission spectrum. This can be interpreted by the absorption of a discrete number of phonons from the acoustic field or the emission of phonons into the acoustic field. The formation of these phononic sidebands is studied in great detail as function of both modulation frequency and amplitude, as well as optical detuning between the resonant light field and the transition energy of the QD. In the latter case, parametric energy transfer between the optical and the acoustic domain can be observed. In the next step, the QD

is dynamically modulated not by one, but by two SAWs of different frequency. In this scenario, the photon spectrum shows additional phonon sidebands which correspond to the sum and difference frequencies of both SAWs and thus showing optomechanical wave mixing of two SAW fields and the optical laser field by the QD transition. Furthermore, phase matching schemes are employed by precisely controlling the relative phase between the mutually coherent SAW fields, enabling deterministic enhancement and suppression of individual sidebands. The high stability, only limited by the capabilities of modern rf electronics, of this phase matching scheme is demonstrated.

Finally, the possibility to enhance the coupling of quantum dots to both photonic and phononic fields by placing these in appropriately adapted environments, so called photonic and phononic crystals, is considered. In this context, a coupled system consisting of a single quantum dot and a photonic nano-cavity is investigated in detail. For this arrangement, a surface acoustic wave is used to dynamically tune the two components in and out of resonance. This has a strong influence on the emission rate of the quantum dot due to the Purcell effect and is ultimately used to realise an acoustically triggered single photon source.

# Zusammenfassung

Halbleiter-Quantenpunkte (engl. Quantum dot, QD) werden aufgrund ihrer überlegenen Leistung als effiziente Quelle von einzelnen und ununterscheidbaren Photonen als wesentlicher Bestandteil zukünftiger Quantentechnologien angesehen. Solche Einzelphotonen sind notwendig, um den Transport von Quanteninformationen über große Entfernungen durch etablierte Glasfasernetzwerke zu ermöglichen. Eine grundlegende Anforderung an Einzelphotonenquellen ist die Möglichkeit, ihre Emissionsenergie präzise abzustimmen und modulieren zu können. Da es sich bei Halbleiter-Quantenpunkten um Festkörpersysteme handelt, ist dies für diese auf Grundlage der Deformationspotentialkopplung möglich. Der Schwerpunkt dieser Arbeit liegt auf der Steuerung und Manipulation der optischen Eigenschaften einzelner Quantenpunkte durch das Deformationspotential, welches von akustischen Oberflächenwellen (engl. surface acoustic wave, SAW) induziert wird. Dabei handelt es sich um mechanische Wellen, die sich auf der Oberfläche eines Kristalles ausbreiten können und sich auf piezoelektrischen Substraten leicht durch Interdigitaltransducer elektrisch anregen lassen.

Zunächst wird die Modulation der Emissionsenergie eines Quantenpunktes durch akustische Oberflächenwellen untersucht, in dem die Photolumineszenz eines Quantenpunktes unter dem Einfluss einer akustischen Oberflächenwelle analysiert wird. Es werden verschiedene experimentelle Messtechniken vorgestellt, die unterschiedlich tiefe Einblicke in die zugrundeliegenden Prozesse ermöglichen und entsprechende Messdaten präsentiert.

Als nächstes wird das Konzept von frequenz-gechirpten Transducern eingeführt. Das Design dieser Schallwandler ermöglicht es ihnen, akustische Oberflächenwellen nicht nur bei diskreten Frequenzen, sondern über breite Frequenzbänder hinweg, anzuregen. Diese Fähigkeit wird demonstriert, indem die optomechanische Antwort eines einzelnen Quantenpunktes über einen weiten Bereich von Oberflächenwellenfrequenzen untersucht wird. Darüber hinaus werden die Eigenschaften von frequenz-gechirpten Transducern ausgenutzt, um eine stabile Phasenbeziehung zwischen der Frequenz einer akustischen Oberflächenwelle und der Wiederholungsrate einer gepulsten Laserquelle herzustellen und somit stroboskopische SAW-Spektroskopie zu ermöglichen.

Um Einzelphotonen von überlegener Qualität hinsichtlich ihrer Kohärenz und Ununterscheidbarkeit zu erhalten, wird zu einer resonanten optischen Anregung der Quantenpunkte übergegangen. Von besonderem Interesse ist dabei die resonante Fluoreszenz eines Quantenpunktes, der dynamisch durch eine akustische Oberflächenwelle moduliert wird. In diesem Regime kann die Bildung diskreter phononischer Seitenbänder im Emissionsspektrum

beobachtet werden. Dies kann durch die Absorption einer diskreten Anzahl von Phononen aus dem akustischen Feld, beziehungsweise die Emission von Phononen in das akustische Feld interpretiert werden. Die Bildung dieser phononischen Seitenbänder wird sowohl in Abhängigkeit von der Modulationsfrequenz und -amplitude, als auch der optischen Verstimmung zwischen dem resonanten Lichtfeld und der Übergangsenergie des QD eingehend untersucht. Im letzteren Fall kann dabei ein parametrischer Energietransfer zwischen der optischen und der akustischen Domäne beobachtet werden. Im nächsten Schritt wird der QD nicht nur durch eine, sondern durch zwei SAWs unterschiedlicher Frequenz dynamisch moduliert. In diesem Szenario zeigt das Emissionsspektrum zusätzliche phononische Seitenbänder, deren Position der Summen- und Differenzfrequenzen beider SAWs entsprechen. Dies zeigt somit die optomechanische Wellenmischung zweier SAW-Felder und des optischen Lichtfeldes durch den QD-Übergang. Darüber hinaus wird, indem die relative Phase zwischen den zueinander kohärenten SAW-Feldern genau eingestellt wird, eine Phasenanpassung ermöglicht, wodurch eine deterministische Verstärkung und Unterdrückung einzelner Seitenbänder erreicht wird. Die hohe Stabilität dieser Phasenanpassung, die nur durch die Leistungsfähigkeit moderner Hochfrequenz-Elektronik begrenzt ist, wird experimentell gezeigt.

Abschließend wird die Möglichkeit betrachtet, die Kopplung eines Quantenpunktes an photonische und phononische Felder zu verstärken, in dem diese in entsprechende angepasste Umgebungen, sogenannten photonischen und phononischen Kristallen, platziert werden. In diesem Zusammenhang wird ein gekoppeltes System, bestehend aus einem einzelnen Quantenpunkt und einem photonischen Nanoresonator, im Detail betrachtet. Dabei wird eine akustische Oberflächenwelle verwendet, um die beiden Komponenten eines solchen Systems dynamisch in und aus der Resonanz zu bringen. Dies hat aufgrund des Purcell-Effekts einen starken Einfluss auf die Emissionsrate des Quantenpunkts und wird letztendlich zur Realisierung einer akustisch ausgelösten Einzelphotonenquelle verwendet.

# Contents

<b>Abstract</b>	<b>i</b>
<b>Zusammenfassung</b>	<b>iii</b>
<b>1. Introduction</b>	<b>1</b>
<b>2. Semiconductor quantum dots</b>	<b>7</b>
2.1. Basics of semiconductors . . . . .	7
2.2. Low dimensional semiconductor systems . . . . .	11
<b>3. Surface acoustic waves</b>	<b>19</b>
3.1. Basic properties . . . . .	19
3.2. Finite Element Modelling of surface acoustic waves . . . . .	23
3.2.1. Surface acoustic waves on GaAs . . . . .	25
3.2.2. Surface acoustic waves on $\text{Al}_x\text{Ga}_{1-x}\text{As}$ . . . . .	28
3.3. Excitation of surface acoustic waves . . . . .	30
<b>4. Samples - Fabrication and structure</b>	<b>35</b>
4.1. Epitaxial growth of semiconductor quantum dots . . . . .	35
4.1.1. Self-assembled InAs QDs . . . . .	35
4.1.2. Etched GaAs/AlGaAs QDs . . . . .	36
4.1.3. Layer structure and resulting sound velocity of the samples . . . . .	37
4.2. Sample fabrication and layout . . . . .	40
4.3. Temperature dependence of the surface acoustic wave velocity . . . . .	41
<b>5. Interfacing quantum dots with surface acoustic waves: Deformation potential coupling</b>	<b>43</b>
5.1. Time-averaged strain modulation . . . . .	45
5.2. Time domain spectroscopy: Time correlated single photon counting . . . . .	50
5.3. Stroboscopic laser excitation . . . . .	53
<b>6. Multiharmonic frequency chirped transducers</b>	<b>59</b>
6.1. Fundamentals of the chirped transducer design . . . . .	60
6.2. Surface acoustic wave transmission . . . . .	63

6.3.	Optomechanical characterisation of chirped transducers . . . . .	66
6.4.	Stroboscopic spectroscopy . . . . .	69
6.4.1.	Time-integrated detection . . . . .	70
6.4.2.	Time-resolved detection . . . . .	74
6.5.	Two tone excitation: acoustic beat . . . . .	76
<b>7.</b>	<b>Resonance fluorescence of a semiconductor quantum dot</b>	<b>81</b>
7.1.	Optically driven two-level system: Semiclassical approach . . . . .	82
7.2.	Dressed state picture: Quantum mechanical approach . . . . .	87
7.3.	Experimental realisation of resonance fluorescence . . . . .	89
7.3.1.	Crossed-polarised resonance fluorescence . . . . .	90
7.3.2.	High resolution detection: Fabry-Pérot-Etalon . . . . .	92
7.4.	Experimental observation of the Mollow triplet . . . . .	95
7.4.1.	Dependence on resonant excitation power . . . . .	95
7.4.2.	Dependence on detuning of resonant laser excitation . . . . .	97
<b>8.</b>	<b>Resonance fluorescence from a dynamically strained quantum dot</b>	<b>101</b>
8.1.	Dependence of phononic sidebands on SAW amplitude . . . . .	103
8.2.	Dependence of phononic sidebands on SAW frequency . . . . .	104
8.3.	Parametric excitation: Dependence of phononic sidebands on optical detuning	106
8.4.	Time domain spectroscopy of phononic sidebands . . . . .	108
8.5.	Acoustic two tone excitation . . . . .	110
8.5.1.	Standing wave . . . . .	111
8.5.2.	Frequency mixing . . . . .	113
8.5.3.	Phase-matched frequency mixing . . . . .	114
8.5.4.	Detuned SAW frequency mixing . . . . .	119
8.5.5.	Further frequency ratios . . . . .	122
8.6.	Conclusion of SAW driven resonance fluorescence . . . . .	124
<b>9.</b>	<b>Quantum dots in tailored photonic and phononic environments</b>	<b>127</b>
9.1.	Photonic crystals nanocavity . . . . .	128
9.1.1.	Static temperature tuning . . . . .	131
9.1.2.	Dynamic SAW tuning . . . . .	133
9.2.	Phononic crystals . . . . .	138
<b>10.</b>	<b>Conclusion and outlook</b>	<b>145</b>
	<b>Appendices</b>	<b>149</b>
<b>A.</b>	<b>Remarks on elastic constants</b>	<b>151</b>
A.1.	Voigt Notation . . . . .	151

---

A.2. Elastic constants of $\text{Al}_x\text{Ga}_{1-x}\text{As}$ . . . . .	152
<b>B. Additional Resonance Fluorescence Measurements</b>	<b>157</b>
B.1. Time-resolved phononic sidebands . . . . .	157
B.2. Detuned optical excitation . . . . .	159
B.3. Detuned SAW frequency mixing . . . . .	160
<b>C. Fabrication of photonic and phononic crystals</b>	<b>161</b>
<b>D. Phononic snowflake waveguides</b>	<b>163</b>
<b>E. List of abbreviations</b>	<b>165</b>
<b>Bibliography</b>	<b>167</b>
<b>List of Publications</b>	<b>179</b>
<b>Danksagung</b>	<b>183</b>



# 1. Introduction

In recent years, quantum computers and quantum technologies in general have become increasingly important and arousing increasing interest, even among the general public [1–3]. For example, Google recently claimed to have reached a milestone in the realisation of a quantum computer, quantum supremacy [4]. This means they solved a problem using a quantum processor in a fraction of the time that a traditional computer would have needed. Although this is a great achievement, there are still many steps to go towards the main goal, the realisation of a full-fledged quantum computer. The great interest in this goal and the great efforts being made to achieve this goal is based on the unique working principle of a quantum computer. For this reason, they are expected to be far superior to classical computers in many but not all areas. In contrast to classical computers using classical bits that can only be in one of two possible well-defined states typically denoted as 0 and 1, quantum computers are based on so-called qubits (short for quantum bit). The basis for a qubit are two distinguishable states (e.g. spin up and down orientation of an electron or horizontal and vertical polarisation of a photon), representing the binary values 0 and 1. In contrast to a classical bit, a qubit is not limited to either one of these states but can be in a coherent superposition of the two states  $|\uparrow\rangle$  and  $|\downarrow\rangle$ :

$$\Psi = \alpha \cdot |\uparrow\rangle + \beta \cdot |\downarrow\rangle$$

with the complex wave amplitudes  $\alpha$  and  $\beta$ , which satisfy the relation  $|\alpha|^2 + |\beta|^2 = 1$ . The superposition of two qubits can be described in the product bases of the respective qubits:

$$\Psi = \alpha \cdot |\uparrow\uparrow\rangle + \beta \cdot |\downarrow\uparrow\rangle + \gamma \cdot |\uparrow\downarrow\rangle + \delta \cdot |\downarrow\downarrow\rangle$$

and thus is characterised by four different wave amplitudes  $\alpha, \beta, \gamma$  and  $\delta$ . In general, an array of  $n$  qubits is characterised by  $2^n$  amplitudes. As long as the state of a qubit array is not measured, it can be simultaneously in all of these states. This allows a quantum computer to perform calculations with a parallelism that cannot be achieved with a classical computer. Because of this property, it is expected that quantum computers can solve certain tasks much faster than classic computers. The best known algorithms to run on a quantum computer are the Grover and Shor algorithms. Grover's algorithm [5] allows for an efficient search in an unstructured database in  $\mathcal{O}(\sqrt{N})$  computational steps, whereas a classical computer performing a linear search requires  $\mathcal{O}(N)$  steps.

Shor's algorithm [6] enables integer factorisation of large numbers within polynomial time. This algorithm is of particular interest in the field of cryptography, as it poses a big risk to common public-key cryptography systems. For public-key cryptography, the message to be sent is encoded with a public-key which is publicly known. The decoding on the other side is only possible with a private key which is known only to the recipient. The security of this technique thus depends on the secrecy of the private key and the practical irreversibility of the encoding. To achieve this irreversibility one-way functions, like the multiplication of prime numbers, are applied. While the multiplication of prime numbers is a simple task that can efficiently be solved by any modern computer, the reversal of this function, the integer factorisation, is expensive, meaning there is no known classical algorithm that allows for integer factorisation in polynomial time. Although the nonexistence of an efficient algorithm for integer factorisation on a classical computer is not proven, it is the basis for current cryptography. Although Shor's algorithm has not yet been implemented on a large scale, and only the factorisation of 15 [7,8] and 21 [9] have been demonstrated so far, alternative cryptography systems are already researched and tested to be used as soon as possible. The need for an alternative method to securely transmit data becomes particularly clear when considering that the security of an encryption must not only be guaranteed at the time of the data transmission but also throughout the entire time in which the transmitted information maintains its value. Indeed, even if a message cannot be cracked right away, it can be stored with the respective public-key and decoded once the necessary technology is available. One possibility is the use of symmetric cryptography, where sender and receiver use the same key to encrypt and decrypt data. Provided this key is purely random and of sufficient length, symmetric cryptography is considered to be robust against quantum algorithms. The vulnerability of symmetric cryptography is the secure exchange of the common key between the sender and the recipient of a message which requires a physically secure channel.

One way to achieve this is a method called quantum key distribution with its best known implementation being the BB84-protocol, proposed by Charles H. Bennett and Gilles Brassard in 1984 [10]. The basis of this protocol is the exchange of quantum states between two parties. Provided this protocol is properly implemented, it allows for a secure exchange of a random key between two parties. Although the key exchange itself it not safe against eavesdropping, an attack can be recognised before the information itself is transmitted. This property arises from the no clone theorem [11–13] and requires that only single quantum states are transmitted. Since mostly photons are used to transmit quantum states, as they can propagate at high speed and with little loss over long distances, a single photon source is required. Most implementations of the BB84 protocol realised so far use strongly attenuated lasers as a light source, which have a high probability of transmitting more than one photon per pulse, making it vulnerable to a "photon number splitting" attack [14].

---

The single photon source investigated in this thesis are semiconductor quantum dots (QD). These nanoscopic objects feature atom-like discrete energy levels, which earned them the name "artificial atom" and makes them an ideal single photon source. Their solid state basis and the associated possibility to implement them on a chip scale, makes them a promising building block for many scalable quantum technologies. By optically exciting single QDs, the emission of both single photons [15] and, taking advantage of the biexciton–exciton decay cascade, pairs of polarisation entangled photons can be obtained [16–18]. Additionally, single spins can be completely controlled by ultrafast optical pulses [19].

Due to their solid state nature, QDs can easily be implemented in electrical circuits, making it easy to control them by electrical means. This allowed for the realisation of electrically triggered emission of both single photons [20] and polarisation entangled pairs of photons [21,22]. Furthermore, electrical fields can be used to switch between different occupancy state of a QD [23,24] and to tune the emission energy of a QD via the quantum confined Stark effect (QCSE) [25]. In addition, QDs can be implemented in tailored photonic environments and thus the strong light matter interaction inherent to solids can be harnessed. In the weak coupling regime, this interaction leads to the Purcell effect that was demonstrated for semiconductor QDs by an enhancement of the radiative decay rate [26]. Beside that, the strong coupling between QD excitons and photons was also realised by placing single QDs in photonic microcavities [27–29]. All these outstanding properties make QDs to an essential link between light and matter.

Furthermore, the solid state base of QDs makes them susceptible to the interaction with phonons. This can be exploited to control and manipulate single QDs by the coherent phonon field of a surface acoustic wave (SAW), which is the main focus of this thesis. Many interesting experiments have been conducted interfacing QDs with propagating SAWs. These range from the control of the QD's occupancy states by sequential carrier injection [30] to the realisation of an acoustically triggered single photon source [31]. In addition, a SAW can dynamically modulate the emission energy of QDs by both the deformation potential coupling [32,33] and, for a piezoelectric substrate, by the SAW's electrical fields via the QCSE [34]. This work will focus almost exclusively on the dynamic modulation of the QD's transition energies via the deformation potential coupling. A detailed summary on the recent advances on the coupling of single semiconductor quantum emitters to the dynamic fields of a SAW can be found in a recent review article [35].

The thesis is structured as follows:

In **chapter 2** the fundamentals of semiconductor quantum dots that are important in the scope of this work are introduced.

**Chapter 3** summarizes the basics of SAWs. This includes the solution of the corresponding wave equations for the material systems used in this work and a short analysis of the resulting strain and electrical fields of a surface acoustic wave. At the end of the chapter, the generation of SAWs on a piezoelectric substrate using metallic electrode structures, so-called interdigital transducers (IDT), is considered.

The design and fabrication of samples that allow to optically probe single semiconductor QDs are treated in **chapter 4**.

Photoluminescence (PL) measurements of single QDs under the influence of a SAW are presented in **chapter 5**. Here, different methods are introduced to observe the SAW induced temporal spectral modulation of the QD emission energy caused by deformation potential coupling.

In **chapter 6**, frequency chirped transducers are introduced. They allow the excitation of SAWs over large frequency bands rather than discrete frequencies. The capability of these IDTs to convert electrical to mechanical energy over a broad range of frequencies is demonstrated by monitoring the optical response of a single QD. Furthermore, the advantage of broad transmission bands is demonstrated by phase-locking a SAW to the train of laser pulses steaming from a mode-locked laser with fixed repetition rate and performing stroboscopic spectroscopy of single QDs.

Approach lanes to obtain single photons of superior properties concerning coherence and indistinguishability, resonance fluorescence, is introduced in **chapter 7**. First, the interaction between a QD, treated as a perfect two-level system, and a resonant light field is treated theoretically. After that, details of the experimental realisation of resonance fluorescence are provided and experimental data of the observed Mollow triplet as a function of both resonant excitation power and detuning between the driving laser and the QD's transition are presented.

In **chapter 8**, the resonant optical excitation in the limit of low Rabi frequencies is combined with the dynamical spectral modulation by a coherent surface acoustic wave. The coherent interaction mixes optical frequencies with acoustic frequencies and a comb of sidebands is generated in the scattered light spectrum. This frequency comb is investigated in details as a function of various parameters including both the amplitude and frequency of the SAW, as well as the optical detuning between the resonant light field and the transition energy of the QD. Finally, the dynamical modulation scheme is extended from a single phonon field to two mutually coherent phonon fields. This enables the mixing of phonons of different frequencies and hence offers further control on the formation of the phononic sidebands.

---

The ability to enhance the coupling of a QD to optical and mechanical fields by embedding in appropriately tailored structures is covered in **chapter 9**. In the first part of this chapter a photonic crystal cavity is used to increase the radiative decay rate of a QD. Furthermore, a SAW is used to dynamically modulate the detuning between a cavity mode and a single QD, thus allowing to trigger the emission of a single photon. The second part of the chapter deals with phononic crystal membranes that offer the opportunity to steer and control the propagation of mechanical waves on a substrate. Different phononic crystal structures compatible with the implementation of QDs are discussed and examined with regard to their mechanical properties. These results pave the way to future research tracks aiming to couple light (photon), sound (phonons) and matter (QD exciton) on the same platform.



## 2. Semiconductor quantum dots

The concept of quantum dots is based on the quantum confinement of charge carriers on length scales close to their respective De Broglie wavelength resulting in the formation of discrete energy states similar to that of an atom. Such a confinement can be realised by the combination of different semiconductor materials with different band gaps  $E_g$ . In this section, the fundamentals of this approach shall be discussed, namely the used material systems, the influence of quantum confinement on the energy states and the resulting optical properties of such systems. The fabrication of semiconductor quantum dots however, will be discussed later in section 4.1.

### 2.1. Basics of semiconductors

As already mentioned, the confinement of charge carriers in a solid can be implemented by a structure consisting of different semiconductor materials, typically referred to as a semiconductor heterostructure. The two most important parameters that have to be considered for the realisation of such heterostructures are the lattice constant  $c$  and the energetic bandgap  $E_g$  of the employed semiconductors. Therefore, in the scope of this work, the compound semiconductors GaAs, AlAs, InAs and their respective ternary alloys  $\text{Al}_x\text{Ga}_{1-x}\text{As}$  and  $\text{In}_x\text{Ga}_{1-x}\text{As}$  are used, since these materials allow for a precise tuning of both lattice constant and bandgap by adjusting the composition of the semiconductors. Since these alloys are composed of group III (Al, Ga, In) and group V (As) elements they are referred to as III-V semiconductors. Most of the III-V-semiconductors crystallise in the zincblende crystal structure which is depicted in figure 2.1(a) for the example of GaAs. It can be described as a combination of two face-centred cubic lattices, one consisting of Ga and the other of As atoms and shifted by  $\frac{1}{4}a$  with respect to each other in all three spatial dimensions.

Part of the electronic band structure of GaAs, covering the valance (VB) and conduction (CB) band, is sketched in figure 2.1(b). For  $T = 0\text{K}$ , the valance band is the highest band which is completely filled by electrons, while the conduction band band is the first unoccupied band. In contrast to a metal, for a semiconductor these two bands are separated by a bandgap  $E_g$ . For GaAs, three local minima in the CB at the X-,  $\Gamma$  and L-point can be identified and, accordingly, three bandgaps  $E_g^X$ ,  $E_g^\Gamma$  and  $E_g^L$  can be defined. The bandgap at the  $\Gamma$ -point  $E_g^\Gamma$  is the smallest one, making GaAs a so-called direct semiconductor which plays an important role in the optical properties of the semiconductor. Electrons can be

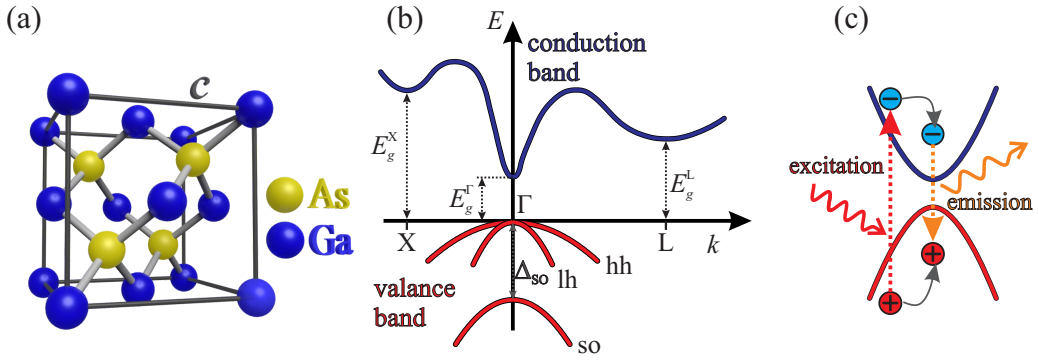


**Figure 2.1.:** (a) Zincblende crystal structure for GaAs. (b) Schematic of the GaAs band structure around the bandgap. (c) Optical excitation and subsequent emission process close to the band edge at the  $\Gamma$ -point.

excited from the VB to the CB by the absorption of a photon, where both energy and momentum of the whole system must be preserved. Since the momentum of a photon is comparatively small such an optical transition happens vertically in the  $E(k)$  diagram, as it is depicted in figure 2.1(c). After the excitation of an electron from the VB to the CB, there is one electron missing in the conduction band which can be described as a quasi-particle with a positive charge called a hole ( $h^+$ ). In contrast to an electron that relaxes to bottom of the CB, the hole relaxes to the top of the VB in order to minimize its energy, where excess energy is typically transferred to the crystal lattice. An  $e^-$  in the CB and a  $h^+$  in the VB can spontaneously recombine, provided they are located at the same place in both real- and  $k$ -space, releasing the energy difference in the form of a photon. This full process, excitation of an  $e^-h^+$ -pair by absorption of a photon, relaxation of the charge carriers to their respective band edges and subsequent emission of a photon of lower energy is referred to as a photoluminescence (PL) process. This process can be utilised to obtain information on the band structure of a semiconductor and is one of the fundamental optical spectroscopy techniques employed in this work.

Close to the  $\Gamma$ -point ( $k = 0$ ), which is the interesting region considering the optical properties of a semiconductor, both valence and conduction band can be approximated by a parabolic function:

$$E(k) = E_0 + \frac{\hbar^2 k^2}{2m^*}, \quad (2.1)$$

where  $m^*$  is referred to as the effective mass and describes the curvature of the band  $E(k)$ :

$$m^* = \hbar \left[ \frac{d^2 E}{dk^2} \right]^{-1} \quad (2.2)$$

This makes it possible to describe the movement of an electron/hole in the CB/VB as analogous to the movement of a free particle in vacuum ( $E = \frac{p^2}{2m}$ ) but with a modified mass, the effective mass.

A closer look at the band structure of GaAs in figure 2.1(b) reveals that, in contrast to the CB, the VB is composed of three sub-bands. Two of these bands are degenerated at the  $\Gamma$ -point but have a different curvature and thus a different effective mass, which is why these two bands are referred to as light-hole (lh) and heavy-hole (hh) band. Separated by  $\Delta_{\text{so}}$  at the  $\Gamma$ -point is the so-called split-off band (so). For the semiconductors considered here,  $\Delta_{\text{so}}$  is large enough ( $\Delta_{\text{so}} = 340 \text{ meV}$  for GaAs [36]) so that the so-band can be neglected for the considerations of the optical properties. The splitting of the VB is caused by the fact that it arises from  $p$ -orbitals with an angular momentum of  $l = 1$ , whereas the CB derives from  $s$ -like orbitals ( $l = 0$ ). This enables the spin-orbit interaction for the VB and subsequently results in the splitting into sub-bands.

At low temperatures, the attractive Coulomb force between an electron and a hole can lead to the formation of a bound state which is referred to as exciton. Such an exciton can be described much like a hydrogen atom and, accordingly, the exciton binding energy is given by:

$$E_X = \frac{e^4}{32\pi^2\hbar^2} \frac{\mu}{\epsilon^2} \approx 4.2 \text{ meV} \quad (2.3)$$

which is in good agreement with experimentally determined values for GaAs [37]. Here  $\mu$  describes the effective reduced mass  $\mu = \left(\frac{1}{m_e^*} + \frac{1}{m_h^*}\right)^{-1}$  and  $\epsilon$  the dielectric constant of the material ( $\epsilon = 13.1 \cdot \epsilon_0$  for GaAs). The spatial extent of an exciton, the exciton radius  $r_X$ , can be determined to be:

$$r_X = \frac{4\pi\hbar^2}{e^2} \frac{\epsilon}{\mu} \approx 13 \text{ nm}. \quad (2.4)$$

Confining an exciton on length scales in the order of  $r_x$  leads to a quantum mechanical confinement and, thus, to the formation of discrete energy levels for the motion of particles in the confined direction. A quantum confinement in all three spatial directions consequently leads to a full quantisation of the energy levels and is the fundamental principle for the formation of quantum dots. To achieve such a confinement different semiconductors with different bandgap energies have to be used. In this work the semiconductors GaAs, AlAs, InAs and their respective ternary alloys  $\text{Al}_x\text{Ga}_{1-x}\text{As}$  and  $\text{In}_x\text{Ga}_{1-x}\text{As}$  are used. The bandgaps for GaAs, AlAs and InAs for the  $\Gamma$ -,  $L$ - and  $X$ -points are summarized in the following table:

## 2. Semiconductor quantum dots

---

	GaAs	AlAs	InAs
$E_g^\Gamma$	1.519 eV [38]	3.099 eV	0.417 eV
$E_g^L$	1.815 eV [39]	2.46 eV	1.133 eV
$E_g^X$	1.981 eV [39]	2.24 eV	1.433 eV

Table 2.1.: Bandgap energies for GaAs, AlAs and InAs at the three high symmetry points in  $k$ -space. [40]

For a ternary alloy ( $A_{1-x}B_x$ ), the dependence of the bandgap on alloy composition can often be described by a quadratic formula [41]:

$$E_g(A_{1-x}B_x) = (1-x) \cdot E_g(A) + x \cdot E_g(B) - x(1-x) \cdot C \quad (2.5)$$

which is basically a linear interpolation between  $E_g(A)$  and  $E_g(B)$ , expanded by a quadratic correction described by the bowing parameter  $C$ . This bowing parameter depends on the ternary alloy and the respective bandgap. For  $Al_xGa_{1-x}As$  and  $In_xGa_{1-x}As$ , the respective parameters for  $C$  are summarized in the following table:

	$Al_xGa_{1-x}As$	$In_xGa_{1-x}As$
$E_g^\Gamma$	$(-0.127 + 1.31 \cdot x)$ eV [42]	0.477 eV [40]
$E_g^L$	0 eV [43]	0.33 eV [40]
$E_g^X$	0.055 eV [44]	1.4 eV [40]

Table 2.2.: Bowing parameter  $C$ , a summary of all parameters can be found in [40]

The resulting bandgaps  $E_g^\Gamma$ ,  $E_g^X$  and  $E_g^L$  for  $Al_xGa_{1-x}As$  are plotted in figure 2.2(a) as a function of  $x$ . With increasing aluminium content  $x$ , all of the bandgap energies increase but with different slopes. This results in the reversal of the band ordering around  $x = 0.4$  and to the transition from a direct to an indirect semiconductor. Besides the bandgap energy, the lattice constant  $c$ , an important parameter that has to be considered for heteroepitaxy, also changes with the composition of a ternary alloy semiconductor. The course of the lattice constant  $c$  as a function of the composition  $x$  can usually be interpolated linearly. For  $Al_xGa_{1-x}As$ , the lattice constant can be described by [45]:

$$c(Al_xGa_{1-x}As) = (5.6533 + 0.0078 \cdot x) \text{Å} \quad (2.6)$$

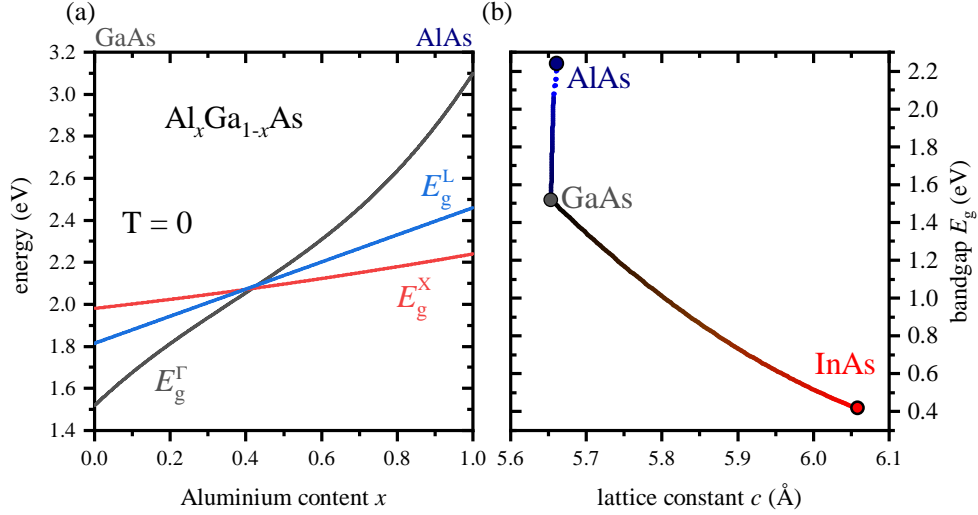


**Figure 2.2.:** (a) Bandgap energies of  $\text{Al}_x\text{Ga}_{1-x}\text{As}$  as a function of aluminium content  $x$ , for the  $\Gamma$ -, L- and X- points. Around  $x = 0.4$ ,  $\text{Al}_x\text{Ga}_{1-x}\text{As}$  is going from a direct to an indirect semiconductor. (b) Bandgap energies as a function of lattice constant  $c$  for AlAs, GaAs, InAs and their ternary alloys. Solid lines denote direct bandgaps, while dotted lines denote indirect bandgaps.

Going from GaAs to AlAs means a relative increase of the lattice constant of well below 1%, making the epitaxial growth of  $\text{Al}_x\text{Ga}_{1-x}\text{As}$  possible for any aluminium content  $x$ . In contrast, for  $\text{In}_x\text{Ga}_{1-x}\text{As}$ , the lattice constant depends much more strongly on the composition [40]:

$$c(\text{In}_x\text{Ga}_{1-x}\text{As}) = (5.6533 + 0.405 \cdot x) \text{Å} \quad (2.7)$$

resulting in an about 7% larger lattice constant  $c$  for InAs compared to GaAs. Figure 2.2(b) shows the bandgap  $E_g$  for  $\text{Al}_x\text{Ga}_{1-x}\text{As}$  and  $\text{Al}_x\text{Ga}_{1-x}\text{As}$  as a function of the lattice constant  $c$ , illustrating the accessible range for the bandgap energies using these semiconductors. While AlAs has a larger bandgap than GaAs, InAs has a smaller one. The dotted line segment indicates the range where  $\text{Al}_x\text{Ga}_{1-x}\text{As}$  is an indirect semiconductor. The strong increase of the lattice constant going from GaAs to InAs can also nicely be seen. Although this lattice constant mismatch prevents epitaxial growth of thick layers of InAs on GaAs, it plays a vital role in the growth of semiconductor quantum dots, which will be considered in section 4.1.

## 2.2. Low dimensional semiconductor systems

Even though the growth of QDs will be considered in a later section (see section 4.1), the confinement potential of a QD and its influence on its energy states and thus optical properties will already be discussed in this section. Figure 2.3(a) shows a transmission

electron micrograph of an InGaAs-QD embedded in a GaAs matrix. This cross-section

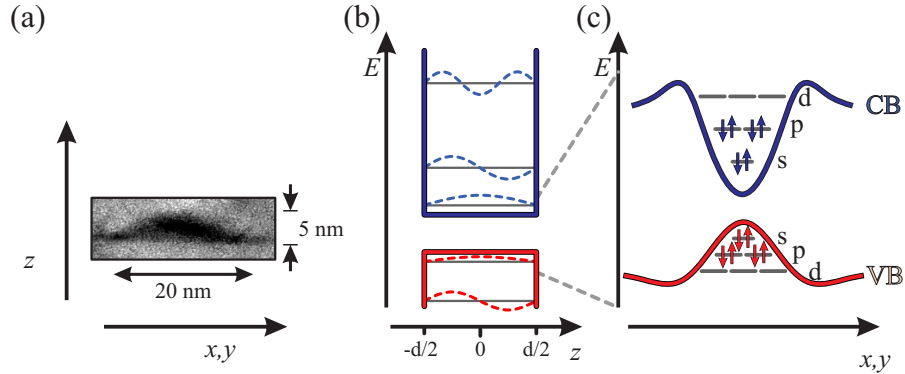


**Figure 2.3.:** (a) Transmission electron micrograph of an  $\text{In}_x\text{Ga}_{1-x}\text{As}$ -QD (dark area) within a GaAs matrix, adapted from [46]. (b) Confinement in the  $z$ -direction can be described by an infinite potential barrier, leading to the formation of sub-bands for both electrons and holes. (c) Additional harmonic potential confinement in  $x$ - and  $y$ -direction results in the formation of discrete states.

reveals the size of the  $\text{In}_x\text{Ga}_{1-x}\text{As}$ -QD, with a height of about 5 nm in the  $z$ -direction (growth direction) and a much larger extension of several tens of nanometres in the  $x$ - and  $y$ -directions. Since the QD itself has a lower bandgap compared to the surrounding GaAs matrix, both electrons and holes are efficiently confined within the QD. For the  $z$ -direction (growth direction), the confinement can be approximated by an infinite potential well of width  $d$ :

$$V_z = \begin{cases} \infty & , \text{ for } -\frac{d}{2} \leq z \leq \frac{d}{2} \\ 0 & , \text{ for } \frac{d}{2} < |z| \end{cases} \quad (2.8)$$

This potential is depicted in figure 2.3(b) for the conduction and valence band. The solutions for this well known particle in a box model are discrete energy levels in the direction of the confinement:

$$E_z^{e,h} = \frac{\pi^2 \hbar^2}{2m_{e,h}} \frac{n_z^2}{d^2} \quad (2.9)$$

The spacing of the energy levels  $E_{n_z}^{e,h}$  increases with decreasing width  $d$  and with the quantum number  $n_z (= 1, 2, 3, \dots)$ . For no further confinement in the  $x$ - and  $z$ -direction, such a confinement is called a quantum well (QW). Particles in such a QW still have a continuous energy band, as the motion in  $x$ - and  $y$ -direction is still continuous but the energy levels are split in  $n_z$  subbands. Although the assumption of infinite potential wells is a strong simplification, it shows the same inverse quadratic dependence of the energy level splitting with confinement length  $d$  as a QD does. As this confinement in the  $z$ -direction is significantly stronger compared to the ones in  $x$ - and  $y$ -direction, only the lowest energy level ( $n_z = 1$ ) with respect to the  $z$ -direction has to be taken into account here. The confinement in the other two spatial directions  $x$  and  $y$  is much weaker and can

be described by a harmonic oscillator potential:

$$V_{x,y} = \frac{1}{2}m^*(\omega_x^2x^2 + \omega_y^2y^2) \quad (2.10)$$

assuming the harmonic oscillator potential is radial symmetric ( $\omega = \omega_x = \omega_y$ ) the energy states can be determined to be:

$$E_{x,y}^{e,h} = \hbar\omega(n_x + n_y + 1) \quad (2.11)$$

with the quantum numbers  $n_x, n_y = 0, 1, 2, \dots$ , one for each spatial direction. The energy of such a two dimensional harmonic oscillator state is given by the sum of both of these quantum numbers  $l = n_x + n_y$ . Following the atom physics nomenclature, the possible energy levels are labelled  $s$ -,  $p$ -,  $d$ -,...-shell for  $l = 0, 1, 2, \dots$ , respectively. With the exception of the lowest shell ( $l = 0$ ), all energetically higher states are degenerate, meaning that different combinations of  $n_x$  and  $n_y$  lead to the same value for  $l$ . In general, for any quantum numbers  $n_x$  and  $n_y$ , there are a total of  $(n_x + n_y + 1) = (l + 1)$  degenerate states. Taking into account that each of these states can be occupied by two electrons/holes with anti-parallel spin, the maximum number of electrons/holes in a given shell  $l$  of the QD is given by:

$$2 \cdot (l + 1) = 2 \cdot (n_x + n_y + 1) \quad (2.12)$$

A schematic of the confinement potential of a QD is shown in figure 2.3 (c). An approximately parabolic confinement potential causes the formation of equally spaced energy levels for electrons in the conduction band and holes in the valance band. Each of these energy states can be occupied by two charge carriers with anti-parallel spin so the  $s$ -,  $p$ - and  $d$ -shells can be occupied by a maximum of two, four and six charge carriers respectively. For the experiments presented in this work, only optical transitions between  $s$ -shells are considered and all higher energy levels can be neglected. According to the previous considerations, the energy difference  $E_{\text{trans}}$  between the  $s$ -shell state in the valance band and the  $s$ -shell in the conduction band is given by the sum of the bandgap  $E_g$  of the material the QD is made of and the confinement energies  $E_z^{e,h}(n_z = 1)$  and  $E_{x,y}^{e,h}(l = 0)$  for the in- and out-of plane confinement for electrons and holes, respectively:

$$E_{\text{trans}} = E_g + \underbrace{E_z^h(n_z = 1) + E_z^e(n_z = 1)}_{z\text{-confinement}} + \underbrace{E_{x,y}^h(l = 0) + E_{x,y}^e(l = 0)}_{x,y\text{-confinement}} = E^e + E^h \quad (2.13)$$

In a first approximation, this energy corresponds to the energy that is emitted in the form of a photon, when an electron and a hole in the  $s$ -shell recombine. For a more detailed consideration, the Coulomb interaction between charge carriers, confined within a QD, has to be taken into account. The energy shift due to Coulomb interaction depends on the number of electrons and holes confined in a QD and therefore has to be considered

separately for different occupancy states. As only s-shell transitions shall be considered here, only four different optically active occupancy states, shown in figure 2.4, have to be taken into account. The simplest charge carrier configuration is the one containing only a

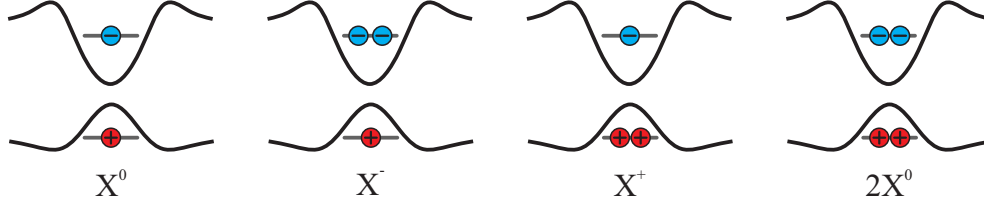


**Figure 2.4.:** All four types of optically active excitonic s-shell states. The neutral exciton  $X^0$  contains one electron and one hole. The charged excitons  $X^-$  and  $X^+$  contain an additional electron or hole. For the neutral biexciton  $2X^0$ , both s-shells are fully filled with two electrons and holes, respectively.

single electron and a single hole, referred to as neutral exciton  $X^0$ . Adding an additional electron or hole leads to the negatively or positively charged exciton  $X^-$  and  $X^+$ . If the s-shells are fully occupied by two electrons and two holes, the excitonic state is called the neutral biexciton  $2X^0$ . The occupancy states containing only one electron or one hole are not considered here as they are not optically active and are thus referred to as dark state. Considering the two different spin orientations that are possible for the charge carriers, the occupancy states shown in figure 2.4 can be further subdivided. For the charged excitons  $X^-$  and  $X^+$ , two configurations can be distinguished for each case and, for the neutral exciton  $X^0$ , there are four different configurations. For two of these spin configurations of the neutral exciton  $X^0$ , the ones with parallel spins for the  $e^-$  and  $h^+$ , are forbidden optical transitions and the respective states are also considered dark excitons.

The absolute energy of an excitonic state is then given by the confinement energies of electrons ( $E^e$ ) and holes ( $E^h$ ) and the Coulomb interaction between the charge carriers confined in the QD. In a first order approximation for the Coulomb interaction all possible interactions between two charge carriers are taken into account. As a result the energies for all optical active s-shell occupancy states are given by:

$$\begin{aligned}
 E_{X^0} &= E^e + E^h - V^{eh} \\
 E_{X^-} &= 2E^e + E^h - 2V^{eh} + V^{ee} \\
 E_{X^+} &= E^e + 2E^h - 2V^{eh} + V^{hh} \\
 E_{2X^0} &= 2E^e + 2E^h - 4V^{eh} + V^{ee} + V^{hh}
 \end{aligned}$$

It can be seen that the attractive interaction between an electron and a hole ( $V^{eh}$ ) leads to a reduction of the overall energy, whereas the repulsive interaction between two electrons ( $V^{ee}$ ) or two holes ( $V^{hh}$ ) leads to an increase of the overall energy. The transition energy of a state, meaning the energy that is released by the recombination of an  $e^-$ - $h^+$ -pair and thus the energy of the emitted photon, is given by the energetic difference between the

initial and final state of the transition:

$$\Delta E = E_{\text{initial}} - E_{\text{final}} \quad (2.14)$$

The energy of a photon emitted from one of the optical active s-shell occupancy states depicted in figure 2.4 is therefore given by:

$$\begin{aligned} \Delta E_{X^0} &= E^e + E^h - V^{\text{eh}} \\ \Delta E_{X^-} &= E^e + E^h - 2V^{\text{eh}} + V^{\text{ee}} \\ \Delta E_{X^+} &= E^e + E^h - 2V^{\text{eh}} + V^{\text{hh}} \\ \Delta E_{2X^0} &= E^e + E^h - 3V^{\text{eh}} + V^{\text{ee}} + V^{\text{hh}} \end{aligned}$$

Since the interaction energies  $V^{\text{ee}}$ ,  $V^{\text{hh}}$  and  $V^{\text{eh}}$  are in general not identical, the different transition energies are not equal. Typical splittings are in the order of several meV, depending on the interaction terms  $V^{\text{xx}}$ . Since the hole wave function is typically more strongly localized than the electron wave function, an ordering of  $V^{\text{ee}} < V^{\text{eh}} < V^{\text{hh}}$  is often found [47]. Therefore, the  $X^+$  emission is expected to be shifted towards higher and the  $X^-$  emission towards lower energies with respect to the  $X^0$  emission. The energy shift ( $\Delta E_{X^0} - \Delta E_{2X^0}$ ) between the neutral exciton and the biexciton is referred to as the biexciton binding energy and is typically positive, meaning the biexciton emission is shifted towards lower energies [48, 49]. This ordering is often found for self-assembled QDs but the exact ordering strongly depends on the geometry of the respective quantum dot and can vary from system to system. In conclusion, the interaction of charge carriers within a QD leads to a splitting of the QDs emission into discrete lines, making it possible to optically address a specific QD transition of a single QD.

The simplest and most common method to probe the energy states of a semiconductor QD (or any other optically active semiconductor) is photoluminescence spectroscopy (PL). This technique is depicted in figure 2.5(a). An above bandgap laser is used to excite electrons from the valance band into the conduction band, leaving behind holes in the valance band. Both electrons and holes relax to their respective energetically most favourable state, where excess energy and momentum is transferred to the crystal lattice in the form of phonons. This relaxation process happens on a fast time scale (typically  $< 1$  ps) and leads to the occupation of the different energy levels of the QDs. Within the characteristic decay time ( $\approx 1$  ns) of such a state, electrons and holes can recombine through the emission of a photon. The emitted photons are collected and detected as a function of their respective energy and, thereby, a PL spectrum is obtained.

Figure 2.5(b) shows a photoluminescence spectrum of a sample containing InGaAs QDs. The spectrum consists of a series of sharp emission lines, originating from different occupancy states of several QDs. As the growth of QDs is a self-organized, statistical process (see section 4.1), the size of a QD and, therefore, its transition energies are distributed over a certain range that can be influenced by the growth parameters. To enable the observation of

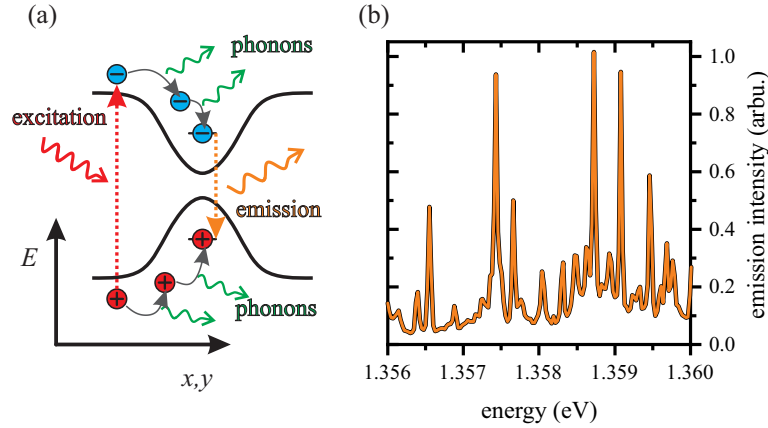


**Figure 2.5.:** (a) Schematic process of photoluminescence. Charge carriers are excited by an above bandgap laser (red arrow). Electrons/holes relax to their respective lowest energetic state in the CB/VB under emission of phonons. From these states, electrons and holes can recombine through photon emission (orange arrow). (b)  $\mu$ -PL spectrum of a sample containing QDs. Sharp emission lines can be attributed to different occupancy states of individual QDs.

single QDs, their respective density has to be sufficiently small, while the spatial resolution of the optical setup has to be high (typically  $\approx 1 \mu\text{m}$ ). This is why corresponding setups are usually referred to as  $\mu$ -PL setups.

To attribute a specific emission line to a certain occupancy state, excitation laser power dependent measurements can be performed. The excitation power determines the number of free charge carriers that can be captured by a QD and thus the occupancy that is formed. More details on this method can be found in the references [48, 49].

A distinction between neutral and charged exciton can be made based on the polarisation of an emission line. As a photon carries a spin of 1 and the angular momentum has to be preserved in an optical transition, the electron and hole involved in a transition have to carry opposite spin. For the neutral exciton  $1X^0$ , this enables two optically active spin configurations ( $(\uparrow\downarrow), (\downarrow\uparrow)$ ). For a perfect QD, these two configurations are degenerate and, depending on the spin orientation, either a left or right circularly polarised photon is emitted. Such a perfect system enables the creation of polarisation entangled photons from the biexciton-exciton cascade [16, 50]. A real QD usually does not exhibit a perfect symmetry, resulting in the cancellation of the degeneration of the two  $X^0$  configurations due to exchange interaction [51]. The  $X^0$  emission therefore splits up in two emission lines, which are linearly polarised perpendicularly to each other and separated by the fine structure splitting (FSS). For the charged excitons  $X^-$  and  $X^+$  and the neutral biexciton  $2X^0$ , at least one charge carrier species is in the singlet state and no fine structure splitting occurs for these states. Though the final state of the biexciton emission, the neutral exciton  $X^0$ , is subject to FSS, so that the biexciton emission line also shows a FSS. The FSS (typically in the range of several tens of  $\mu\text{eV}$ ) can be identified by polarisation dependent

PL measurements and thus allows for a distinction between neutral and charged excitons. In the context of this work, only individual emission lines will be considered, consequently the identification of the associated occupancy state is of less importance. To ensure that an emission line contains only the light of a single QD and not the emission of several QDs in close proximity that coincidentally emit at the same energy, one can measure a distinct characteristic of a single QD: single photon emission. Since after the decay of a certain occupancy state, it takes a certain time to re-populate this state, photon from this state can be emitted in the meantime. Such a single emission line stemming from a single QD can be considered a single photon source. This means that only one photon is emitted at a time, something that does not occur for classical light sources. The experimental

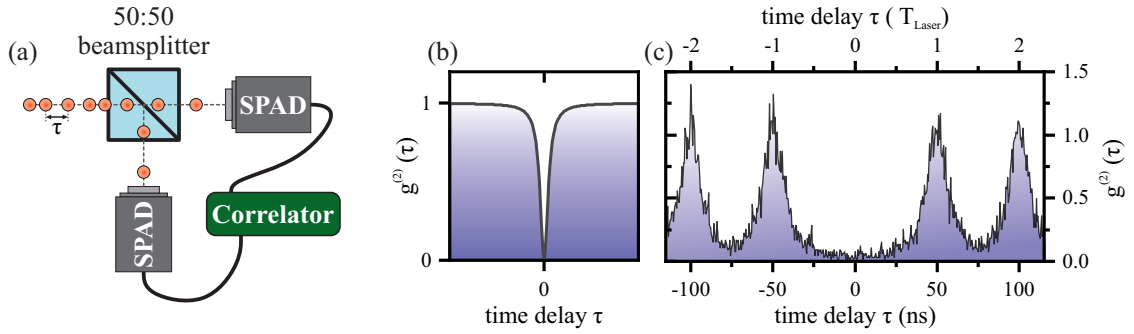


**Figure 2.6.:** (a) Schematic of a Hanbury Brown and Twiss (HBT) interferometer. The incoming optical signal is divided by a beam splitter, detected by two single photon avalanche diodes (SPAD). The second order correlation function  $g^{(2)}$ , the time difference  $\tau$  between a detection event at the two detectors, is determined by a correlator. (b) Schematic of the  $g^{(2)}$  function expected for a continuously pumped two level system. The dip at  $\tau = 0$  proves single photon emission. (c) Measured  $g^{(2)}$  function for a QD excited with a pulsed laser, showing correlation peaks separated by the laser pulse period  $T_{\text{laser}}$ . Here, the missing peak at  $\tau = 0$  indicates single photon emission.

proof of single photon emission can be provided by the use of a Hanbury Brown and Twiss interferometer (HBT), as depicted in figure 2.6. The collected light is split in two paths by a 50:50 beam splitter and detected by two single photon avalanche diodes (SPAD). The electrical detection signal of the two SPADs is then correlated, meaning the time difference  $\tau$  in which the two detectors detect a photon is determined and saved in a histogram. This histogram corresponds to the second order correlation function  $g^{(2)}(\tau)$  of the collected light. In the case of single photon emission, it is not possible to detect a photon at both detectors simultaneously, resulting in  $g^{(2)}(\tau = 0) = 0$ , which is referred to as photon anti-bunching. A direct measurement of the intensity as a function of time with a single detector and a subsequent calculation of the intensity correlation is not possible, due to shortcomings of commercially available detectors<sup>1</sup>. Figure 2.6(b) shows the expected  $g^{(2)}(\tau)$  function

<sup>1</sup>Typical detectors with a time resolution faster than the decay time of a QD, provide no information on the number of photons that triggered a count. Furthermore, these detectors have dead times of several tens of nanoseconds, within which no further photons can be detected.

of a QD excited by a continuous wave (cw) laser, showing a characteristic dip at  $\tau = 0$ . This anti-bunching dip is a direct evidence of single-photon emission and the width of this dip reflects the decay time  $\Gamma_{\text{QD}}$  of the QD. In figure 2.6(c), the measured  $g^{(2)}$  function of a QD, excited by a pulsed laser ( $f_{\text{laser}} = \frac{1}{T_{\text{laser}}} = 20$  MHz), is shown. Here, individual correlation peaks<sup>2</sup>, separated by  $1/20$  MHz = 50 ns, can be seen, while the central peak at  $\tau = 0$  is missing, indicating single photon emission. The advantage of pulsed excitation is the lower requirement on the detectors time resolution that is no longer set by the decay time  $\Gamma_{\text{QD}}$  of the QD but by the repetition period of the exciting laser. For semiconductor QDs, single photon emission was first demonstrated in 2000 [15].

---

<sup>2</sup>Note that the temporal width of the correlation peaks is comparatively large, indicating very slow decay time  $\Gamma_{\text{QD}}$ . This is because the investigated QD is located within the photonic bandgap of a photonic crystal, resulting in a greatly enhanced decay time. This will be covered in detail in section 9.1.1.

## 3. Surface acoustic waves

Surface acoustic waves (SAW) are mechanical waves that propagate along the surface of a solid. These acoustic modes are confined to small volumes close to the surface and can propagate over large distances with only low dissipation. The industrial significance of SAWs is justified by their low propagation velocities and the possibility to easily excite SAWs by electrical signals on a piezoelectric substrate. These properties allow easy conversion of electrical radio frequency (rf) signals to small wavelength SAWs and thus enable the realisation of high quality frequency filters on a chip scale. Such SAW filters are an integral part of modern wireless communication networks (mobile phones, wireless LAN...). Furthermore, SAWs are suitable for controlling and manipulating quantum systems as they can be easily generated up to the low Gigahertz range and strongly interact with any system that is located at or close to the surface of a substrate.

In this chapter, the basic wave equations describing SAW propagation are treated first. After that, the solution of these wave equations is carried out by means of the finite element method (FEM) for GaAs and  $\text{Al}_x\text{Ga}_{1-x}\text{As}$ , the material systems used in this work. Finally, the excitation of SAWs on piezoelectric substrates using so-called interdigital transducer (IDT) is addressed.

A more detailed derivation for the surface acoustic wave equations and the basic properties of SAWs can be found in various textbooks [52–55].

### 3.1. Basic properties

First, any particle (elementary region of the material) inside a solid with an equilibrium position of  $\mathbf{x} = (x_1, x_2, x_3)$  is considered. If this particle is displaced by  $\mathbf{u} = (u_1, u_2, u_3)$  from its equilibrium, it has a new position  $\mathbf{x} + \mathbf{u}$  and internal forces try to restore the equilibrium. As there will be no internal forces when the material is displaced or rotated as a whole, it is more convenient to look at the deformation of the material, rather than the displacement. This deformation is described by the strain tensor  $\mathbf{S}$ , defined by:

$$S_{ij}(x_1, x_2, x_3) = \frac{1}{2} \left( \frac{\partial u_i}{\partial x_j} + \frac{\partial u_j}{\partial x_i} \right) \quad i, j = 1, 2, 3 \quad (3.1)$$

for a point  $\mathbf{x}$ . According to this definition, the strain is zero for a displacement  $\left( \frac{\partial u_i}{\partial x_j} = 0 \right)$  and a rotation  $\left( \frac{\partial u_i}{\partial x_j} = -\frac{\partial u_j}{\partial x_i} \right)$  of the material as a whole. As it can be seen in equation 3.1,

the strain tensor is symmetrical ( $S_{ij} = S_{ji}$ ). Therefore, only six of its nine components are independent. The internal forces of the material are described by the stress tensor  $T_{ij}$ . For an elastic material, stress and strain are proportional for small strain:

$$T_{ij}(x_1, x_2, x_3) = c_{ijkl} S_{kl} \quad i, j, k, l = 1, 2, 3 \quad (3.2)$$

Accordingly, the stress tensor shows the same symmetry as the strain tensor and has also only six independent components. The proportionality constant  $c_{ijkl}$  is called the stiffness (elasticity) tensor and is in general a fourth rank tensor ( $3 \times 3 \times 3 \times 3$ ) with 81 components. Due to the symmetry of  $S_{ij}$  and  $T_{ij}$  only 36 of these components are independent ( $c_{ijkl} = c_{jikl}$ ,  $c_{ijkl} = c_{ijlk}$ ). These relations are known as the minor symmetries of the stiffness tensor. In addition, due to thermodynamic reasons, there exists a strain energy density function  $W$  for elastic materials that is related to the stress by

$$T_{ij} = \frac{\partial W}{\partial S_{ij}} \quad (3.3)$$

With the help of equation 3.2 the stiffness tensor can be rewritten as:

$$c_{ijkl} = \frac{\partial^2 W}{\partial S_{ij} \partial S_{kl}} \quad (3.4)$$

Because the order of the differentiation is irrelevant (symmetry of second derivatives), the relation  $c_{ijkl} = c_{klij}$ , known as the major symmetry, must apply for the stiffness tensor and the number of independent components is further reduced to 21. Depending on the symmetry of the material, this number can be reduced even further. A cubic system like GaAs, for example, has only three different elements in its stiffness tensor.

Since we are not interested in static but dynamic deformations of the material, the displacement  $u(x)$  is a function of time and thus subject to Newton's second law of motion. So the force per unit volume equals the acceleration times the density  $\rho$  of the material, which is known as the wave equation:

$$\rho \frac{\partial^2 u_i}{\partial t^2} = \frac{\partial T_{ij}}{\partial x_j} \quad (3.5)$$

This equation is valid for anisotropic elastic materials but neglects piezoelectricity, which occurs in many crystals that lack internal symmetry. This effect leads to a coupling of elastic and electromagnetic waves by coupling elastic stresses and strains to electric fields and displacements. As will be shown later, the effect of piezoelectricity on the elastic behaviour is often weak but plays a crucial role for surface acoustic wave applications, as it allows the simple excitation of such waves by electrical signals. This will be discussed in the last section of this chapter (see section 3.3).

For a piezoelectric material, the stress at a certain point does not only depend on the strain but also on the electric field  $\mathcal{E}$  at this point. So in a piezoelectric material equation 3.2 has to be extended and becomes:

$$T_{ij}(x_1, x_2, x_3) = c_{ijkl}S_{kl} - e_{kij}\mathcal{E} \quad i, j, k, l = 1, 2, 3 \quad (3.6)$$

Vice versa the electric displacement of a piezoelectric does not only depend on the electrical field but also on the strain:

$$D_i = \epsilon_{ij}\mathcal{E}_j + e_{ijk}S_{jk} \quad (3.7)$$

where  $\epsilon_{ij}$  is the permittivity tensor of the material. The tensor  $e_{kij}$  relating elastic and electric fields is the piezoelectric tensor and has the symmetry  $e_{ijk} = e_{ikj}$ . Due to the coupling between elastic and electric fields, Newton's equation of motion and the Maxwell equations have to be solved simultaneously, resulting in two solutions. First an electromagnetic wave that is accompanied by mechanical strains, where most of the energy is concentrated in the electromagnetic part. As only elastic waves are of interest here, this solution can be neglected. The second solution is an elastic wave accompanied by electrical fields that travels with a speed five orders of magnitude smaller than the speed of light  $c_{\text{light}}$ . Due to this low propagation velocity, the magnetic field arising from the time dependent electric field can be neglected and the Maxwell equation simplifies to  $\nabla \times \mathcal{E} = -\frac{\partial B}{\partial t} \approx 0$  and thus, like in electrostatics, the electric field can be derived from a scalar potential:

$$\mathcal{E}_i = -\frac{\partial \Phi}{\partial x_i} \quad (3.8)$$

By using this relation in the definition of the stress in a piezoelectric, given in equation 3.6, inserting this in the elastic wave equation 3.5 and not forgetting the strain definition, the equation of motion for an elastic piezoelectric material can be written as:

$$\rho \frac{\partial^2 u_i}{\partial t^2} = e_{kij} \frac{\partial^2 \Phi}{\partial x_j \partial x_k} + c_{ijkl} \frac{\partial^2 u_k}{\partial x_j \partial x_l} \quad (3.9)$$

Assuming the material to be an insulator, there are no sources for the electrical displacement fields, which means that  $\nabla D = 0$  and thus equation 3.7 becomes:

$$e_{jkl} \frac{\partial^2 u_l}{\partial x_j \partial x_k} - \epsilon_{jk} \frac{\partial^2 \Phi}{\partial x_j \partial x_k} = 0 \quad (3.10)$$

The equations 3.9 and 3.10 provide a total of four equations. The four solutions for  $u_i$  and  $\Phi$  and with it the wave propagation in a piezoelectric can be determined, provided that proper boundary conditions are applied.

As surface acoustic waves, propagating along a surface, are of interest here, an infinite crystal that occupies the half space  $x_3 < 0$  is considered. At the surface of the material,

### 3. Surface acoustic waves

---

there can be no stress components perpendicular to the surface, leading to the mechanical boundary condition:

$$T_{31} = T_{32} = T_{33} = 0|_{x_3=0} \quad (3.11)$$

Due to this boundary condition, the material is less rigid at the surface, which results in a lower phase velocity for waves propagating at the surface compared to waves in the bulk material. Since only these waves are of interest here, another boundary condition for the displacement can be introduced:

$$u_i = 0|_{x_3 \rightarrow -\infty} \quad (3.12)$$

As piezoelectric materials are considered, electrical boundary conditions need to be defined in addition to mechanical boundary conditions. On the one hand, the electric potential at the surface/interface of the piezoelectric has to be continuous

$$\Phi|_{\substack{x_3 \rightarrow 0 \\ x_3 < 0}} = \Phi|_{\substack{x_3 \rightarrow 0 \\ x_3 > 0}} \quad (3.13)$$

and, on the other hand, like the displacement, the potential has to vanish far away from the surface:

$$\Phi = 0|_{x_3 \rightarrow \pm\infty} \quad (3.14)$$

The boundary conditions for the electrical fields depend on the material occupying the half-space ( $x_3 > 0$ ). If the material is a perfect dielectric (no free charges), the normal component of the electrical displacement field  $D_3$  and the tangential components of the electric field  $E_{1,2}$  are continuous. If the surface is covered by a metal, the electric potential and the tangential fields ( $E_{1,2}$   $D_{1,2}$ ) vanish at the surface/interface and the normal component of the electric displacement field  $D_3$  is no longer continuous.

The different boundary conditions have influence on the phase velocity of a surface wave. Therefore, two extreme cases for the velocity, depending on the permittivity  $\epsilon_d$  of the adjacent medium, can be distinguished:

- **short-circuit condition:** the surface is covered by a thin metallic film ( $\Phi|_{x_3=0} = 0$ ;  $\epsilon_d = \infty$ ) that eliminates the tangential electrical fields on the surface ( $D_1|_{x_3=0} = 0$ ) leading to a velocity  $v_\infty$
- **open-circuit condition:** the surface is covered with a hypothetical medium with permittivity  $\epsilon_d = 0$ , leading to  $D_3|_{x_3=0} = 0$  and to a phase velocity of  $v_0$

For the experiments shown here, vacuum/air ( $\epsilon_d = 1$ ) lies on top of the crystal leading to a phase velocity of  $v_r$  that lies between the two extreme cases  $v_0 > v_r > v_\infty$  but close to the open circuit condition  $v_0 \approx v_r$ .

Using these two extreme cases, the electromechanical coupling coefficient  $K_S$  can be defined:

$$K_S^2 = \frac{v_0^2 - v_\infty^2}{v_0^2 + \frac{\epsilon_d}{\epsilon_p} v_\infty^2}, \quad (3.15)$$

with  $\epsilon_p$  being the permittivity of the piezoelectric. The square of the coupling coefficient  $K_S^2$  indicates the portion of electrical energy that is converted to mechanical energy, if applied to the surface. Therefore  $0 \leq K_S \leq 1$  applies for the coupling coefficient and it is a measure of how well a particular material (depending on surface orientation and direction of wave propagation) is suited for the excitation of surface acoustic waves using electrical signals as it will be described in section 3.3.

The solution of the surface wave that is important for this work is the so-called Rayleigh wave [56], named after Lord Rayleigh who first described it in 1885. These Rayleigh waves are polarised in the plane defined by the surface normal and the propagation direction, also known as the sagittal plane. Due to the complexity of the equations, it is usually not possible to analytically find this solution for an anisotropic material. Therefore, the solution of the wave equations by means of finite element modelling (FEM) will be discussed in the following section.

## 3.2. Finite Element Modelling of surface acoustic waves

Since the sought solution is a wave that is periodic in space, considerations can be limited to one unit cell of the expected wave mode. Applying appropriate boundary conditions to this unit cell, the Rayleigh wave modes are given by the eigenfrequency and - mode of the unit cell, which can be determined using an eigenfrequency-solver. The first step in

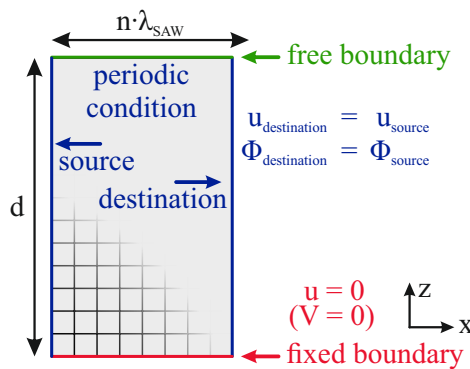


**Figure 3.1.:** Basic structure of a unit cell used to simulate surface acoustic wave by FEM. By setting the appropriate boundary conditions, the surface acoustic wave mode is an eigenmode of the unit cell.

this process is to define such a unit cell and the appropriate boundary conditions, which is shown in figure 3.1. In the following considerations, the propagation of the wave is assumed to be in the  $x$ -direction and the surface normal is assumed to be the  $z$ -direction. As for Rayleigh waves, the motion of a particle is limited to the sagittal  $(x, z)$  plane displacement and electric potentials are constant along the  $y$ -direction. This means that in this direction the material is considered to be infinite and thus the strain in this direction can be assumed to be zero, simplifying the simulation to two dimensions. In the  $x$ -direction, the wave is periodic. Therefore, the length of the unit cell in this direction is defined as a multiple integer of the surface acoustic wave wavelength,  $n \cdot \lambda_{\text{SAW}}$ , thus periodic boundary conditions are applied for both the displacement  $u$  and the electric potential  $\Phi$ . One of the two boundaries in  $x$ -direction is defined as source, the other as destination and the displacement  $u$  and potential  $\Phi$  for the destination boundary are set equal to the values of the source boundary ( $u_{\text{destination}} = u_{\text{source}}$ ,  $\Phi_{\text{destination}} = \Phi_{\text{source}}$ ). For the surface ( $z = 0$ ) of the unit cell, a free boundary condition is applied, meaning that there are no constrains or loads acting on this surface. Defining a boundary condition for the bottom of the unit cell is difficult, as there is no periodicity, nor a real boundary within the material in this direction <sup>1</sup>. When defining a bottom boundary condition, advantage has to be taken of the fact that the wave itself is confined to a small layer near the surface and decays exponentially within the material. If the height  $d$  of the unit cell is chosen to be sufficiently large ( $\approx 3 - 4 \cdot \lambda_{\text{SAW}}$ ), the bottom boundary can be assumed as being mechanically fully constrained (zero displacement in all directions) and having a constant electric potential (it is most convenient to set this potential to zero, thus defining a fixed reference). After defining this unit cell, it is assigned a material and its corresponding values for density  $\rho$ , elasticity tensor  $c$ , coupling matrix  $e$  and dielectric permittivity  $\epsilon$  are fixed. The elastic parameters used for the simulations presented in this work are summarized in Appendix A. In the next step, the unit cell is divided in finite elements and the underlying electro-mechanical equations are numerically solved for each of these elements, ensuring continuity to all neighbouring elements. This allows to find the eigenmodes and the corresponding eigenfrequencies for a given unit cell. The size of the finite elements must be chosen small enough to sufficiently approximate the physical problem but not too small, in order to limit the computational complexity of the problem. From the obtained eigenfrequency, the sound velocity  $v_{\text{SAW}}$  of the material can be determined by

$$v_{\text{SAW}} = \lambda_{\text{SAW}} \cdot f_{\text{SAW}} \quad (3.16)$$

in which  $\lambda_{\text{SAW}}$  is determined by the width of the unit cell. The sound velocity determined by equation 3.16 is a constant for a given material and crystal orientation, accordingly the corresponding value of  $\lambda_{\text{SAW}}$  does not have an effect on the obtained solution. When

---

<sup>1</sup>The thickness of the sample is considered to be much larger than the acoustic wavelength  $d \gg \lambda_{\text{SAW}}$ , if this is not the case so-called lamb Waves have to be considered.

elements that do not scale with the acoustic wavelength are introduced, dispersion has to be taken into account, which will be shown in section 4.1.3.

Beside the eigenfrequency, the associated eigenmode is also obtained by the simulation. This eigenmode contains the motion pattern of the particles in the system and the spatial profile of the electric potential. From this displacement and potential field, further parameters like hydrostatic pressure and electric fields can be calculated, considering the geometry of the unit cell. It has to be noted that only the shape and the relative amplitude and not the absolute amplitude of the eigenmode is meaningful. In order to determine the absolute amplitudes, the actual excitation of the oscillation and the damping of the system has to be taken into account. In order to be able to compare the result of different simulations, the amplitudes have to be normalized. In the scope of this work, this is done with respect to a maximum surface displacement of 1 nm in the  $z$ -direction ( $A_z = u_{z,\max}|_{z=0} = 1 \text{ nm}$ ), as this value is experimentally accessible, for instance, by means of optical interferometry [57].

### 3.2.1. Surface acoustic waves on GaAs

In this section, the most important characteristics of surface acoustic wave are explained for the example of GaAs, the material predominantly used in this work. For surface acoustic waves in GaAs, the propagation along the [110] direction on a (001)-oriented GaAs surface is of interest, since for this orientation the piezoelectric coupling is maximum. The required material parameters are summarized in Appendix A. For all simulations shown in this work, the material parameters are adapted to low temperature ( $T = 10 \text{ K}$ ) to meet the conditions under which the optical experiments were performed. Under these conditions, the FEM simulations yield a sound velocity of  $v_{\text{SAW}} = 2904 \frac{\text{m}}{\text{s}}$  for this crystal cut.

#### Mode Profile

In figure 3.2, the spatial mode profile of the Rayleigh wave is shown where the spatial dimensions are given in units of the SAW wavelength ( $\lambda_{\text{SAW}}$ ). All given quantities are normalized to a maximum surface displacement in the  $z$ -direction of  $A_z = 1 \text{ nm}$ . In the lower panel, the course of the two displacement components  $u_x$  and  $u_z$  and of the hydrostatic pressure  $p$  along the surface ( $z = 0$ ) are shown. All of these three components show the expected sinusoidal dependence. The  $\pi/2$ -phase shift between the displacement components and their different amplitudes reflect the characteristic elliptical rolling motion of a Rayleigh type wave. The hydrostatic pressure, shown by the colour code, is defined as the trace of the stress tensor:

$$p = -\frac{1}{3}(\mathbf{T}_{11} + \mathbf{T}_{22} + \mathbf{T}_{33}) = -\frac{1}{3}\text{tr}(\mathbf{T}) \quad (3.17)$$

and is thus proportional to the spatial derivative of the displacement. That means that, additionally to the wave amplitude  $A_z$ , the pressure  $p$  scales to the inverse wavelength and

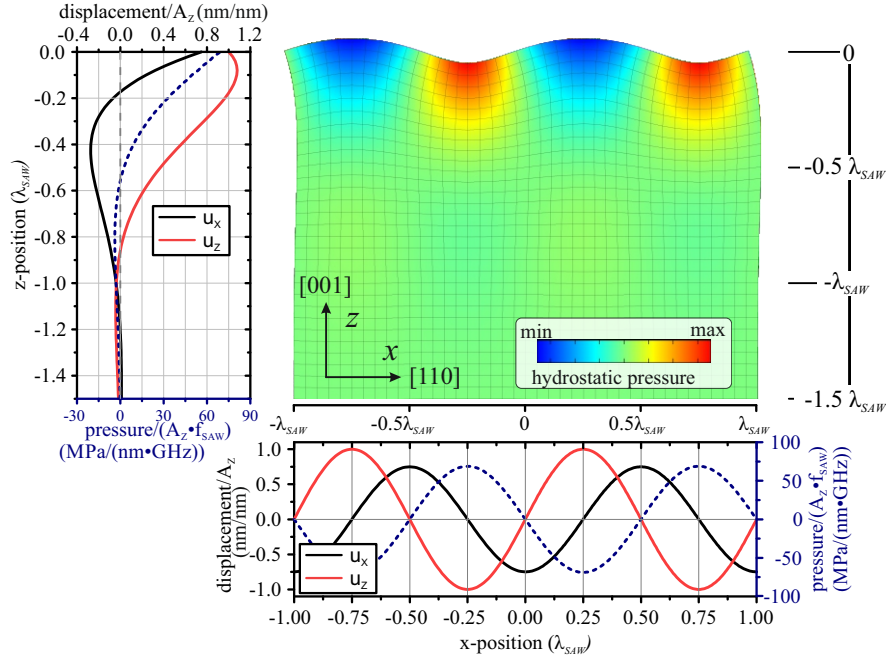


**Figure 3.2.:** Mechanical characteristics of Rayleigh wave propagation along the  $[110]$ -direction on a  $(001)$  GaAs surface. Centre panel: displacement profile ( $u_x, u_z$ ) with color overlay of hydrostatic pressure  $p$ . The displacement is not to scale. Lower panel: displacement components  $\mathbf{u}_x$  and  $\mathbf{u}_z$  and hydrostatic pressure  $\mathbf{p}$  along the surface. Left panel: depth dependence of the amplitudes of  $\mathbf{u}_x$ ,  $\mathbf{u}_z$  and  $\mathbf{p}$ . All values are scaled to  $A_z = 1$  nm and  $p$  additionally to  $f_{\text{SAW}} = 1$  GHz.

so, assuming a homogeneous and non-dispersive material, scales linearly to the surface acoustic wave frequency  $f_{\text{SAW}}$ . Hence, the values for  $p$  are scaled to a fixed surface acoustic wave frequency of  $f_{\text{SAW}} = 1$  GHz. In the left panel of figure 3.2, the respective amplitudes of the oscillations along the propagation direction for  $u_x$ ,  $u_z$  and  $p$ , again scaled with respect to  $A_z = 1$  nm and, for  $p$ , also with respect to  $f_{\text{SAW}} = 1$  GHz, are shown as a function of depth within the substrate. Since Rayleigh-type waves are strongly confined to the surface, the amplitudes are maximal at or close to the surface and decay rapidly within the material over a length scale of approximately  $0.8 \cdot \lambda_{\text{SAW}}$ .

Because GaAs is piezoelectric, the mechanical deformation induces a piezoelectric potential. This potential  $\Phi$  is shown in the colour plot in figure 3.3 with the associated electrical fields  $\mathcal{E}_x$  and  $\mathcal{E}_y$  indicated as arrows. The lower panel shows the electric potential and the electrical fields along the surface of the substrate. All values are scaled relative to the surface displacement ( $A_z = 1$  nm) and the electrical fields are additionally scaled to  $f_{\text{SAW}} = 1$  GHz, as they are proportional to the spatial derivative of the electric potential. The  $\pi/2$ -phase shift between the electrical field components reflects the gyrating motion of the electric field vector along the propagation direction or with time at a fixed point. In the left panel, the  $z$ -dependence of the amplitudes for  $\mathcal{E}_x$ ,  $\mathcal{E}_z$  and  $\Phi$  are shown. Again

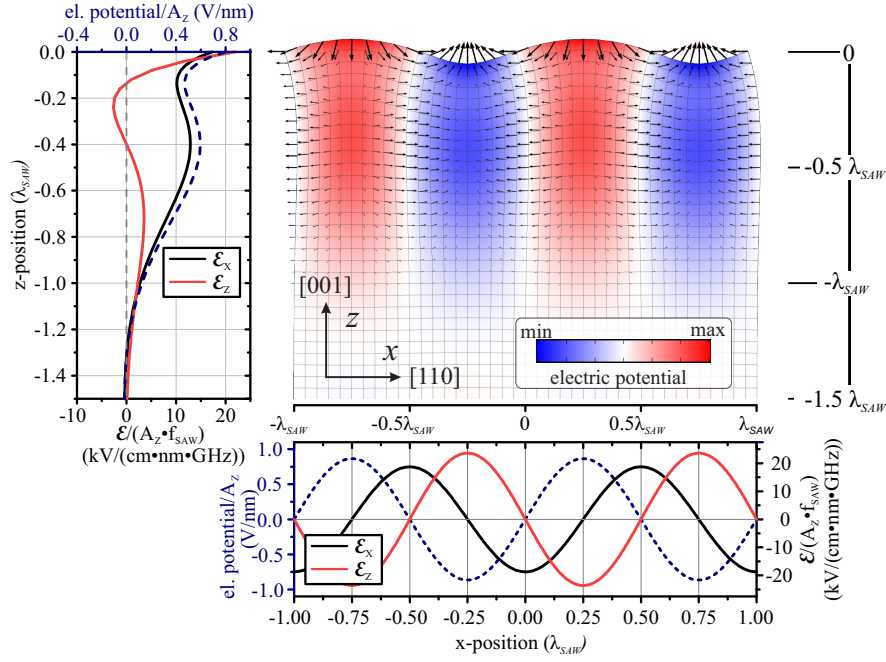


**Figure 3.3.:** Electrical characteristics of a Rayleigh wave propagation along the  $[110]$ -direction on a  $(001)$  GaAs surface. Centre panel: displacement profile  $(u_x, u_z)$  (not to scale) with colour overlay of the electric potential  $\Phi$ . The arrows indicate direction and strength of the electric field  $\mathcal{E}$  at the mesh nodes. Lower panel: electric field components  $\mathcal{E}_x$  and  $\mathcal{E}_z$  and electric pressure  $\Phi$  along the surface. Left panel: depth dependence of the amplitudes of  $\mathcal{E}_x$ ,  $\mathcal{E}_z$  and  $\Phi$ . All values are scaled to  $A_z = 1$  nm and the electric field components  $\mathcal{E}_x$  and  $\mathcal{E}_z$  additionally to  $f_{\text{SAW}} = 1$  GHz.

the maximal amplitudes occur at the surface and a second maximum occurs within the substrate, before the amplitudes rapidly decay with the depth in the material.

For the measurements shown in this dissertation, the piezoelectric potential and the associated fields only have negligible influence on the optical transitions of the quantum dots. Nevertheless, the piezoelectric coupling plays a vital role in the excitation of surface acoustic waves as it will be shown in section 3.3.

### Frequency dependence

The results presented so far scale linearly with the amplitude  $A_z$ , the frequency  $f_{\text{SAW}}$  and thus also with the wavelength  $\lambda_{\text{SAW}}$  of the surface acoustic wave. For the samples investigated in this thesis, the QDs are located at a fixed depth  $d$  beneath the surface of the substrate. Therefore, their position does not scale with respect to  $\lambda_{\text{SAW}}$  and the SAW-QD interaction will depend on  $f_{\text{SAW}}$ . In order to take this into account, the so far obtained results can be scaled with respect to a fixed depth  $-d$  as it is shown in figure 3.4. In this graph, it can be seen that for a GaAs-substrate the highest hydrostatic pressure is achieved for  $f_{\text{SAW}} \cdot d \approx 0.6$  GHz  $\cdot$   $\mu\text{m}$ , indicated by the dashed blue line in figure 3.4. This

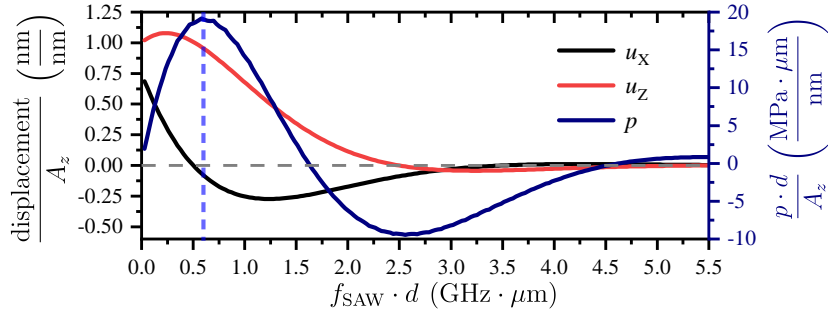


**Figure 3.4.:** Displacement amplitudes for  $u_x$  and  $u_z$  (left axis) and hydrostatic pressure  $p$  (right axis) as function of  $f_{\text{SAW}}$  at a fixed depth  $d$  beneath the surface. In order to obtain the amplitudes for  $u_x$ ,  $u_z$  and  $p$  (normalized to  $A_z = 1$  nm respectively) as a function of  $f_{\text{SAW}}$  at a fixed depth  $d$ , the  $x$ -axis and the pressure axis (right) have to be divided by  $d$ .

means that at a depth of  $d = 1 \mu\text{m}$  the highest pressure is reached for  $f_{\text{SAW}} \approx 0.6$  GHz and, accordingly, for  $d = 0.5 \mu\text{m}$  at  $f_{\text{SAW}} \approx 1.2$  GHz and so on. Furthermore, it can be seen that the pressure rapidly decreases with increasing frequency. For a given depth  $d$  beneath the surface, this sets an upper limit for the frequency at which quantum dots at this specific depth can be influenced by the hydrostatic pressure created by a surface acoustic wave. Placing QDs closer to the surface shifts this upper boundary towards higher frequencies.

### 3.2.2. Surface acoustic waves on $\text{Al}_x\text{Ga}_{1-x}\text{As}$

So far we only considered GaAs as a substrate material but the growth of QDs on a GaAs substrate in general requires the incorporation of layers of different materials, predominantly  $\text{Al}_x\text{Ga}_{1-x}\text{As}$ , which will be shown in section 4.1. The exact influence of these materials on the elastic properties of a material, most interestingly the sound velocity  $v_{\text{SAW}}$ , strongly depends on the specific structure of the substrate. Furthermore, since a layered structure does not scale with the acoustic wavelength  $\lambda_{\text{SAW}}$ , the sound velocity becomes dispersive. All that, makes general statements about layered structures difficult. To provide a general idea on how the aluminium content  $x$  of  $\text{Al}_x\text{Ga}_{1-x}\text{As}$  influences the elastic properties, an isotropic substrate is considered in this section and the dependence on the aluminium content is investigated. The elastic constants for  $\text{Al}_x\text{Ga}_{1-x}\text{As}$  are given in Appendix A.2. Using these constants, the sound velocities for different aluminium contents  $x$  were determined by FEM, again adapting the elastic constants for low temperatures ( $T = 10$  K). The so calculated sound velocities  $v_{\text{SAW}}$  are shown in figure 3.5(a) as a function of aluminium content  $x$  (blue dots  $\bullet$ ). There, it can be seen that with increasing aluminium content  $x$  the sound velocity  $v_{\text{SAW}}$  rises from about  $2900 \frac{\text{m}}{\text{s}}$  for GaAs to about  $3460 \frac{\text{m}}{\text{s}}$  for AlAs. A closer look at the elastic constants in Appendix A.2 reveals that the elasticity tensor is only weakly affected by the aluminium content, whereas the density strongly depends on the aluminium content and decreases by about 30% going from GaAs to AlAs. This

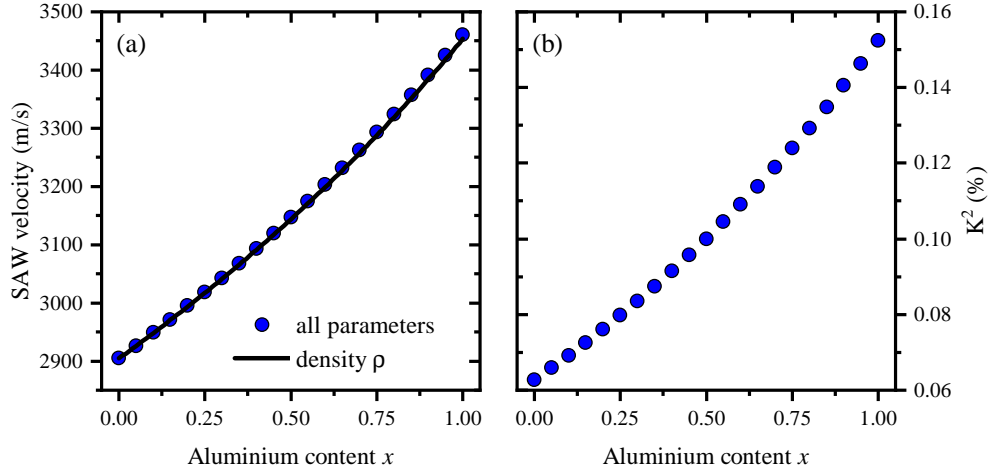


**Figure 3.5.:** Simulated elastic properties for a surface acoustic wave along the [110]-direction of a (001)-Al <sub>$x$</sub> Ga<sub>1- $x$</sub> As surface as a function of aluminium content  $x$ . (a) Surface acoustic wave velocity as a function of  $x$ , where all parameters (blue dots •) or only the density  $\rho$  (solid line) is adapted to the aluminium content. (b) Electromechanical coupling coefficient  $K_S^2$  as a function of  $x$ .

suggests the conclusion that the change in the velocity is mostly caused by the change of the density. This can easily be checked with the help of FEM by just changing the density with aluminium content  $x$ , while the other elastic constants are left the same as for GaAs, independent of  $x$ . The values for  $v_{SAW}$  obtained by these simulations are shown by the solid line in figure 3.5. It can be seen that both simulations are in very good agreement, solely for high aluminium contents  $x$  a small deviation arise.

The velocity of a sound wave in a solid is in general inversely proportional to the square root of the density:

$$v \propto \sqrt{\frac{1}{\rho}} \quad (3.18)$$

Going from GaAs to AlAs, thus reducing the density to 70% of its initial value, this dependence predicts an increase of the surface acoustic wave velocity by 19%, which is nicely reproduced by the simulations. These simulations show that for the mechanical properties of the surface acoustic wave propagation for Al <sub>$x$</sub> Ga<sub>1- $x$</sub> As it is sufficient to only adapt the density and neglect the change of the other elastic constants.

The same does not apply if one is interested in the piezoelectric properties and fields that accompany the mechanical wave, as the piezoelectric coupling coefficient shows an increase of about 40% of its absolute value going from GaAs to AlAs. For this work, the most important property, which results from the piezoelectricity of an Al <sub>$x$</sub> Ga<sub>1- $x$</sub> As substrate, is the possibility to excite surface acoustic wave using electrical signals (see section 3.3). The efficiency of this transformation of electrical to mechanical energy is characterised by the electromechanical coupling coefficient  $K_S^2$ .

To determine  $K_S^2$ , the sound velocities for the open ( $v_0$ ) and short ( $v_\infty$ ) circuit condition have to be determined. From these velocities, the electromechanical coupling coefficient  $K_S^2$  can be determined using equation 3.15. The so obtained values for  $K_S^2$  are shown in figure 3.5(b) as a function of aluminium content  $x$ . It can be seen that with rising aluminium content  $x$  and thus an increasing absolute value of the piezoelectric tensor  $e$  (see equation A.9), the electromechanical coupling coefficient  $K_S^2$  shows a significant increase. Starting from a value of 0.06% for GaAs,  $K_S^2$  increases by a factor of 2.5 to 0.15% for AlAs. Meaning that with a higher aluminium content in the substrate, the piezoelectricity will gain importance. In comparison to other materials used for SAW devices, the values for  $K_S^2$  for AlAs are similar to the ones reported for Quartz ( $K_{S,\text{Quartz}}^2 = 0.16\%$  [58]) but much smaller than that for  $\text{LiNbO}_3$  ( $K_{S,\text{LiNbO}_3}^2 = 5.3\%$  (for a  $128^\circ$  Y-Cut) [59]) which is most commonly used for SAW applications. So in summary, it can be said that even though the electromechanical coupling coefficient increases with the aluminium content  $x$  in  $\text{Al}_x\text{Ga}_{1-x}\text{As}$ , it is still too small to have a big impact on the surface acoustic wave propagation and thus plays not a dominant role in the experiments presented in this work.

### 3.3. Excitation of surface acoustic waves

In this section, we consider the excitation of surface acoustic waves on piezoelectric substrates. As already mentioned,  $\text{Al}_x\text{Ga}_{1-x}\text{As}$  is, as most III-V compound semiconductors, a rather weak piezoelectric material but still allows the excitation of surface acoustic waves by electrical signals using the inverse piezoelectric effect. This means that a deformation of the substrate can be induced by applying an electric voltage. In order to employ this effect to create surface acoustic waves, the deformation must couple to the SAW mode. This imposes demands on the geometry of the electrodes used to apply the electrical potential to the substrate. Such an arrangement of metal electrodes is called an interdigital transducer (IDT) and the simplest implementation of such a structure, a so-called split-1 IDT, is depicted in 3.6. It consists of an array of two interdigitating comb-shaped electrodes that are deposited on the surface of the substrate. The most important parameter of an IDT is the periodicity  $\lambda_{\text{IDT}}$  of the metal electrodes. If a radio frequency (rf) signal is applied, a surface acoustic wave is excited, provided the frequency of this signal  $f_{\text{rf}}$  fulfils the resonance condition of the IDT:

$$f_{\text{rf}} = \frac{v_{\text{IDT}}}{\lambda_{\text{IDT}}} \quad (3.19)$$

This resonance condition states that the mechanical distortion that propagates from each electrode when a rf-signal is applied, has to constructively interfere with the waves created at all other fingers in order to efficiently launch a surface acoustic wave along the  $\pm x$ -directions (symmetric IDTs are not directional).

At this point, it should be noted that the resonance condition of equation 3.19 must be fulfilled with respect to the surface acoustic wave velocity of the IDT  $v_{\text{IDT}}$  and not with

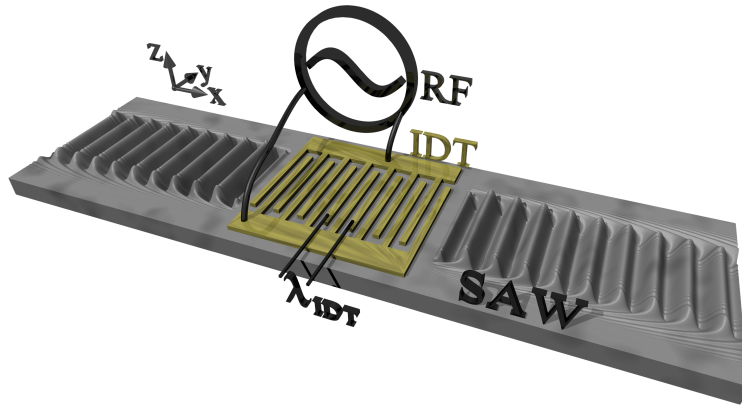


**Figure 3.6.:** Schematic representation of the mode of operation of an interdigital transducer (IDT). When a rf-signal with a frequency matching the resonance condition set by  $\lambda_{\text{IDT}}$  (equation 3.19) is applied between the two interlocking electrodes of an IDT, surface acoustic waves are launched, propagating in both  $+x$ - and  $-x$ -direction.

the wave velocity of the bare substrate  $v_{\text{SAW}}$ . As the IDT itself represents a disturbance of the free surface, these two velocities are in general not identical. For  $\text{Al}_x\text{Ga}_{1-x}\text{As}$ , this disturbance is mostly caused by an additional mass loading, as the change of the electrical boundaries do barely affect  $v_{\text{SAW}}$  due to the small  $K_S^2$ . For a given metal, the effect of the mass loading depends on the ratio  $\frac{d_{\text{IDT}}}{\lambda_{\text{SAW}}}$  between the thickness of the IDT electrodes  $d_{\text{IDT}}$  and the surface acoustic wavelength  $\lambda_{\text{SAW}}$  [59]. The thickness of the IDT metallisation is typically around  $d_{\text{IDT}} = 50 \text{ nm}$ . The frequencies  $f_{\text{SAW}}$  used in this thesis are  $< 1.45 \text{ GHz}$ , setting a lower limit for the acoustic wavelength of  $\lambda_{\text{SAW}} > 2 \mu\text{m}$ . Thus, for the frequency range of interest, it applies  $d_{\text{IDT}} \ll \lambda_{\text{SAW}}$  and the mass loading can be neglected. It is therefore assumed that  $v_{\text{SAW}} \approx v_{\text{IDT}}$  and  $\lambda_{\text{SAW}} \approx \lambda_{\text{IDT}}$ .

Other important parameters of an IDT are the aperture  $A_{\text{IDT}}$ , the length  $L_{\text{IDT}}$  and the metallisation ratio  $\eta$ . The aperture  $A_{\text{IDT}}$  is defined by the overlap between fingers of different polarity and therefore determines the width of the wavefront (see figure 3.7(a)). The metallisation ratio is the ratio between the width of a finger  $w_f$  and the width of the spacing between two fingers. Typically, a value of  $\eta = 0.5$  is chosen, setting the width of a finger in a Split-1 IDT to  $w_f = \frac{\lambda}{4}$ .

To mathematically describe the frequency response of an IDT, an impulse model [60,61] can be used. In this model, each finger  $n$  is considered as the source of a plane wave propagation in  $x$ -direction:

$$A_n \exp\left(i2\pi f \left(\frac{x_n}{v_{\text{SAW}}} - t\right)\right) \quad (3.20)$$

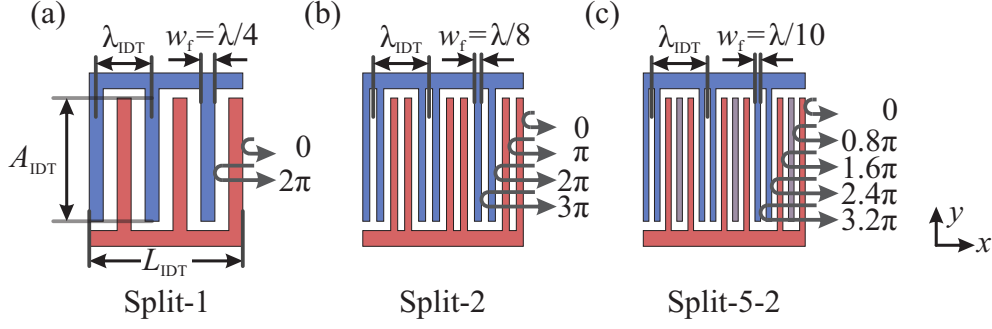


**Figure 3.7.:** Sketch of the geometries for a (a) Split-1, (b) Split-2 and (c) Split-5-2 IDT. The respective finger widths  $w_f$  refer to a metallisation ratio of  $\eta = 0.5$ . Arrows indicate an incoming wave from the right that is reflected at the IDT fingers, leading to the given phase shifts between the different partial waves of the reflected signal.

In this expression,  $A_n$  is the amplitude emitted by the  $n$ -th finger, where the sign of the amplitude reflects the polarity of the respective finger. The magnitude of  $A_n$  depends on the length of a specific finger, making it possible to realise certain filter characteristic for surface acoustic wave filter devices by modulating  $A_n$  along the IDT. However, as this leads to a non-uniform wave excitation across the IDT aperture, this procedure is not used in the scope of this work. The value  $x_n$  denotes the position of the  $n$ -th finger and determines the phase shift between waves emitted from different fingers. The overall frequency response  $H(f)$  is then obtained by summation over all  $n$  waves emitted from the IDT fingers. The capability of an IDT to launch a surface acoustic wave at a specific frequency  $f$  is then given by the magnitude of the frequency response, called the amplitude response:

$$|H(f)| = \left| \sum_{n=1}^N A_n \exp\left(i2\pi \frac{fx_n}{v_{\text{SAW}}}\right) \right| \quad (3.21)$$

This expression basically corresponds to the Fourier transform of the spatial finger arrangement.

To evaluate the amplitude response for a split-1 transducer,  $A_n = (-1)^n$  and  $x_n = n \cdot \frac{\lambda_{\text{IDT}}}{2}$  has to be inserted into equation 3.21. The result for an IDT of length  $L_{\text{IDT}} = 400 \mu\text{m}$  and resonance frequency  $f_{\text{SAW}} = 500 \text{ MHz}$  on a GaAs-substrate ( $v_{\text{SAW}} = 2904 \frac{\text{m}}{\text{s}}$ ) is shown in figure 3.8(a). Beside the peak at the IDT's fundamental frequency  $f_{\text{SAW},1} = 500 \text{ MHz}$ , additional peaks at the odd harmonics  $f_{\text{SAW},n} = (2 \cdot n + 1) \cdot f_{\text{SAW},1}$ , with  $n = 1, 2, 3, \dots$ , can be seen. This means that a given IDT cannot only generate SAWs at its fundamental frequency but also at certain harmonics. For a split-1 IDT, the even harmonics are suppressed as the resulting wave would have the same piezoelectric potential at all IDT fingers, meaning that no electrical energy can be transferred in the respective surface wave mode by applying a voltage between the IDT electrodes.

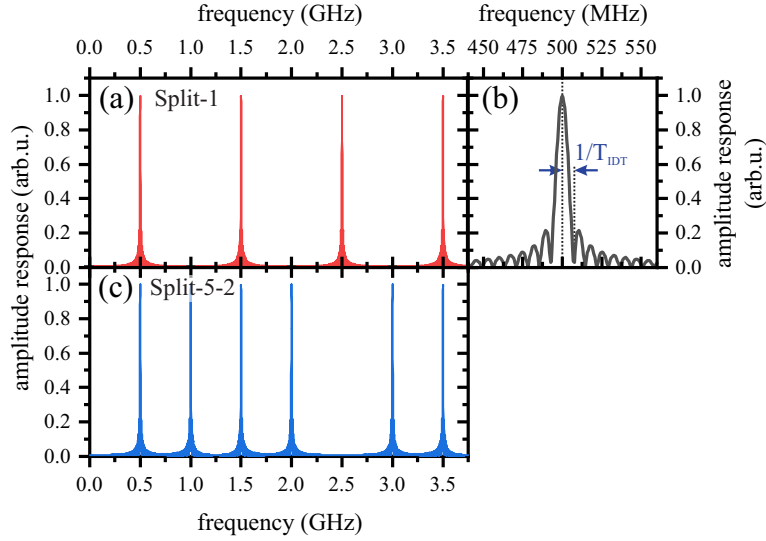


**Figure 3.8.:** Amplitude response  $|H(f)|$  for a split-1 (a) and split-5-2 (c) IDT, with a fundamental frequency of  $f_{\text{SAW},1} = 500$  MHz and a length of  $L_{\text{IDT}} = 400 \mu\text{m}$  on a GaAs substrate. (b) Zoom-in at the transmission at the fundamental frequency of (a), revealing the Fraunhofer diffraction pattern caused by the finite length of the IDT.

In order to realise an IDT that is capable of generating both even and odd harmonics, a non-symmetric finger geometry has to be used, for example, the split-5-2 geometry shown in figure 3.7(c) [62]. This IDT consists of 5 fingers per period  $\lambda_0$ , where two fingers each are connected to one of the two electrodes and one finger is connected to neither electrode. This dummy finger serves no electrical purpose but is needed to achieve a constant mass loading and suppress reflections within the IDT. The amplitude response of such a split-5-2 IDT is shown in figure 3.7(c), revealing peaks at  $f_{\text{SAW},n} = n \cdot f_{\text{SAW},1}$ , with  $n = 1, 2, 3, 4, 6, \dots$ . The same reason for the suppression of the even harmonics for the split-1 IDT is responsible for the loss of the 5<sup>th</sup> harmonic for the split-5-2. An enlargement of a peak in the amplitude response is shown in figure 3.8(b), revealing a characteristic Fraunhofer diffraction pattern. This pattern is caused by the finite length  $L_{\text{IDT}}$  of the IDT that can be described by a rectangular function in the spatial finger arrangement  $x_n$ . Upon calculating the amplitude response in equation 3.21 so forming the Fourier transforms of the spatial finger arrangement, this leads to the formation of the observed  $\left| \text{sinc}(f) = \frac{\sin(f)}{f} \right|$  envelope function. The zero points in the amplitude response are thus given by the temporal length of the IDT  $T_{\text{IDT}} = \frac{L_{\text{IDT}}}{v_{\text{SAW}}}$ . This is also the shortest SAW pulse that can be generated by an IDT.

The impulse model provides a good indication of the behaviour of an IDT. However, certain points are neglected by this simple model. For example, the impulse model treats each finger as a point like source, while in reality they have a finite width  $w_f$ . This finite width

leads, similar to the finite length of the IDT  $L_{\text{IDT}}$ , to an other  $\left| \frac{\sin(f)}{f} \right|$  envelope function that is centred at the origin ( $f = 0 \text{ Hz}$ ) and superimposes the amplitude response, strongly reducing the response for higher harmonics. The width of this envelope function depends on the width of the fingers  $w_f$ . The first zero point of the envelope function is given by  $\left( \frac{v_{\text{SAW}}}{w_{\text{finger}}} = \frac{\lambda_0}{w_f} \cdot f_{\text{SAW},1} \right)$ , which also provides an upper limit for the IDTs operating range. This limit can be shifted towards higher frequencies by using thinner fingers or geometries with more fingers per period  $\lambda_0$ , like the split-2 geometry shown in figure 3.7(b).

Mostly the second approach is chosen, as it allows to maintain a metallisation factor of  $\eta = 0.5$  and thus minimises the effects caused by internal reflections at the IDT fingers. These reflections especially take effect when IDTs are used in a delay line configuration. Assuming the IDTs shown in figure 3.7 are used as receivers for a SAW entering the IDT from the right side, part of this incoming wave is reflected at each finger, as illustrated by the arrows. Depending on the respective finger positions, the reflected partial waves have different phases with respect to each other. For a split-1 IDT, the phase shift between waves reflected at two successive fingers is  $2\pi$  and thus these always interfere constructively. For split-2 and split-5-2 IDTs on the other hand, the phase shifts are  $\pi$  and  $0.8\pi$  respectively. This means that the reflected waves of two successive fingers for split-2 IDTs and of five successive fingers for split-5-2 IDTs interfere destructively and cancel themselves out, strongly reducing the reflectivity of these IDTs.

## 4. Samples - Fabrication and structure

In this chapter, the design and fabrication of the investigated samples is addressed. In the first part, the epitaxial growth of semiconductor quantum dots is described and the SAW velocity for the resulting QD substrates is examined. The second part describes the fabrication and the layout of the IDT structures used to excite SAWs. In the last part, the influence of temperature on the propagation of a SAW is shortly discussed.

### 4.1. Epitaxial growth of semiconductor quantum dots

There are various methods for the fabrication of semiconductor QDs, which can be divided in two main categories. The first one are colloidal QDs where QDs are formed in a solution by chemical processes. The second one is the epitaxial growth of QDs on a host substrate. In this work, epitaxially grown QDs were used, as they can be directly grown on a host substrate that allows for the propagation of SAWs. Additionally, under appropriate growth conditions, low enough QD densities can be realised, enabling the optical excitation of single QDs. For this work, two different types of self-assembled QD were used, InAs- and GaAs-QDs. Both types of QDs were grown by molecular beam epitaxy but with different processes. These two different processes will be described briefly below.

#### 4.1.1. Self-assembled InAs QDs

For the fabrication of InGaAs-QDs on a GaAs-substrate, the so-called Stranski–Krastanov growth [64–66] can be used. Besides the Volmer–Weber and the Frank–van der Merwe growth, this is one of the fundamental thin-film growth processes [67].

This process depends on the lattice mismatch between GaAs and InGaAs (see figure 2.2), leading to the formation of InGaAs islands. When InGaAs is deposited on GaAs, an epitaxial layer of InGaAs, called the wetting layer (WL), is formed first. Due to the lattice mismatch this layer is strongly strained and, with increasing thickness of the WL, the strain energy increases until a critical thickness is reached. The formation of InGaAs islands is then energetically favourable as it reduces the strain (see figure 4.1(a)). These islands are overgrown by GaAs in order to passivate defects on the surface, which would otherwise deteriorate optical properties of the QDs and to ensure a three dimensional confinement of charge carriers within the InGaAs islands, having a smaller bandgap than the surrounding GaAs. Both position and size of the QDs are statistically distributed, but the width and

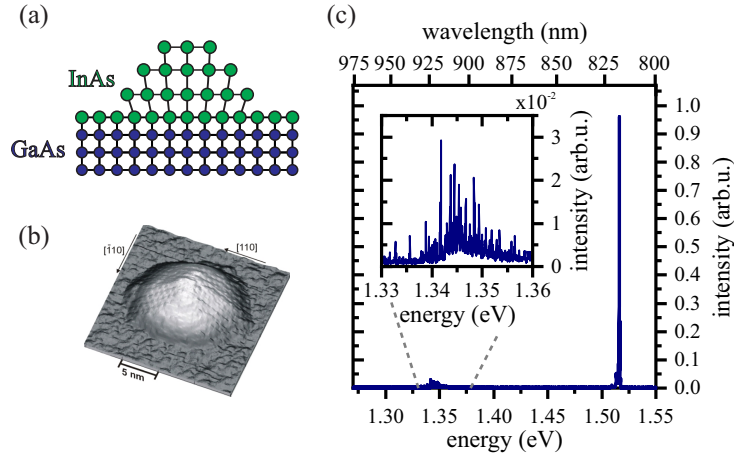


**Figure 4.1.:** (a) Schematic of the Stranski–Krastanov growth. When depositing InAs on GaAs, first a 2D layer (wetting layer) of InAs is formed, before island growth sets in at a specific thickness, leading to the formation of QDs. (b) Scanning tunneling microscope image of an uncovered InAs-QD on GaAs, showing its spherical geometry. Adapted from Márquez et al. [63]. (c) PL spectrum of a sample containing self-assembled InAs-QDs. QD emission can be observed as discrete lines below the bulk GaAs ( $\approx 1.52$  eV) emission.

centre of this distribution can be controlled via the growth parameters (temperature and ratio between In- and Ga-flux). As precise control of these parameters can be challenging, QDs are often grown with a gradient of In-content across the wafer. To achieve this, the rotation of the wafer, which normally ensures a uniform growth over the entire wafer, is stopped during the InGaAs deposition, leading to a gradient of the In to Ga ratio across the wafer. At the side of the wafer with low In-content, a coherent layer of InGaAs without any island growth is formed. With increasing In-content and thus lattice mismatch along the wafer, island growth becomes more and more dominant, leading to an increased density of QDs along the wafer. For the following optical experiments, a part of the wafer with a low enough density is selected so that optical addressing of single QDs is possible.

A typical emission spectrum of a sample containing self-assembled InGaAs QDs is shown in figure 4.1 (b). The dominant peak at around  $\approx 1.52$  eV corresponds to the GaAs bulk emission. At lower energies, in this case in the range of 1.33 – 1.36 eV, the emission of the InGaAs QDs can be identified by its characteristic discrete emission lines.

#### 4.1.2. Etched GaAs/AlGaAs QDs

For GaAs/Al<sub>x</sub>Ga<sub>1-x</sub>As QDs, a Stranski–Krastanov growth is not possible since the lattice mismatch is neglectable for all aluminium contents  $x$ . Therefore, a different approach is needed, namely local droplet etching (LDE). This method can be used to etch nanoholes into a GaAs substrate using liquid droplets of Ga [68]. The sample used in this work was fabricated by Atkins et al. [69] using a technique summarized in figure 4.2(a).

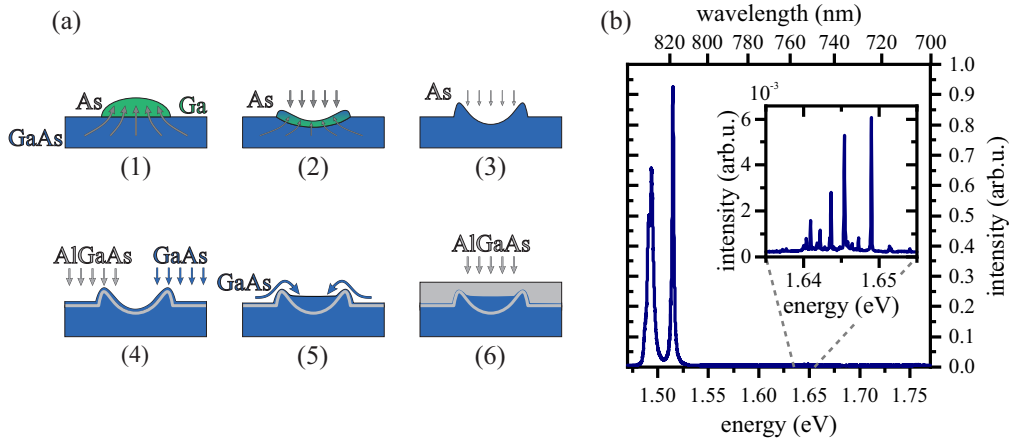


**Figure 4.2.:** (a) Schematic of QD fabrication by liquid Ga-droplet etching. First, nano-holes are etched into the GaAs substrate by liquid droplets of Ga (1-3). After that, the hole is overgrown by AlGaAs (4), filled with GaAs (5) and capped with AlGaAs (6). (b) PL spectrum of a wafer containing etched GaAs-QDs. Here, the QD emission is shifted to higher energies with respect to the GaAs emission.

The process starts with the deposition of Gallium on a GaAs substrate, leading to the formation of Ga droplets (1). Due to the gradient of the As concentration, As from the substrate starts to dissolve in the droplet and the droplet spreads out (2), partially re-crystallising at the edge of the droplet. Under As flux, the droplet then fully crystallised and a nano-hole in the GaAs substrate is left (3). The nano-holes are then over-grown by a layer of  $\text{Al}_x\text{Ga}_{1-x}\text{As}$ , serving as a barrier for the QDs and a layer of GaAs (4). After that, in a short pause of the growth process, the GaAs migrates towards the nano-holes, filling these up and thus forming GaAs-QDs (5). The final step is the overgrowth by  $\text{Al}_x\text{Ga}_{1-x}\text{As}$  to passivate the surface and to ensure effective carrier confinement within the QD (6).

A typical spectrum of a sample containing GaAs/ $\text{Al}_x\text{Ga}_{1-x}\text{As}$ -QDs is shown in figure 4.2(b). Again, the spectrum is dominated by the bulk GaAs emission around 1.52 eV. The energy of the QD emission depends on the respective growth conditions and the associated size of the nano-holes and is here located around 1.65 eV [69].

#### 4.1.3. Layer structure and resulting sound velocity of the samples

In this section, the layer structure of the used samples and its effect on the respective surface acoustic wave velocities shall be explained. In total, two different QD samples have been investigated. One containing AlGaAs/GaAs-QDs grown by liquid droplet etching, the other containing InGaAs-QDs fabricated by Stranski-Krastanov growth. The first sample, denoted "O404", was fabricated in the research group of Oliver G. Schmidt<sup>1</sup> and Armando

<sup>1</sup>Leibniz-Institut für Festkörper und Werkstoffuntersuchung, Dresden

#### 4. Samples - Fabrication and structure

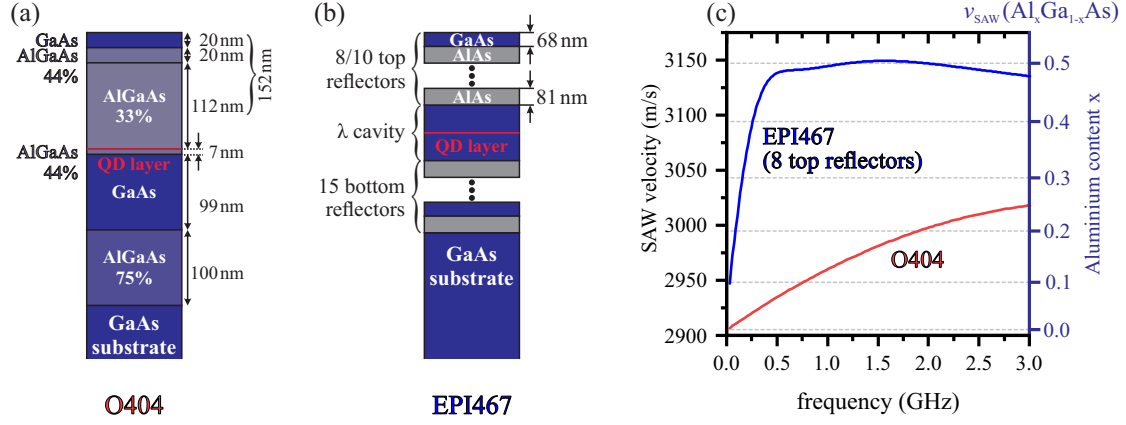


**Figure 4.3.:** (a),(b) Layer structure of the two investigated QD samples. Both samples are grown by molecular beam epitaxy (MBE) on a GaAs substrate. (a) Sample "O404" contains a layer of etched GaAs-QDs in an AlGaAs matrix. (b) Sample "EPI467" contains a layer of self-assembled InAs-QDs, embedded in a planar cavity formed by two distributed Bragg reflectors (DBR). (c) Simulated Rayleigh wave velocities for both samples as a function of SAW frequency, showing a dispersive behaviour due to the layered structure of the samples.

Rastelli<sup>2</sup> (see reference [69]). The second one, denoted "EPI467", was fabricated by K. Müller<sup>3</sup> in the research group of J. Finley<sup>3</sup> using Stranski-Krastanov growth. The layer structures for both samples are shown in figure 4.3(a) and (b), respectively.

#### O404

For this sample, the GaAs-QDs are located 154 nm below the surface of the substrate between two layers of  $\text{Al}_x\text{Ga}_{1-x}\text{As}$  with an aluminium content of  $x = 0.44$  and  $x = 0.33$  respectively. To prevent oxidation of the AlGaAs, the sample is capped by a layer of GaAs. Besides the AlGaAs layer needed for QD confinement, there is an additional 99 nm GaAs and 100 nm  $\text{Al}_{0.75}\text{Ga}_{0.25}\text{As}$  layer below the QDs and above the GaAs host substrate. This additional layer of AlGaAs serves as a sacrificial layer and can be removed with hydrofluoric acid to obtain a  $\approx 250$  nm membrane containing QDs that can be transferred to a different substrate. This was done for this specific sample in reference [70], where the membrane was transferred onto piezoelectric actuators to tune the emission energy of the QDs by applying strain. For the experiments presented here, this sacrificial layer serves no purpose but has to be taken into account when determining the SAW velocity. This QD sample was used for the PL measurements presented in chapters 5 and 6.

<sup>2</sup>Institute of Semiconductor and Solid State Physics, Johannes Kepler University Linz

<sup>3</sup>Walter Schottky Institut, Technische Universität München

**EPI467**

This sample contains a single layer of InGaAs-QDs. To enhance the fluorescence and the coupling to a resonant light field, as this will be important for later resonance fluorescence experiments, the QD-layer is embedded in a planar optical  $\lambda$  cavity formed by two distributed Bragg reflectors (DBRs). These Bragg reflectors consist of alternating layers of GaAs and AlAs with an optical thickness of  $\lambda_{\text{Bragg}}/4$ .

Due to the different refractive indices of GaAs ( $n_{\text{GaAs}} \approx 3.38$ ) and AlAs ( $n_{\text{AlAs}} \approx 2.82$ ), incident light is partly reflected at each GaAs/AlAs interface. For vertically incident light of wavelength  $\lambda_{\text{Bragg}}$ , the reflections at two consecutive interfaces have a phase difference of  $2\pi$  (taking into account the  $\pi$ -phase shift when reflection takes place at the higher refractive index material) and thus interfere constructively, leading to a high reflectivity. To preferably redirect the QD fluorescence towards the surface of the sample, where the light is collected, there are more reflector pairs below (15) the QD layer than above (10 pairs). The DBR cavity was designed to match the emission of the QDs at around  $\lambda_{\text{Bragg}} = 920$  nm, leading to a thickness of  $\lambda_{\text{GaAs}}/4 = 68$  nm and  $\lambda_{\text{AlAs}}/4 = 81$  nm for the layers of GaAs and AlAs respectively.

This sample was used for the resonance fluorescence measurements presented in chapter 7. Since the QDs are located relatively deep within the sample (about  $1.63 \mu\text{m}$  for 10 top reflector pairs), the hydrostatic pressure induced by a SAW is relatively small. Therefore, for the measurements presented in chapter 8, where resonance fluorescence is combined with dynamic SAW modulation, a sample was used from which two top reflector pairs have been removed. This was realised by digital etching of AlAs layers with hydrofluoric acid and GaAs layers with a mixture of citric acid and hydrogen peroxide. Removing two reflector pairs brings the QD layer about 300 nm closer to the surface, resulting in a stronger coupling of SAWs to QDs in the frequency range of interest.

When IDTs with a specific resonance frequency shall be processed on one of these samples, the exact sound velocity has to be known. Since the samples are composed of layers of different materials, the surface acoustic wave velocity is in general expected to be dispersive. Using the finite element method described in section 3.2, the SAW velocity  $v_{\text{SAW}}$  can be determined as a function of frequency when the respective layer structures given in figure 4.3(a) and (b) are considered. The so determined velocities for both of the samples are shown in figure 4.3(c) as a function of SAW frequency  $f_{\text{SAW}}$ . The right  $y$ -axis relates the obtained velocities (left  $y$ -axis) to the ones expected for a sample consisting only of  $\text{Al}_x\text{Ga}_{1-x}\text{As}$  with an aluminium content  $x$ . For both of the investigated structures, the sound velocity approaches  $\approx 2900 \frac{\text{m}}{\text{s}}$  for low SAW frequencies ( $f_{\text{SAW}} \rightarrow 0$ ). This corresponds to the sound velocity of pure GaAs and is expected as, for small frequencies and thus large wavelengths  $\lambda_{\text{SAW}}$ , the wave propagates predominantly in the GaAs host substrate. With increasing frequency and decreasing wavelength, the

wave shifts towards the surface of the sample and thus towards the layered structure. As the SAW velocity increases with aluminium content for  $\text{Al}_x\text{Ga}_{1-x}\text{As}$  (see figure 3.5(a)), the SAW velocity increases for both samples with the frequency. For the sample "O404", with a comparatively thin layer structure of thickness  $\approx 360$  nm and medium aluminium content  $x$ , the velocity increases relatively evenly to about  $3020 \frac{\text{m}}{\text{s}}$  at  $f_{\text{SAW}} = 3$  GHz. In contrast to that, the sample EPI467 shows a very strong increase initially and reaches a velocity of almost  $3150 \frac{\text{m}}{\text{s}}$  at 0.5 GHz. With further increasing frequency, the SAW velocity stays relatively constant as it is already entirely determined by the  $\approx 3.8 \mu\text{m}$  thick Bragg structure. The effective sound velocity of the Bragg structure arises from the fact that it consists of approximately equal parts of GaAs and AlAs, resulting in an averaged velocity that corresponds to the SAW velocity of  $\text{Al}_{0.5}\text{Ga}_{0.5}\text{As}$ .

## 4.2. Sample fabrication and layout

In order to electrically excite SAWs on a sample containing QDs, IDTs have to be processed on the surface. Therefore, small pieces (typically sizes up to  $6 \text{ mm} \times 9 \text{ mm}$ ) are broken out of the respective wafer. In the case of InGaAs-QDs, care has to be taken to select a part of the wafer with a QD density that allows optically addressing single QDs. IDTs are then fabricated directly on the surface of the sample by a standard lift-off process using a resist mask patterned by electron-beam lithography (EBL). For metallisation, 5 nm of titanium as an adhesion layer, and 50 nm aluminium, responsible for the conductivity, are deposited. IDTs are oriented along the [110]-direction of the GaAs substrate and typically arranged in

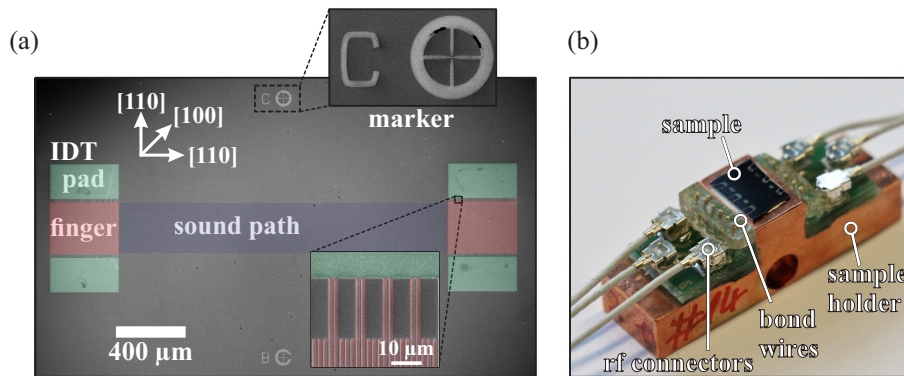


**Figure 4.4.:** (a) Scanning electron micrograph of a delay line. Fingers and contact pads of the two opposite IDTs are coloured red and green respectively. The common sound path of the IDTs is shown in blue. The two enlargements show a marker, used for orientation on the sample, and the fingers of the split-5-2 IDT. (b) A sample with several delay lines is mounted to a copper sample holder. Electrical contact between sample holder and IDT contact pads is realised by wire-bonding.

a delay line configuration, meaning that two identical IDTs are placed opposite to each other as shown in the scanning electron micrograph in figure 4.4(a). This offers the advantage

that the IDTs can simply be characterised by measuring the transmission between the two IDTs, where one acts as a sender, while the other serves as a receiver. In addition to the IDTs, markers are fabricated on the sample away from the sound paths of the IDTs to allow for easy orientation and navigation on the sample. For further measurements, the sample is mounted to a custom designed sample carrier, as shown in figure 4.4(b) which can be inserted into the low temperature cryostat. To ensure good thermal contact, the sample is glued to the copper carrier using a silver adhesive. For the electrical contact of the IDTs, the sample carrier is equipped with two printed circuit boards (PCB), containing miniature radio frequency connectors (Hirose U.FL) for the connection to the cabling of the cryostat and pins for the connection to the sample. Contact between the IDT pads and the gold plated pins on the PCB is realised by wire bonding. The sample carrier allows for individual contacting of up to six IDTs, whereas the cryostat itself is equipped with only two radio frequency cables to reduce the heat input to the sample.

### 4.3. Temperature dependence of the surface acoustic wave velocity

When fabricating IDTs and characterising them at room temperature one has to take into account that in general the SAW wave velocity and thus the resonance frequency changes with temperature. To quantify this shift, the transmission of a delay line consisting of two identical split-5-2 IDTs, fabricated on a sample of type "EPI467", was investigated as a function of sample temperature. Figure 4.5(a) shows the transmission of the delay

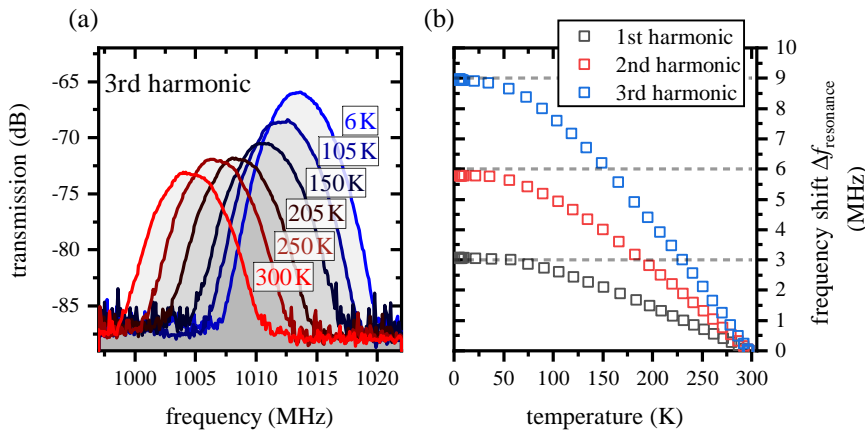


**Figure 4.5.:** Temperature dependence of the transmission characteristics of a delay line, consisting of split-5-2 IDTs. (a) Transmission peaks of the third harmonic for various temperatures. With decreasing temperature, the resonance frequency clearly shifts to higher frequencies. (b) Relative frequency shifts with respect to room temperature for the first three harmonics of the delay line. The total shift corresponds to 0.9% of the respective resonance frequency.

line for the third harmonic of the IDTs at various temperatures. It can be seen that with decreasing temperatures, the resonance peaks shift towards higher frequencies, which means the SAW velocity  $v_{\text{SAW}}$  increases with decreasing temperatures. For the case shown here, the resonance frequency shifts from 1.0045 GHz at 300 K to 1.0135 GHz at 6 K, corresponding to a total frequency shift of 9 MHz or 0.9 %.

Figure 4.5(b) shows the relative resonance frequency shifts  $\Delta f_{\text{resonance}}$ , going from 300 K to 5 K, for the first three harmonics of the delay line. For all three harmonics, an approximately linear increase of the resonance frequency can be observed when going from 300 K to 100 K but with different slopes for the respective harmonics. With further decreasing temperatures, the relative changes of the resonance frequencies slow down and, for 5 K, saturates at 0.9 % of the respective room temperature resonance frequency. So a total frequency shift  $\Delta f_{\text{resonance}}$  of 3, 6 and 9 MHz is observed for the first  $f_{\text{SAW},1} = 333$  MHz, second  $f_{\text{SAW},2} = 670$  MHz and third  $f_{\text{SAW},3} = 1005$  MHz harmonic respectively.

Furthermore, in figure 4.5(a) an increasing transmission amplitude can be observed going to lower temperatures. This indicates a stronger electro-mechanical coupling coefficient  $K^2$  at lower temperatures. However, a quantification of this effect on basis of the presented data is not possible as simultaneously an increased attenuation of the rf-cabling is expected for low temperatures, partially counteracting this effect.

## 5. Interfacing quantum dots with surface acoustic waves: Deformation potential coupling

When QDs are interfaced with propagating SAWs the optical emission properties can be influenced by both the SAW's piezoelectric and strain fields. A detailed overview on the fundamental couplings between a SAW and a QD and the performed experiments can be found in [35].

The dominant contribution of the gyrating electric field on the control of QDs is caused by the SAW induced spatio-temporal carrier dynamics (STCD). On a semiconductor substrate, the SAW's piezoelectric fields cause a type-II band edge modulation, is periodic both in time and space. Thus, stability points for  $e^-$  in the conduction and  $h^+$  in the valence band are created, separated by  $\lambda_{\text{SAW}}/2$  and propagate along with the wave. In a quantum well (QW), this leads to the dissociation of photo-generated excitons and, subsequently, to the spatial separation of  $e^-$  and  $h^+$ . This results in both the suppression of the optical emission of the QW and the ambipolar transport of charge carriers with the propagating SAW [71, 72]. For any quantum emitter that is coupled to a continuous two dimensional system acting as a transport channel, this effect can be used to control the occupancy state of the emitter. Depending on the local electrical fields at the position of the quantum emitter at a given time during the acoustic cycle, a certain charge carrier species is predominantly injected into the quantum emitter, influencing the occupancy state that is formed [30, 73, 74]. Furthermore, controlling the time of photo-excitation during the acoustic cycle allows switching between neutral and charge exciton [75].

An alternative approach to control of the QD's occupancy state relies on the actual transport of charge carriers to the position of the QD. To this end, excitons are photo-generated several acoustic wavelengths away from the QD, dissociated by the piezoelectric fields and transported along with the propagating SAW towards the QD. The quantum emitter then acts as a trap and catches  $e^-$  and  $h^+$  which are transported alternately to the emitter [76]. This sequential charge carrier injection even allows for the realisation of triggered single photon sources [31, 77].

These effects, caused by SAW induced STCD, are characterised by a dependence of the emission intensity associated to a certain occupancy state on the amplitude of the SAW and the time during the acoustic cycle. In the course of this work, no such intensity

modulations could be observed, and thus the influence of STCD can be neglected for the investigated samples. This can be justified, for example, by the fact that the investigated QDs are not coupled to a continuous system at lower energies, and thus an efficient charge carrier transport cannot take place.

The second effect that modifies the emission of a QD is caused by the SAW's strain field. In general, strain influences the lattice constant of a crystal and thus, in the case of a semiconductor, also the bandgap energy  $E_g$ . While compressive strain decreases the lattice constant, resulting in an increase of  $E_g$ , tensile strain increases the lattice constant and results in a decrease of  $E_g$ . This effect is referred to as deformation potential coupling and is in first order proportional to the local hydrostatic pressure or volumetric strain  $\frac{\Delta V}{V}$ . As a SAW is characterised by a dynamic pressure field  $p(x, t) = p_0 \cdot \sin(\omega_{\text{SAW}}t + k_x x)$ , it also induces a dynamic energy shift of the bandgap:

$$\Delta E_{\text{strain}}(x, t) = \frac{dE_g}{dp} \cdot p(x, t) = \frac{dE_g}{dp} \cdot p_0 \cdot \sin(\omega_{\text{SAW}}t + k_x x) \quad (5.1)$$

where  $\frac{dE_g}{dp}$  quantifies the strength of the deformation coupling. This parameter depends on the material and is for bulk GaAs given by  $115 \frac{\mu\text{eV}}{\text{MPa}}$  [78]. Since the transition energy of a QD depends on the bandgap (see equation 2.13), this energy variation can directly be observed for a dynamically strained QD as a spectral shift of the discrete emission lines [32, 33, 79, 80]. The periodic modulation of the QD's emission energy follows exactly the frequency  $f_{\text{SAW}}$  of the SAW, and the modulation amplitude depends linearly on the amplitude of the pressure field and thus the amplitude of the SAW.

At this point, it should be noted that not only the strain but also the electric field of the SAW can cause a spectral shift of the emission energy of a QD. This occurs due to the quantum confined stark effect (QCSE) [81] and is based on the polarisation of excitons confined in a quantum system. The energy shift caused by the QCSE is given by:

$$\Delta E_{\text{QCSE}} = -\beta \mathcal{E}^2 \quad (5.2)$$

It depends on the polarisability  $\beta$  of the exciton and the quadratic electrical field  $\mathcal{E}$  and always leads to a decrease, i.e. a red-shift of the emission energy. This effect can be used to statically tune the emission energy of a QD by applying a constant external electrical field [82]. The periodic piezoelectric fields of a SAW can also lead to periodic tuning of the emission energy [34]. Due to the quadratic dependence on the electrical field, this spectral modulation has twice the SAW frequency and increases quadratically with the SAW amplitude and can thus be easily distinguished from the strain modulation.

For the experiments presented in this work, no spectral shift caused by a SAW induced QCSE was observed, most likely as the electro-mechanical coupling constant  $K^2$  of GaAs and thus the piezoelectric fields are comparatively small. Therefore, further considerations

will be limited to the deformation potential coupling. In order to probe this by probing the optical response of a semiconductor quantum dot, different excitation and detection schemes can be applied. These techniques differ in the complexity of their implementations and provide different deep insights into the surface acoustic wave induced dynamics. The most important techniques with their respective advantages and disadvantages will be described in this chapter.

## 5.1. Time-averaged strain modulation

The easiest implementation to investigate the coupling between a quantum dot and a surface acoustic wave is depicted in figure 5.1. This experimental configuration consists of three main components, the SAW excitation, the optical excitation and the optical detection, which operate independently of each other. In the case of a modulated excitation, the optical and SAW excitation need to be synchronised, which, however, does not change the fundamental working principle and will be described later in this section. The radio frequency (rf) signal for the SAW excitation is provided by a rf signal generator (*Stanford Research Systems*, SG384). The free parameters for the SAW excitation are the frequency of the rf signal  $f_{\text{rf}}$  and its amplitude  $P_{\text{rf}}$  that can both be set by the signal generator. For experiments that require high amplitudes, an additional rf amplifier (*Mini-Circuits*, ZHL-42-W+) is used to further boost the signal, before it is applied to the rf input of the cryostat. Optical excitation is realised by a diode laser emitting light with a wavelength of either  $\lambda_{\text{laser}} = 660 \text{ nm}$  (*PicoQuant*, LDH-D-C-660) or  $\lambda_{\text{laser}} = 833 \text{ nm}$  (*PicoQuant*, LDH-D-C-840) depending on the sample under investigation. The respective laser diodes are controlled by a laser driver unit (*PicoQuant*, PDL 800-D) that allows adjustment of the laser current and thus the optical output power ( $P_{\text{laser}}$ ). Furthermore, the laser can be operated in continuous wave or pulsed mode. In the pulsed operation mode, the laser diode emits light pulses with a minimum length of  $\tau_{\text{laser}} \approx 70 \text{ ps}$  (for  $\lambda_{\text{laser}} = 660 \text{ nm}$ ) or  $\tau_{\text{laser}} \approx 95 \text{ ps}$  (for  $\lambda_{\text{laser}} = 833 \text{ nm}$ ) respectively. The repetition rate  $f_{\text{laser}}$  is set either by an external source or by one of two internal frequency oscillators with a base frequency of either 80 MHz or 1 MHz, which can be further adjusted by a binary divider that allows to set six division ratios (1, 2, 4, 8, 16, 32) of the respective base frequency. The collected emission of a quantum dot is spectrally dispersed by a grating monochromator with a focal length of 0.75 m (*Princeton Instruments*, SP-2750). The dispersed light is then detected by a liquid nitrogen cooled charge coupled device (*Princeton Instruments*, Spec-10) that allows to acquire a time-integrated multichannel spectrum (see lower panel of figure 5.1). In the experimental setup described here, typical integration times are in the order of seconds ( $\approx 1 - 10 \text{ s}$ ). Therefore several orders of magnitude larger than typical surface acoustic wave periods ( $T_{\text{SAW}} < 5 \text{ ns}$ ), leading to an averaging of the collected emission over many SAW cycles. Furthermore, the optical excitation occurs equally distributed over an

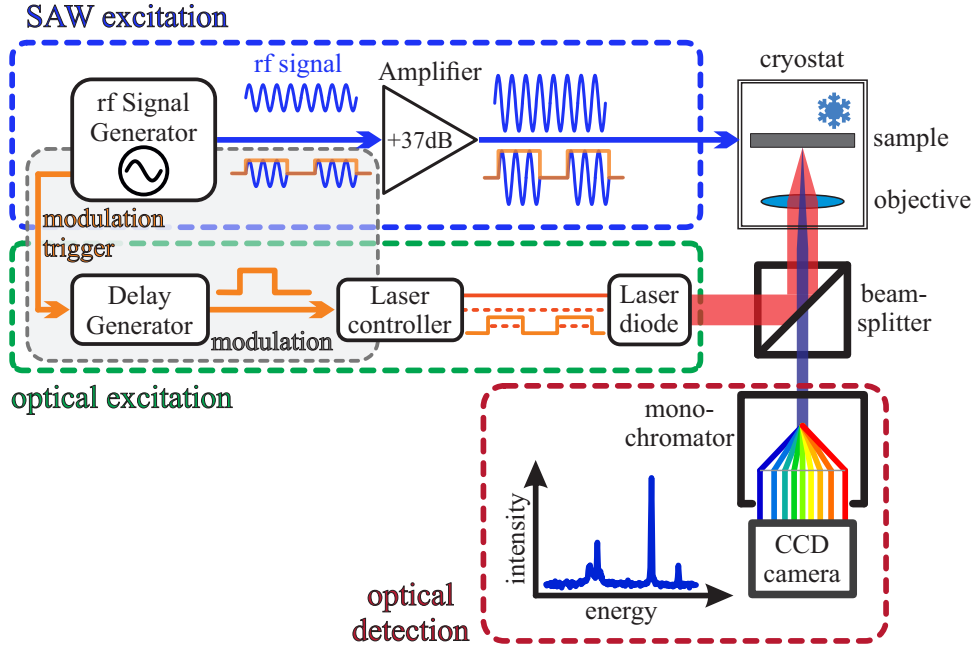


**Figure 5.1.:** Experimental setup to probe the time-averaged coupling between SAW and QD. The setup can be divided in three main components, SAW excitation (blue box), optical excitation (green box) and optical detection (red box). In this configuration, the three components are operated independently of each other, except for a modulated excitation where the gate signals for SAW and optical excitation have to be synchronised (see figure 5.3). The optical signal obtained by this method is averaged over many acoustic cycles. Therefore, no temporal information on the SAW induced dynamics can be deduced.

acoustic cycle for cw-excitation or is equally averaged over many acoustic cycles for pulsed excitation. Therefore, the emission collected in a time-averaged spectrum steams from all different times of the acoustic cycle to the same part. The line shape of a time-integrated spectrum can then be described by the integral of a time modulated (see equation 5.1) Lorentzian line over one acoustic cycle:

$$\begin{aligned}
 I(E) &= I_0 + f_{rf} \frac{2w}{\pi} \int_0^{1/f_{rf}} \frac{A_0}{4 \{E - [\Delta E \sin(2\pi f_{rf} t)]\}^2 + w^2} dt = \\
 &= I_0 + \frac{w}{\pi^2} \int_0^{2\pi} \frac{A_0}{4 \{E - [\Delta E \sin(t)]\}^2 + w^2} dt
 \end{aligned} \tag{5.3}$$

The formation of such a line shape is vividly illustrated in figure 5.2(a). Due to the surface acoustic waves strain fields, the Lorentzian emission line of a quantum dot (grey) is sinusoidally modulated in time (see equation 5.1). As the excitation occurs evenly at all times during the acoustic cycle, the amplitude of the Lorentzians is constant in

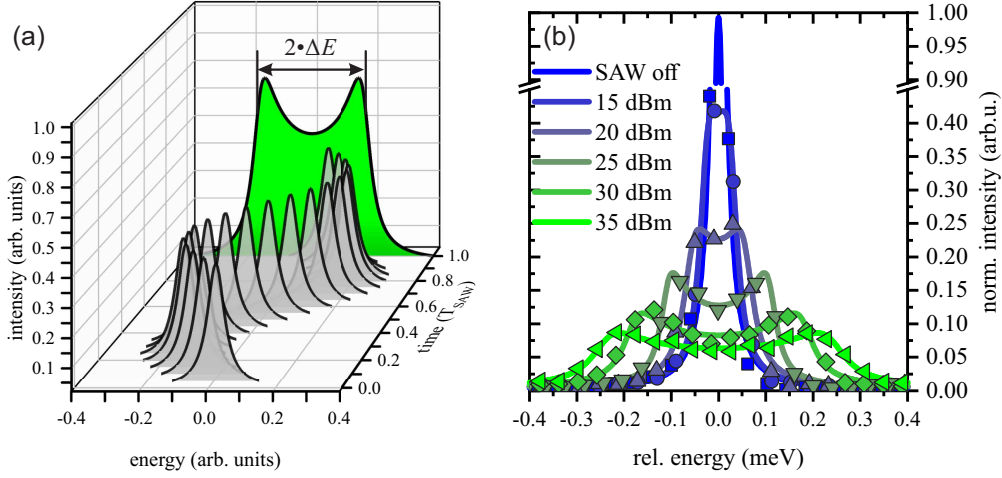


**Figure 5.2.:** (a) Modelled spectral tuning of a QD emission line by the strain field of a SAW. Over one acoustic cycle  $T_{\text{SAW}}$  the Lorentzian emission line (grey) is modulated sinusoidally. Integration over a full acoustic cycle leads to the green spectrum, described by equation 5.3 (b) Experimental time-averaged spectra (points) from a dynamically ( $f_{\text{SAW}} = 800$  MHz) strained QD for different amplitudes of the acoustic wave. Solid lines are best fits of equation 5.3. From these fits the amplitude  $\Delta E$  of the dynamic modulation can be extracted. With increasing power  $P_{\text{rf}}$  applied to the IDT, an increased broadening of the spectra is observed. Note the axis break for the  $y$ -axis.

time. Integration over one acoustic cycle leads to the green averaged spectrum, showing a distinctive double peak structure.

Figure 5.2(b) shows experimental time-averaged spectra of a quantum dot strained by a  $f_{\text{rf}} = 800$  MHz surface acoustic wave for different amplitudes  $P_{\text{rf}}$  of the driving rf signal. Solid lines are best fits of equation 5.3 to the experimental data (points). For no surface acoustic wave applied (light blue), the QD emission exhibits a Lorentzian line shape. With increasing power  $P_{\text{rf}}$  and thus increasing amplitude of the SAW, the emission shows a pronounced spectral broadening, whereas the total emission intensity stays constant (note the break in the  $y$ -axis between 0.5 and 0.9). For high  $P_{\text{rf}}$ , the characteristic double-peak structure arises. As it can be seen in figure 5.2(b), the experimental data can be nicely reproduced by equation 5.3. These fits provide a value for the amplitude  $\Delta E$  of the dynamic broadening, which, in turn, make it possible to quantify the local hydrostatic pressure at the position of the quantum dot.

A modification of this measurement technique is the introduction of a modulated excitation scheme. Since the conversion of electrical to mechanical energy at the IDT is not lossless, heat is also generated besides the SAW, which causes the sample to heat up. As this may cause unwanted thermal effects, especially for high electric powers  $P_{\text{rf}}$ , measures can be taken to prevent these unwanted influences. One way to realise this is to go from a continuous excitation scheme to a modulated one, meaning that both SAW and optical excitation occurs not continuously but in discrete pulses, as illustrated in figure 5.1. The

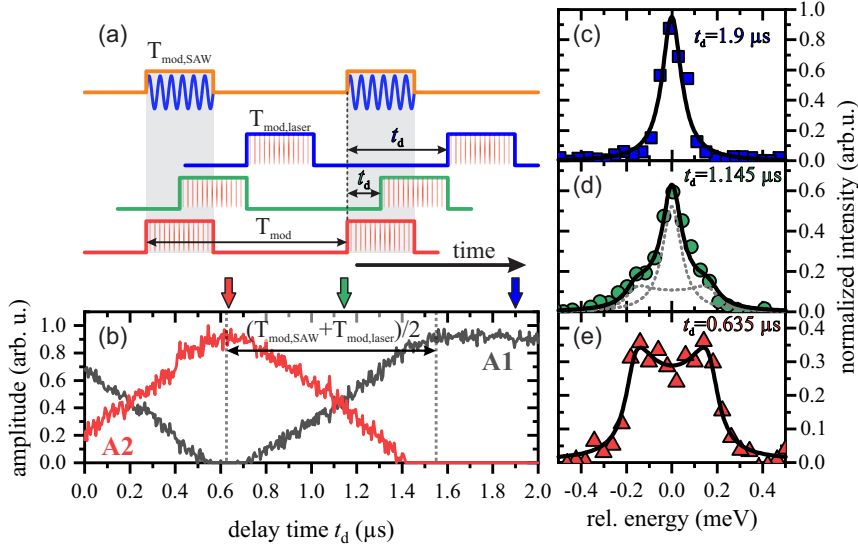


**Figure 5.3.:** Modulated SAW excitation. (a) To minimize heating of the sample and to avoid interference effects from reflected waves the SAW is often excited in pulses of length  $T_{\text{mod,SAW}}$ . To only obtain an optical signal when the QD is under the influence of a SAW, also the laser has to be modulated too ( $T_{\text{mod,laser}} \leq T_{\text{mod,SAW}}$ ) and the respective gate signal has to be delayed by  $t_d$  to ensure both excitations overlap in time at the QD. (b) Emission arising from the unstrained (A1) and strained (A2) part of the QD emission as a function of  $t_d$  and thus different temporal overlap between optical and SAW excitation. (c-e) Time-averaged spectra for no overlap (c), 50% overlap (d) and full overlap (e) between  $T_{\text{mod,laser}}$  and  $T_{\text{mod,SAW}}$ . The respective delay times  $t_d$  are marked with arrows in (b).

rf signal generator used to excite the SAW offers the possibility for pulsed modulation of the rf signal and both the length of the pulses  $T_{\text{mod,SAW}}$  and the pulse period  $T_{\text{mod}}$  can be set, as illustrated in figure 5.3(a). To ensure that the quantum dot is only excited at times when it is dynamically strained by the SAW, the optical excitation has to be modulated too. This can be realised by applying a matching gate signal of length  $T_{\text{mod,laser}}$  to the laser drivers gating input. It should be noted here, that the laser driver allows this kind of modulation only in the pulsed operation mode. For the modulation of the laser in cw mode, additional equipment would be necessary (e.g. **Electro-Optic Modulators (EOM)**). This gate signal is created by a delay generator (*Stanford Research Systems, DG645*) (see figure 5.1). The modulated excitation scheme is depicted in figure 5.3(a). Whenever the signal generator emits a rf-pulse, the delay generator is triggered to emit a square pulse of length  $T_{\text{mod,laser}}$ , delayed by a time  $t_d$ . This delay time  $t_d$  has to be adjusted to ensure that both laser and SAW excitation overlap in time at the position of the QD that is under investigation. The value of  $t_d$  depends on the different signal propagation times of the two excitations and is, due to the relative slow SAW velocity  $v_{\text{SAW}}$ , mostly dependent on the propagation length of the SAW from the IDT to the QD.

In order to determine  $t_d$  experimentally, the emission spectrum of a quantum dot is measured as a function of  $t_d$ . Spectra, recorded under modulated excitation with  $T_{\text{mod,laser}} = T_{\text{mod,SAW}} = 1 \mu\text{s}$  and  $T_{\text{mod}} = 10 \mu\text{s}$ , for three distinctive cases of  $t_d$  are shown in figure 5.3(c-e). If there is no overlap between SAW and laser pulses (case (c)), the recorded emission is not affected by the dynamic strain fields of the SAW, and the emission has a simple Lorentzian line shape. If both signals are fully overlapping the collected emission stems from times during which the QD is dynamically strained, and the characteristic double-peak structure, described by equation 5.3, becomes apparent (case (e)). If the two gated excitations overlap only partially (case (d)), the recorded emission can be described by the sum of an unperturbed Lorentzian and a dynamically modulated Lorentzian (equation 5.3):

$$I(E) = I_0 + \frac{2 \cdot A1}{\pi} \cdot \frac{w}{4(E - E_0)^2 + w^2} + \frac{A2 \cdot w}{\pi^2} \int_0^{2\pi} \frac{1}{4\{E_0 - [\Delta E \sin(t)]\}^2 + w^2} dt \quad (5.4)$$

Figure 5.3(b) shows the contributions of unperturbed (A1) and dynamically modulated (A2) emission, determined by fitting equation 5.4 to the respective spectra as a function of  $t_d$ . Starting with a partial overlap at  $t_d = 0$ , the overlap between SAW and laser excitation increases with  $t_d$ . Therefore, A2 increases and A1 decreases, while the overall emission (A1 + A2) stays constant. The overlap reaches a maximum at about  $t_d = 0.635 \mu\text{s}$ . In the further course of  $t_d$ , the overlap is reduced again, and, accordingly, A2 is decreases, while A1 increases. At about  $t_d = 1.55 \mu\text{s}$ , the two gate signal are completely shifted from each other, and the recorded emission can be fully described by a Lorentzian line shape. The distance between maximum and minimum of A1 or A2 depends on the length of the respective pulsed signals and is given by  $\frac{T_{\text{mod,laser}} + T_{\text{mod,SAW}}}{2}$ . The experimentally derived value of  $\approx 0.92 \mu\text{s}$  is slightly smaller than the expected value of  $1 \mu\text{s}$ . This is most likely caused by the fact that the gate length of the SAW and laser excitation at the QD are shorter than set by the signal/delay generator, as the SAW needs time to build up and the actual laser gate starts/stops with the first/last laser pulse within one gate period. To make sure that optical excitation takes only place when the full SAW amplitude is reached at the position of the QD and to allow for a small margin of error in the determination of  $t_d$ , the optical gate length is typically chosen to be smaller than the SAW gate length ( $T_{\text{mod,laser}} < T_{\text{mod,SAW}}$ ).

The reduction of heat load due to the employed modulated excitation scheme can be quantified by the duty cycle of the surface acoustic wave, defined as  $\frac{T_{\text{mod,SAW}}}{T_{\text{mod}}}$ . Typical values for the duty cycle used in the scope of this work range from 10 to 20%, which is sufficient to strongly reduce but not to exclude heating of the sample for high rf amplitudes  $P_{\text{rf}}$ . However, effects caused by thermal fluctuations occur on timescales longer then  $T_{\text{SAW}}$  meaning that the thermal conditions of the QD does not change during one modulation period  $T_{\text{mod}}$ . Exciting and probing the QD only between two SAW pulses and collecting

the respective emission reveals the quasi-static thermal conditions of the QD and makes it possible to distinguish these thermal effects from the dynamic modulation mediated by the SAW.

Furthermore, adjustment of the duty cycle, either by changing of the pulse length  $T_{\text{mod,SAW}}$  or the modulation frequency  $f_{\text{mod}} = \frac{1}{T_{\text{mod}}}$  allows for a precise control of the sample temperature and provides an additional quasi-static tuning mechanism for nano-systems, which will be used in section 9.1 [83].

The disadvantage of the modulated excitation scheme is a reduction of the optical duty cycle  $\frac{T_{\text{mod,laser}}}{T_{\text{mod}}}$  resulting in a reduced average emission intensity and correspondingly longer acquisition times necessary to collect the same number of photons.

The experimental setup presented in this section here provides a simple way to measure the local strain amplitude induced by a SAW. However, due to the time-averaging excitation and the time-integrating detection the time dependence of the modulation cannot be resolved.

## 5.2. Time domain spectroscopy: Time correlated single photon counting

In order to fully resolve the SAW driven dynamics, time domain detection has to be applied. In this case, the time-integrating detector (CCD) is replaced by a single photon avalanche diode (SPAD) allowing for a time-resolved detection with a high time resolution ( $< 50$  ps). These detectors are avalanche diodes which are operated well beyond their breakdown voltage, meaning that a single photon is sufficient to trigger an avalanche breakdown, which can then be detected electrically. This operation principle has the consequence that, after each avalanche breakdown, the detector has a dead time in which no events can be detected. These dead times are typically in the range of 50 – 80 ns, which is significantly larger than typical SAW periods used in this work ( $T_{\text{SAW}} < 5$  ns). Furthermore, even if sufficiently fast detection without dead time was possible, the maximum number of photon during one acoustic cycle  $T_{\text{SAW}}$  is limited by the lifetime  $\Gamma_{\text{QD}}$  of the QD. This makes the detection of more than one photon during one acoustic cycle and thus the observation of the SAW induced dynamics in real-time impossible. To observe such fast processes a technique called *Time-correlated single photon counting* (TCSPC) can be used. In this technique, the system under study is periodically excited, and optically detected single-photon events are correlated with the excitation. The most important application of TCSPC is the measurement of the fluorescence lifetime of a system. For that purpose, the system is excited with a pulsed light source and, for each detected photon, the time  $\tau$  since the last excitation is measured. Repeating this excitation cycle many times and entering the respective values determined for  $\tau$  in a histogram reveals the temporal decay characteristics of the system. To measure the dynamic spectral modulation induced by a

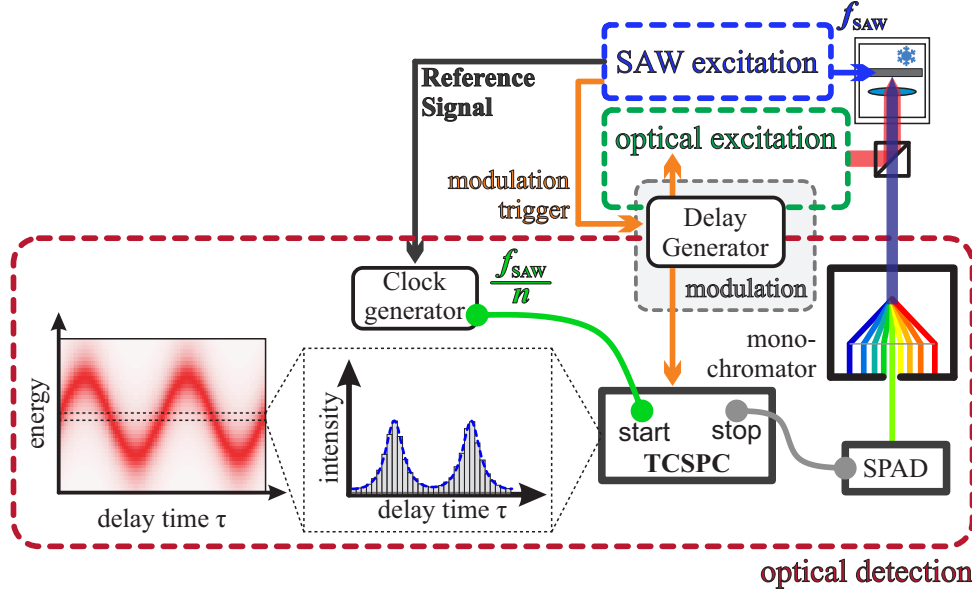


**Figure 5.4.:** Experimental setup to measure SAW induced dynamics on the optical emission of a QD in the time domain, using time correlated single photon counting (TCSPC). Whereas optical and SAW excitation remains unchanged, the time-integrated multi-channel optical detector (CCD) is replaced by a time-resolved single-channel detector (SPAD). The detected single photon events are correlated to a clock signal with a frequency being an integer fraction of  $f_{\text{SAW}}$  and thus the delay time  $\tau$  between reference signal and photon event is obtained for every detected photon. Collecting these delay times  $\tau$  over many SAW cycles and presenting them in a histogram reveals the temporal dynamic at a fixed energy (middle plot of lower panel). Repeating this measurement for different energies reveals the full energy-time dynamic introduced by the SAW (colour plot in lower panel).

SAW using TCSPC, the experimental configuration depicted in figure 5.4 is used. Both optical and SAW excitation remains unchanged from the configuration described in the previous subsection, which is used to measure the time-integrated response. On average, the QD is optically excited evenly over all phases by the laser diode, operating either in cw- or pulsed-mode operation. The collected PL emission of a single QD is spectrally filtered by a grating monochromator and photons with a specific energy  $E_{\text{detection}}$  are detected by a SPAD (*Micro Photon Devices*, PDM) with a time resolution of  $\tau_{\text{res}} < 50$  ps. The photon counts are then correlated by a two-channel TCSPC module (*PicoQuant*, PicoHarp 300) with a synchronisation signal of frequency  $\frac{f_{\text{SAW}}}{n}$ . This signal is provided by a clock generator (*Stanford Research System*, CG635). Using an integer fraction  $n$  of the SAW frequency  $f_{\text{SAW}}$  is necessary to ensure that the rate of the reference signal stays below 84 MHz, the maximum synchronisation rate of the TCSPC module. The TCSPC module basically works like a stopwatch, where the sync-signal (re)starts the clock at every  $n$ -th SAW cycle and a photon counting event stops the time measurement. To ensure that the

sync-signal triggers a restart of the TCSPC at always the same phase with respect to the SAW, the clock generator and the signal generator exciting the SAW have to be locked to the same reference oscillator. This measurement is repeated for many acoustic cycles, and the delay times  $\tau$  between sync-trigger and photon count are plotted in a histogram (see lower middle plot in figure 5.4). Whenever the emission energy of the QD  $E(t)$  matches the detection energy  $E_{\text{detection}}$ , an increased number of counts can be observed in the so obtained time traces. This measurement can be repeated for different detection energies  $E_{\text{detection}}$  and thus the full spectral and temporal evolution of the QD signal can be observed (see colour plot in figure 5.4). When a modulated excitation scheme is used, an additional gate signal can be used to prevent the TCSPC module from acquiring data in times when the QD is not optically excited. This minimizes the number of dark counts, meaning counts that are detected by SPAD but are not related to a photon emission event of the QD. Therefore the signal-to-noise ratio of the measurement is improved.

Figure 5.5 shows the spectral and temporal modulation of a QD dynamically strained

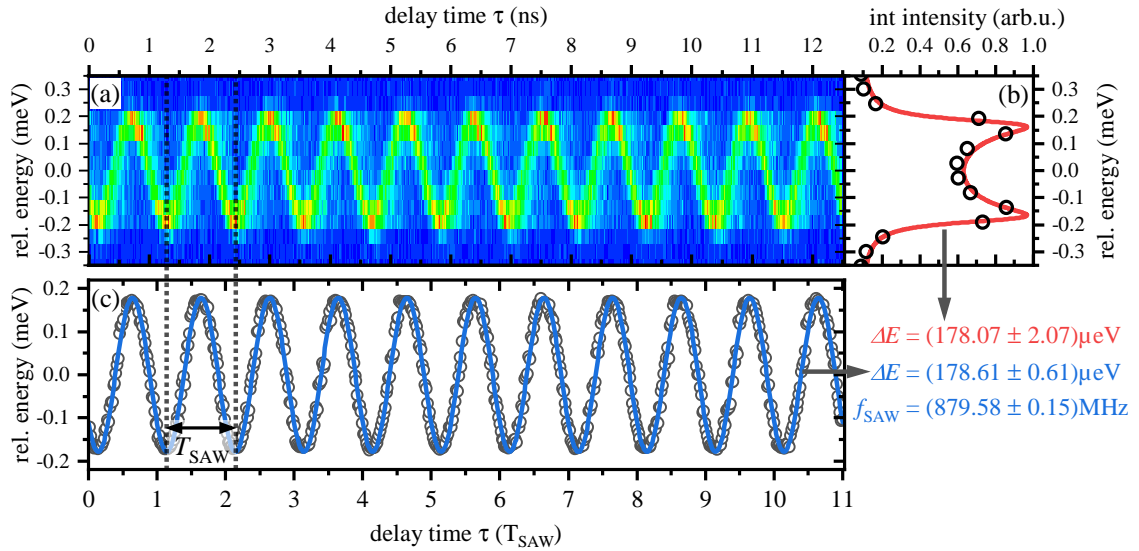


**Figure 5.5.:** Spectral modulation of a QD strained by a SAW ( $f_{\text{SAW}} = 880 \text{ MHz}$ ,  $P_{\text{rf}} = 24 \text{ dBm}$ ) in the time domain, measured by time correlated single photon counting (TCSPC). (a) False colour representation of the spectral modulation over 11 SAW cycles revealing a sinusoidal modulation. (b) Data of (a) integrated over time, revealing the characteristic double-peak structure. (c) Spectral peak positions as a function of time (points) extracted from (a).

by a  $f_{\text{SAW}} = 880 \text{ MHz}$  SAW, measured by TCSPC. The amplitude of the electrical signal exciting the SAW was set to  $P_{\text{rf}} = 24 \text{ dBm}$  and the rate of the synchronisation signal was set to  $\frac{f_{\text{SAW}}}{11} = 80 \text{ MHz}$ , meaning that the measured time range of  $\tau$  extends over 11 surface acoustic wave cycles  $T_{\text{SAW}} = \frac{1}{f_{\text{SAW}}} = 1.136 \text{ ns}$ . Optical excitation was realised by a  $\lambda_{\text{laser}} = 840 \text{ nm}$  diode laser in continuous wave mode, consequently the emission intensity

is expected to be uniform over time. Figure 5.5(a) shows the acquired data in a false colour representation. The expected sinusoidal modulation in time is nicely resolved. An increase of the emission intensity is observed at the turning points of the sinusoidal modulation, as at this points the modulation rate  $\left(\frac{dE(t)}{dt}\right)$  is lower, leading to an accumulation of the emission intensity at these energies. In figure 5.5(b), the time-integrated emission intensity (points) as a function of photon energy is depicted. This time-integrated emission shows the already considered double-peak structure and can be fitted by equation 5.3 (solid red line), revealing a modulation amplitude of  $\Delta E \approx 178 \mu\text{eV}$ .

For a closer investigation of spectral modulation in the time domain, the intensity as a function of energy  $I(E)$  is fitted by a Lorentzian function for each delay time  $\tau$ , revealing the emission energy as a function of time  $E_0(\tau)$ , shown as points in figure 5.5(c). Here, the sinusoidal modulation can be seen and, by fitting the data with a sine function (solid line), a modulation frequency of  $f_{\text{SAW}} \approx 879.58 \text{ MHz}$  and a modulation amplitude of  $\Delta E \approx 178 \mu\text{eV}$  are obtained, being in good agreement with the amplitude obtained from the fit in figure 5.5(b). The experimentally determined value for  $f_{\text{SAW}}$  is also very close to the one set by the signal generator ( $f_{\text{SAW}} = 880 \text{ MHz}$ ). Small deviations may arise from limited time and spectral resolution and small differences between the time bases for the SAW excitation (signal generator) and for the detection (TCSPC module).

In conclusion, we showed that TCSPC offers a possibility to observe SAW induced effects in the time domain. However, it must be noted that data obtained by this technique is the result of time correlation to a sync-signal, integrated over many excitation cycles and not measured in real-time. This means that every time dependent effect that is not at least an integer multiple or integer fraction of the synchronisation signal and thus of the SAW frequency  $f_{\text{SAW}}$  cannot be resolved by this technique. Furthermore, due to the single-channel detection, the acquisition time is strongly increased with respect to time-integrated detection. So if only the amplitude of a dynamic SAW modulation is to be determined, time-integrated detection is to be preferred.

### 5.3. Stroboscopic laser excitation

To make use of the advantages of time-integrated detection (easy implementation and low acquisition times) but to still to be able to resolve the temporal dynamics induced by a SAW, a stroboscopic laser excitation scheme, as shown in figure 5.6, can be applied. The part of the setup used for the SAW excitation remains unchanged and, for the optical detection, a time-integrated multi-channel detection, using a monochromator and a CCD camera, is applied. The QD is optically excited by a diode laser in pulsed mode operation but, instead of the internal oscillator source, an external signal is used to trigger the emission of the laser pulses. This trigger signal is provided by a clock generator and is set to a frequency of  $\frac{f_{\text{SAW}}}{n}$ , ensuring that the SAW and optical excitation are phase-locked

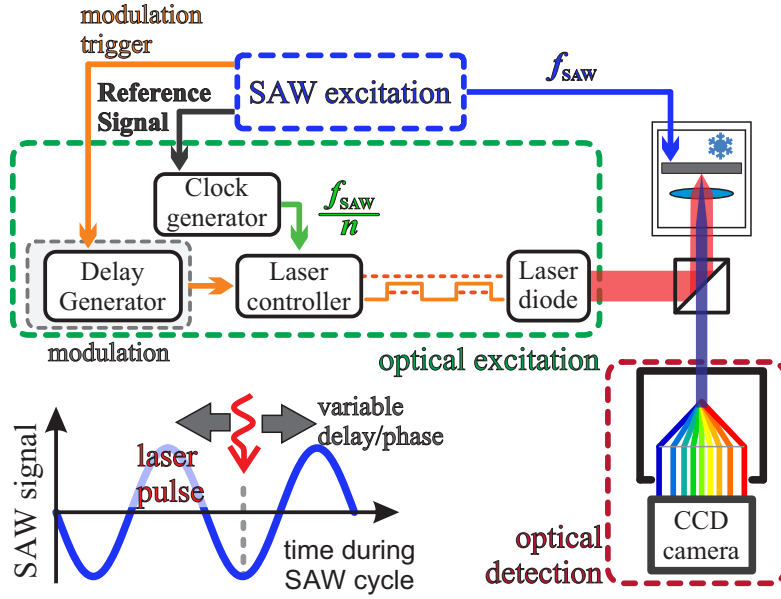


**Figure 5.6.:** Stroboscopic excitation. The experimental setup is very similar to the one used to measure the time-averaged SAW coupling, shown in figure 5.1. Here, a pulsed laser source is used, with a repetition rate locked to the rf generator and set to an integer fraction of  $f_{\text{SAW}}$ . Optical excitation accordingly occurs at fixed but tunable times during the acoustic cycle (lower panel). Although the optical detection is time-integrated, the stroboscopic excitation allows to resolve dynamic processes.

with respect to each other. Coupling the SAW and optical excitation in such a way ensures that the following relation is established:

$$f_{\text{SAW}} = n \cdot f_{\text{laser}} \quad (5.5)$$

This means that two successive laser pulses excite the QD at the same time during an acoustic cycle. The time of excitation during an acoustic cycle can be scanned by tuning the relative phase between the two electrical signals, which can easily be adjusted by the signal or clock generator (see bottom panel of figure 5.6).

In order to understand the time-integrated spectra obtained under stroboscopic excitation, the evolution of the experiment in the time domain has to be considered. After optical excitation, the QD decays exponentially within a certain time period defined by the decay rate  $\Gamma_{\text{QD}}$  of the QD. Simultaneously, the emission energy is dynamically modulated, as the SAW propagates further along the sample. Therefore the shape of the time-integrated spectrum depends strongly on the ratio  $\frac{\tau_{\text{QD}}}{T_{\text{SAW}}}$  between the decay time of the QD and the SAW period. In the limit of low SAW frequencies  $f_{\text{SAW}}$  so if  $\tau_{\text{QD}} \ll T_{\text{SAW}}$ , the decay of the QD takes place on a much faster timescale than the spectral modulation. Thus, the energy of the detected photons corresponds to the transition energy of the QD at the time

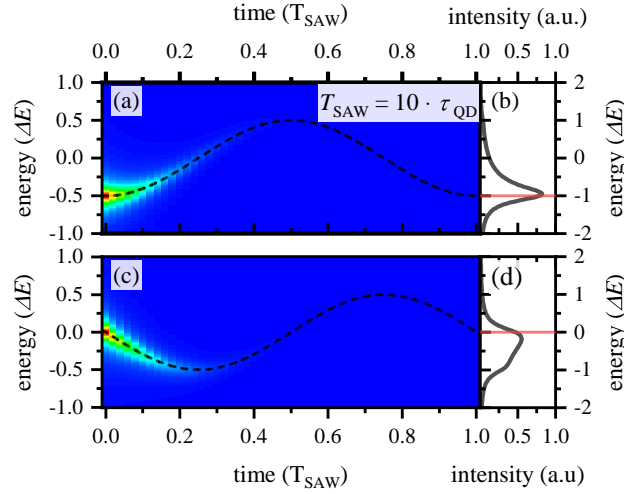


**Figure 5.7.:** (a,c) Calculated time dependent modulation of a QD, with  $\tau_{\text{QD}} = 0.1 \cdot T_{\text{SAW}}$ , under stroboscopic excitation. Optical excitation takes places at  $t = 0$ . The emission intensity decays exponentially and the emission energy follows the SAW induced modulation (dashed line). Depending on the excitation time during the acoustic cycle, the time-integrated emission is broadened (b,d).

of excitation. So the tuning of the excitation time allows the identification of the SAW induced spectral shift as a function of time during the acoustic cycle.

For higher frequencies, when  $\tau_{\text{QD}}$  and  $T_{\text{SAW}}$  become comparable, both decay and spectral modulation of the QD emission have to be taken into account. This case is schematically depicted in figure 5.7 for  $T_{\text{SAW}} = 10 \cdot \tau_{\text{D}}$ . The QD is excited at  $t = 0$  at the negative turning point (figure 5.7(a)) or at the zero-crossing point (figure 5.7(c)) of the spectral modulation. As time progresses, the emission intensity decays exponentially, and the energy follows a sinusoidal modulation, indicated by the dashed black lines. In the time-integrated spectra, this leads to a broadening of the emission as shown in figure 5.7(b) and (d) for the two cases respectively. Due to the spectral modulation, the detected emission is shifted away from the energy of the QD at the time of excitation (red lines) and towards the direction of the spectral modulation. This effect is more pronounced for excitation near the zero-crossing point of the modulation (d), as the modulation velocity is largest during these times, whereas for excitation near the turning points (b) the modulation is slower, and the emission energy stays longer within a certain energy range around the initial emission energy.

In the limit of very high SAW frequencies, meaning  $T_{\text{SAW}} \ll \tau_{\text{QD}}$ , the emission can be considered to be equally distributed over all acoustic phases and the time-integrated emission spectrum approaches the characteristic double peak structure described by equation 5.3, independently of the time of excitation.

Figure 5.8 shows time-integrated experimental data for a stroboscopically excited QD,

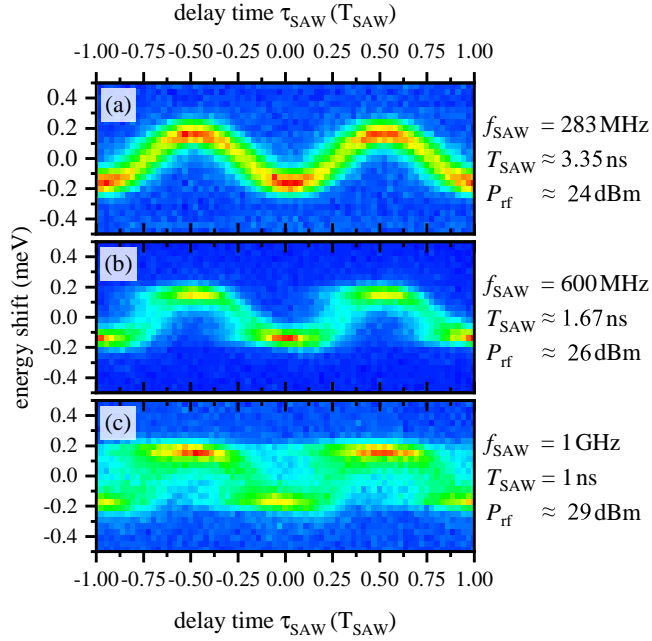


**Figure 5.8.:** Stroboscopic excitation scan for a QD over two acoustic cycles for three different SAW frequencies  $f_{\text{SAW}}$ . The SAW excitation amplitude  $P_{\text{rf}}$  was adjusted for each frequency to achieve comparable modulation amplitudes  $\Delta E$ . (a)  $P_{\text{rf}} = 24$  dBm,  $f_{\text{SAW}} = 283$  MHz (b)  $P_{\text{rf}} = 26$  dBm,  $f_{\text{SAW}} = 600$  MHz (c)  $P_{\text{rf}} = 29$  dBm,  $f_{\text{SAW}} = 1$  GHz

where the time of excitation has been tuned over two acoustic cycles for three different SAW frequencies. The respective amplitudes  $P_{\text{rf}}$  of the electric signal exciting the SAW have been adjusted to compensate for frequency dependent efficiencies of the SAW excitation and deformation potential coupling, thus to achieve a constant modulation amplitude  $\Delta E$ . For the data presented in figure 5.8(a), the frequency of the SAW was set to  $f_{\text{SAW}} = 283$  MHz, consequently the SAW period  $T_{\text{SAW}} \approx 3.35$  ns was noticeably larger than the decay time of the QD, which is in the order of  $\tau_{\text{QD}} \approx 0.2$  ns. The sinusoidal spectral modulation can nicely be resolved, and the information obtained about the spectral modulation is equivalent to the informations obtained by a measurement in the time domain using TCSPC. Although the overall emission for a given excitation time/phase is constant, higher peak emission intensities are observed at the turning points of the modulation. This indicates that the width of the emission peaks is smaller at the turning points than in between, when the modulation velocity is higher. This is already the first sign indicating spectral broadening, as the period of the spectral modulation is already fast enough to cause a spectral shift within the decay time of the QD.

As it can be seen in figure 5.8(b) and (c), this effect strongly increases with decreasing SAW period  $T_{\text{SAW}}$ , hence increasing SAW frequency  $f_{\text{SAW}}$ . This becomes especially clear when the system is excited at the falling ( $\tau_{\text{SAW}} \approx -0.25 \cdot T_{\text{SAW}}$  and  $\tau_{\text{SAW}} \approx 0.75 \cdot T_{\text{SAW}}$ ) or

rising ( $\tau_{\text{SAW}} \approx -0.75 \cdot T_{\text{SAW}}$  and  $\tau_{\text{SAW}} \approx 0.25 \cdot T_{\text{SAW}}$ ) edge of the modulation. When the QD is excited at one of these specific phases of the modulation, an increasing part of the emission is shifted towards the respective turning point that is passed next by the spectral modulation. This leads to the observed pronounced distortion of the emission spectra and makes it increasingly difficult to draw conclusions on the nature of the underlying modulation.

An analytical description of the experimental data is possible by a modified version of equation 5.3 that takes into account that the QD is excited only at a specific time  $\tau_{\text{SAW}}$  during the acoustic cycle and decays exponentially:

$$A_0 \rightarrow A(t) = A_0 \cdot \exp\left(-\frac{t}{\tau_{\text{QD}}}\right)$$

$$I(E) = I_0 + \frac{w}{\pi^2} \int_0^\infty \frac{A(t)}{4 \left\{ E - \left[ \Delta E \sin\left(\frac{2\pi}{T_{\text{SAW}}}t + \tau_{\text{SAW}}\right) \right] \right\}^2 + w^2} dt \quad (5.6)$$

Here, the constant emission amplitude  $A_0$  was replaced by an exponentially decaying amplitude  $A(t)$ , a phase factor  $\tau_{\text{SAW}}$  was implemented for the spectral modulation to define the time of excitation with respect to the modulation, and the integration limits were adjusted to integrate over all emission created by an excitation pulse. Like equation 5.3, this equation is only valid if the spectral modulation can be described by single sinusoidal function.

In summary, it can be said that, for low enough SAW frequencies  $f_{\text{SAW}}$ , stroboscopic excitation in combination with time-integrated detection is a technique that provides equivalent results as TCSPC measurements but, due to the multi-channel detection, at smaller acquisition times. So in the low frequency limit, this technique is the preferable method. With increasing frequency and the associated increased distortion of the emission spectra, time domain detection is the more suitable choice.

Finally, it should be mentioned that stroboscopic excitation and time domain spectroscopy (TCSPC) can be combined, making it possible to observe both spectral modulation and exponential decay in the time domain. This technique was, for example, used in reference [83] to monitor the emission of a QD that is dynamically tuned in and out of resonance with a photonic crystal nanocavity, which will be considered in section 9.1.2.



## 6. Multiharmonic frequency chirped transducers

So far only IDTs with a constant finger spacing were presented, which only allows for the excitation of a single frequency and, depending on the specific finger arrangement, its respective higher harmonics. Such IDTs structures are commercially used in modern signal processing and communication technologies as frequency filters. The advantages of these filters are their simple structure enabling easy and thus cost-efficient fabrication. Furthermore, they also allow for a compact filter design, as due to the comparable low sound velocity the wavelength of an electrical waves can be shrunk to small dimensions. This makes it possible to realise filters with a wide range of frequency on the scale of integrated chips. [55]

Therefore, a constant finger spacing is suitable for the use as a filter but may not always be the best solution for controlling nano structures. For stroboscopic experiments, where the SAW needs to be coupled to an external excitation sources of constant repetition rate, IDTs with a precise resonance frequency have to be fabricated. Such experiments include, for example, phase and time-resolved X-ray diffraction measurements on SAWs, where the SAW needs to be locked to the X-ray pulse train of a synchrotron [84–86]. Fabricating IDTs with a specific resonance frequency is of course possible but can be challenging, especially on layered structures with a dispersive sound velocity and for measurements at different temperatures and thus sound velocities<sup>1</sup>. Furthermore, for the creation of nano-mechanical waveforms by additive Fourier synthesis of surface acoustic waves, a fundamental frequency and their respective integer multiples are required [79]. Due to the inherent dispersion of the sound velocity for layered structures, the higher harmonics of a transducer do not match with the integer multiples of the fundamental frequency, complicating such kind of experiments.

These problems can be overcome and the frequency be obtained as an additional tuning parameter by introducing a linear variation of the IDT's finger spacing along the propagation direction, thereby the sharp resonances of a transducer are replaced by wide frequency bands. The so obtained IDTs are referred to as chirped transducers and are to be differentiated from

---

<sup>1</sup>To overcome the problem of temperature dependent sound velocities and thus transmission frequencies in commercial SAW filters, these are commonly fabricated on substrates (e.g. quartz), for which the sound velocity depends only weakly on the temperature and thus the transmission frequency does not shift with temperature.

so-called tapered IDTs, in which the periodicity varies over the transducer aperture [87]. The first commercial application of chirped transducers was the use in the dispersive delay lines, i.e. delay lines for which the time delay changes with the frequency [88]. Such delay lines were used for pulse compression of frequency chirped pulses in radar systems in order to increase their range resolution [89, 90].

In the first part of this section, the geometry of the chirped transducer and the resulting expected frequency response is introduced. After that the capability of these transducers to generate frequency over a wide range is confirmed by measuring both the transmission of a chirped delay line and the optomechanical response of a QD to the generated SAWs. Finally, the advantages of chirped transducers over conventional designs are demonstrated by performing stroboscopic experiments with a mode-locked laser of fixed repetition rate and realising a fast amplitude modulation of sinusoidal spectral modulation, thus creating a beat of SAW waves.

The main results of this chapter were published in *Physical Review Applied* under the title “Multiharmonic Frequency-Chirped Transducers for Surface-Acoustic-Wave Optomechanics” [91].

## 6.1. Fundamentals of the chirped transducer design

A schematic of the used device layout is shown in figure 6.1(a). IDTs are patterned directly on the (Al,Ga)As heterostructure containing a single layer of strain-free GaAs/(Al,Ga)As QDs. The IDT itself has a split-5-2 configuration combined with a variation of the period  $\lambda(x)$  along the axis of the IDT ( $x$ ). For the transducers considered here, the periodicity is a linear function of the position  $x$ :

$$\lambda(x) = \lambda_0 + \frac{\lambda_1 - \lambda_0}{L_{\text{IDT}}} \cdot x = \lambda_0 + \frac{\Delta\lambda}{L_{\text{IDT}}} \cdot x = \lambda_0 + \alpha \cdot x \quad (6.1)$$

So the periodicity of the IDT changes linearly over the length  $L_{\text{IDT}}$  of the transducer from  $\lambda_0$  at one side to  $\lambda_1$  at the other side. The gradient of the wavelength change is described by the dimensionless chirp parameter  $\alpha$ :

$$\alpha = \frac{d\lambda(x)}{dx} = \frac{\lambda_1 - \lambda_0}{L_{\text{IDT}}} = \frac{\Delta\lambda}{L_{\text{IDT}}} \quad (6.2)$$

Thus the fundamental resonance frequency and their respective higher harmonics  $n$  also become a function of the position  $x$  within the transducer:

$$f_{\text{SAW},n}(x) = n \cdot \frac{v_{\text{SAW}}}{\lambda(x)} = n \cdot \frac{v_{\text{SAW}}}{\lambda_0 + \alpha \cdot x} \quad (6.3)$$

So a chirped transducer is capable to transduce power between electrical and mechanical domain not only at a well-defined resonance frequency but over a broad frequency range. The width  $\Delta f_{\text{SAW},n}$  of these frequency bands is defined by:

$$\begin{aligned} \Delta f_{\text{SAW},n} &= n \left( \frac{v_{\text{SAW}}}{\lambda_0} - \frac{v_{\text{SAW}}}{\lambda_0 + \alpha \cdot L_{\text{IDT}}} \right) = n \left( \frac{v_{\text{SAW}}}{\lambda_0} - \frac{v_{\text{SAW}}}{\lambda_1} \right) = \\ &= n \cdot \Delta f_{\text{SAW},1} \end{aligned} \quad (6.4)$$

For this work, two different types of IDTs were investigated, one with a bandwidth of  $\Delta f_{\text{SAW},1} \approx 50.7$  MHz for the fundamental band ( $n = 1$ ), denoted as IDT1, the other with a bandwidth of  $\Delta f_{\text{SAW},1} \approx 101.3$  MHz, denoted as IDT2. The aperture was chosen to be  $A_{\text{IDT}} = 300 \mu\text{m}$  for both types of transducers and the length of the IDT was limited to  $L_{\text{IDT}} = 400 \mu\text{m}$ , consequently IDT1 consists of 190 and IDT2 of 205 finger-electrodes arranged in a split-5-2 geometry. A scanning electron microscope (SEM) image of IDT2 is shown in figure 6.1(b). On the top and bottom electrode pads, the aluminium bond wires used to contact the transducer electrically with the rf connectors in the cryostat can be seen. The two enlargements show the two ends of the IDT, nicely revealing the variation

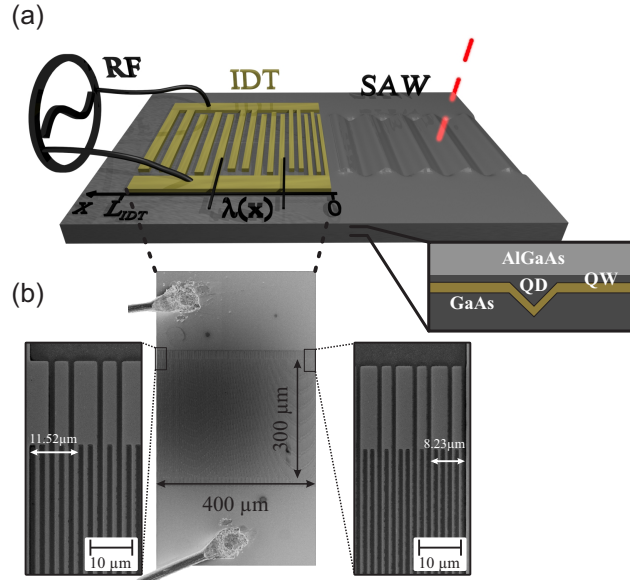


**Figure 6.1.:** Device layout of a chirped IDT. (a) Metal IDT patterned on a (Al,Ga)As heterostructure. The IDT layout combines a split-5-2 configuration with a linear variation of the finger periodicity  $\lambda(x)$  along the x-direction, corresponding to the [110] crystal direction of the GaAs substrate. (b) SEM images of a chirped IDTs (IDT2). Centre: Overview of the full IDT. Bonding wires can be seen on both electrodes. Left: Enlargement of the region at which the long-wavelength (low frequency) SAW is generated. Right: Enlargement of the region at which short-wavelength (high frequency) SAW is generated.

## 6. Multiharmonic frequency chirped transducers

in wavelength  $\lambda_{\text{SAW}}$  from one end to the other. The transducers were directly fabricated on an (Al,Ga)As heterostructure containing a single layer of strain-free (Al,Ga)As QDs. As seen in section 4.1.3 this sample (O404) shows a comparatively small dispersion for the sound velocity, and thus a constant SAW velocity of  $v_{\text{SAW}} = 2920 \frac{\text{m}}{\text{s}}$  is assumed for the following considerations. A summary of all design parameters for the respective transducer structures is given in table 6.1. As described in section 3.3, the amplitude response of an

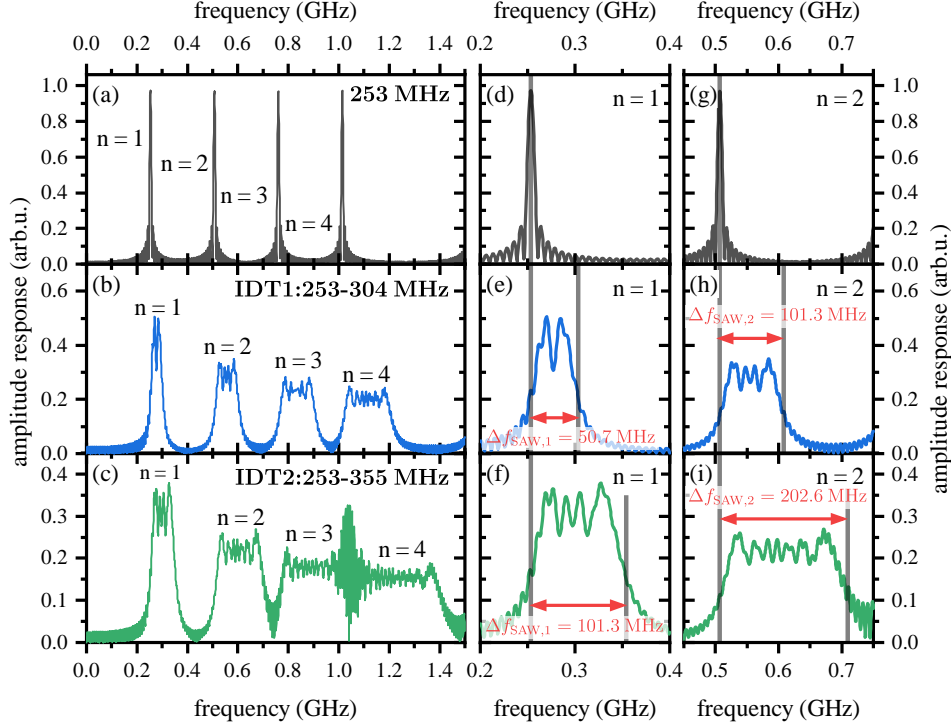


**Figure 6.2.:** Amplitude response for split-5-2 IDTs with a constant finger spacing ((a),(d),(g)) and with a chirped configuration according the design of IDT1 ((b),(e),(h)) and IDT2 ((c),(f),(i)), derived from equation 3.21. (a-c) Overview over the first four harmonics, (d-f) first harmonic and (g-i) second harmonic of the respective IDT structures.

IDT can be calculated using an impulse model (see equation 3.21). This is also possible for chirped IDT structures, where, instead of a periodic finger arrangement  $x_n$ , the respective fingers positions for a chirped structure are used. The so obtained amplitude responses are shown in figure 6.2 for IDT1, IDT2 and a reference split-5-2 IDT (grey) with equidistant

	$\lambda_0$	$\lambda_1$	$\Delta\lambda$	$\alpha$	$f_{\text{SAW},1}(L_{\text{IDT}})$	$\Delta f_{\text{SAW},1}$
IDT1	$9.6 \mu\text{m}$	$11.52 \mu\text{m}$	$1.92 \mu\text{m}$	$4.8 \cdot 10^{-3}$	253 MHz	50.7 MHz
IDT2	$8.23 \mu\text{m}$	$11.52 \mu\text{m}$	$3.29 \mu\text{m}$	$8.255 \cdot 10^{-3}$	253 MHz	101.3 MHz

Table 6.1.: Summary of design parameters of fabricated chirped IDTs

fingers and the same "fundamental" frequency of 253 MHz.

As already discussed in chapter 3.3, the non-chirped split-5-2 transducer shows four equidistant transmission peaks of the same height in the amplitude response. In contrast to that, the chirped transducers show broad transmission bands rather than discrete peaks. Furthermore, the height of these transmission bands decreases for higher harmonics  $n$ , while their respective width increases. The bandwidth of IDT2 is, at a given harmonic  $n$ , twice as big compared to IDT1, reflecting the larger chirp parameter  $\alpha$  for IDT2 (see table 6.1).

Looking at the enlargements of the first two harmonics for the chirped transducers, it can be nicely seen that the bandwidth increases by a factor of two from  $\Delta f_{\text{SAW},1} = 50.7$  MHz to  $\Delta f_{\text{SAW},2} = 101.3$  MHz for IDT1 and from  $\Delta f_{\text{SAW},1} = 101.3$  MHz to  $\Delta f_{\text{SAW},2} = 202.6$  MHz for IDT2. This reflects the linear dependence of the bandwidth on the number  $n$  of the respective harmonic, predicted by equation 6.4.

The decrease of height in the amplitude response for higher harmonics can be explained by the number of fingers that contribute to the excitation of a SAW at a given frequency. Since the bandwidth increases with higher harmonics but the number of fingers stays constant, the number of fingers being in resonance with a given frequency of the applied electrical signal decreases towards higher harmonics. This in turn leads directly to a reduction of the excited SAW amplitude at higher harmonics.

For IDT2, the bandwidth  $\Delta f_{\text{SAW}}$  is sufficiently large to cause an overlap between the high frequency part of the  $n = 3$  band (760 – 1064 MHz) and the low frequency part of the  $n = 4$  band (1014 – 1419 MHz), giving rise to a quasi-continuous frequency band. In the frequency range where the two bands overlap, a strongly oscillating behaviour of the amplitude response can be observed (see figure 6.2(c)). When an electrical signal with a frequency in this range is applied to the transducer, the resonance condition is fulfilled at two different positions of the IDT, hence two SAWs are launched at two different locations. These two waves can interfere destructively or constructively, depending on their relative phase shift. As the phase shift between the two waves changes with frequency, the observed interference pattern is created.

## 6.2. Surface acoustic wave transmission

The easiest way to characterise a chirped transducer is by measuring the transmission of a delay line consisting of two identical IDTs. An experimental setup for measuring the transmission is sketched in figure 6.3(a). A SAW is launched at the transmitting IDT by the use of a signal generator in combination with an amplifier to achieve sufficiently high acoustic powers. At the receiver IDT, (part of) the SAW is converted back to an electrical signal and detected in the time domain using an oscilloscope. The SAW is excited in pulses, making it possible to differentiate between electromagnetic crosstalk,

being transmitted over air/vacuum and the actually signal caused by the transmitted SAW. Fourier transforming the acquired waveform reveals amplitudes for all frequency components the transmitted signal is composed of.

Figure 6.3(b) shows the measured transmission amplitude at the driving frequency  $f_{rf}$

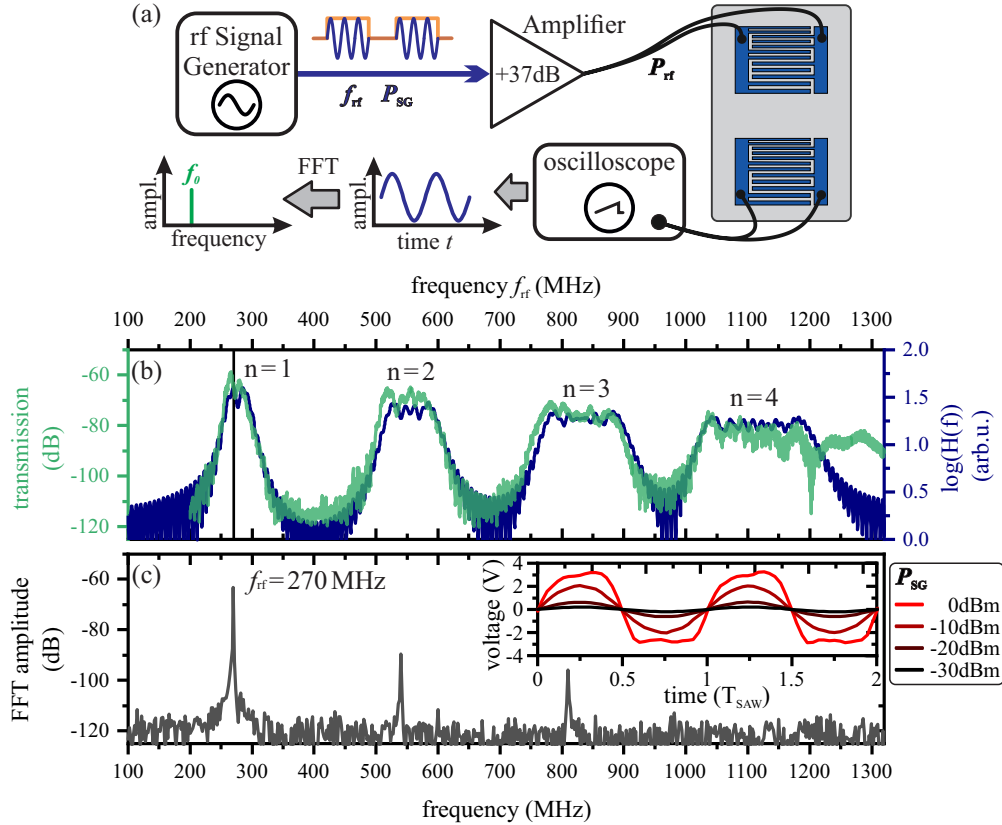


**Figure 6.3.:** Transmission of a chirped delay line. (a) Experimental setup used to measure the transmission of a delay line. A SAW is generated at the transmitter IDT. The transmitted wave is detected by the receiver IDT and analysed by an oscilloscope in the time domain. (b) Amplitude of transmitted wave (green) is in good agreement with calculated amplitude response (blue). (c) Fourier transform of the transmitted signal with nominal 320 MHz at  $P_{rf} = 32$  dBm. Higher harmonics occur due to non-linear effects of the amplifier at high powers. Inset shows the output signal of the amplifier for different input powers  $P_{SG}$  of a sinusoidal wave. For high input powers, the amplifier saturates, resulting in a clipped output waveform.

(green) of a delay line consisting of IDT1-IDTs as a function of  $f_{rf}$ . In addition to the measured transmission amplitude, the calculated amplitude response for the corresponding IDT is also shown (blue). Due to the low electromechanical coupling coefficient of GaAs and the fact that for a transmission experiment the signal needs to be converted twice between mechanical and electrical domain, a comparatively high rf-power of the exciting electrical signal was chosen ( $P_{rf} = 32$  dBm). The experiment was carried out at room

temperature and the sample was mounted on a different sample holder than for the later optical experiments thus, the absolute values of the transmission cannot be compared directly. It can be seen that the measured transmission is in good agreement to the expected amplitude response. Both relative height and frequency of the respective transmission bands  $n$  show a high level of agreement. Only a slight shift in frequency can be seen, most clearly for the  $n = 2$  and  $n = 3$  bands. This shift can be caused by uncertainties in the determination of the sound velocity  $v_{\text{SAW}}$  and the fact that the measurements were performed at room temperature whereas the amplitude response was calculated based on the low temperature sound velocity so a shift of about 3 MHz between measurement and calculation is expected (see section 4.3). In the course of the fourth transmission band, a slight decrease of the transmitted amplitude can be seen, most likely due to higher attenuation in the electric wiring at higher frequencies. Furthermore, a strong deviation from the expected behaviour can be seen beyond the  $n = 4$  band ( $f > 1$  GHz). For these frequencies, the measured transmission is no longer determined by the transmitted SAW signal but by electromagnetic crosstalk caused by insufficient impedance matching of the wiring at high frequencies.

Figure 6.3(c) shows the full FFT spectrum of the transmitted wave for a driving frequency of  $f_{\text{rf}} = 270$  MHz. There, it can clearly be seen that beside the driving frequency  $f_{\text{rf}}$ , set by the signal generator, the transmitted signal shows additional frequency components at twice and triple the frequency  $f_{\text{rf}}$ . This occurrence of higher harmonics points towards a non-linear effect within the transmission experiment. As source of this non-linearity, the amplifier at high input amplitudes can be identified. This is illustrated in the inset of figure 6.3(c), where the output waveform of the amplifier for different input powers  $P_{\text{SG}}$  is shown (with an additional 10 dBm attenuator after the amplifier to stay within the input limits of the oscilloscope). For high input amplitudes ( $P_{\text{SG}} > -10$  dBm), the amplifier gain is no longer linear and the output shows increasing deviations from the input waveform due to saturation of the amplifier. This results in a clipped output waveform and thus to the occurrence of higher harmonics in the output signal. Although, this non-linearity is not caused by the sample itself but the experimental setup, special care has to be taken using chirped transducers. This is due to the broad transmission bands that make the presence of those higher harmonics within the transmission bands of the transducer more likely and lead higher chance of conversion into SAW. In theory, the same would be true for standard (non-chirped) IDTs but a small dispersion in sound velocity, conceivably caused by the mass-loading of the IDT itself, causes the higher harmonics of the transducer to not exactly match with an integer multiple of the fundamental frequency. So for standard IDTs, the higher harmonics are often filtered out or, at least, strongly attenuated by the IDTs transfer function.

### 6.3. Optomechanical characterisation of chirped transducers

In order to optomechanically characterise the chirped transducers, the emission of single quantum dots is measured as a function of the SAW frequency  $f_{\text{SAW}}$ . Therefore, the sample is mounted into a closed cycle cryostat, cooled down to about  $T = 4$  K, and emission spectra are acquired for different frequencies  $f_{\text{rf}}$  of the rf-signal that is applied to the respective IDTs. For all frequencies  $f_{\text{rf}}$ , the amplitude of the signal is kept constant at  $P_{\text{rf}} = 27$  dBm. Optical excitation was realised by a pulsed ( $f_{\text{laser}} = 80$  MHz) diode laser ( $\lambda_{\text{laser}} = 660$  nm). To ensure  $f_{\text{laser}}$  and  $f_{\text{SAW}}$  are incommensurable, meaning the dynamic modulation of the QD is always averaged over the full acoustic cycle in one time-integrated spectrum, two independent reference oscillators are used for SAW and laser excitation. In order to minimize heating of the sample, the SAW was launched in pulses of  $2 \mu\text{s}$  with a modulation period of  $10 \mu\text{s}$  (duty cycle 20%). To ensure optical excitation only when the SAW is active at the position of the QD, the laser was also modulated with a pulse length of  $1.5 \mu\text{s}$ , thus with an optic duty cycle of 15%. The such obtained dynamical modulated spectra are plotted in a false colour representation with respect to their respective unperturbed emission energy  $E_0$  as a function of the driving frequency  $f_{\text{rf}}$  in figure 6.4(a) and (b) for IDT1 and IDT2, respectively.<sup>2</sup> The respective unperturbed emission energy  $E_0$  was determined individually for each frequency  $f_{\text{rf}}$  by shifting the two windows for SAW and laser excitation against each other and optically exciting the QD when the SAW has already passed by. This makes it possible to correct the data shown in figure 6.4 for small shifts in emission energy  $E_0$  caused by different thermal loads at different driving frequencies  $f_{\text{rf}}$ . For both IDTs, a pronounced spectral broadening of the emission can be observed for all four harmonics ( $n = 1, 2, 3, 4$ ) of the split-5-2 IDTs. To analyse the spectral broadening  $\Delta E$  as a function of  $f_{\text{rf}}$  in more details, the experimental data was fitted with equation 5.3. The so obtained values for  $\Delta E$  are shown in figure 6.4(b) and (d) for IDT1 and IDT2 respectively. The grey shaded area represents the amplitude response for the respective IDTs and the red horizontal line marks the resolution limit of the used spectrometer, thus indicates the smallest value of  $\Delta E$  that can be resolved. For both types of IDTs, the observed spectral broadening is in good agreement with the frequency ranges predicted by the amplitude response model and both position and bandwidth of the frequency bands are nicely reproduced. The fast oscillating behaviour in the region where the  $n = 3$  and  $n = 4$  transmission bands of IDT2 overlap is also observed in the spectral broadening of the QD emission.

Deviations from the simple amplitude response model can be seen when looking at the amplitude  $\Delta E$  of the spectral broadening. The amplitude response predicts a steady decrease of the amplitude with increasing harmonic  $n$ , which is also confirmed by the

<sup>2</sup>The data shown in figure 6.4 for IDT1 is the same published in [91], IDT2 was also the same as in this publication but the data was measured with a new cabling, allowing for SAW excitation above 1.2 GHz. So, in contrast to the data shown in [91], the full  $n = 4$  band can be resolved for IDT2.

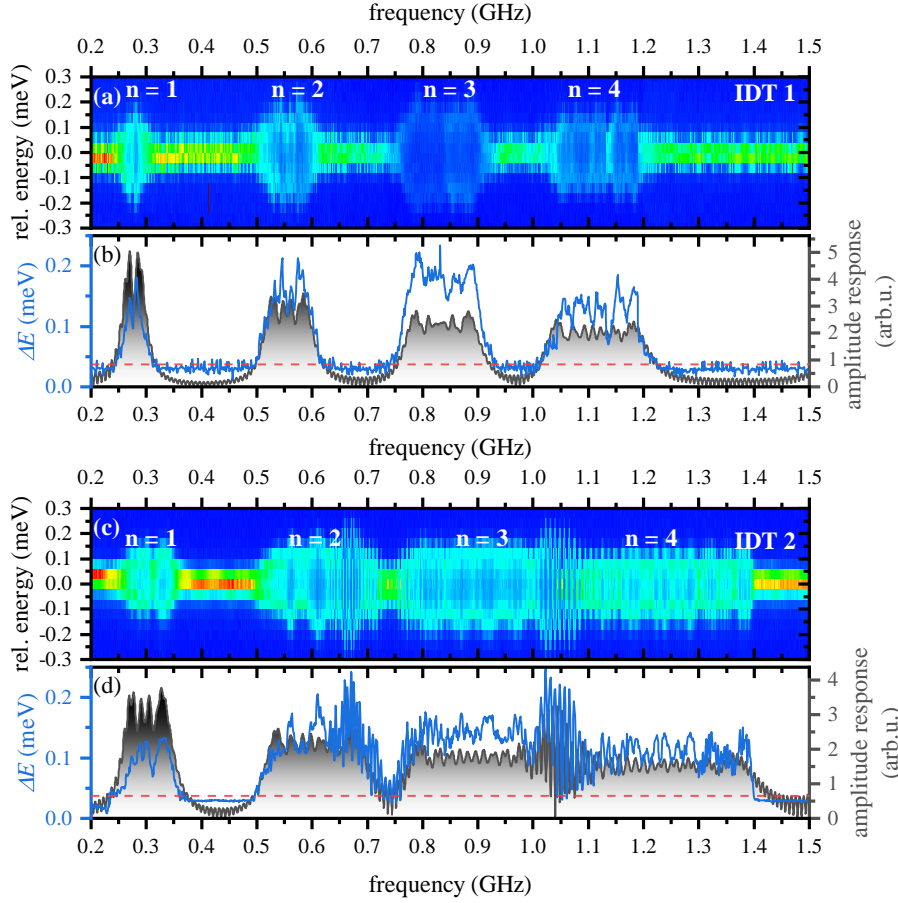


**Figure 6.4.:** False-colour plot of the normalized emission intensity as a function of  $f_{\text{SAW}}$  and relative emission energy for IDT1 (a) and IDT2 (c). In (b) and (d), the respective values for  $\Delta E$ , extracted from the measured spectra, are shown as a function of  $f_{\text{SAW}}$ . The grey shaded area marks the course of the calculated amplitude response. The red dashed line shows the resolution limit of the used spectrometer  $\approx 9$  GHz.

electrical transmission measurements (see figure 6.3). In contrast to that, the spectral broadening  $\Delta E$  slightly increases from the  $n = 1$ , over the  $n = 2$  to the  $n = 3$  and, for the  $n = 4$  band, decreases again to about the height of the  $n = 1$  band for both types of IDTs. These deviations arise from the fact that, when looking at the optomechanical response of a QD, not only the efficiency of the transducer, like in transmission measurements, but also the optomechanical coupling strength between SAW and QD has to be taken into account. For the specific sample used here ("O404"), the quantum dot layer is located at a depth of about  $d = 0.153$  nm below the surface of the substrate. According to the calculations shown in figure 3.4, a maximum for the hydro-static pressure and thus for the deformation potential coupling is expected at a SAW frequency of  $f_{\text{SAW}} \approx \frac{0.6 \text{ GHz} \cdot \mu\text{m}}{153 \text{ nm}} \approx 3.9$  GHz. So the decreasing

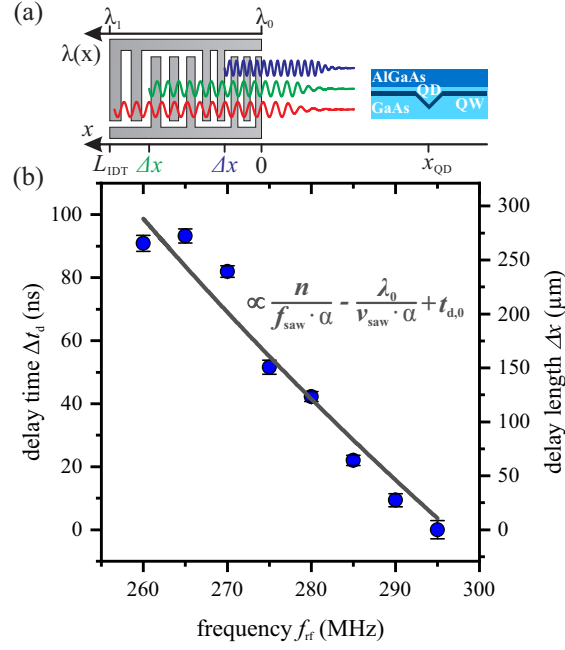


**Figure 6.5.:** Local SAW generation in a chirped transducer. (a) Illustration of the frequency dependent variation of the SAW’s propagation length  $\Delta x$  from the point of excitation along the axis of the IDT (left) to the fixed position of the sensor QD. (b) Measured  $\Delta x$  as a function of frequency across the  $n = 1$  band of IDT1 (symbols) and expected dependence given by equation 6.6 (solid line).

penetration depth of the SAW and the associated shift of the pressure maximum towards the QD-layer with increasing frequency partially counteracts the decreasing efficiency of the IDTs and the cryostat-wiring.

In contrast to traditional non-chirped IDTs, for chirped transducers, a SAW is not generated evenly over the whole length of the IDT. For a given applied frequency  $f_{\text{rf}}$ , only a small section of the IDT matches the resonance condition 3.19 for  $f_{\text{rf}}$ . This is illustrated in figure 6.5(a). As a consequence, the distance the SAW has to cover before reaching a specific QD, and thus the time delay  $t_d$  for modulated excitation varies with the frequency  $f_{\text{rf}}$ . The maximum shift in delay time  $\Delta t_d$ , meaning the difference in delay time  $t_d$  between the largest and the smallest frequency of a transmission band  $n$ , depends on the length  $L_{\text{IDT}}$  of the IDT:

$$\Delta t_d = \frac{L_{\text{IDT}}}{v_{\text{SAW}}} = \frac{400 \mu\text{m}}{2920 \frac{\text{m}}{\text{s}}} \approx 137 \text{ ns} \quad (6.5)$$

For the IDTs considered here, a maximum shift in delay time  $\Delta t_d \approx 137 \text{ ns}$  is expected. This shift must be taken into account when conducting measurements with a modulated excitation scheme and changing the frequency  $f_{\text{rf}}$ . In this case, the delay between laser and SAW excitation has to be adjusted with respect to the applied frequency  $f_{\text{rf}}$  or, as it

has been done in the previously shown measurements (figure 6.4), the SAW gate  $T_{\text{mod,SAW}}$  must be sufficiently larger than the laser gate  $T_{\text{mod,laser}}$ , to always ensure an active SAW at the QD during optical excitation.

The frequency dependent shift of the point of SAW generation can be determined in a pulsed measurement by measuring the corresponding  $t_d$  for a complete overlap of the two gates as a function of frequency  $f_{\text{rf}}$ . For that, both optical and SAW excitation are applied in equally long pulses ( $T_{\text{mod,SAW}} = T_{\text{mod,laser}} = 1 \mu\text{s}$ ), and time-integrated spectra as function of relative delay  $t_d$  between both gates are recorded. From these spectra the relative delay times  $t_d$  for a complete overlap of both signal can be determined, as it is described in figure 5.3. The so obtained values for  $\Delta x$  and  $\Delta t_d$  are shown as a function of the frequency  $f_{\text{SAW}}$  for IDT1 in figure 6.5(b). The frequency  $f_{\text{rf}}$  of the signal applied to the IDT is tuned across the first band of the respective IDT.

The relative delay shifts  $\Delta t_d$  and the corresponding change in the propagation length  $\Delta x = \Delta t_d \cdot v_{\text{SAW}}$  are given with respect to the values obtained for the highest frequency ( $t_{d,0}$ ). The delay shift is expected to have the following frequency dependence:

$$\Delta t_d (f_{\text{rf}}) = \frac{\Delta x}{v_{\text{SAW}}} = \frac{1}{v_{\text{SAW}}} \cdot \frac{\lambda(x) - \lambda_0}{\alpha} = \frac{n}{\alpha \cdot f_{\text{SAW}}(x)} - \frac{\lambda_0}{\alpha \cdot v_{\text{SAW}}} \quad (6.6)$$

This dependence, with the respective values for IDT1 (see table 6.1), is shown in figure 6.5(b) as a solid grey line and is in good agreement with the experimental data.

## 6.4. Stroboscopic spectroscopy

In order to perform stroboscopic SAW spectroscopy, the same technique as described in section 5.3, using an externally triggerable diode laser, could be applied. However, here, a different approach shall be shown, which makes use of the chirped IDT's advantage to allow SAW excitation over a broad frequency range. This makes it possible to realise a stable phase-lock between a SAW and the pulses of a mode-locked laser with a fixed repetition rate. The optical excitation was realised by a mode-locked tunable fibre laser (*TOPTICA Photonics*, FFpro TVIS) with a fixed repetition rate of  $f_{\text{laser}} = 80 \text{ MHz}$  and an emission wavelength of about 640 nm. In addition to the  $< 1 \text{ ps}$  long laser pulses, the laser provides also an electrical monitor signal of the internal oscillator, allowing to synchronise an external experiment (e.g. life measurements using TCSPC) to the generated laser pulses. This electrical signal, shown in figure 6.6(a) as a **darkblue** line, is in accordance to the *Nuclear Instrumentation Module* (NIM) standard for logical signals. The Fourier transform of this signal, shown in figure 6.6(b) reveals the signal to be composed of the lasers fundamental frequency  $f_{\text{laser}} = 80 \text{ MHz}$  and a variety of higher harmonics  $n \cdot f_{\text{laser}}$ . The fourth harmonic of the laser frequency  $4 \cdot f_{\text{laser}} = 320 \text{ MHz}$  lies within the first transmission band of IDT2. This makes it possible to filter the respective frequency component from the

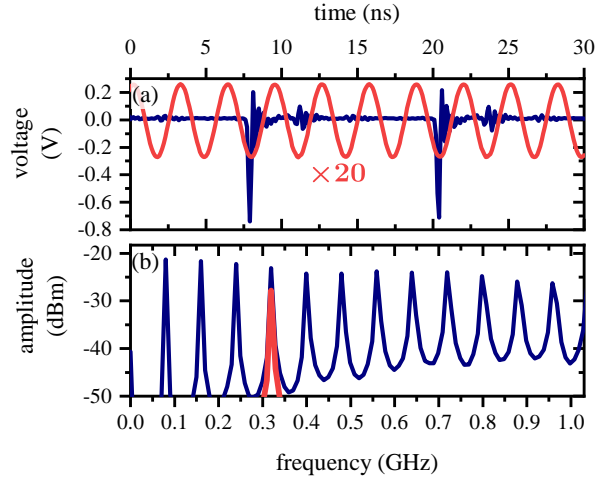


**Figure 6.6.:** (a) Monitor output (blue) of the mode-locked laser, providing a 80 MHz signal accordingly to the Nuclear Instrumentation Module standard for logical signals (NIM). (b) Fourier transform of the monitor output reveals the NIM signal to be composed of the laser's base frequency  $f_{\text{laser}} = 80$  MHz and higher harmonics of it. The red lines in (a) and (b) correspond to the 320 MHz component of the monitor output, filtered by a pass-band filter.

monitor signal, using an appropriate band-pass filter and, after adjusting the amplitude of this signal, directly applying it to IDT2. For frequency filtering, a commercially available frequency band-pass filter (*Mini-Circuits*, SXBP-310+) with a pass band ranging from 300 MHz to 320 MHz and an insertion loss of about 4.2 dB at 320 MHz was used. The so filtered NIM monitor signal is shown as a red solid line in figure 6.6 (a) and its respective Fourier transform in (b), confirming that the filtered signal is indeed a pure sinusoidal signal with a frequency of 320 MHz. By directly applying this filtered signal to the IDT, the condition for stroboscopic excitation (see equation 5.5) is inherently fulfilled:

$$f_{\text{SAW}} = 4 \cdot f_{\text{laser}} \quad (6.7)$$

#### 6.4.1. Time-integrated detection

The setup for stroboscopic SAW spectroscopy using a mode-locked laser is depicted in figure 6.7. This setup can be divided in two parts, one for the optical excitation of the QDs (green box) and one for the SAW excitation (blue box). The mode-locked laser is the central component of the setup, as it provides both the electrical signal for the SAW excitation and the laser pulses for the optical excitation. Furthermore, it ensures the phase coupling between the optical and the SAW excitation required for stroboscopic excitation. Tuning the relative phase of the two excitations can be realised by either delaying the optical signal with respect to the electrical signal or the other way around. This can be realised by varying the propagation length from laser to sample for the respective signal,

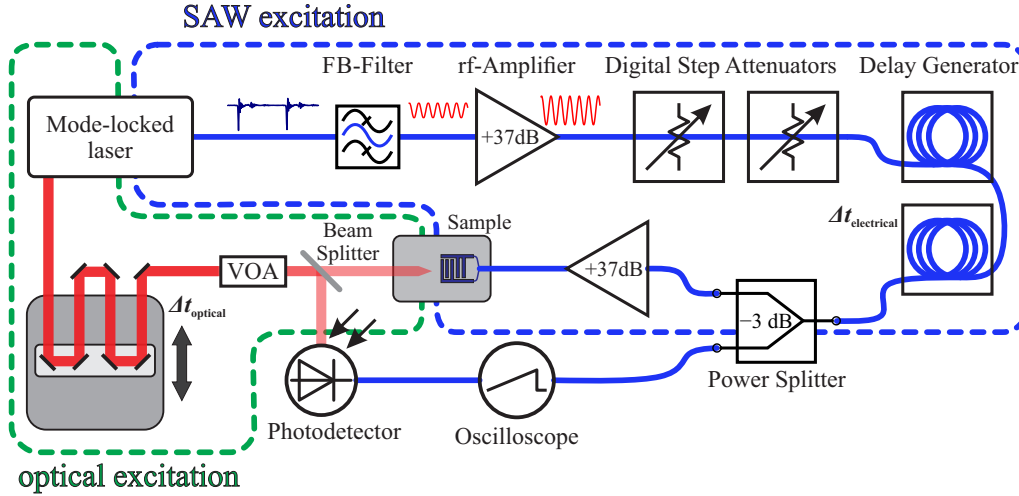


**Figure 6.7.:** Experimental setup used for stroboscopic phase-locked excitation and time-integrated detection. Electrical signals are depicted by blue connections and the optical path by red ones. The electrical monitor output of a mode-locked laser is filtered and amplified so it can be used to excite a  $f_{\text{SAW}} = 320 \text{ MHz} = 4 \cdot f_{\text{laser}}$  SAW. The tuning of the relative phase between SAW and laser excitation is realised by delaying the electrical ( $\Delta t_{\text{electrical}}$ ) or optical ( $\Delta t_{\text{optical}}$ ) signal using either an electrical delay generator or an optical delay stage. The exact phase relation between optical and SAW excitation is determined by a photodetector and an oscilloscope measuring the relative phase between optical and electrical signal.

which will now briefly be discussed for both methods.

The approach for delaying the electrical signal for the SAW excitation is shown in figure 6.7. After the  $4 \cdot f_{\text{laser}} = 320 \text{ MHz}$  is isolated from the electric monitor output of the laser, the signal is sent through two cable-based electrical delay systems (*Ortec*, 425 Delay). These delay systems are made of cables of different lengths, which delay the electrical signal by 1, 2, 4, 8 or 16 ns and can be interconnected in any combination, thus allowing to tune the electrical delay  $\Delta t_{\text{electrical}}$  from 0 to 62 ns in discrete steps of 1 ns. The relative phase shift between electrical and optical excitation in units of  $T_{\text{SAW}}$  is then defined by:

$$\tau_{\text{SAW}} = -\Delta t_{\text{electrical}} \bmod T_{\text{SAW}} \quad (6.8)$$

Since for an increasing electrical delay  $\Delta t_{\text{electrical}}$  the cable length has to be increased ( $\approx 22 \frac{\text{cm}}{\text{ns}}$ ), the cable-length dependent losses also increase with increasing delay. These losses have to be compensated for to ensure that the QD is strained by a SAW with constant amplitude for all delays  $\Delta t_{\text{electrical}}$ . This is realised by a combination of two constant gain amplifiers (*Mini-Circuits*, ZHL-42W+) with a gain of  $\approx 37 \text{ dB}$  each and two digital step attenuators (*Mini-Circuits*, ZFAT-124 and ZFAT-R512). The combination of these attenuators has a total insertion loss of about 5 dBm and a variable attenuation up to 10.5 dBm that can be tuned in discrete steps of 0.5 dB. In order to determine

the amplitude of the electrical signal exciting the SAW, the signal is split by a  $-3$  dB rf beam splitter (*Mini-Circuits*, ZFSC-2-372-S+) before final amplification and analysed by a 2-GHz-bandwidth oscilloscope (*Teledyne LeCroy*, Waverunner 62Zi). In addition to the amplitude of the electrical signal, the oscilloscope is used to measure the exact phase relation between SAW and optical excitation. Therefore, the optical signal is split by a 50:50 beam splitter and one half of the signal is analysed by a high-speed photodetector (*Newport*, 818-BB-21) triggering the oscilloscope in the event of a laser pulse.

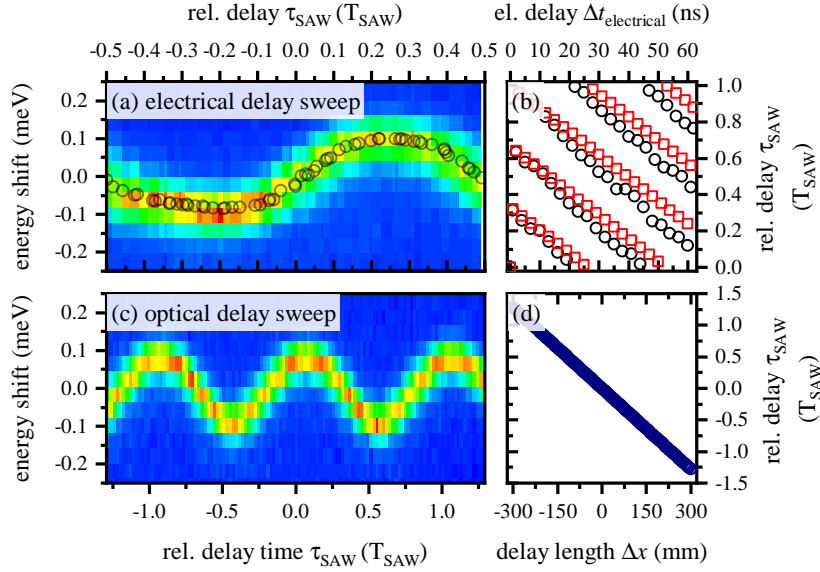


**Figure 6.8.:** (a),(c) Time-integrated spectra as a function of energy shift and excitation time  $\tau_{\text{SAW}}$  during the acoustic cycle plotted in false-colour representation. The excitation time  $\tau_{\text{SAW}}$  was tuned by varying  $\Delta t_{\text{electrical}}$  (a) and  $\Delta t_{\text{optical}}$  (c). A characteristic sinusoidal modulation is observed in both complementary and independent experiments. Circles in (a) mark the respective position of the emission maximum as a function of  $\tau_{\text{SAW}}$ , showing the non-uniformly distributed values for  $\tau_{\text{SAW}}$  when tuning  $\Delta t_{\text{electrical}}$ . (b) Expected (red squares) and measured (black circles) dependence of  $\tau_{\text{SAW}}$  on  $\Delta t_{\text{electrical}}$ , showing clear deviations introduced by the cable-based delay system and confirming the need to determine  $\tau_{\text{SAW}}$  experimentally. (d) Dependence of  $\tau_{\text{SAW}}$  on  $\Delta_{\text{optical}}$ , demonstrating the high timing accuracy when using optical delay lines.

In figure 6.8(a), the time-integrated emission intensity of a single QD is shown as a function of the spectral shift with respect to the unperturbed emission energy of the QD and measured relative delay  $\tau_{\text{SAW}}$ , obtained by varying  $\Delta t_{\text{electrical}}$  from 0 to 62 ns. The attenuators were adjusted to achieve a constant power level of  $-10$  dBm at the oscilloscope and thus, after final amplification, a constant power level of  $P_{\text{rf}} = 27$  dBm is applied to the IDT. The characteristic sinusoidal modulation induced by the strain fields of the surface acoustic wave can nicely be seen, proving efficient functioning of the experimental implementation. Figure 6.8(b) shows the measured relative delay  $\tau_{\text{SAW}}$  (black circles) and

the expected relative delay obtained from equation 6.8 as a function of nominal electrical delay  $\Delta t_{\text{electrical}}$ . As it can be seen, there is an increasing deviation between expected and measured relative phase  $\tau_{\text{SAW}}$  with increasing electrical delay  $\Delta t_{\text{electrical}}$ . This is caused by deviations of the actual delay introduced by the delay system and shows the necessity to experimentally determine the actual values for  $\tau_{\text{SAW}}$  in order to achieve the best possible phase resolution. As these errors are inherent to the used electrical delay system, a one-time calibration of the relative delay  $\tau_{\text{SAW}}$  and attenuation caused by the delay system as a function of set-electrical delay  $\Delta t_{\text{electrical}}$  would be sufficient. This would make both oscilloscope and photo-detector obsolete for further measurements, which further simplifies the experimental setup shown in figure 6.7. Nevertheless, due to the discrete nature of the delay system, this method does not allow for equidistant or arbitrary values of  $\tau_{\text{SAW}}$ , which becomes clear when looking at the circles in figure 6.8(a), marking the peak position for each measurement.

An alternative method to overcome this disadvantage is also depicted in figure 6.7 and is based on introducing a delay  $\Delta t_{\text{optical}}$  in the optical branch of the setup, while keeping the electrical delay  $\Delta t_{\text{electrical}}$  constant. This has the advantage that cable length dependent losses do not have to be compensated, while tuning  $\tau_{\text{SAW}}$ . Change of the optical path length is realised by an optical delay line, consisting of a motorized linear stage equipped with mirrors which shift the incident beam and reflect it back in parallel. For the delay line configuration used here (see figure 6.7), moving the stage by  $\Delta x$  leads to a change of the optical path length of  $4 \cdot \Delta x$ , as the beam travels twice back and forth along the variable delay. The relative delay  $\tau_{\text{SAW}}$  as a function of delay stage position  $\Delta x$  is thus given by:

$$\tau_{\text{SAW}} = \frac{4 \cdot \Delta x}{c_{\text{light}}} \cdot \frac{1}{T_{\text{SAW}}} \quad (6.9)$$

The delay stage used here (*Newport*, M-IMS600LM) allows for a linear displacement of up to 0.6 m and accordingly for a maximum temporal delay of 8 ns ( $\hat{=} 2.56 \cdot T_{\text{SAW}}$  at 320 MHz).<sup>3</sup> This method allows for a quasi-continuous tuning with high temporal resolution (absolute bi-directional accuracy  $\approx 100$  fs and bi-directional repeatability  $\approx 3.3$  fs), exceeding the pulse length of most laser sources. A monitoring of the actual relative delay  $\tau_{\text{SAW}}$  is thus, not necessary, as the introduced phase error is significantly smaller than other limiting factors (lifetime  $\tau_{\text{QD}}$  of the QD; pulse length of laser) and  $\tau_{\text{SAW}}$  as a function of  $\Delta x$  follows precisely the expected behaviour (see figure 6.8(d) and equation 6.9). To avoid a shift of the focused laser spot on the sample and thus a change of the optical excitation condition associated with a beam shift caused by the delay stage when changing  $\Delta x$ , the laser beam is coupled in a single-mode fibre after passing through the optical delay stage. Thereby, the alignment of the optical excitation is decoupled from the delay stage and a beam shift

<sup>3</sup>Construction and characterisation of the optical delay line was supported by Anja Vogeles as part of her lab course and by Lennart Kappl as part of his bachelor thesis.

only affects the coupling efficiency into the fibre. The change in coupling efficiency can than be simply compensated by actively stabilising the optical laser power entering the PL setup with the help of a powermeter and a computer controlled fibre coupled electronic variable optical attenuator (VOA, *Thorlabs*, V600A). Figure 6.8(c) shows stroboscopic data from a QD, dynamically strained by a SAW, under comparable conditions as for the data shown in figure 6.8(a), where the relative delay  $\tau_{\text{SAW}}$  between SAW and optical excitation was continuously tuned by varying  $\Delta t_{\text{optical}}$ . The optical delay  $\Delta t_{\text{optical}}$  was tuned over the entire delay range accessible to the delay stage, corresponding to a relative delay shift over the range of  $2.56 \cdot T_{\text{SAW}}$ . Accordingly, the dynamic oscillation of the QD emission energy is visible over 2.5 SAW periods, confirming that the change of  $\Delta t_{\text{optical}}$  is equivalent to changing the relative delay  $\tau_{\text{SAW}}$  via  $\Delta t_{\text{electrical}}$ .

#### 6.4.2. Time-resolved detection

In this subsection, full time domain spectroscopy shall be demonstrated, by combining stroboscopic excitation and time-resolved detection. To achieve this, the experimental configuration shown in the previous subsection (see figure 6.7) has to be slightly altered to meet the new requirements. When implementing time-resolved measurements the monitor signal of the laser is not only needed for SAW excitation but also as a reference signal for TCSPC. The adapted experimental setup is depicted in figure 6.9. The NIM-monitor

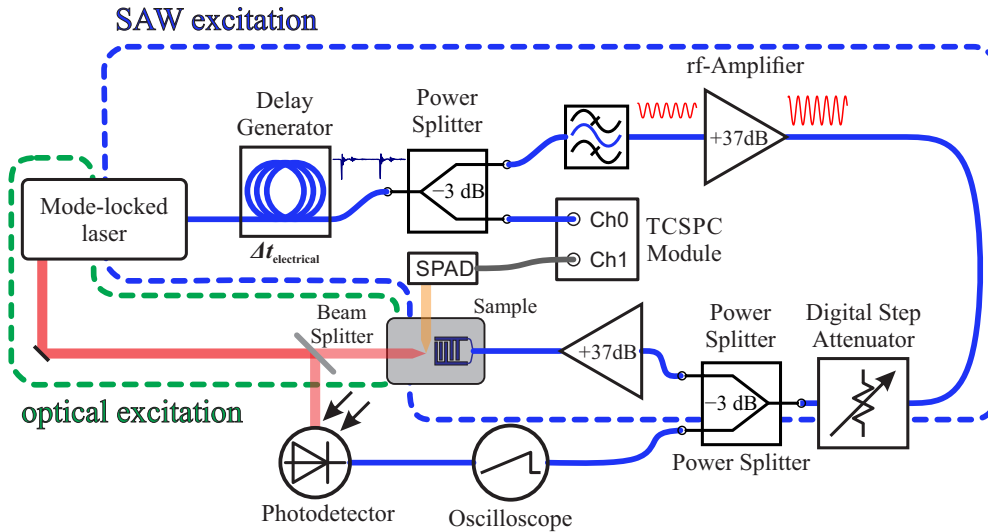


**Figure 6.9.:** Experimental setup for stroboscopic phase-locked excitation and time-resolved detection. Electrical signals are depicted by blue connections, optical signals by red ones. The monitor signal of the laser is split up in two signals, one serves as reference for the TCSPC measurement, the other one, after being filtered and amplified, is used to excite the SAW. Relative excitation time  $\tau_{\text{SAW}}$  is tuned by varying  $\Delta t_{\text{electrical}}$  of the monitor signal, before splitting it. Emission of the QD is detected by a SPAD connected to a TCSPC module.

signal of the mode-locked laser is split in two by an additional  $-3$  dB rf beam splitter. One of the signals is then used to excite the SAW, consequently the 320 MHz frequency component is filtered out and amplified to the necessary amplitude, as already shown. The second signal output of the rf splitter is directly connected to the reference input of a time-correlated single-photon-counting (TCSPC) module (*PicoQuant*, PicoHarp 300). The time of optical excitation during the acoustic cycle is again controlled by setting the corresponding electrical delay  $\Delta t_{\text{electrical}}$ . The electrical delay of the monitor signal is introduced before splitting the signal, in order to resolve the set time delay in the time-resolved measurements. Here, care has to be taken when setting the trigger level of the reference input of the TCSPC module. As the amplitude of the reference signal changes with electrical  $\Delta t_{\text{electrical}}$ , the TCSPC trigger has to be adjusted such that the trigger time is largely independent of  $\Delta t_{\text{electrical}}$ . The emission of the QD is spectrally filtered by a monochromator and detected in the time domain by a single-photon avalanche diode (SPAD), the electrical output of which is connected to the second input of the TCSPC module. A calculation of the expected temporal evolution of the QD emission is shown in

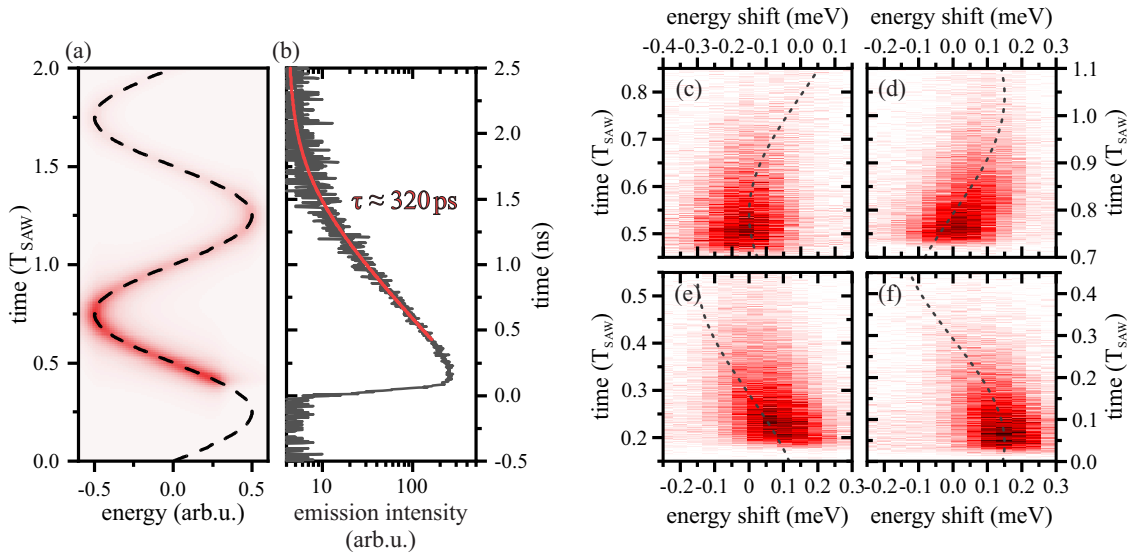


**Figure 6.10.:** (a) Expected spectrally and time-resolved emission of a QD under the influence of a SAW. The emission intensity decays exponentially, while the emission energy is sinusoidally modulated. (b) Decay curve of a QD showing an exponential decay with a decay time of  $\tau_{\text{QD}} \approx 320$  ps. (c)-(f) Time-resolved emission spectra of a single QD for four different values of  $\Delta t_{\text{electrical}}$  so for different photoexcitation times with respect to the acoustic cycle. The emission intensity is colour coded and plotted as function of relative energy shift and time  $t$  during the acoustic cycle. The spectral evolution of the measured signal precisely follows the SAW induced modulation observed in time-integrated, stroboscopic measurements (see figure 6.8), indicated by grey dotted line.

figure 6.10(a) as a function of photon energy and the emission intensity being colour coded.

The QD is optically excited at  $\approx 0.4 \cdot T_{\text{SAW}}$  and decays exponentially with a time constant of  $\tau \approx 0.4 \cdot T_{\text{SAW}}$ , while the emission energy is modulated sinusoidally in time. Figures 6.10(c)-(d) show measurements obtained by stroboscopic excitation and time- and energy-resolved detection for four different  $\Delta t_{\text{electrical}}$ , thus four different photo-excitation times during the acoustic cycle. The grey dashed lines show the expected sinusoidal modulation of the emission energy with time. First of all, it stands out that the measured emission intensity of the QD decays much faster than it is modelled in 6.10(a). The reason is the actually much faster decay time of the QDs on a time scale of  $\tau_{\text{QD}} \approx 0.32 \text{ ns} \approx 0.1 \cdot T_{\text{SAW}}$ , as it can be seen with the decay curve in figure 6.10(b). Thus, the temporal evolution of the emission energy can only be resolved in a short time interval after the photoexcitation of the QD.

For the case shown in 6.10(c), the optical excitation of the QD occurs at  $\approx 0.5 \cdot T_{\text{SAW}}$ , shortly before the negative extremum of the spectral modulation. As the modulation speed is small close to the extrema of the modulation, no pronounced change of the emission energy is observed within the decay time of the QD, and the emission energy stays constant. This drastically changes when the QD is excited close to the rising (d) or the falling (e) edge of the modulation. Under these conditions, the emission energy shifts rapidly towards higher and lower photon energies respectively. As this shift is fast enough to cause a significant spectral shift within  $\tau_{\text{QD}}$ , it can be resolved in the experimental data. Consequently, the emission energy nicely follows the expected spectral modulation. In the last case shown in figure 6.10(f), photoexcitation takes place at  $\approx 0.05 \cdot T_{\text{SAW}}$  at the maximum of the spectral modulation. Here, the emission energy stays initially constant and then starts to shift towards lower energies, as the energy shift accelerates, again in good agreement with the expected spectral evolution.

## 6.5. Two tone excitation: acoustic beat

Like any wave phenomenon, SAWs are subject to the principle of superposition of waves. Thus, the generation of SAWs is not only limited to waveforms of a single frequency, but more complex waveforms can be generated by superimposing waves of different frequencies and/or amplitudes. Schüle in et al. [79] demonstrated this using the fundamental harmonics of a split-5-2 transducer to perform additive Fourier synthesis of different waveforms. Depending on the relative amplitudes and the relative phase relations between the superimposed harmonics, different waveforms like square, saw-tooth and  $\delta$ -pulse waveforms can be generated.

Using chirped transducers removes the restriction to discrete frequencies defined by the harmonics of the transducers, enabling the realisation of more complex waveforms and the use of modulation techniques like frequency and amplitude modulation. Considering two

harmonic waves with the same amplitude  $A_0$  and any frequencies  $f_1$  and  $f_2$ :

$$\begin{aligned} A_1(t) &= A_0 \sin(2\pi f_1 t) \\ A_2(t) &= A_0 \sin(2\pi f_2 t) \end{aligned} \quad (6.10)$$

By applying trigonometric identities, the superposition of these waves can in general be written as:

$$\begin{aligned} A_S(t) &= A_1(t) + A_2(t) = A_0 \sin(2\pi f_1 t) + A_0 \sin(2\pi f_2 t) \\ &= 2A_0 \cdot \sin\left(2\pi \left(\frac{f_1 + f_2}{2}\right) t\right) \cdot \cos\left(2\pi \left(\frac{f_1 - f_2}{2}\right) t\right) \end{aligned} \quad (6.11)$$

In the case of two very similar frequencies, this waveform can be interpreted as an oscillation with frequency  $\frac{f_1+f_2}{2}$  whose amplitude is periodically modulated at a frequency of  $\frac{f_1-f_2}{2}$ , so the slower oscillation is an envelope for the faster oscillation. This effect is called beat and is best known for its occurrence in acoustics. When two sound waves with slightly different frequencies are superimposed, a tone is heard that corresponds to the average of both frequencies. The volume of this tone is modulated with a rate given by the difference of both frequencies, the so-called beat frequency  $f_{\text{beat}} = |f_1 - f_2|$ . The beat frequency is twice the frequency of the amplitude modulation, as the heard volume depends on the magnitude but not the phase of the envelope function.

To demonstrate the superposition of two SAWs, the optomechanical response of a QD to such a wave was measured in the time domain using the time-correlated single photon counting (TCSPC) technique described in section 5.2. Two rf-signal generators are used to generate waves with frequencies  $f_1 = 800$  MHz and  $f_2 = 880$  MHz and an amplitude of  $P_{\text{rf}} = -10$  dBm each. The two signals are superimposed using a rf-power combiner (*Mini-Circuits*, ZFSC-2-372+), and the resulting waveform is amplified by 37 dB (*Mini-Circuits*, ZHL-42-W+) before it is applied to a chirped transducer (IDT2). The two frequency components of the superimposed waveform are within a transmission band of the transducer. Therefore, the complete waveform is transferred from the electrical to the mechanical domain. The expected mechanical wave can thus be described as a sinusoidal wave with frequency:

$$f_s = \frac{f_1 + f_2}{2} = 840 \text{ MHz} \quad (6.12)$$

and an envelope of frequency:

$$f_e = \frac{f_2 - f_1}{2} = 40 \text{ MHz} \quad (6.13)$$

## 6. Multiharmonic frequency chirped transducers

To ensure that both frequencies can be resolved in a TCSPC measurement, the frequencies  $f_1$  and  $f_2$  must be chosen as such that  $f_e$  is a multiple integer fraction of  $f_s$ . This ensures that, within one period of the envelope  $T_e = \frac{1}{f_e} = 25$  ns, there is an integer number fast oscillations  $T_e = \frac{1}{f_s} \approx 1.19$  ns and the waveform repeats every  $T_e$ . The reference for the TCSPC measurement is provided by the clock generator and set to a frequency of  $\frac{f_e}{2} = 20$  MHz so the measurement window covers two envelope periods ( $= 2 \cdot T_e = 50$  ns). Both signal generators and the clock generator are locked to the same reference oscillator to make sure that the phase relation between all involved frequencies and, thus, the superposition is stable over time. The so obtained time and energy resolved evolution of the emission from

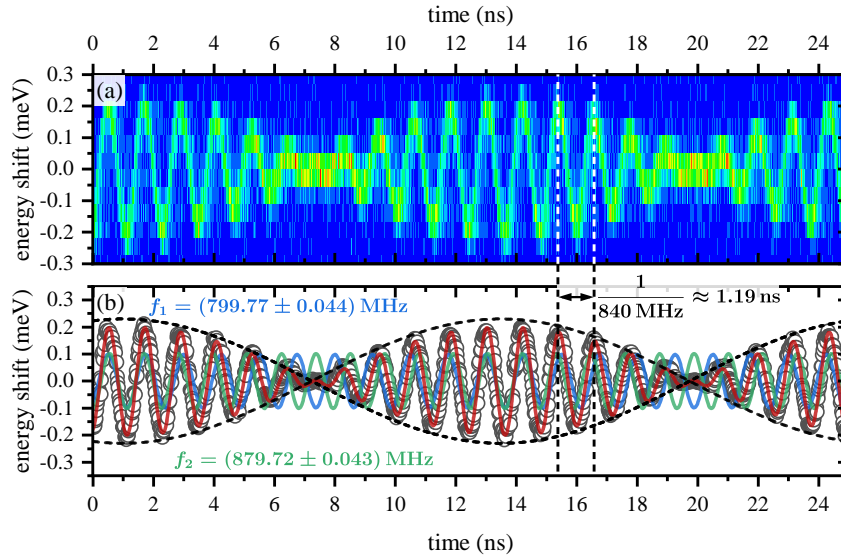


**Figure 6.11.:** (a) Spectral- and time-resolved modulation of a QD emission line, strained by the superposition of two SAWs with frequencies  $f_1 = 800$  MHz and  $f_2 = 880$  MHz. The periodic amplitude modulation with a period of  $T_e = \left(\frac{f_2 - f_1}{2}\right)^{-1} = 25$  ns can clearly be resolved. (b) Peak position extracted from (a) (black circles). The peak positions can be nicely fitted by a sum of two sine functions (red line), where the individual components (blue and green lines) reproduce the set values for the frequency and amplitude ratio of the two oscillations. The envelope functions of the amplitude modulation are shown as black dashed lines.

a QD, strained by the superposition of two SAWs is shown in figure 6.11 over a time period of  $T_e = 25$  ns. In 6.11(a), the emission intensity is colour-coded and, as expected, the temporal evolution of the emission energy can be described by a periodic oscillation with a sinusoidally modulated amplitude. The nodes of the amplitude modulation are at about 7.5 ns and 20 ns and the antinodes at 1.25 ns and 13.75 ns. The time interval between two (anti-)nodes is therefore 12.5 ns, corresponding to the expected value of  $\frac{T_e}{2}$ . For a more detailed analysis, the peak position for every measured time interval were determined and plotted in figure 6.11(b) as black circles. A fit of the experimental data with the sum of

two sine functions, shown as red line in figure 6.11(b), achieves excellent agreement with the data. Additionally, the two individual sine components of the fit are shown as blue and green lines. The two frequencies  $f_1$  and  $f_2$  for the individual components extracted from the fit and especially their ratio  $\frac{f_2}{f_1} \approx (1.1 \pm 10^{-4})$  is in very good agreement with the values set by the two signal generators ( $\frac{f_2}{f_1} = 1.1$ ). Furthermore, the amplitude ratio of the two components  $\frac{A_2}{A_1} \approx 1.03 \pm 0.008$  shows only minimal deviations from the set Values ( $\frac{A_2}{A_1} = 1$ ).

Looking at the two individual oscillations in figure 6.11, one can see that they are out of phase at the nodes of the amplitude modulation, thus interfering destructively and, due to their equal amplitude, they cancel each other out completely. In contrast to that, the two waves interfere constructively at the antinodes and the resulting energy shift is twice as big as it would be expected for each of the two components alone. As marked in figure 6.11(b) the separation of two maxima/minima of the fast oscillation is  $\approx 1.19$  ns, corresponding to a frequency of  $\approx 840$  MHz and thus is in agreement with equation 6.12. The envelope functions, limiting the amplitude of the oscillation with  $f_s = 840$  MHz, are shown in figure 6.11(b) as dashed black lines and their frequency  $f_e = 40$  MHz is consistent with the expectations from equation 6.13.

In conclusion, in this chapter an ITD design was demonstrated that combines a multiharmonic architecture with a frequency chirp and thus allows for the excitation of SAWs over large frequency bands. This capability was verified by measuring both the transmission of a chirped delay line and the optical response of a single QD as a function of rf-frequency applied to the transducers. In general, such a frequency chirped design simplifies the fabrication of IDTs for applications that require SAWs of a certain precise frequency/wavelength. This allows the phase-locked coupling to an additional external free-running excitation source, like mode-locked lasers, as it was shown here or the adjustment of the wavelength to the separation of two arms of a SAW driven Mach-Zehnder interferometer [92]. Furthermore, it enables, or at least simplifies, the additive Fourier synthesis of nano-mechanical waveforms, by superimposing higher harmonics of a SAW [79]. This can be challenging with non-chirped transducers, as higher harmonics of a transducer do not necessarily correspond to integer multiples of the fundamental frequency. This is caused by dispersive sound velocities in layered structures and the mass-loading of the IDT itself. These limitations can be bypassed by introducing a frequency chirp, thus enabling SAW induced modulations on ultra-fast time scales and, for example, the realisation of SAW-gated Landau-Zener transitions in a QD-nanocavity system [93]. Due to these reasons, the use of chirped transducers paves the way towards arbitrary waveform synthesis for nano-mechanical waves over a wide range of frequencies. Such tailored phonon fields will prove not only useful for the manipulation of quantum systems but also for SAW-based spectroscopy techniques, nano-mechanical manipulation and in acoustic quantum technologies.



## 7. Resonance fluorescence of a semiconductor quantum dot

Besides a high probability of single photon emission, often referred to as purity of a source, an ideal single photon source must fulfil a number of additional features to be suited for quantum information processes. These requirements include a great brightness of the source and a large coherence and indistinguishability of the emitted photon stream. The brightness describes the efficiency of a single photon source. For an ideal source, single photons are emitted in a controlled and reproducible manner, for example at each excitation pulse of an optical excitation. The coherence is a measure for the phase stability of the emitted photons and thus describes the ability to enable a stable interference between the emitted photons. This property can be quantified by the coherence time  $T_2$  of a quantum emitter and is related to the spectral linewidth  $\Gamma$  of the emitted light:

$$\Gamma = \frac{1}{T_2} = \frac{1}{2T_1} + \frac{1}{T_2^*} \quad (7.1)$$

Dephasing, meaning the loss of coherence, can be caused by two different mechanisms. Firstly, by a population decay, caused by both radiative and non-radiative decay processes of the excited state. This is described by the decay time  $T_1$ , whose upper limit is set by the radiative decay time of a state. Secondly, by the so-called pure dephasing, where the phase of an excited state is altered by scattering processes, while the population of the state remains unaffected. This is described by the pure dephasing time  $T_2^*$ . When environmental fluctuations and thus pure dephasing can be neglected,  $T_2 = 2T_1$  applies, which is known as the Fourier transform limit and is an important requirement in order to obtain indistinguishable photons. Such photons are characterised by the fact that they are identical in all their attributes, like energy (wavelength), spectral bandwidth and polarisation. The degree of indistinguishability of a single photon source can be determined via the Hong-Ou-Mandel effect, which occurs in case of interference between two identical photons [94].

These properties, which are desired from an ideal single photon source, do not only depend on the source itself but are also strongly determined by the applied excitation scheme. In the PL measurements presented so far only the non-resonant excitation of the QDs was considered. A schematic of the fundamental excitation and relaxation process of photoluminescence is shown in figure 7.1(a). Charge carriers are photo-generated by an excitation

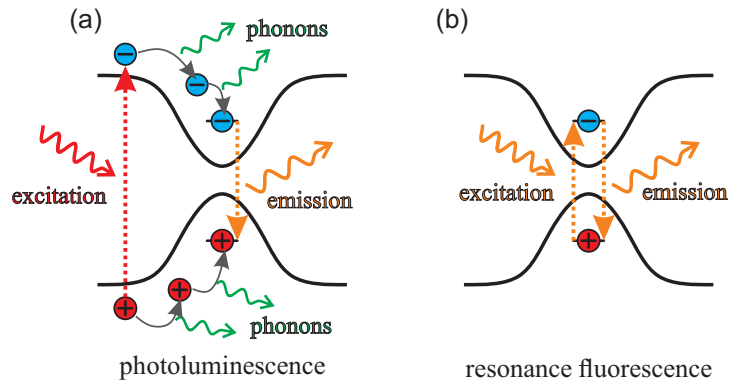


**Figure 7.1.:** Comparison of the optical excitation and relaxation processes of photoluminescence (a) and resonance fluorescence (b) spectroscopy.

laser in an energetic continuum above the discrete energy states of the QD. Subsequently, charge carriers relax via non-radiative processes, for example by emitting phonons, into their respective energetic minima, before a photon can be emitted from the  $s$ -shell. The uncertainty introduced by these relaxation process limits the indistinguishability of the emitted photons. Furthermore, additional free charge carriers, that are generated in the vicinity of the QDs introduce additional decoherence via carrier-carrier scattering. This means that an emitted photon is neither coherent to the respective excitation photon, nor to subsequently emitted photons from the same energy level. To overcome these limitations, instead of non-resonant excitation of a QD, a strictly resonant excitation scheme can be applied. This means, that the energy of the excitation photons corresponds to the transitions energy of the respective state, thus avoiding the generation of additional charge carriers and relaxation processes. This technique is usually referred to as resonance fluorescence (RF, not be confused with rf for radio frequency) and allows for the generation of single photons with superior properties. [95]

The first part of this chapter deals with the theoretical fundamentals of resonance fluorescence and serves as a basis for the later experiments. The second part describes the experimental implementation of resonance fluorescence. Finally, RF measurements on a single QD in the limit of strong resonant optical fields are presented. Resonance fluorescence of a QD under the influence of a SAW, thus being dynamically strained, will then be covered in chapter 8.

## 7.1. Optically driven two-level system: Semiclassical approach

In this section, a brief introduction on the theory of resonance fluorescence shall be given. As the interaction between a two level system and a resonant optical field is a fundamental

problem in quantum optics, more detailed descriptions of this problem can be found in various quantum optics text books [96,97].

In the following, only a single excited state  $a$  of QD that is not influenced and does not interact with any other state is considered. Under these assumptions, a QD can be treated as a perfect two-level system (TLS), thus can always be described by the quantum superposition of two independent states, the ground and excited state. The Hamiltonian of such an optically resonantly driven two level system can be written as:

$$\mathcal{H} = \mathcal{H}_0 + \mathcal{H}_{\text{int}} \quad (7.2)$$

The first part  $\mathcal{H}_0$  of the Hamiltonian describes the unperturbed two level system, consisting of ground  $|g\rangle$  and excited state  $|e\rangle$ , with their respective energy eigenvalues  $\omega_g$  and  $\omega_e$  and can be written as:

$$\mathcal{H}_0 = \hbar\omega_g |g\rangle \langle g| + \hbar\omega_e |e\rangle \langle e| \quad (7.3)$$

The second term  $\mathcal{H}_{\text{int}}$  of the Hamiltonian describes the interaction between the TLS and the driving optical field. In the dipole approximation (wavelength of the driving field is much larger compared to the dimension of the TLS), this term can be written as:

$$\mathcal{H}_{\text{int}} = -e\mathbf{x}\mathbf{E}(t) = -(\mathbf{d}_{g,e}\sigma_- + \mathbf{d}_{e,g}\sigma_+)\mathcal{E}(t), \quad (7.4)$$

where  $\mathbf{d}_{g,e} = \mathbf{d}_{e,g}^* = e \langle g|\mathbf{x}|e\rangle$  is the matrix element of the electric dipole moment,  $\mathcal{E}(t)$  the electric field of the optical driving field and  $\sigma_+ = |e\rangle \langle g|$  and  $\sigma_- = |g\rangle \langle e|$  the raising and lowering operators. As the TLS is described by quantised states, whereas the light field is treated classically, this approach is semi-classical. The driving electrical field has a frequency of  $\omega_1$  and is assumed to be linearly polarised along the  $x$ -direction:

$$\mathcal{E}(t) = \mathcal{E}_0 \cos(\omega_1 t) \quad (7.5)$$

The Rabi frequency is defined as:

$$\Omega = \frac{|\mathbf{d}_{g,e}||\mathcal{E}|}{\hbar} \quad (7.6)$$

Applying the rotating wave approximation, the Hamiltonian of the optically driven TLS can be written in the rotating frame of  $\omega_1 = \omega_0 + \Delta_{\text{opt}}$  as:

$$\mathcal{H}_s = \frac{\hbar\Delta_{\text{opt}}}{2} (|g\rangle \langle g| - |e\rangle \langle e|) + \frac{\hbar\Omega}{2} (\sigma_+ - \sigma_-) \quad (7.7)$$

The state of the considered system can be described by the density matrix:

$$\rho = |\Psi\rangle \langle \Psi| = \rho_{gg} |g\rangle \langle g| + \rho_{eg} |e\rangle \langle g| + \rho_{eg} |e\rangle \langle g| + \rho_{ee} |e\rangle \langle e|, \quad (7.8)$$

with the properties

$$\rho_{gg} + \rho_{ee} = 1 \quad \rho_{ge} = \rho_{eg}^* \quad (7.9)$$

The time evolution of the system is described by a Master equation:

$$\frac{d}{dt}\rho = -\frac{i}{\hbar}[\mathcal{H}_s, \rho] + L[\rho] \quad (7.10)$$

where the radiative decay of the system is described by the Lindblad term:

$$L[\rho] = \Gamma \left( \sigma_- \rho \sigma_+ - \frac{1}{2} \{ \sigma_+ \sigma_-, \rho \} \right) \quad (7.11)$$

with  $\Gamma$  being the radiative decay rate of the TLS. The equations of motion for the elements of the density matrix, known as the optical Bloch equations are then given by:

$$\frac{d}{dt}\rho_{ee} = -\frac{d}{dt}\rho_{gg} = \frac{i\Omega}{2}(\rho_{ge} - \rho_{eg}) - \rho_{ee}\Gamma \quad (7.12)$$

$$\frac{d}{dt}\rho_{ge} = \frac{d}{dt}\rho_{eg}^* = \frac{i\Omega}{2}(\rho_{gg} - \rho_{ee}) - (i\Delta_{\text{opt}} + \Gamma/2)\rho_{ge} \quad (7.13)$$

From the solution of these Bloch equations the expectation values of the atomic operators can be derived:

$$\begin{aligned} \langle \sigma_-(t) \rangle &= \rho_{eg}(t) \exp(-\omega_1 t) \\ \langle \sigma_+(t) \rangle &= \rho_{ge}(t) \exp(-\omega_1 t) \end{aligned} \quad (7.14)$$

To gain information on the emitted fluorescence light of the system one has to calculate the correlation functions of the electric field operators. This first order correlation function can be written in terms of the first-order correlation function for the TLS:

$$g^{(1)}(\tau) = \langle E^-(r, t) E^+(r, t + \tau) \rangle = I_0(t) \langle \sigma_+(t) \sigma_-(t + \tau) \rangle \quad (7.15)$$

with

$$I_0(r) = \left( \frac{e\omega_0^2}{4\pi\epsilon_0 c^2} \frac{\mathbf{d}_{g,e}(r - r_0)}{|r - r_0|^2} \right)^2 \quad (7.16)$$

So, in order to calculate  $g^{(1)}$ , the two-time (first order) products of the atomic raising and lowering operators are needed. However, the Master equation of the system yields only the single time expectation values 7.14. This problem can be solved using the quantum regression theorem that allows for the calculation of the two-time correlation function from a single-time correlation function.

For the problem considered here, in the case of full resonance between the TLS and the optical driving laser ( $\omega_1 = \omega_0 \rightarrow \Delta_{\text{opt}} = 0$ ), the correlation of the emitted field is given

by [96]:

$$\begin{aligned}
 g^{(1)}(\tau) &= \langle E^-(r, t) E^+(r, t + \tau) \rangle = I_0(t) \langle \sigma_+(t) \sigma_-(t + \tau) \rangle = \\
 &= I_0(r) e^{-i\omega_0 \tau} \left( \frac{\Omega^2}{\Gamma^2 + 2\Omega^2} \right) \left\{ \frac{\Gamma^2}{\Gamma^2 + 2\Omega^2} + \frac{e^{-\Gamma\tau/2}}{2} + \right. \\
 &\quad \left. + \frac{e^{-3\Gamma\tau/4}}{4} \left[ e^{-i\mu\tau} (P + iQ) + e^{i\mu\tau} (P - iQ) \right] \right\} \quad (7.17)
 \end{aligned}$$

with  $\mu = \left( \Omega^2 - \frac{\Gamma^2}{16} \right)^{1/2}$ ,  $I_0(r)$  given in equation 7.16 and the dimensionless constants  $P$  and  $Q$ :

$$P = \frac{2\Omega^2 - \Gamma^2}{2\Omega^2 + \Gamma^2} \quad Q = \frac{\Gamma}{4\mu} \frac{10\Omega^2 - \Gamma^2}{2\Omega^2 + \Gamma^2} \quad (7.18)$$

According to the Wiener-Khinchin-theorem, the fluorescence spectrum is given by the Fourier transform of the two-time (first order) correlation function of the emitted field:

$$S(r, \omega) = \frac{1}{\pi} \text{RE} \int_0^\infty \langle E^-(r, t) E^+(r, t) \rangle \exp(i\omega\tau) d\tau \quad (7.19)$$

Applying this to the correlation function 7.17 for the emitted light field, the full resonance fluorescence spectrum is revealed to be [97]:

$$\begin{aligned}
 S(r, \omega) &= \frac{I_0(r)}{2\pi} \left[ 2\pi \frac{\Omega^2}{\Gamma^2 + 2\Omega^2} \delta(\omega - \omega_0) + \frac{1}{4} \frac{3\Gamma/4}{(\omega - \Omega - \omega_0)^2 + (3\Gamma/4)^2} \right. \\
 &\quad \left. + \frac{1}{2} \frac{\Gamma/2}{(\omega - \omega_0)^2 + (\Gamma/2)^2} + \frac{1}{4} \frac{3\Gamma/4}{(\omega + \Omega - \omega_0)^2 + (3\Gamma/4)^2} \right] \quad (7.20)
 \end{aligned}$$

The so obtained spectrum was first described in 1969 by Mollow [98] and consists of four terms. The first term is described by a delta function and is referred to as the coherent (elastic) part of the spectrum, as the emission frequency matches the optical driving frequencies. The other three terms describe Lorentzian-shaped peaks at the positions  $\omega_0 - \Omega$ ,  $\omega_0$  and  $\omega_0 + \Omega$ . These three peaks are called the Mollow triplet and represent the incoherent (inelastic) part of the resonance fluorescence spectrum. How strong the coherent and incoherent part contribute to the overall spectrum strongly depends on the strength of the optical driving field and thus on the Rabi frequency  $\Omega$ . The total fluorescent intensity, divided into coherent and incoherent part, can be written as [99]:

$$I_{\text{total}} = I_{\text{in}} \left[ \underbrace{\frac{1}{2} \left( \frac{\sqrt{2}\Omega/\Gamma}{1 + 2(\Omega/\Gamma)^2} \right)^2}_{I_{\text{coherent}}} + \underbrace{\frac{1}{2} \left( \frac{2(\Omega/\Gamma)^2}{1 + 2(\Omega/\Gamma)^2} \right)^2}_{I_{\text{incoherent}}} \right] \quad (7.21)$$

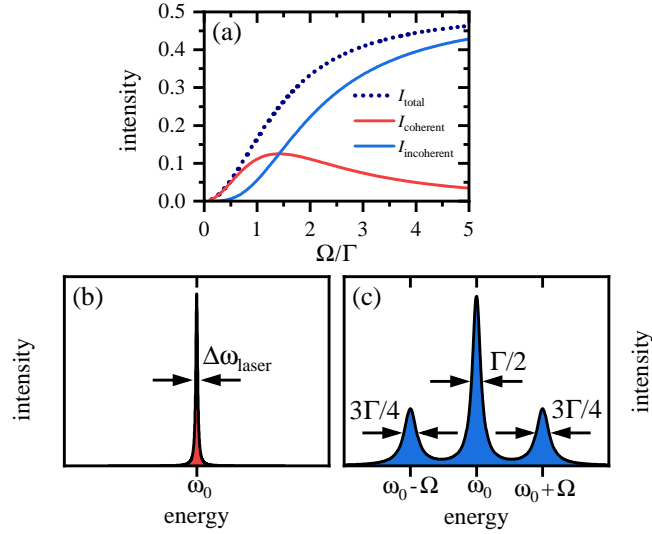


**Figure 7.2.:** (a) Resonance fluorescence intensity as a function of Rabi frequency for both the coherent and incoherent contribution, according to equation 7.21. (b) Resonance fluorescence spectra in the low driving field limit. The spectrum is dominated by the coherent part of the RF signal and mimics the spectral shape of the driving field. (c) RF spectrum in the strong field limit, showing the characteristic, incoherent Mollow triplet.

where  $I_{\text{in}}$  is the incident intensity. The intensities  $I_{\text{total}}$ ,  $I_{\text{coherent}}$  and  $I_{\text{incoherent}}$  are plotted in figure 7.2(a) as a function of the Rabi frequency  $\Omega$ . It can be seen that in the limit of low Rabi frequencies the fluorescence signal is dominated by the coherent emission. With increasing optical driving strength, the coherent emission initially increases, followed later by the incoherent part. At  $\Omega = \sqrt{2}\Gamma$  both parts contribute equally to the overall fluorescence signal. With further increasing Rabi frequency, the incoherent part continues to rise, while the coherent part starts to decrease again. At strong driving fields the fluorescence signal is then dominated by the incoherent contribution, hence the Mollow triplet. As the resonance fluorescence spectra in the weak and strong field regime are remarkably different, these two regimes will be briefly considered separately in the following.

#### The weak field limit $\Omega \ll \Gamma/4$

As already discussed, in the weak field regime ( $\Omega \ll \Gamma/4$ ) the resonance fluorescence spectrum is described by a  $\delta$ -function. In this regime, the QD's transition dipole does not oscillate with its natural frequency  $\omega_0$  but with the frequency of the driving field  $\omega_1$ . As depicted in the figure 7.2(b), the spectral-shape of the emitted light is determined by the driving laser. However, the photon statistic is non-classical, showing clear anti-bunching in the intensity auto-correlation function ( $g^{(2)}(\tau = 0) = 0$ ), hence confirming single photon emission. This makes it possible to generate single photons with a spectral linewidth that is not limited by the lifetime of the QD transition (Fourier limit). This behaviour was

shown for semiconductor QD independently by Nguyen et al. [100] and Matthiesen et al. [101]. Due to the unique properties of such a single photon source, the authors referred to it as "ultra-coherent" single-photon source or a single photon source with "subnatural linewidth", respectively. Since the waveform is defined by the driving laser, single photons with arbitrary synthesised waveforms can be obtained and the emitted photons are phase coherent with the driving laser on timescales of several seconds [102].

### The strong field limit $\Omega \gg \Gamma/4$

In the strong field limit, when the Rabi frequency is noticeably larger than the decay rate of the QD, the TLS can coherently interact several times with the driving field before spontaneously emitting a photon. As already mentioned, in this regime the fluorescence spectrum is dominated by the Mollow triplet, sketched in figure 7.2(c). According to equation 7.20, the triplet consists of three peaks at  $\omega_0 - \Omega$ ,  $\omega_0$  and  $\omega_0 + \Omega$ . The central peak ( $\omega = \omega_0$ ), called the Rayleigh peak, has a linewidth of  $\Gamma/2$ , while the two side peaks ( $\omega = \omega_0 \pm \Omega$ ) have a linewidth of  $3\Gamma/4$ . Furthermore, the central peak has twice the emission intensity than both of the side peaks. First observations of Mollow triplets were done on atomic sodium [103, 104] in 1974/1975 in an orthogonal excitation and detection geometry. Due to the challenge of suppressing the excitation light field in the detection, the first observations of Mollow triplets for semiconductor quantum dots were not achieved until 2007/2009 [105, 106].

## 7.2. Dressed state picture: Quantum mechanical approach

In addition to the semi-classical model introduced in the previous subsection, the formation of Mollow triplets can be explained in the so-called dressed state approach. In this physically more intuitive approach, in the case of strong coupling between light field and TLS, the system is described by the Jaynes-Cummings Hamiltonian [107]:

$$\mathcal{H}_{\text{JC}} = \mathcal{H}_{\text{QD}} + \mathcal{H}_{\text{laser}} + \mathcal{H}_{\text{int}} = \hbar\omega_{\text{QD}}\sigma^+\sigma^- + \hbar\omega_{\text{laser}}a^+a^- + \hbar g(a^+\sigma^- + \sigma^+a^-) \quad (7.22)$$

This is a completely quantum mechanical approach since the light field is quantised as well. The Hamiltonian consists of three terms, the first two describing the uncoupled TLS and the light field and the last term describing the coupling between the two systems. The first term  $\mathcal{H}_{\text{QD}}$  of the JC-Hamiltonian describes the TLS with  $\sigma^+ = |e\rangle\langle g|$  and  $\sigma^- = |g\rangle\langle e|$  being the creation and annihilation operator of the TLS.  $\mathcal{H}_{\text{laser}}$  describes the laser light field with the bosonic creation and annihilation operators  $a^+$  and  $a^-$ . The last term  $\mathcal{H}_{\text{int}}$  describes the interaction between light field and QD, with the coupling constant  $g$ . This interaction term describes the transition of the TLS from the excited to the ground state, while increasing the number of photons  $n$  in the light field by one and the reverse process, where the number of photons is decreased by one and the TLS goes from the ground state

to the excited state. Assuming the light field is resonant to the TLS's transition energy ( $\omega_{\text{laser}} = \omega_{\text{QD}} = \omega_0$ ), the bare state with the QD in the ground state and  $n + 1$  photons in the light field is degenerate with the bare states with the QD in the excited state and  $n$  photons in the cavity, as depicted on the left side of the figure 7.3(a). The coupling of the two systems lifts this degeneracy and leads to the formation of so-called dressed states:

$$\begin{aligned} |1(n)\rangle &= \frac{1}{\sqrt{2}} |n, g\rangle - \frac{1}{\sqrt{2}} |n-1, e\rangle \\ |2(n)\rangle &= \frac{1}{\sqrt{2}} |n, g\rangle + \frac{1}{\sqrt{2}} |n-1, e\rangle \end{aligned} \quad (7.23)$$

The energy eigenvalue for the  $n$ -th level is given by:

$$E_n^\pm = \left(n + \frac{1}{2}\right) \hbar\omega_0 \pm \sqrt{n+1} \hbar g_0 \quad (7.24)$$

So each level  $n$  splits up in a doublet with a splitting of:

$$\Delta E = 2\sqrt{n+1} g_0 \hbar = \Omega_n \hbar \quad (7.25)$$

where  $\Omega_n = 2\sqrt{n+1} \cdot g_0$  describes the  $n$ -photon Rabi frequency. Note, that since the number of photons  $n$  is proportional to the square of the electric field amplitude  $\mathcal{E}^2$ , the definition of  $\Omega_n$  is equivalent to the definition of the Rabi frequency in equation 7.6. The

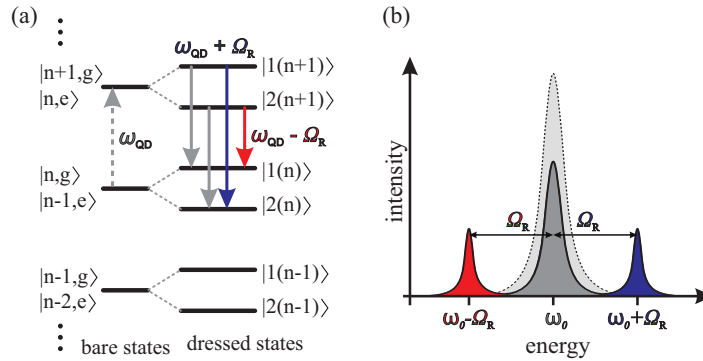


**Figure 7.3.:** (a) Formation of dressed states in a resonantly driven TLS. The originally degenerate bare states split up in doublets, separated by the Rabi frequency  $\Omega$ . Arrows indicate the allowed optical transitions, explaining the origin of the Mollow triplet. (b) Schematic of the Mollow triplet. The colour of the peaks indicate which of the transitions shown in (a) contribute to the respective peak.

so formed level structure, called the Jaynes-Cummings ladder, is shown on the right hand side of figure 7.3(a). The incoherent emission in the strong field regime stems from the four different spontaneous decay paths between the dressed state manifolds of the  $n$ -th and  $(n - 1)$ -th level, shown in the schematic. The transition energy of the respective

transmissions depend on the energy of the initial and final state and can be simplified for large photon numbers  $n$ , when  $\sqrt{n+1} \approx \sqrt{n}$ :

$$\begin{aligned}
 E_n^+ - E_{n-1}^+ &= \hbar\omega_0 + \underbrace{(\sqrt{n+1} - \sqrt{n})}_{\approx 0} \hbar g_0 \approx \hbar\omega_0 \\
 E_n^- - E_{n-1}^+ &= \hbar\omega_0 + \underbrace{(-\sqrt{n+1} - \sqrt{n})}_{\approx -2\sqrt{n+1}} \hbar g_0 \approx \hbar\omega_0 - \hbar\Omega_n \\
 E_n^- - E_{n-1}^- &= \hbar\omega_0 + \underbrace{(-\sqrt{n+1} + \sqrt{n})}_{\approx 0} \hbar g_0 \approx \hbar\omega_0 \\
 E_n^+ - E_{n-1}^- &= \hbar\omega_0 + \underbrace{(+\sqrt{n+1} + \sqrt{n})}_{\approx +2\sqrt{n+1}} \hbar g_0 \approx \hbar\omega_0 + \hbar\Omega_n
 \end{aligned}$$

So two of the decay pathways have a transition energy equal to the QD transition  $\omega_0 = \omega_{\text{QD}}$ , while the other two are shifted by  $\pm\Omega_n$ , leading to the formation of the distinctive Mollow triplet depicted in figure 7.3(b). Since the dressed states are superpositions of bare states with equal coefficients  $\frac{1}{\sqrt{2}}$  (see equation 7.23), each of the four transitions has the same probability and thus the central peak has twice the emission intensity of each sideband. The use of the large photon approximation can be justified by the small coupling strength  $g_0$  in the considered system so many photons are necessary to achieve a measurable effect. Furthermore, since the results obtained in the large photon number approximation match the results in the previous section, the classical treatment of the light field in the previous subsection is supported.

### 7.3. Experimental realisation of resonance fluorescence

One of the biggest challenges for the experimental implementation of resonance fluorescence is the distinction between photons emitted from the QD and photons that come from the excitation laser. As the two-level system is excited resonantly, both types of photons have the same energy (wavelength) and the laser cannot simply be suppressed using spectral filters like in photoluminescence. For semiconductor QDs, this problem was first solved in 2007, using an orthogonal geometry for excitation and detection [105]. There the QDs were embedded in a planar cavity formed by two distributed Bragg reflectors (DBR), one above and one below the QD-layer. Accordingly, the geometry of the cavity was adjusted so that its resonance frequency overlaps with the transition energy of the QD. Resonant laser light is then injected from the side directly into the planar cavity and is efficiently trapped there. The resonance fluorescence signal is then detected from the top, perpendicular to the planar cavity and thus to the excitation laser. Although this technique can be used to resonantly excite a QD, while it is periodically strained by a SAW, as shown by Metcalfe

and co-workers [108], a different approach was used for this work. This alternative approach is based on a crossed polarised alignment of the excitation and detection polarisation and was first introduced in 2009 by Vamivakas and co-workers [106].

Once the separation between RF signal and laser light was realised, resonance fluorescence of single QDs could be measured. However, initial measurements on single QDs showed that the resonance fluorescence of the neutral exciton transition is highly inefficient. This is usually attributed to the formation of dark states, formed by capturing an additional charge carrier or by reversing the spin of a charge carrier of the exciton. These dark states have long lifetimes, as they are not optically active. Furthermore, they prevent further resonant excitation, since the initial transition is no longer accessible. This limitation can be lifted by adding an additional weak non-resonant laser to the excitation light, which strongly increases the RF efficiency. This optical gating effect can be explained on the one hand by the stabilisation of the neutral exciton by providing additional charge carriers, which neutralise emerging dark states [109]. On the other hand, it can be attributed to photodoping by the additional charge carriers, making it possible to resonantly excite the trion transitions, which are not susceptible to the formation of dark states [110,111]. In both cases, adding a weak non-resonant laser stabilises the charge carrier configuration of the QD and thus restores the two-level properties of the QD and enables efficient RF.

In the first part of this section, the experimental realisation of the cross-polarised excitation/detection scheme used in this work is introduced. In order to analyse the collected RF signal of a single QD, a spectral resolution is necessary, which clearly exceeds the one of a conventional grating monochromator. For that reason, in the second part of this chapter, the use of a Fabry-Pérot (FP) etalon for recording high resolution spectra is explained.

### 7.3.1. Crossed-polarised resonance fluorescence

The advantage of the cross-polarised technique is that it is less demanding on the geometry of the sample, as no planar cavity is needed, and also on the configuration of the optical setup, as no optical side access is necessary and a conventional confocal arrangement of the excitation and detection path can be used. Kuhlmann et al [112] provide a detailed description of how this technique can be experimentally realised. The setup, build for the experiments shown in this work, is depicted in figure 7.4. The main component of the setup is a confocal microscope, the same used for the previously shown PL experiments but now equipped with additional polarisation optics. Instead of a 50:50 beamsplitter a polarising beamsplitter (PBS), where s-polarised light is reflected and p-polarised light is transmitted, is used. The excitation light is reflected by the PBS towards the sample, mounted in the cryostat. To ensure, that the excitation beam is only s-polarised an additional linear polariser in the excitation path is necessary, as the extinction ratio of the PBS in reflection ( $\approx 10^2$ ) is much weaker than in transmission ( $\approx 10^3 - 10^4$ ). The s-polarised laser beam is

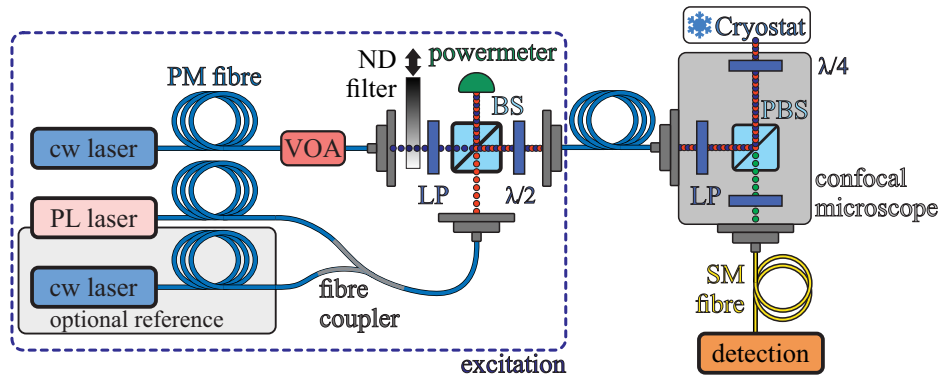


**Figure 7.4.:** Experimental setup used for resonance fluorescence spectroscopy. The left part (blue dashed box) shows the combination of up to three laser sources into one polarisation maintaining (PM) optical fibre. The different sources are combined using fibre and freespace beamsplitters. The polarisation of the laser light is controlled by linear polarisers (LP) and  $\lambda/2$ -waveplates. A variable neutral density (ND) filter and/or a variable optical attenuator (VOA) are used to control the resonant laser power. The right part shows the confocal microscope, equipped with polarisation optics and spatial filtering to suppress reflected laser light.

then focused on the sample by an objective, hence the polarisation of light is no longer only perpendicular to the surface normal of the sample but also contains components that are not parallel or perpendicular to the plane of incidence. As a consequence, part of the reflected laser light that is collected by the same objective is p-polarised and thus not suppressed by the PBS. However, the image of the reflected p-polarised beam has a four-leaf clover pattern with a minimum at the centre [113]. This makes it possible to suppress these unwanted components by spatially filtering the detected signal. This is achieved here by coupling the reflected beam into a single mode (SM) fibre (core diameter  $\approx 5 \mu\text{m}$ ). Furthermore, coupling into a fibre has the advantage that the alignment of the confocal microscope can be decoupled from the alignment of the detection system. Before coupling into the SM fibre leading to the detection system, the detected light is sent through a second linear polariser to further increase the suppression of the remaining laser background. Another indispensable optical component in the confocal microscope is a  $\lambda/4$ -waveplate between microscope and cryostat. This waveplate is necessary to correct for birefringence introduced, e.g., by optical windows or the objective. Moreover, it allows to rotate the polarisation of the excitation light so that the reflected part is transmitted through the PBS, making the alignment of the setup much easier. This experimental setup, combining both spatial and polarisation filtering in a confocal microscope, is capable of filtering out the background excitation laser light and thus enables to collect only the resonance fluorescence signal of a resonantly driven QD.

For the resonant excitation of a QD, up to three different laser sources have been used, which were combined within a single polarisation maintaining (PM) fibre before entering

the confocal microscope setup, as shown on the left hand side in figure 7.4 (blue dashed box). For the resonant excitation of the QD, a tunable continuous-wave diode laser with a narrow bandwidth ( $< 100$  kHz) was used (*TOPTICA Photonics*, DLpro). This laser can be tuned into resonance with the transition energy of a QD. The feedback of the laser cavity, meaning the wavelength that is enhanced by the cavity, can be tuned by the rotation of an optical grating, allowing for a coarse tuning of the laser wavelength over a range of about  $\approx 905 - 980$  nm. Fine tuning is realised by changing the length of the laser cavity with the help of a mirror mounted on a piezoelectric actuator. This can either be done manually at the laser's drive electronic or remotely by a programmable voltage source (*National Instruments*, PCI-6221) that is connected to the respective input of the laser driver. The laser cavity itself is temperature stabilised, ensuring the long-term stability of the lasers emission energy/wavelength. The resonant laser power was adjusted with the help of a fibre coupled voltage controlled optical attenuator (VOA) (attenuation up to 30dB) or with a variable neutral density filter (free space) mounted on a computer controlled linear stage (attenuation up to 40dB).

The second laser is a diode laser emitting light with an energy ( $\approx 840$  nm) above the bandgap of the wetting layer and is used for non-resonant excitation (PL) of the QDs and to optically gate the QD in order to significantly increase the RF efficiency. As a third optional laser source, a second tunable diode laser (*TOPTICA Photonics*, DLpro) is used to serve as a fixed energy reference for experiments where the resonant excitation energy is tuned with respect to the transition energy of the QD. PL and reference laser are combined by a fibre based beamsplitter and afterwards combined with the resonant laser by a free-space beamsplitter. Using free space components has the advantage that both polarisation and intensity of the resonant laser can be precisely adjusted and kept constant over long periods of time, which is a key requirement for long term experiments. Furthermore, the intensity of the resonant laser can be measured by a power meter and, under consideration of the constant coupling efficiency between the two parts of the experiment, the resonant excitation power at the QD can be determined (PL and reference laser add a constant offset to the measured value). Combining the laser sources in a single PM-fibre before entering the confocal microscope ensures that all used laser sources are co-parallel and switching between PL and RF measurement can easily be realised, without changing the alignment of the setup. Furthermore, as both resonant and PL lasers are needed simultaneously for RF, this method allows for a more efficient collection compared to the alternative, where PL and resonant laser are combined with an additional BS within the confocal microscope.

### 7.3.2. High resolution detection: Fabry-Pérot-Etalon

To achieve a sufficiently high spectral resolution in detection and to resolve the features expected for RF in the resolved sideband regime, a piezo-tunable Fabry-Pérot-etalon has been used. Such an etalon consists of two partly reflecting, parallel mirrors with a high

reflectivity, forming an optical cavity. When light that fulfils the resonance conditions enters the etalon, it is transmitted, otherwise destructive interference within the cavity leads to a strong suppression of the transmission. As the length  $L_{\text{etalon}}$  of the used etalon (*LightMachinery*) can be tuned by a piezoelectric actuator, it can be used as a tunable frequency filter. Figure 7.5 (c) shows the transmission of a narrow-band laser

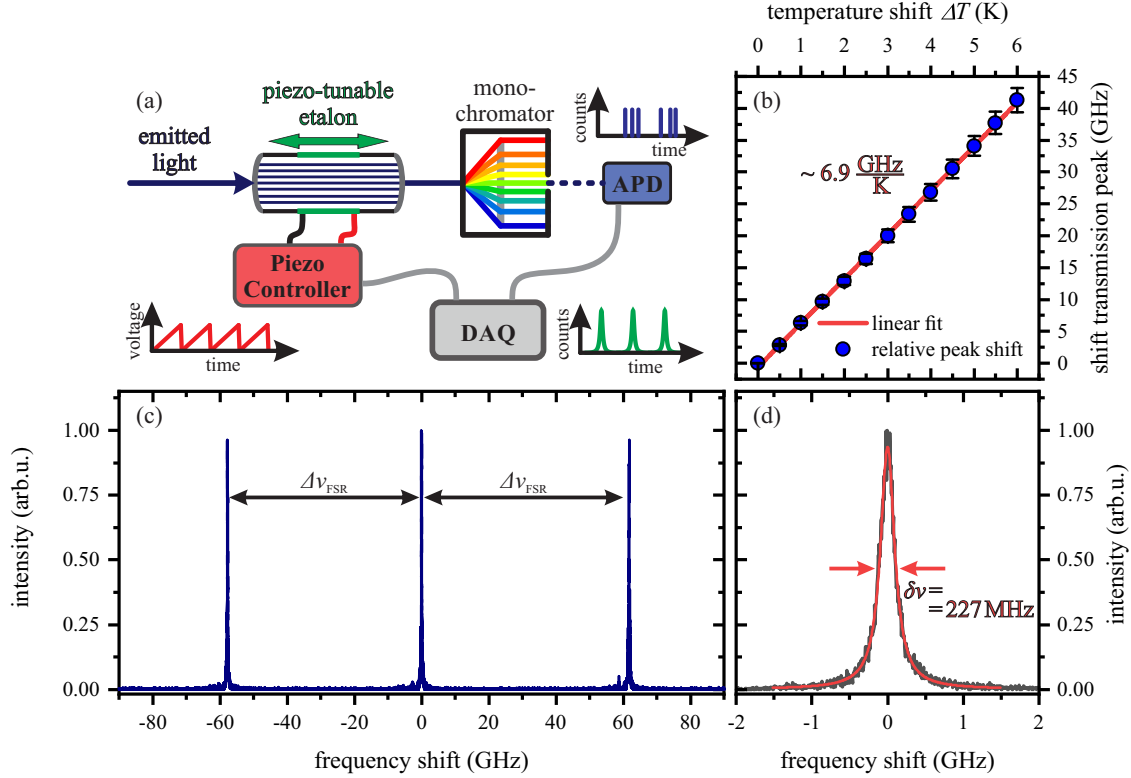


**Figure 7.5.:** High resolution spectroscopy using a Fabry-Pérot etalon. (a) Implementation of the etalon to record high resolution spectra by tuning the etalon’s transmission frequency. (b) Strong temperature dependence of the etalon’s transmission peak, showing the need for an active temperature stabilisation. (c) Transmission spectrum of the etalon showing discrete peaks, separated by the free spectral range (FSR,  $\Delta\nu_{\text{FSR}} \approx 60 \text{ GHz}$ ) of the etalon. (d) Enlargement of one of the transmission peaks in (a), revealing a resolution of  $\delta\nu = 227 \text{ MHz}$  for the etalon.

( $\delta\nu_{\text{laser}} < 100 \text{ kHz}$ ) through the etalon as a function of the cavity length  $L_{\text{etalon}}$ , tuned by the piezo actuator. The transmission spectrum reveals several sharp equidistant transmission peaks. The distance between two adjacent peaks is referred to as the free spectral range (FSR)  $\Delta\nu_{\text{FSR}}$  and depends on the refractive index  $n$  of the cavity and the length of the cavity (Note that the tuning range of  $L_{\text{etalon}}$  is much smaller than the length of the etalon itself. Thus the FSR can be considered constant):

$$\Delta\nu_{\text{FSR}} = \frac{c_{\text{light}}}{2nL_{\text{etalon}}} \approx 59.7 \text{ GHz} \quad (7.26)$$

Therefore, the FSR is a key attribute of an etalon and only depends on the geometry of the etalon and the material it is made of. For the used etalon ( $L_{\text{etalon}} \approx 2.51$  mm, air-spaced  $n = 1$ ), the FSR is about  $\Delta\nu_{\text{FSR}} \approx 60$  GHz. A closer look at the central transmission peak (see figure 7.5(d)) reveals that the transmission peak has a Lorentzian line shape with a FWHM of  $\delta\nu = 227$  MHz. As for this measurement a narrowband light source was used, this linewidth directly reflects the resolution  $\delta\nu$  of the etalon. With both the FSR and the resolution, the finesse  $\mathcal{F}$  of an etalon can be defined:

$$\mathcal{F} = \frac{\Delta\nu_{\text{FSR}}}{\delta\nu} \approx 263 \quad (7.27)$$

The finesse  $\mathcal{F}$  is fully determined by the losses in the Fabry-Pérot cavity and is accordingly a measure for the quality factor of the etalon. Using this Fabry-Pérot etalon, a high spectral resolution of 227 MHz can be achieved. This corresponds to an energy resolution of  $0.94 \mu\text{eV}$  or a wavelength resolution of 0.64 pm at a centre wavelength of 920 nm. By comparison to the used monochromator, which can reach a resolution up to about 9 GHz, the spectral resolution is increased by a factor of 40. However, due to the equally spaced transmission peaks, only relative and no absolute energies/frequencies can be determined. In addition, as the etalon acts as a tunable filter, multichannel detection is no longer possible, resulting in longer acquisition times for a single spectrum.

Furthermore, the etalon is highly sensitive to its environmental conditions, in particular to the temperature. This is shown in figure 7.5(b), where the relative shift of a transmission peak was determined as a function of the etalon temperature. With increasing temperature, the transmission peak shifts linearly towards higher frequencies at rate of  $6.9 \frac{\text{GHz}}{\text{K}}$  corresponding to  $30 \frac{\delta\nu}{\nu}$ . This large temperature dependence constitutes a major problem, especially due to the relative long integration times caused by the single channel detection scheme. This problem is tackled by two different approaches. On the one hand, the etalon is mounted in a home-made temperature stabilised housing, strongly reducing the thermal drift. On the other hand, the etalon is integrated into the optical detection system and operated in a way that allows for a subsequent compensation of residual thermal drift on long time scales of several minutes and hours. This implementation is shown schematically in figure 7.5(a). The light to be analysed is filtered by the etalon and subsequently by a monochromator to filter all transmissions peaks of the etalon but one and is finally detected by a single photon detector (APD). Both the recording of the APD counts and the detuning of the etalon is controlled by a data acquisition system (DAQ) (*National Instruments*, PCI-6221). To tune the etalon length, the DAQ system provides a sawtooth signal that controls the output voltage of a piezo amplifier (*Thorlabs*, KPZ101), which in turn tunes the etalon. Thereby, the etalon is scanned continuously, typically with a frequency of 1 Hz, over the desired frequency range. The DAQ system records every photon count and relates it to the current detuning of the etalon so every second a spectrum

is obtained. This process is continuously repeated and, typically, 30 of these 1 s-spectra are summed up to a single spectrum and saved to the hard drive of a computer. On the timescales necessary to acquire such a spectrum, no pronounced influences due to thermal drift are expected and to achieve longer integration times several of these spectra can be combined. To eliminate the influence of thermal drift on long timescales the single spectra can be aligned with respect to a bright, spectrally fixed feature, usually the Rayleigh line of the RF signal or the emission energy/frequency of the reference laser, before summing them up.

## 7.4. Experimental observation of the Mollow triplet

In this subsection, the previously introduced experimental setup is used to investigate the formation of Mollow triplets in a semiconductor quantum dot. To this purpose, a single QD transmission line, centred at around 1.342 eV (924 nm), was selected using conventional photoluminescence spectroscopy. The resonant laser was tuned into resonance with the respective emission line, and the collected emission was analysed using the Fabry-Pérot etalon. In order to calibrate the energy/frequency scale of the etalon, meaning the relation between the voltage applied to the etalon's piezo-actuators and the relative frequency shift of the transmission bands, the etalon is tuned over a large energy/frequency range covering more than two FSRs. Hence, the final high resolution spectra contain three times the desired spectral features, separated by the known FSR ( $\approx 60$  GHz), and the relative frequency shift can be calibrated with respect to the piezo-voltage, assuming a linear relation between voltage and frequency shift. To further increase the suppression of the background laser radiation, meaning laser light that is just reflected at the sample and not suppressed by the polarisation optics, for each spectrum presented in this section, the laser background signal was measured and subtracted from the resonance fluorescence spectra. To achieve this, the weak PL laser, gating the RF signal, was turned off, leading to a strong decrease of RF efficiency while the residual laser background is unaffected and can directly be measured.

In the first part of this section, the dependence of the Rabi frequency on the excitation power of the resonant laser was investigated. In the second part, the influence of a frequency detuning between excitation laser and QD transition was examined.

### 7.4.1. Dependence on resonant excitation power

High resolution resonance fluorescence spectra for various laser excitation powers  $P_{\text{laser}}$  are plotted in figure 7.6 (a). The resonant laser power was tuned over almost two orders of magnitude, from  $P_0 = 64$  nW to  $97 \cdot P_0 = 6.2$   $\mu$ W. The specified values for  $P_{\text{laser}}$  were measured before resonant and PL laser were combined in one optical fibre, entering the confocal microscope (see figure 7.4) but were corrected in terms of coupling efficiency

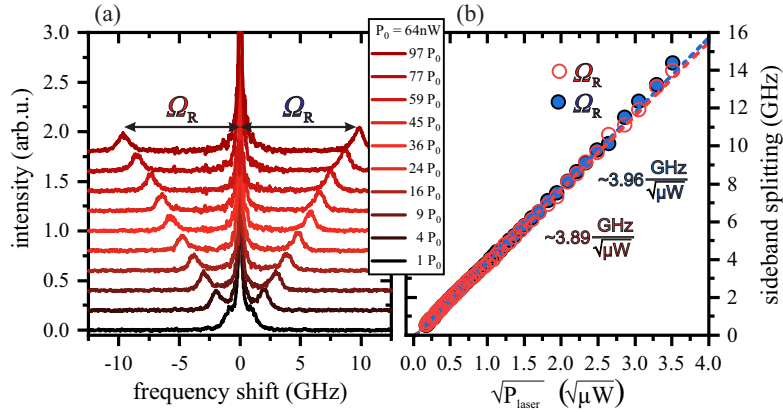


**Figure 7.6.:** Excitation power dependent Mollow triplets **(a)** High resolution spectra for various resonant laser excitation powers  $P_{\text{laser}}$ . With increasing  $P_{\text{laser}}$ , an increasing splitting and therefore Rabi frequency is observed. For clarity, the shown spectra are plotted with a constant offset. **(b)** Rabi frequencies extracted from **(a)** as a function of  $\sqrt{P_{\text{laser}}}$ , showing nicely the expected linear behaviour.

between the point of measurement and the optical output of the confocal microscope. The given values then indicate the optical laser power before entering the cryostat and being focused onto the sample. The power of the PL laser used to optically gate the system was set to  $P_{\text{PL-laser}} \approx 6 \text{ nW}$ . At low excitation powers (black line) the spectrum consists of a peak, centred at  $\omega = 0$ , corresponding to the Rayleigh peak and two shoulders at both flanks of the central peak. With increasing excitation power  $P_{\text{laser}}$ , these shoulders further shift away from the Rayleigh peak and form the expected Mollow sidebands. For the spectrum with the highest resonant excitation power shown here, the sideband splitting and hence the Rabi frequency, reaches values of almost 10 GHz.

From the resonance fluorescence spectra, the sideband splitting is extracted by least square fits of the individual spectra with the sum of three Lorentzian peak functions. The absolute values for the energy splitting and thus for the Rabi frequency  $\Omega_{\text{R}}$  are plotted in figure 7.6(b) as a function of  $\sqrt{P_{\text{laser}}}$ . As seen in section 7.1, the Rabi frequency  $\Omega_{\text{R}}$  is directly proportional to the electric field amplitude, thus to the square root of the photon number  $\sqrt{n}$ . Since these two parameters in turn depend linearly on the square root of the measured excitation field intensity  $\sqrt{P_{\text{laser}}}$ , a linear behaviour for  $\Omega_{\text{R}}(\sqrt{P_{\text{laser}}})$  is expected. This is nicely reproduced by the data shown in figure 7.6(b) and the respective linear fits (dashed lines). Only at high excitation intensities, small deviations from the linear fit can be observed, possibly related to deviations in measuring the excitation powers or an increasing non-linear behaviour of the etalon's frequency shift for larger frequency detunings. This may also be the cause for the slightly different slopes of  $3.96 \frac{\text{GHz}}{\sqrt{\mu\text{W}}}$  and  $3.89 \frac{\text{GHz}}{\sqrt{\mu\text{W}}}$  for the Rabi frequencies derived from the splitting of the blue and red sidebands, respectively. This slope is sometimes referred to as effective dipole momentum, as it depends on the

coupling between the electrical field amplitude of the driving light and the dipole moment of the QD transition (see equation 7.6). It depends on the dipole moment of the transition, which may vary for different QDs, on the relative orientation of the electrical field with respect to the dipole moment but also on the photonic environment the QD is located in. For the sample used here, the QDs are embedded in a planar cavity (see section 4.1), increasing the strength of the light field at the position of the QD and thus the effective dipole momentum. Similar results ( $\approx 4 \frac{\text{GHz}}{\sqrt{\mu\text{W}}}$ ) have been achieved when the resonant optical field at the QD is enhanced by the use of a solid immersion lenses [106].

In contrast to the side peaks, which completely arise from the incoherent part of the resonance fluorescence, the central peak is expected to be comprised of different components, namely both coherent and incoherent parts of the RF emission, as well as maybe not fully suppressed laser background. Since the distinction between these components is difficult and their relative ratio depends on the excitation intensity (Rabi frequency), a comparison of peak amplitudes and line widths is not addressed here.

#### 7.4.2. Dependence on detuning of resonant laser excitation

In the next step, the influence of a detuned excitation on the formation of Mollow triplets is investigated. For that reason, a detuning  $\Delta_{\text{opt}}$  between laser  $\omega_{\text{laser}}$  and QD transmission  $\omega_0$  is introduced:

$$\Delta_{\text{opt}} = \omega_{\text{laser}} - \omega_0 \quad (7.28)$$

The necessary fine tuning of the laser frequency was experimentally implemented by piezo tuning the length of the laser cavity, enabling a total mode hopping free tuning range of up to  $\approx 25$  GHz. Since the detuning  $\Delta_{\text{opt}}$  cannot be expected to depend linearly on the voltage applied to the piezo actuator of the laser cavity, a second stabilised narrow-band laser is used to serve as a fixed frequency reference. To this purpose, the reference laser was mixed with the resonant and PL laser and sent through the optical setup (see figure 7.4). The reference laser was detuned far enough, so as to exclude any interaction with the TLS but close enough to be visible in the high resolution spectra. The power and polarisation of the reference laser was adjusted such that sufficient light can pass through the cross-polarised optical setup and is clearly visible in the acquired single spectra.<sup>1</sup>

RF spectra at different detunings between  $\Delta_{\text{opt}} \approx -4$  GHz and  $\Delta_{\text{opt}} \approx 4$  GHz, a constant resonant excitation power of  $P_{\text{laser}} = 0.8 \mu\text{W}$  and a non-resonant excitation power of  $P_{\text{PL-laser}} \approx 2$  nW are shown in figure 7.7(a). It can be seen, that the central (Rayleigh) emission peak follows the detuning, while the relative peak splitting between Rayleigh and side-peak increases with the absolute detuning  $|\Delta_{\text{opt}}|$  but stays symmetric with respect

<sup>1</sup>For the measurements shown here, the reference laser was tuned to  $\omega_{\text{ref}} = -25$  GHz so it is not visible in the spectra in figure 7.7(a).

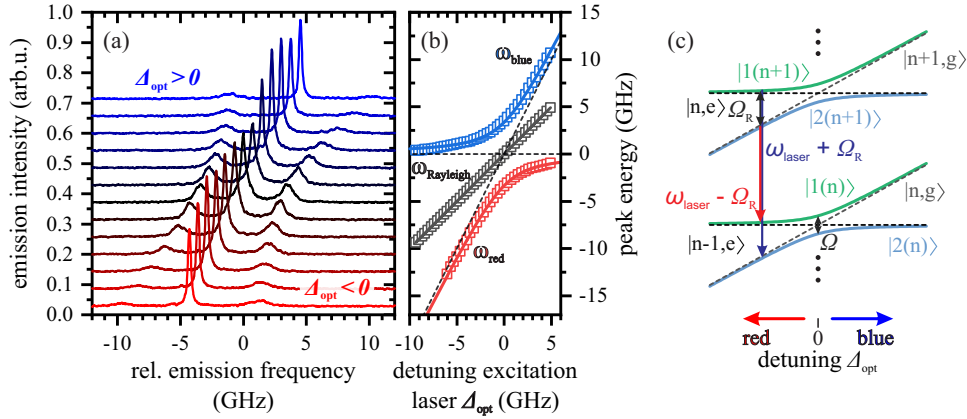


**Figure 7.7.:** (a) RF spectra recorded at different excitation detunings  $\Delta_{\text{opt}}$  but at a constant excitation intensity of  $P_{\text{laser}} = 0.8 \mu\text{W}$ . For clarity, the spectra are plotted with a constant offset. (b) Peak positions for the Rayleigh peak and the red and blue side-bands as a function of detuning  $\Delta_{\text{opt}}$ . The solid lines are best fits with equation 7.32, showing good agreement with the theory. (c) Evolution of the Jaynes-Cummings ladder as a function of  $\Delta_{\text{opt}}$ .

to the central peak. For a detuned excitation, the Rabi frequency is no longer described by the bare Rabi frequency (equation 7.6) used so far but rather by the generalised Rabi frequency  $\Omega_{\text{R}}$ , which also depends on the optical excitation detuning:

$$\Omega_{\text{R}} = \sqrt{\Omega^2 + \Delta_{\text{opt}}^2} \quad (7.29)$$

Furthermore, the dressed states can no longer be described as an even superposition of ground and excited state (see equation 7.23) but rather by [114]:

$$\begin{aligned} |1(n)\rangle &= c |g, n\rangle - s |e, n-1\rangle \\ |2(n)\rangle &= s |g, n\rangle + c |e, n-1\rangle \\ c &= \sqrt{\frac{\Omega_{\text{R}} + \Delta_{\text{opt}}}{2\Omega_{\text{R}}}} \quad s = \sqrt{\frac{\Omega_{\text{R}} - \Delta_{\text{opt}}}{2\Omega_{\text{R}}}} \end{aligned} \quad (7.30)$$

This means that depending on the detuning  $\Delta_{\text{opt}}$ , the dressed states  $|1(n)\rangle$  and  $|2(n)\rangle$  have a larger ground or excited state character. The corresponding energy eigenvalues are given by:

$$E_n^{\pm} = \hbar \left( n + \frac{1}{2} \right) \omega_c \pm \hbar \underbrace{\sqrt{\Omega^2 + \Delta_{\text{opt}}^2}}_{\Omega_{\text{R}}} \quad (7.31)$$

This modified Jaynes-Cummings ladder, as a function of detuning, is depicted in figure 7.7(c). Figure 7.7(b) shows the peak positions for the red ( $\omega_{\text{red}}$ ) and blue ( $\omega_{\text{blue}}$ ) side-band and for the central Rayleigh peak ( $\omega_{\text{Rayleigh}}$ ) as a function of the laser detuning  $\Delta_{\text{opt}}$ . The

peaks positions nicely follow their respective expected behaviour, indicated by the solid lines:

$$\begin{aligned}\omega_{\text{red}} &= \Delta_{\text{opt}} - \sqrt{\Omega^2 + \Delta_{\text{opt}}^2} \\ \omega_{\text{Rayleigh}} &= \Delta_{\text{opt}} \\ \omega_{\text{blue}} &= \Delta_{\text{opt}} + \sqrt{\Omega^2 + \Delta_{\text{opt}}^2}\end{aligned}\tag{7.32}$$

For large positive (negative) detunings,  $\omega_{\text{blue}}$  ( $\omega_{\text{red}}$ ) approximates the line defined by  $\omega = 2 \cdot \Delta_{\text{opt}}$  and for large negative (positive) detunings  $\omega_{\text{blue}}$  ( $\omega_{\text{red}}$ ) approximates  $\omega = 0$ . Both of these lines are indicated by the dashed lines in figure 7.7(b). The solid lines for  $\omega_{\text{red}}$ ,  $\omega_{\text{blue}}$  and ( $\omega_{\text{Rayleigh}}$ ) represent best fits with the respective functions 7.32 and a common value for the only free parameter, the bare Rabi frequency  $\Omega$ . This fit yields a bare Rabi frequency of  $\Omega = 3.36 \pm 0.01$  GHz, resulting in an effective dipole moment of about  $3.75 \frac{\text{GHz}}{\sqrt{\mu\text{W}}}$ , comparable to the value obtained for the QD investigated in the previous subsection (7.4.2).

According to equations 7.30, the composition of the dressed states depends on the optical detuning  $\Delta_{\text{opt}}$ . For a blue detuning ( $\Delta_{\text{opt}} > 0$ ), the  $|1(n)\rangle$  state has more ground state ( $|n, g\rangle$ ), while the  $|2(n+1)\rangle$  has an increasing excited state character. Since the collected resonance fluorescence emission steams from the spontaneous optical decay of the QD, an increased probability to detect a photon from the transition between  $|2(n+1)\rangle$  and  $|1(n)\rangle$ , thus a photon of energy  $\omega_{\text{red}}$ , is expected. At the same time, it is less likely to detect a  $\omega_{\text{blue}}$  photon from the transition between  $|1(n+1)\rangle$  ( $|g\rangle$ -character) and  $|2(n)\rangle$  ( $|e\rangle$ -character). As a result, for a blue detuned optical excitation, the amplitude of the red sideband increases, while the amplitude of the blue sideband decreases. For a red detuned excitation, the exact opposite case occurs and more  $\omega_{\text{blue}}$  than  $\omega_{\text{red}}$  photons are detected. This is directly reflected by the dependence of the respective sideband amplitudes on the detuning  $\Delta_{\text{opt}}$  and can nicely be seen in the spectra shown in figure 7.7(a).

A detailed analysis, including a theoretical model, of the sideband width as a function of detuning can be found in the references [115, 116].



## 8. Resonance fluorescence from a dynamically strained quantum dot

In the previous chapter, the QD transition was only driven by an optical field. In this chapter, the optical driving will be extended by a dynamic modulation of the transition energy  $\omega_{\text{QD}}$  using propagating SAWs. The Hamiltonian, describing the new system, must then be extended by a time dependent transition energy (frequency)  $\Delta(t)$  of the two-level system.

$$\mathcal{H}_s = \hbar\Delta(t) |e\rangle \langle e| + \frac{\hbar\Omega}{2} (\sigma_+ - \sigma_-) \quad (8.1)$$

Here, the influence of the SAW is simply considered by a sinusoidal variation of the QD's transition energy:

$$\Delta(t) = \omega_{\text{QD}} + \Delta\omega_{\text{SAW}} \cdot \cos(\omega_{\text{SAW}} \cdot t) \quad (8.2)$$

In this approach, like in the previous chapter, the QD is described as a two level system, while both optical and mechanical fields are described classically, making this a semi-classical approach. Starting from this Hamiltonian, an analytical model for the resonance fluorescence signal of a dynamically strained QD was developed by Daniel Wigger<sup>1</sup>, Tilmann Kuhn<sup>1</sup> and Paweł Machnikowski<sup>2</sup>. This model shows an excellent agreement with the experimental data that will be presented in this chapter but will not be considered in more details in the scope of this work. More details on the model can be found in the corresponding preprint [117].

The experiments presented in this chapter were supported by Maximilian Nägele as a part of his bachelor thesis. A schematic of the sampled used for the experiments presented in this chapter is shown in figure 8.1(a). IDTs were directly fabricated on the surface of a sample containing a layer of InGaAs-QDs, embedded in a planar Bragg cavity. This is the same type of sample used in the previous chapter ("EPI467") but two of the initially ten top reflector pairs were removed by digital chemical wet etching. This brings the QD-layer about 300 nm closer to the surface, greatly enhancing their coupling to SAWs, especially at higher frequencies  $> 1$  GHz. On the other hand, removing reflector pairs reduces the reflectivity of the top DBR and thus the  $Q$ -factor of the planar cavity. This results in a decreased coupling of the QDs to the resonant light field, which is reflected by a smaller effective dipole momentum of about  $\approx 0.25 \frac{\text{GHz}}{\sqrt{\mu\text{W}}}$ , compared to  $\approx 3.75 - 4 \frac{\text{GHz}}{\sqrt{\mu\text{W}}}$  obtained in

<sup>1</sup>Institut für Festkörpertheorie, Universität Münster, Germany.

<sup>2</sup>Department of Theoretical Physics, Wrocław University of Science and Technology, Poland

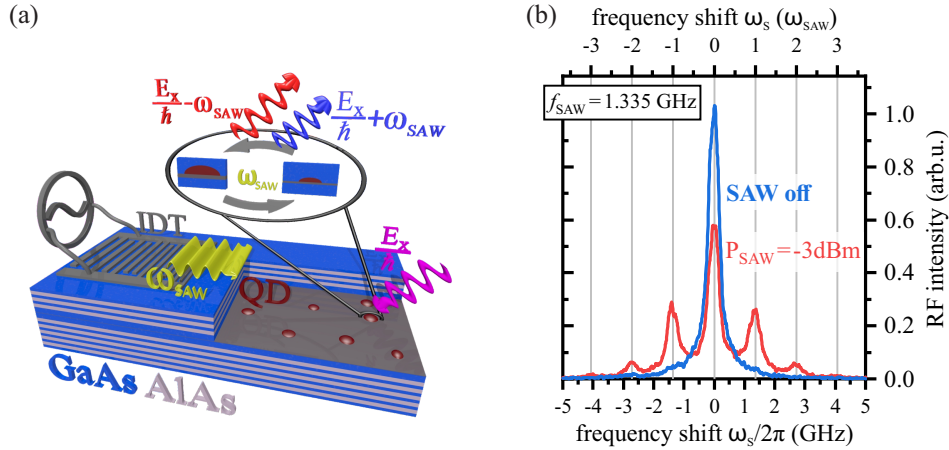


**Figure 8.1.:** (a) Schematic of the used sample. QDs are embedded in a planar Bragg cavity formed by alternating layers of GaAs and AlAs. Transducers are fabricated directly on the surface of the sample. (b) Resonance fluorescence spectra of a unstrained QD (blue) and a QD strained by a  $\omega_{\text{SAW}}$  SAW. The periodic modulation of the SAW leads to the formation of phononic sidebands on either side of the Rayleigh line (zero phonon line (ZPL)), separated by  $\omega_{\text{SAW}}$ .

the previously shown measurements with ten top reflector pairs.

However, all experiments shown in this chapter are limited to the limit of low Rabi frequencies, meaning Rabi frequencies much smaller than the radiative decay rate  $\Omega_{\text{R}} \ll \Gamma$ . Figure 8.1(b) shows two high resolution spectra of a QD, being resonantly driven by a  $P_{\text{laser}} \approx 0.576 \mu\text{W}$  laser field, thus at a Rabi frequency of  $\Omega_{\text{R}} \approx 190 \text{ MHz}$ . The blue curve represents the RF spectrum with no SAW applied. It consists only of a narrow central peak referred to as the zero phonon line (ZPL), stemming from the laser light being resonantly scattered at the two-level system. For the red spectrum, a continuous SAW of frequency  $f_{\text{SAW}} = 1.355 \text{ GHz}$  and power  $P_{\text{SAW}} = -3 \text{ dBm}$  is applied to the QD, dynamically modulating its transition energy. This leads to the formation of equidistant sidebands on both sides of the ZPL, while the intensity of the ZPL decreases. The splitting of these sidebands with respect to the ZPL is given by a multiple integer of the SAW frequency  $\omega_{\text{SAW}}$ . These sidebands can be interpreted as arising from the absorption of a phonon from the SAW field or the stimulated emission of a phonon into the SAW field. Therefore, the emerging sidebands are referred to as phononic sidebands (PSB).

This phenomenon was first shown in 2010 by Metcalfe et al. [108] for QDs in a planar cavity, by using optical side excitation and detection perpendicular to the surface of the sample. In addition, the emergence of SAW induced phononic sidebands was reported by Villa et al. for QDs embedded in a pillar micro-cavity using a cross polarised RF excitation-detection scheme [118].

In this section, the formation of PSBs and its dependence on SAW amplitude  $P_{\text{rf}}$ , frequency  $f_{\text{SAW}}$  and the optical detuning  $\Delta_{\text{opt}}$  shall be investigated in more details. Furthermore, the

SAW induced sidebands are examined in the time domain. In the last part of this chapter, the resonance fluorescence of a QD interacting with two mutually coherent SAW fields is investigated. In this case, non-linear phonon mixing results in the formation of phononic sidebands with a characteristic amplitude structure, which depends on the phase between the two waves. Introducing a slight detuning between the phonon fields results in sideband oscillations in the time domain that can be observed over several hours, demonstrating the enormous coherence times of the phonon fields.

## 8.1. Dependence of phononic sidebands on SAW amplitude

The formation of PSBs via phonon assisted transitions is schematically shown in figure 8.2(a). The stimulated emission of phonons leads to a decrease of energy, while the absorption of phonons leads to an increase of energy of the photons scattered at the TLS, giving rise to the formation of the red and blue sidebands respectively. Since the involved coherent phonons have a well-defined energy  $\hbar \cdot \omega_{\text{SAW}}$ , well-defined by the frequency of the SAW, these PSBs are equidistant. The number of phonons  $n$  being emitted/absorbed

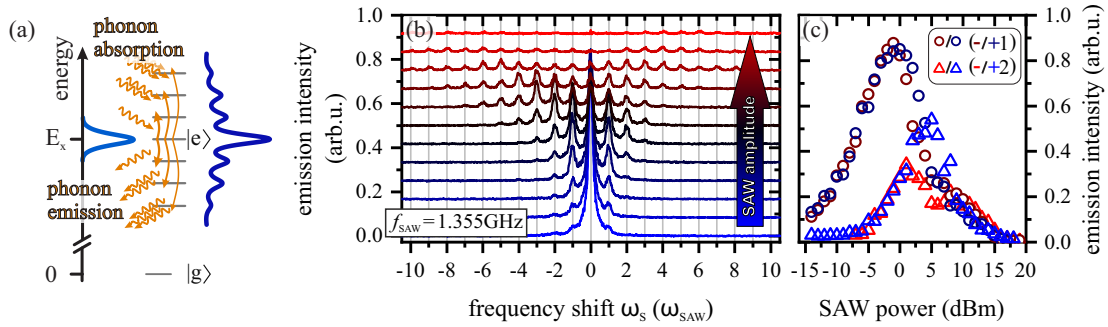


**Figure 8.2.:** (a) Schematic representation of the phonon assisted transitions, leading to the formation of PSBs. (b) High resolution spectra of a resonantly driven QD, for different SAW powers  $P_{\text{SAW}}$ .  $P_{\text{SAW}}$  increases from  $-15$  dBm (bottom, blue spectrum) to  $15$  dBm (top, red spectrum) in constant steps of  $3$  dB. For clarity, the spectra are plotted with a constant offset. (c) Integrated emission of the first two red and blue sidebands as a function of  $P_{\text{SAW}}$ .

in a single photon scattering process depends on the phonon density and thus on the SAW amplitude. This is reflected in the high resolution spectra depicted in figure 8.2(a). Here, the QD is dynamically strained by a  $1.355$  GHz SAW and an amplitude  $P_{\text{rf}}$  tuned from  $-15$  dBm (blue spectrum) to  $15$  dBm (red spectrum) in constant increments of  $3$  dB. For the lowest SAW amplitudes, barely any PSBs can be resolved and the spectrum is entirely dominated by the ZPL. With increasing  $P_{\text{rf}}$ , the  $(\pm 1)$  PSBs start to emerge first, followed by the  $(\pm 2)$  PSBs and so on, while the intensity of the ZPL decreases. For a SAW amplitude of about  $P_{\text{rf}} = 0$  dBm, the intensity of the  $(\pm 1)$  PSBs reaches its maximum and decreases again with further increasing  $P_{\text{rf}}$ . This confirms our assumption that, with

increasing SAW amplitude, transitions involving an increasing number  $n$  of phonons become more likely. For high amplitudes  $P_{\text{rf}}$ , the emission increasingly shifts away from the ZPL towards higher and lower energetic PSBs and the overall emission intensity is spread over an increased number of sidebands.

This behaviour can also nicely be seen in figure 8.2(c), where the intensities of the ( $\pm 1$ ) and ( $\pm 2$ ) PSBs are plotted as a function of  $P_{\text{rf}}$ . At first, only the intensities of the first red ( $-1$ ) and blue ( $+1$ ) sideband increase to the same extent, then reach a maximum around  $P_{\text{rf}} = 0$  dBm, before decreasing again. The ( $\pm 2$ ) PSBs show the same behaviour but delayed in  $P_{\text{rf}}$ .

A closer examination of the ( $\pm 2$ ) PSB intensities in figure 8.2(c), reveals a non uniform intensity course around 5 dBm, where the ( $+1$ ) sideband has its maximum but the ( $-1$ ) sideband intensity already dropped significantly. The same asymmetry can also be seen in the spectra for high amplitudes in figure 8.2(b), where the emission is shifted further red than blue with respect to the ZPL. This asymmetry is attributed to a small increase in temperature with increasing SAW amplitude which results in a red shift of the QD transition frequency  $\omega_0$ . As the frequency of the resonant laser  $\omega_{\text{laser}}$  stays constant, this results in a detuning  $\Delta_{\text{opt}} = \omega_{\text{laser}} - \omega_0$  of the optical excitation. The effect of detuned excitation on the SAW induced phononic sidebands will be treated in more detail in section 8.3.

## 8.2. Dependence of phononic sidebands on SAW frequency

So far, it has been shown that the average number of phonons  $n$  involved in a phonon assisted photon scattering process can be tuned via the SAW amplitude. As a second parameter of the SAW field, the dependence on the SAW frequency  $f_{\text{SAW}}$ , thus the phonon energy  $\hbar \cdot \omega_{\text{SAW}}$ , shall be discussed here.

Figure 8.3(a) shows RF spectra recorded under low resonant excitation power (200 nW) for three different SAW frequencies  $f_{\text{SAW}}$ . The three frequencies of 677.5 MHz, 1015 MHz and 1355 MHz correspond to the second, third and fourth harmonic of a (non-chirped) split-5-2 IDT with a fundamental frequency of about 333 MHz. For all three spectra, PSBs can be resolved with a splitting set by the respective phonon frequency  $\omega_{\text{SAW}}$ . Although the amplitude of the exciting rf-signal was kept constant at  $P_{\text{rf}} = -8$  dBm for all three measurements, the number of PSB  $n$  that can be observed varies strongly between the different measurements. While, for the lowest frequency, four PSB on each side of the ZPL can be resolved, this number decreases to three or two for the higher frequencies. A key parameter that defines the strength of the phonon field, and thus the intensities of the PSBs, is the dimensionless relative SAW modulation amplitude  $D$ :

$$D = \frac{\Delta_0}{\omega_{\text{SAW}}}, \quad (8.3)$$

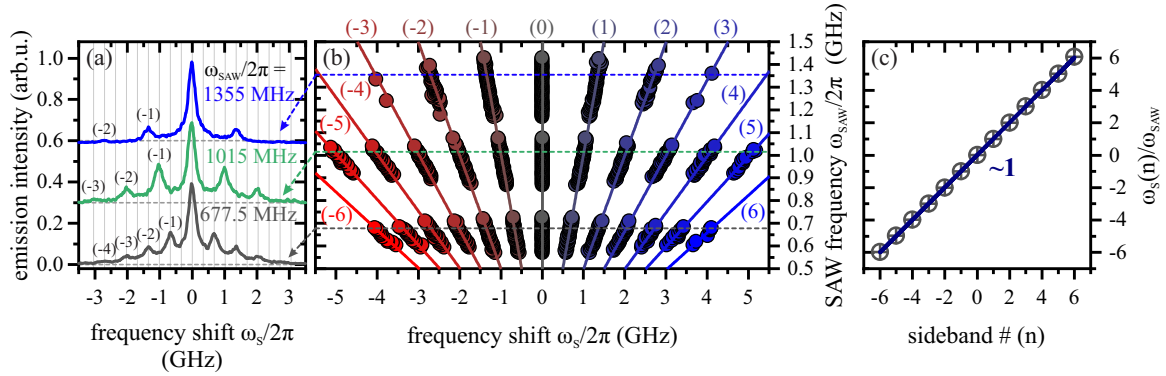


**Figure 8.3.:** (a) Resonance fluorescence spectra of a QD strained by SAWs with three different frequencies  $\omega_{\text{SAW}}$ , corresponding to the first, second and third overtone of a split-5-2 transducer. (b) Shift of PSBs as a function of  $\omega_{\text{SAW}}$ , tuned over three transmission bands of a single split-5-2 chirped transducer. Solid lines are linear fits of the respective sideband positions. (c) Slope of the sideband shift as a function of sideband index ( $n$ ), confirming  $\omega_S(n) = n \cdot \omega_{\text{SAW}}$ .

determined by the SAW frequency  $\omega_{\text{SAW}}$  and the SAW induced periodical deformation potential modulation  $\Delta_0$ . This relative amplitude can be considered as a phonon density. Since the energy that is put into SAW generation, and thus the energy in the phonon field, is kept constant as  $f_{\text{SAW}}$  is varied, the mean phonon number is expected to decrease with increasing energy (frequency) of the phonons. Furthermore, the penetration depth of a SAW, and thus the induced modulation amplitude, strongly depends on the frequency (wavelength) of the SAW (see figure 3.4). As the QDs used for this experiment are located relatively deep below the surface ( $\approx 1.3 \mu\text{m}$ ) a strong decrease of the modulation amplitude  $\Delta_0$  is expected with increasing frequency, within the frequency range covered in this experiment. Overall, these two effects cause a strong decrease of the relative SAW amplitude  $D$  with frequency at the position of the QDs, explaining the smaller number of PSBs being observed for higher frequencies.

To cover a large frequency range, rather than discrete frequencies and to enable a continuous tunability of  $\omega_{\text{SAW}}$ , chirped transducers have been employed. The IDT was designed to cover the frequency range of 300 – 350 MHz by its fundamental band. In figure 8.3(b), the positions  $\omega_S(n)$  of the PSBs are plotted as a function of SAW frequency  $f_{\text{SAW}} = \frac{\omega_{\text{SAW}}}{2\pi}$ , ranging from 0.5 GHz to 1.5 GHz. PSBs can be observed within three frequency bands of increasing bandwidth that correspond to the second, third and fourth transmission band of the IDT. The rf-amplitude was kept constant at  $P_{\text{rf}} = 14 \text{ dBm}$  across all SAW frequencies  $\omega_{\text{SAW}}$ . This rf-amplitude is significantly larger than the one applied for the measurements presented in figure 8.3(a) in order to observe a larger number of sidebands and, especially, to compensate for the lower efficiency of the chirped transducer compared to the non-chirped one. Again, the number of PSBs that can be resolved decreases with increasing frequency, indicating a decrease of the relative SAW amplitude  $D$  with frequency.

The solid lines in figure 8.3(b) are linear fits of the respective sideband positions as a function of  $\omega_{\text{SAW}}$ , nicely confirming the expected behaviour:

$$\omega_S(n) = n \cdot \omega_{\text{SAW}} \quad (8.4)$$

for all sideband indices  $n$  ( $= 0, \pm 1, \pm 2, \dots$ ) and over the entire SAW frequency range. The slopes extracted from the fits are plotted against their respective sideband indices  $n$  in figure 8.3(c). As expected, the slope of the sideband shift  $\omega_S(n)/\omega_{\text{SAW}}$  matches precisely the sideband number  $n$ .

The fact that the PSB splitting is exclusively determined by  $\omega_{\text{SAW}}$ , which can be set with high accuracy, makes it possible to use it as an energy standard. Instead of calibrating the etalon frequency shift  $\omega_S$  with respect to its free spectral range (FSR = 60 GHz) it is possible to calibrate it with respect to PSB splitting and thus with respect to  $\omega_{\text{SAW}}$ . This allows to significantly reduce the frequency range  $\omega_S$  that needs to be covered when acquiring high resolution spectra and so the necessary integration times are reduced.

### 8.3. Parametric excitation: Dependence of phononic sidebands on optical detuning

In this section, the influence of an optical detuning  $\Delta_{\text{opt}} = \omega_{\text{laser}} - \omega_0$  between QD transition  $\omega_0$  and resonant laser  $\omega_{\text{laser}}$  on the formation of PSBs is discussed. The experimental procedure was the same as for the measurements presented in section 7.4.2 but the QD was optically driven in the limit of low Rabi frequencies, while being dynamically strained by a  $f_{\text{SAW}} = 1.3$  GHz SAW excited via a chirped transducer ( $P_{\text{rf}} = 17$  dBm).

This detuned excitation scheme, depicted in figure 8.4(a), facilitates the parametric energy conversion between phononic and photonic domain. The black curves in the center show the well known case of strict resonant excitation, resulting in the formation of a symmetric RF spectrum with an equal number of PSBs on both sides of the ZPL. The symmetry of the RF spectrum is lifted when a finite detuning  $\Delta_{\text{opt}}$  is introduced. This means that, depending on the sign of the detuning, energy is transferred from the photonic to the phononic domain or vice versa.

Spectra recorded for detunings  $\Delta_{\text{opt}}$  that agree with integer multiples of the SAW frequency  $\omega_{\text{SAW}}$  are shown in figure 8.4(b). The point of origin ( $\omega_S = 0$ ) was set to match the transition energy of the QD, i.e. the ZPL for zero detuning. The yellow arrows mark the spectral position of the exciting laser, thus the peak corresponding to the resonantly scattered part (ZPL). The case for a vanishing detuning ( $\Delta_{\text{opt}} = 0$ , black spectrum) has already been considered and leads to a spectrum that is symmetric with respect to the ZPL. There is an equal number of sidebands on both sides of the ZPL with matching intensities for the  $(\pm n)$  sidebands. When introducing a detuning  $\Delta_{\text{opt}}$ , this is no longer

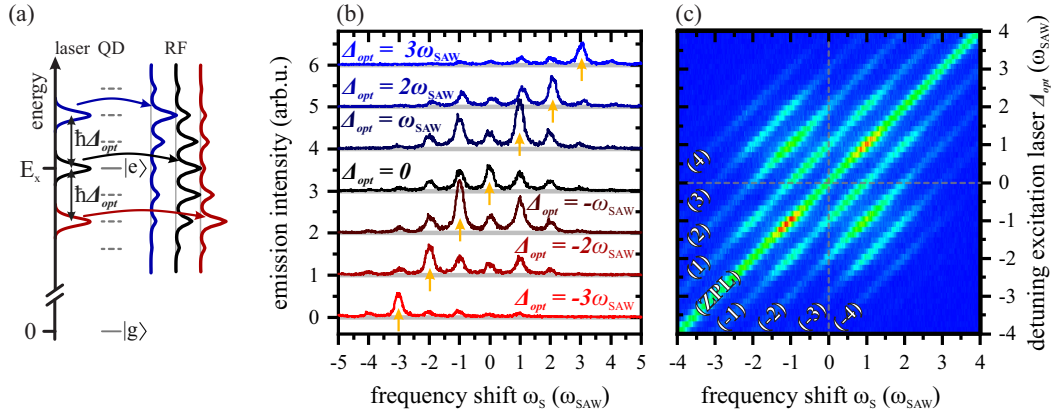


**Figure 8.4.:** (a) Schematic picture of an optically detuned RF of a dynamically strained QD. (b) RF spectra for detunings  $\Delta_{opt}$  being multiple integers of  $\omega_{SAW}$ , ranging from  $-3 \cdot \omega_{SAW}$  to  $3 \cdot \omega_{SAW}$ . The yellow arrows mark the driving laser (ZPL) for the respective spectra. (c) False colour representation of RF spectra for a continuous variation of the detuning  $\Delta_{opt}$ .

the case, and the spectra become increasingly asymmetrical. For instance, for a detuning of  $\Delta_{opt} = -1 \cdot \omega_{SAW}$ , the PSBs directly next to the ZPL are weak than the PSB at  $\omega_s = 1 \cdot \omega_{SAW}$ . Furthermore, RF spectra with the same absolute detuning  $|\Delta_{opt}|$  but a different sign are identical but mirrored at  $\omega_s = 0$  ( $\Delta_{opt} \rightarrow -\Delta_{opt}, \omega_s \rightarrow -\omega_s$ ). For all spectra, the dominant peak corresponds to the respective ZPL (indicated by the yellow arrows), which shifts with the excitation laser.

In order to provide a complete picture of the underlying mechanisms of detuned excitation,  $\Delta_{opt}$  was tuned continuously from  $-4$  to  $+4$  GHz. The respective experimentally measured scattered photon intensity is shown in figure 8.4(c) in a false-colour representation as a function of relative frequency shift  $\omega_s$  and excitation detuning  $\Delta_{opt}$ . The dominant diagonal line ( $\omega_s = \Delta_{opt}$ ) corresponds to the elastically scattered photons, the ZPL. Parallel to this, shifted by  $n \cdot \omega_{SAW}$  in frequency, are the PSBs with their respective sideband index being indicated in the brackets. The arising intensity pattern is clearly symmetric with respect to the ZPL. A clear enhancement of the RF signal can also be observed for detunings of multiple integers of  $\omega_{SAW}$ , thus  $\Delta_{opt} = \pm n \cdot \omega_{SAW}$ . This is a direct evidence for a resonant parametric coupling between the light field and an integer number of phonons.

To understand the observed intensity pattern, one has to consider that the SAW induced modulation of the exciton energy causes an oscillation of the exciton coherence, giving rise to the formation of the PSBs. The amplitudes of the respective PSBs depend, among other things, on the frequency of these rotations. As the RF signal is accumulated over an excitonic lifetime, faster frequency components are averaged out. For a vanishing detuning  $\Delta_{opt} = 0$ , the oscillation frequency thus only depends on the relative sideband position  $\omega_s$  and as a consequence the higher sidebands exhibit a lower intensities. An additional detuning  $\Delta_{opt}$  can be considered by a constant offset to the excitonic transition energy (see

equation 8.2;  $\Delta(t) \rightarrow \Delta(t) + \Delta_{\text{opt}}$ ). This causes an additional rotation in the Hamiltonian with frequency  $\Delta_{\text{opt}}$ . This additional rotation can interfere constructively or destructively, depending on the sign of the detuning, with the SAW induced rotation and thus alter the intensity of certain PSBs.

In the following, an optical detuning of  $\Delta_{\text{opt}} = \omega_{\text{SAW}}$  is considered. This detuning causes an additional rotation of the exciton coherence with a frequency  $\omega_{\text{SAW}}$ . In this case, the sideband appearing at  $\omega_{\text{S}} = 0$  carries only the rotation induced by the detuning, leading to a reduction of the peak intensity. For the peak at  $\omega_{\text{S}} = -\omega_{\text{SAW}}$ , the two rotations induced by the SAW and the detuning compensate for each other, resulting in an increase of the respective peak amplitude. The strongest peak at  $\omega_{\text{S}} = \omega_{\text{SAW}}$ , marked by the yellow arrow, is the ZPL and accordingly carries the un-scattered contribution of the laser in addition to the two compensating rotations, making it the strongest contribution in the spectrum.

For all detunings  $\Delta_{\text{opt}}$ , the emission at  $\omega_{\text{S}} = 0$  carries only the rotation caused by the detuning and thus the respective peak intensities for integer detunings ( $\Delta_{\text{opt}} = n \cdot \omega_{\text{SAW}}$ ) decrease with increasing detuning. As a consequence, measuring the RF signal as a function of  $\omega_{\text{S}}$  for zero detuning yields the same result as measuring the intensity at  $\omega_{\text{S}} = 0$  as a function of  $\Delta_{\text{opt}}$ . In other words, the intensity along the horizontal ( $\Delta_{\text{opt}} = 0$ ) and vertical ( $\omega_{\text{S}} = 0$ ) cut-lines, indicated by the dashed lines in figure 8.4(c), is identical. This also explains the mirror symmetry of the intensity pattern with respect to the ZPL.

The simple model, which states that the PSB intensity depends only on the distance to the ZPL, applies only for small relative phonon amplitudes  $\Delta$ , as it could be seen in section 8.1. Detuning dependent measurements for higher SAW amplitudes are presented in Appendix B.2. With increasing modulation amplitude and thus increasing number of PSBs, the respective sideband intensities at vanishing detuning no longer solely depend on their respective sideband index  $n$ . Accordingly, a full theoretical treatment, taking into account all aspects of the underlying mechanisms, must be applied to reproduce the experimental data. The overall symmetry of the measured intensity pattern, however, remains.

## 8.4. Time domain spectroscopy of phononic sidebands

In order to investigate the evolution of PSBs in the time domain, the experimental setup depicted in figure 8.5(a) was used. This is basically the same setup that was introduced in section 5.2, although, here, the RF signal is spectrally filtered by the FP-etalon rather than by the monochromator. Instead of continuously tuning the etalon with a 1 Hz-saw-tooth function, it is scanned in discrete energy steps and time transients are recorded for each discrete step. This makes the measurement more sensitive to a thermal drift of the transmission energy of the etalon, as a subsequent compensation of the drift is no longer possible. However, the active temperature stabilisation of the etalon reduces the drift significantly below the sideband splitting within the measurement time. The reference

signal for the time correlated single photon counting was provided by a clock generator and set to an integer fraction of the SAW frequency  $\frac{f_{\text{SAW}}}{n}$  so that any periodic process in the time domain, whose periodicity is coupled to the SAW period  $T_{\text{SAW}}$ , can be resolved. The such measured time-transients, covering a time range of  $3.5 \cdot T_{\text{SAW}}$ , are plotted in a false-colour representation in figure 8.5(b) as a function of energy. The time-integrated emission as a function of energy is plotted in panel (c), showing that although the etalon was not tuned continuously, the individual PSB could still be resolved nicely and the time-integrated emission can be used to calibrate the energy-axis for this experiment.

The time transients reveal a clear oscillation of the PSB intensities following the frequency

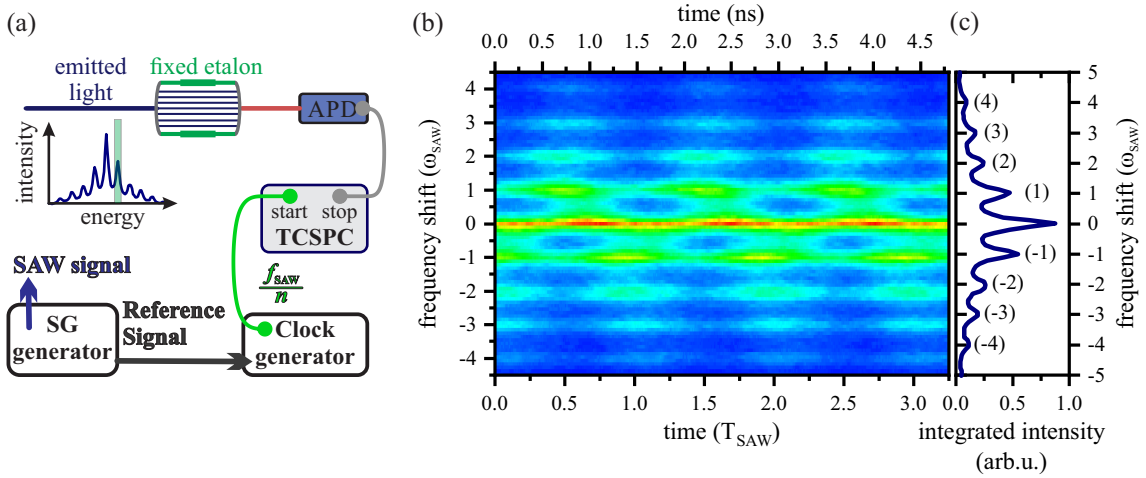


**Figure 8.5.:** (a) Experimental setup to measure the formation of PSBs in the time domain. The transmission energy of the etalon is changed in discrete steps and for each step a time-transient is recorded using TCSPC. (b) Time and energy resolved RF signal of a QD that is dynamically strained by a SAW ( $f_{\text{SAW}} = 677.5 \text{ MHz}$ ,  $P_{\text{rf}} = -5 \text{ dBm}$ ). Oscillations of the sideband intensities with frequency  $f_{\text{SAW}}$ , that are anti-correlated for red and blue sidebands, can clearly be resolved. (c) Time-integrated RF intensity as a function of energy, showing distinct PSBs, symmetric to the ZPL.

of the SAW  $f_{\text{SAW}} = 677.5 \text{ MHz}$  ( $T_{\text{SAW}} \approx 1.48 \text{ ns}$ ). These oscillations are clearly anti-correlated for the red and blue PSBs respectively. This means that the emission of phonons into the SAW field, leading to the formation of red PSBs, happens at a separate time as the absorption of phonons from the SAW-field, leading to the formation of blue PSBs. Furthermore, it indicates that, whenever the change of the energy shift of the QD transition is positive, thus shifts towards higher energies, the absorption of phonons is the dominant process. Half a SAW period later, when the transition energy shifts towards lower energies, the situation is reversed and the emission of phonons, thus the formation of red PSBs, becomes dominant.

In addition, it is noticeable that, despite the comparatively low SAW frequency, the time-transients are clearly smeared out in time. This can be explained by two effects. First of

all, the absorption and/or emission of phonons does not happen at a single point in time. Phonon absorption and emission processes are rather accumulated over the entire lifetime of the excitonic state. Similar to the already shown stroboscopic PL measurements (see figure 5.8), this leads to the observed smearing of the measurements, when the radiative decay time becomes comparable to or is larger than the SAW period  $T_{\text{SAW}}$ . Furthermore, the time resolution  $\Delta t$  of the experiment is not limited by the time resolution of the detector, like in the previously shown time-resolved measurements, but, due to the high spectral resolution of the etalon, by the uncertainty principle for energy and time. Therefore, the maximum resolution is determined by the spectral resolution of the etalon  $\delta\nu = 227$  MHz:

$$\Delta t \geq \frac{1}{4\pi\delta\nu} \approx 0.35 \text{ ns}, \quad (8.5)$$

In order to best resolve the SAW induced dynamics, the lowest harmonic of the IDT, for which the sideband splitting could still be resolved, was chosen. This counteracts both effects by increasing  $T_{\text{SAW}}$  and thus maximizing the time resolution  $\Delta t$  and minimizing the decay time  $\tau$ , both in units of the SAW period  $T_{\text{SAW}}$ .

Further measurements at higher SAW frequencies  $f_{\text{SAW}}$  are presented in the appendix B.1. There, it can be clearly seen that, with increasing  $f_{\text{SAW}}$ , intensity oscillations become less pronounced, as both phonon processes are accumulated over large portion of the SAW period and time resolution is decreased in units of  $T_{\text{SAW}}$ .

## 8.5. Acoustic two tone excitation

It has previously been shown that the manipulation of QDs with surface acoustic waves is not limited to monochromatic waves containing only a single frequency, but different frequency components can be added up, to generate more complex nano-mechanical waveforms. So it is possible to perform additive Fourier synthesis of SAWs, using different harmonics of an IDT [79]. In section 6.5 of this work, it has been shown that the use of chirped transducers lifts the limitation to discrete harmonics of an IDT and enables the combination of waves with a variety of different frequencies. The combination of SAWs, emitted from different IDTs, is also possible, as long as they share a common sound-path, like for two IDTs in a delay line, or their respective sound-paths cross each other.

In this section, a QD is strained by the combination of two SAW fields and the resulting effect on the formation of PSBs is investigated. First of all, the combination of two counterpropagating SAWs with identical amplitude and frequency forming a standing wave is considered. After that, the combination of two waves with arbitrary frequencies and, finally, of two frequencies with an integer frequency ratio, and thus a stable phase relation between both waves is investigated.

## 8.5.1. Standing wave

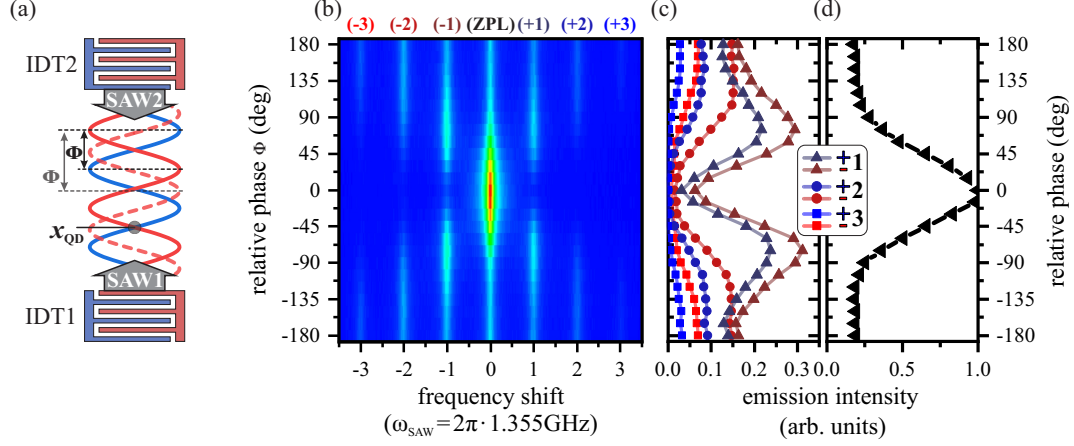


**Figure 8.6.:** (a) Both IDTs of a delay line are used to excite two SAWs of identical frequency and amplitude. The superposition of both waves creates a standing wave. The effective amplitude of the standing wave at the QD position  $x_{\text{QD}}$  can be tuned by the relative phase  $\phi$  between the individual waves. (b) PSBs of a QD dynamically strained by a standing wave as a function of the relative phase  $\phi$  between the two individual counterpropagating waves. (c,d) Emission intensities of the  $(\pm 1, \pm 2, \pm 3)$  sidebands (c) and the ZPL (d), as a function of  $\phi$ . The lines are guide for the eye.

The first case considered here is a standing wave that is created by a superposition of two identical counterpropagating waves. The used experimental configuration is shown in figure 8.6(a). The QD under investigation is located within a delay line formed by two identical IDTs (split-5-2, non-chirped). Both transducers are connected to a signal generator each, exciting a SAW of frequency  $f_{\text{SAW}} = 1.355 \text{ GHz}$  and amplitude  $P_{\text{rf}} = 0 \text{ dBm}$ . To ensure that the frequencies of both generators are truly identical and both signals maintain a constant phase relation, both generators are referenced to a common oscillator. The superposition of both waves at the position of the QD can be expressed as the sum of the individual waves:

$$A_{\text{SAW1}} = A \cdot \sin\left(\frac{2\pi x}{\lambda} + 2\pi f_{\text{SAW}}t + \phi_1\right)$$

$$A_{\text{SAW2}} = A \cdot \sin\left(\frac{2\pi x}{\lambda} - 2\pi f_{\text{SAW}}t + \phi_2\right)$$

Using trigonometric identities, the sum of the individual waves can be written as:

$$\begin{aligned}
 A_{\text{standing}} &= A_{\text{SAW1}} + A_{\text{SAW2}} = \\
 &= \underbrace{2A \cdot \sin\left(\frac{2\pi x}{\lambda} + \frac{\phi_1 + \phi_2}{2}\right)}_{\text{effective amplitude}} \cos\left(2\pi f_{\text{SAW}}t + \frac{\phi_1 - \phi_2}{2}\right) \quad (8.6)
 \end{aligned}$$

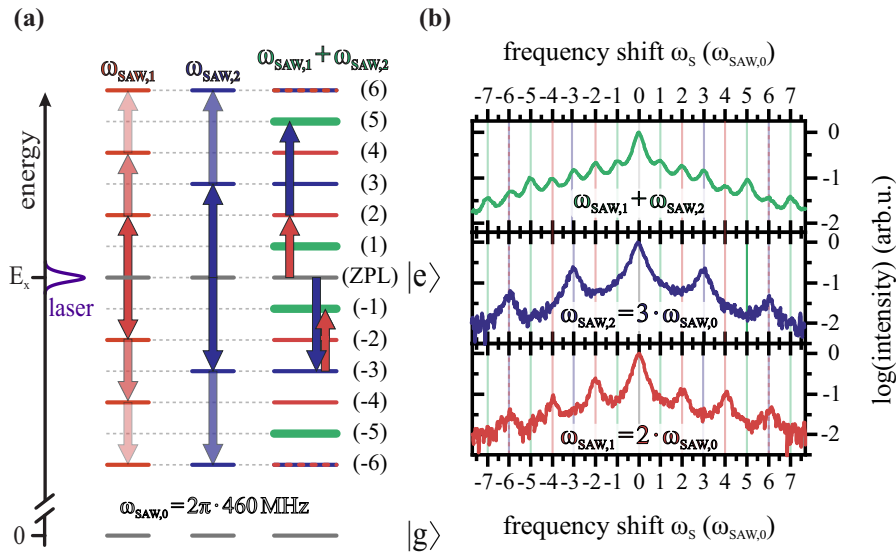
where  $\Phi_1$  and  $\Phi_2$  are the respective phases of the two waves at the QD position accounting for both the phase difference of the exciting rf-signal and the phase difference introduced by the relative position of the QD to the respective IDTs. The resulting wave form (equation 8.6) consists of two components: One oscillating in time with the frequency  $f_{\text{SAW}}$  of the individual waves, the other describing an effective amplitude, which depends on the position  $x$  and the relative phase between the individual waves  $\phi = \phi_1 - \phi_2$ . For a given relative phase  $\phi$ , the resulting waveform comprises so-called nodes, where the amplitude is always zero. Two adjacent nodes are spatially separated by  $\lambda/2$ . Between two nodes is an anti-node, where the amplitude has a maximum of  $2A$ . As the QD is located at a fixed position  $x_{\text{QD}}$ , the effective amplitude can be adjusted by changing the relative phase  $\phi$  (see figure 8.6(a)).

Figure 8.6(b) shows the RF-signal of a QD strained by a standing wave as a function of the relative phase  $\phi$ . For  $\phi = 0$ , the standing wave has a node at the position of the QD and so only the ZPL is visible in the spectrum. With an increasing absolute phase shift, the effective amplitude increases and more and more sidebands become visible in the spectra, while the intensity of the ZPL decreases. This is also clearly reflected in the figures 8.6(c) and (d), where the emission intensities of the  $(\pm 1, \pm 2, \pm 3)$  side-bands and the ZPL, extracted from Lorentzian-Peak fits, are plotted as a function of  $\phi$ . For  $\phi = 0$ , a maximum for the ZPL intensity is observed, while the sideband intensities show a minimum at or at least close to zero. For a phase shift of  $\phi = 75^\circ$ , the  $(\pm 1)$  have a maximum in intensity that decreases again with higher phase shift, while the intensities  $(\pm 2, \pm 3)$  increase continuously. In figure 8.6(c), it also becomes apparent that the red side-bands have a slightly lower emission than their blue counterparts, indicating a small optical detuning  $\Delta_{\text{opt}} > 0$ . Furthermore, the intensity of the  $(\pm 1)$  does not reach zero for  $\phi = 0$ , when the node of the standing wave is expected. This can be explained by a slight difference in amplitudes for the individual waves. In this case, the superposition of the waves is composed of a standing wave and an additional propagating wave with an amplitude corresponding to the amplitude difference.

This technique can, for example, be used to change the strain modulation amplitude for a QD and thus the number of PSBs, while keeping the thermal load on the sample constant. Therefore, optical detunings induced by a temperature drift, when changing the modulation amplitude (rf-amplitude), as it was observed in section 8.1 for high SAW amplitudes, can be avoided.

### 8.5.2. Frequency mixing

As it has already been shown (see figure 8.3), the IDTs used in this work are not limited to a single frequency, making it possible to strain a QD simultaneously by two SAW fields with different frequencies. For the following measurements, a delay line consisting of identical chirped IDTs was used, one IDT emitting a SAW of frequency  $\omega_{\text{SAW},1} = 2\pi \cdot 920$  MHz ( $P_{\text{rf},1} = 2$  dBm), the other of  $\omega_{\text{SAW},2} = 2\pi \cdot 1380$  MHz ( $P_{\text{rf},2} = 14$  dBm). However, for this experiment, it would be possible to use a single one of these IDTs to generate both frequencies simultaneously. Figure 8.7(a) shows a schematic of the PSB alignment where either only the  $\omega_{\text{SAW},1}$  SAW (red) or only the  $\omega_{\text{SAW},2}$  SAW (blue) or both SAWs (green) are excited. The PSB for all three cases are labelled with respect to  $\omega_{\text{SAW},0} = 2\pi \cdot 460$  MHz, which is the greatest common divisor for both SAW components, as  $\omega_{\text{SAW},1} = 2 \cdot \omega_{\text{SAW},0}$  and  $\omega_{\text{SAW},2} = 3 \cdot \omega_{\text{SAW},0}$ . For only one of the two SAWs active, this corresponds to cases already considered and equidistant PSBs are expected on both sides of the ZPL, formed by the emission or absorption of phonons of the respective frequencies. This is confirmed by the respective spectra shown in figure 8.7(b). When only the  $\omega_{\text{SAW},1}$  SAW is excited (bottom, red spectrum), PSBs are visible at  $(\pm 2n \cdot \omega_{\text{SAW},0})$ . If, however, only the  $\omega_{\text{SAW},2}$  SAW is excited (middle, blue spectrum), PSBs at  $(\pm 3n \cdot \omega_{\text{SAW},0})$  can be resolved.



**Figure 8.7.:** (a) Schematic alignment of the PSBs of a QD strained by either only  $\omega_{\text{SAW},1}$  (red) or only  $\omega_{\text{SAW},2}$  (blue) or simultaneously by the combination both SAWs (green). Arrows show possible phonon emission (downwards) and absorption (upwards) processes, involving phonons of the respective frequencies. (b) RF spectra recorded for only  $\omega_{\text{SAW},1}$  (red) or only  $\omega_{\text{SAW},2}$  (blue) being active. For the green (phase-averaged) spectrum, the QD was simultaneously strained by both SAWs. Intensities are presented on a logarithmic scale.

For the green spectrum in figure 8.7(b), the QD is strained by both waves simultaneously. Since both frequencies  $\omega_{\text{SAW},1}$  and  $\omega_{\text{SAW},2}$  are an integer multiple of  $\omega_{\text{SAW},0}$ , they have a stable phase relation with respect to each other, provided both signal generators are locked to the same reference oscillator. The shown spectrum was phase-averaged over all of these phases. The dependence of the RF spectra on the phase between two SAW fields straining a QD will be discussed in the next sections. In addition to the  $(\pm 2, \pm 3, \pm 4, \pm 6, \dots)$  PSBs that have been observed in at least one the two other spectra and can be formed by the absorption/emission of  $\omega_{\text{SAW},1}$ -phonons (red) or  $\omega_{\text{SAW},2}$ -phonons (blue), sidebands at  $(\pm 1, \pm 5)$  occur. These sidebands can only be achieved by processes involving both  $\omega_{\text{SAW},1}$  and  $\omega_{\text{SAW},2}$ -phonons. Possible processes leading to these PSBs are depicted on the right side of figure 8.7(a). The  $(\pm 5)$  PSBs, for instance, can be formed by the absorption/emission of one  $\omega_{\text{SAW},1}$ -phonon and one  $\omega_{\text{SAW},2}$ -phonon each. Whereas the  $(\pm 1)$  sideband can be formed when the two phonon fields act in opposite directions, meaning a  $\omega_{\text{SAW},1}$ -phonon is emitted/absorbed and a  $\omega_{\text{SAW},2}$ -phonon is absorbed/emitted. These processes, involving one phonon of each SAW field, can be written as:

$$(\pm 1 \cdot \omega_{\text{SAW},0}) = (\mp \omega_{\text{SAW},1} \pm \omega_{\text{SAW},2}) = (\mp 2 \cdot \omega_{\text{SAW},0} \pm 3 \cdot \omega_{\text{SAW},0}) \quad (8.7)$$

$$(\pm 5 \cdot \omega_{\text{SAW},0}) = (\pm \omega_{\text{SAW},1} \pm \omega_{\text{SAW},2}) = (\pm 2 \cdot \omega_{\text{SAW},0} \pm 3 \cdot \omega_{\text{SAW},0}) \quad (8.8)$$

This can be generalised for processes involving  $m \cdot \omega_{\text{SAW},1}$ -phonons and  $n \cdot \omega_{\text{SAW},2}$ -phonons:

$$(m \cdot \omega_{\text{SAW},1} + n \cdot \omega_{\text{SAW},2}) = (2m + 3n)\omega_0, \quad m, n = 0, \pm 1, \pm 2, \dots \quad (8.9)$$

In this expression, the total number of phonons involved in a specific process is given by  $|m| + |n|$ . Taking those multiple phonons processes into account, there are in general different possibilities (combinations of  $n$  and  $m$ ) that lead to the same PSB. For example, the  $(\pm 7)$  PSB can either be achieved by a three-phonons-process ( $m = \pm 2, n = \pm 1$ ) or by a four-phonons-process ( $m = \mp 1, n = \pm 3$ ). The biggest difference between these two processes, apart from the number of involved phonons, is the relative direction in which the two phonon fields act. In the first case, both fields act in the same direction, meaning that both  $\omega_{\text{SAW},1}$ - and  $\omega_{\text{SAW},2}$ -phonons are either absorbed or emitted, whereas in the second case one kind of phonon is emitted, while the other is absorbed. Under certain circumstances, this can be used to enhance or suppress specific processes, as it will be shown in the following sections.

### 8.5.3. Phase-matched frequency mixing

As already mentioned in the previous section, the relative phase alignment between two phonon fields plays an important role for processes involving phonons of both of these fields. The most straight forward implementation of this was already considered in section 8.5.1,

where the phase between two counter propagating waves of identical frequency determines the degree of constructive or destructive interference at the position of the QD. This can be generalised to phonon fields of different frequencies. However, to visualize the influence of specific phase alignments in time-integrated measurements, the two phonon fields must have a recurring and stable phase relation, one is thus limited to integer ratios of the phonon frequencies. In other words, the two phonon fields must be mutually coherent. Although this is the case in the previous section (frequency ratio 2:3), a frequency ratio of 1:2 is considered first, meaning  $\omega_{\text{SAW},2} = 2 \cdot \omega_{\text{SAW},1}$ , as for this case the fundamental processes can be understood more easily.

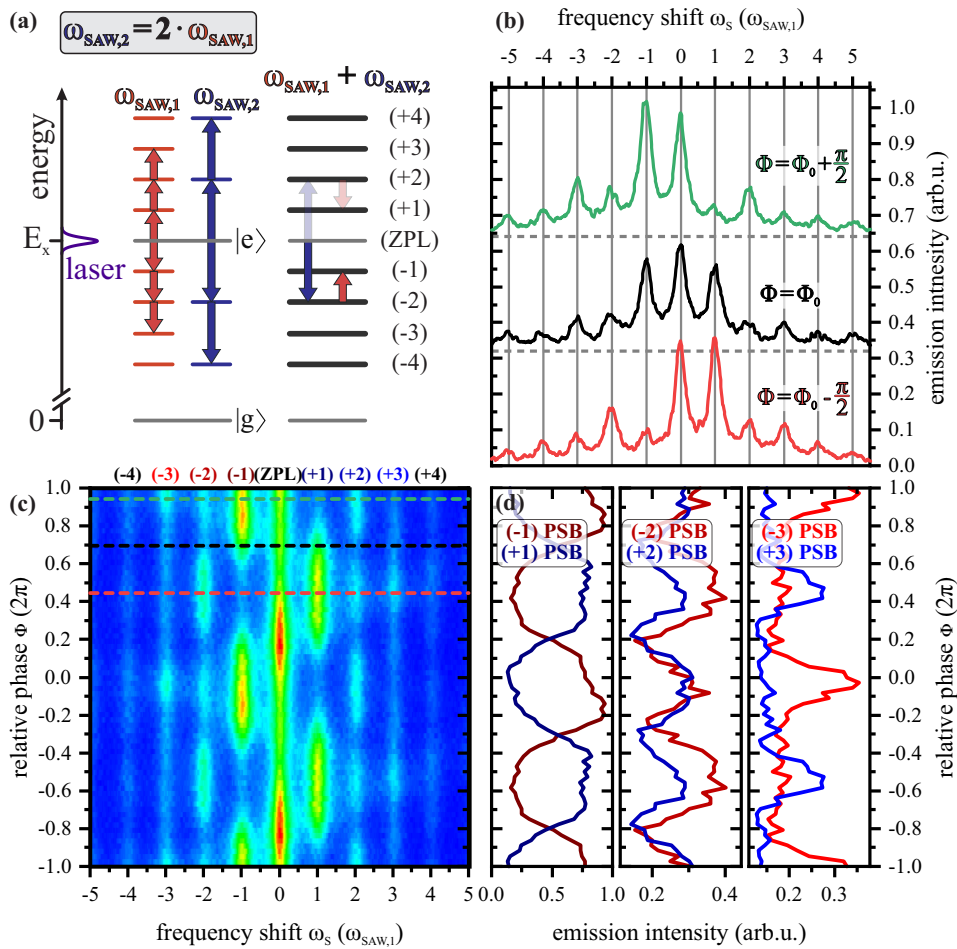


**Figure 8.8.:** (a) PSB alignment for the combination of two phonon fields  $\omega_{\text{SAW},1}$  and  $\omega_{\text{SAW},2}$  with a frequency ratio of 1:2. (b) RF spectra for different relative phases  $\Phi_0$ , revealing a strong dependence of the relative PSB intensities on  $\Phi$ . (c) False-colour representation of the RF spectra for a continuously tuned relative phase  $\Phi$ . (d) Sideband intensities for the  $(\pm 1)$ ,  $(\pm 2)$  and  $(\pm 3)$  PSBs.

The respective PSB alignment for this case is depicted in figure 8.8(a). The two frequency components  $\omega_{\text{SAW},1}$  and  $\omega_{\text{SAW},2}$  form equally spaced PSBs around the ZPL, whereas the  $\omega_{\text{SAW},2}$  sidebands are aligned with every second  $\omega_{\text{SAW},1}$  sideband. In contrast to previously considered case, here the combination of  $\omega_{\text{SAW},1}$ - and  $\omega_{\text{SAW},2}$ -phonons do not enable the formation of further PSBs that are only accessible by processes involving both kinds of phonons. However, combining both waves allows the creation of PSBs by additional multi-phonon processes, containing both  $\omega_{\text{SAW},1}$ - and  $\omega_{\text{SAW},2}$ -phonons. One of the simplest of these processes is depicted on the right hand side of figure 8.8(a), showing the "destructive" superposition of a  $\omega_{\text{SAW},1}$ - and a  $\omega_{\text{SAW},2}$ -phonon, leading to the formation of the  $(\pm 1)\omega_{\text{SAW},1}$ -sideband, depending on the direction of the respective processes.

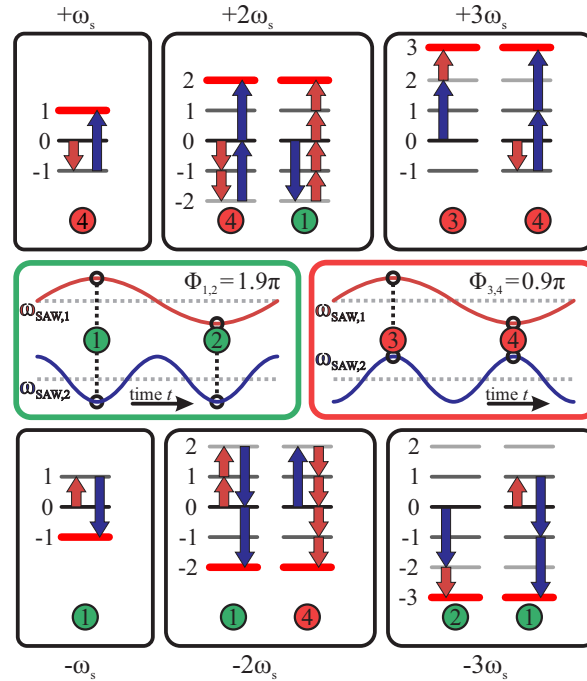
For the experimental implementation, SAW frequencies of  $\omega_{\text{SAW},1} = 2\pi \cdot 677.5 \text{ MHz}$  and  $\omega_{\text{SAW},2} = 2 \cdot \omega_{\text{SAW},1} = 2\pi \cdot 1355 \text{ MHz}$ , the second and third harmonic of the used split-5-2 transducer, have been chosen. The rf-signals were provided by two signal generators, coupled to a common reference oscillator and had amplitudes of  $P_{\text{rf},1} = 0 \text{ dBm}$  and  $P_{\text{rf},2} = 2 \text{ dBm}$ , respectively. Both signals were combined by a rf-power combiner before entering the cryostat and applied to the same IDT. The relative phase  $\Phi$  between the two rf-signals, and thus between the two phonon fields, was tuned by phase shifting the rf-output of the signal generator creating the higher frequency component.

Figure 8.8(b) shows three RF spectra for three particular phases  $\Phi$  which are shifted by  $\frac{\pi}{2}$  with respect to each other. The centre spectrum (black) looks like the well-known case, with equally spaced PSBs and symmetric intensities of the PSBs with respect to the ZPL. This drastically changes when the phase between the two SAWs is shifted by  $+\frac{\pi}{2}$  (top, green spectrum). Although the position of the PSBs remains the same, the intensity distribution becomes highly asymmetric. This becomes especially clear when looking at the  $(\pm 1)$  PSBs. While the emission of the  $(-1)$  sideband increases slightly, now exceeding the emission of the ZPL, the emission of the  $(+1)$  sideband is almost completely suppressed. Shifting the relative phase in the other direction, shown in the bottom (red) spectrum, the situation is reversed and the  $(-1)$  PSB is suppressed, while the  $(+1)$  PSB is enhanced.

To study this effect in more detail, the phase  $\Phi$  was tuned continuously over  $2\pi$  and the intensity of the scattered photons was measured as a function of  $\omega_S$ . The corresponding data is presented in a false-colour representation in figure 8.8(c), as a function of  $\Phi$  and  $\omega_S$ . There, the measured data is plotted twice so a relative phase range of  $4\pi$  is covered and thus the underlying processes can be seen more clearly. The phases of the previously discussed spectra are marked by the dashed lines with the respective colours. It can clearly be seen that the RF-signal, especially the intensities of individual sidebands, strongly depends on the relative phase  $\Phi$ , and that the overall intensity distribution oscillates with a periodicity of  $\Delta\Phi = 2\pi$ . Furthermore, it is noticeable that the intensity oscillations of a given negative sideband  $(-n)$  is identical to its positive counterpart  $(+1)$  but shifted by  $\pi$  in phase  $\Phi$ . Therefore, shifting the phase by  $\pi$  results in a spectrum that is mirrored

at the ZPL ( $I(\Phi = \Phi_0, \omega_S) = I(\Phi = \Phi_0 + \pi, -\omega_S)$ ). This becomes particularly evident when looking at the extracted sideband intensities as a function of phase  $\Phi$ , plotted in figure 8.8(d) for the  $(\pm 1)$ ,  $(\pm 2)$  and  $(\pm 3)$  PSBs. Both the  $(\pm 1)$  and the  $(\pm 3)$  sidebands exhibit one intensity maximum per  $2\pi$  period and the positive and negative sidebands are in-phase respectively. On the other hand, each sideband is in phase opposition to its respective counterpart with an opposite sign of the sideband index  $n$ . In contrast to the  $(\pm 1, \pm 3)$  sidebands, the  $(\pm 2)$  PSBs exhibit two maxima per  $2\pi$ . Upon closer inspection, one recognizes that these two maxima are not equivalent but differ in their phase widths. For the  $(+2)$  PSB, the maximum at  $\Phi = 0$  is wider compared to the ones at  $\Phi = \pm\pi$ , whereas for the  $(-2)$  PSB the situation is reversed.

To understand the appearance of the observed intensity oscillations as a function of the relative phase  $\Phi$  between the two phonon fields  $\omega_{\text{SAW},1}$  and  $\omega_{\text{SAW},2}$ , one has to consider any phonon process leading to a specific PSB. In the following, a simplified model is provided that vividly and qualitatively explains the emergence of the phase-dependent PSBs. The basis of this consideration are the findings of subsection 8.4 that the probability of emitting or absorbing a phonon oscillates in time with the frequency of the SAW, whereas the



**Figure 8.9.:** Schematic representation of the dominant multi-phonon processes involving both  $\omega_{\text{SAW},1}$ - and  $\omega_{\text{SAW},2}$ -phonons, for the first three blue (top panels) and red (bottom panels) PSBs. Numbers in the circles correspond to the relative alignments of the two phonon fields, shown in the centre panels, necessary for the respective process. As shown in the centre panels, two of these alignments each can be related to the relative phases  $\Phi_{1,2}$  (1, 2) and  $\Phi_{3,4}$  (3, 4).

maximum probabilities for emission and absorption are separated in time by  $T_{\text{SAW}}/2$ . For the case considered here, the absorption and emission of  $\omega_{\text{SAW},1}$ - and  $\omega_{\text{SAW},2}$ -phonons do not happen independently but depends on  $\Phi$ . This is depicted in the two central panels of figure 8.9 for two particular phases  $\Phi_{1,2}$  and  $\Phi_{3,4}$ . The absolute values for these two phases are chosen to match the respective phases in figure 8.8. The sinusoids indicate the probability of a phonon process as a function of time for the two different phonon fields. There, the positive deflections (above the dashed grey line) indicate the probability for phonon absorption and, correspondingly, negative deflections indicate the probability for phonon emission. What distinguishes these two phases is the fact that the extrema of the phonon emission/absorption probability for the two fields overlap at two-times within one SAW cycle (defined by the lower frequency  $\omega_{\text{SAW},1}$ ). Considering only the extrema of the two phonon fields, four different combinations, depending on the direction of the respective phonon processes, are possible. These four combinations can be separated in two groups of two where each group can be related to one of the two relative phase alignments pictured in the central panel of figure 8.9. These different combinations are labeled ①, ②, ③ and ④, respectively, where the colour indicates the phase, at which the combination occurs. The dominating phonon processes for the combinations are summarized in the following table, where an up arrow ( $\uparrow$ ) indicates phonon absorption and a down arrow ( $\downarrow$ ) phonon emission:

	$\omega_{\text{SAW},1}$	$\omega_{\text{SAW},2}$
①	$\uparrow$	$\downarrow$
②	$\downarrow$	$\downarrow$
③	$\uparrow$	$\uparrow$
④	$\downarrow$	$\uparrow$

Each multi-phonon process, including both  $\omega_{\text{SAW},1}$ - and  $\omega_{\text{SAW},2}$ -phonons, which leads to a specific PSB, can now be related to the specific alignments (①-④) of the two phonon fields and thus to a specific phase  $\Phi$  between the fields. The dominant multi-phonon processes, meaning the ones involving the fewest number of phonons, are depicted for the first three blue and red sidebands in the top and bottom panels of figure 8.9. In order to reach one of the ( $\pm 1$ ) sidebands, the two phonon fields must interfere destructively, meaning one type of phonon is emitted, while the other is absorbed. If a  $\omega_{\text{SAW},1}$ -phonon is emitted and a  $\omega_{\text{SAW},2}$ -phonon absorbed, the (+1) sideband is formed. The necessary alignment is given for ④. For the ( $-1$ ) PSB, both phonon processes must switch sign and are thus must likely to happen at ① and the ( $-1$ ) PSB is thus shifted by  $\pi$  with respect to the (+1) PSB. This explains the  $2\pi$  periodic anti-correlated intensity oscillations for the ( $\pm 1$ ) PSBs. For the ( $\pm 2$ ) PSBs, two processes with a comparable number of involved phonons, and thus probability, can be identified. For both of the sidebands, one of these processes can be related to one of the two phases  $\Phi_{1,2}$  and  $\Phi_{3,4}$  which leads to the observed two intensity maxima per SAW cycle for the ( $\pm 2$ ) PSBs. Furthermore, the process involving a higher

number of  $\omega_{\text{SAW},2}$ -phonons (● for (+2) and ● for (-2)) is expected to be more sensitive to the relative phase  $\Phi$ , since the probability oscillates twice as fast in time. For these cases, a narrower intensity peak is expected for ( $\pm 2$ ) that correlates with the peak for ( $\pm 1$ ) sideband. This is nicely confirmed by the experimental data presented in figure 8.8(d). Finally, for the ( $\pm 3$ ) sidebands, two multi-phonon-processes with similar probability can be found. However, both processes leading to one of the PSBs can be related to the same phase,  $\Phi_{3,4}$  for (+3) and  $\Phi_{1,2}$  for (-3). This results in one maximum per period and the observed correlation between the maxima for the (+1) and (+3) PSBs and between the maxima for the (-1) and (-3) PSBs.

Although this simple consideration can explain the most important characteristics of the phase dependent intensity oscillations presented in figure 8.8(c), it may only be considered as an approximation. The strongest simplification lies in the fact that only fixed points in time and thus static alignments of the phonon fields are considered. In reality, multi-phonon processes must not happen simultaneously but can be distributed over the radiative lifetime of the QD. The temporal evolution of the phonon fields must therefore be taken into account. This leads to further possible processes by which a given PSB can be formed, especially loop processes, where the same kind of phonon is absorbed and emitted within one radiative decay time.

#### 8.5.4. Detuned SAW frequency mixing

In this section, the behaviour of the PSBs for slight deviations from the strict criteria  $\omega_{\text{SAW},2} = 2 \cdot \omega_{\text{SAW},1}$  shall be investigated. Therefore, a small frequency detuning  $\Delta_{\text{SAW}}$  is deliberately added to the higher SAW frequency component  $\omega_{\text{SAW},2}$ :

$$\omega_{\text{SAW},2} = 2 \cdot \omega_{\text{SAW},1} + \Delta_{\text{SAW}} \quad (8.10)$$

Small in this context means considerably smaller than the linewidth of the resonant laser ( $\approx 100$  kHz) and thus smaller than the linewidth of the PSBs. The resulting PSB alignments are depicted in figure 8.10(a). For such small detunings, the two frequencies can still be considered to fulfil the strict condition  $\omega_{\text{SAW},2} = 2 \cdot \omega_{\text{SAW},1}$  but with a time depended phase  $\Phi(t) = \Delta_{\text{SAW}} \cdot t$ :

$$\sin(\omega_{\text{SAW},2}t) = \sin((2 \cdot \omega_{\text{SAW},1} + \Delta_{\text{SAW}})t) = \sin(2 \cdot \omega_{\text{SAW},1}t + \underbrace{\Delta_{\text{SAW}}t}_{\Phi(t)}) \quad (8.11)$$

Therefore, the relative phase between the two oscillations  $\omega_{\text{SAW},1}$  and  $\omega_{\text{SAW},2}$  changes linearly by  $2\pi$  within a period of  $T_{\Delta} = \frac{2\pi}{\Delta_{\text{SAW}}}$ .

Measured RF spectra for a detuning of  $\Delta_{\text{SAW}} = 2\pi \cdot 0.1$  mHz as a function of time are shown in figure 8.10(b). The two phonon fields are excited with a chirped transducer and have frequencies of  $\omega_{\text{SAW},1} = 2\pi \cdot 650$  MHz and  $\omega_{\text{SAW},2} = 2\pi \cdot 1.3$  GHz +  $\Delta_{\text{SAW}}$ . The rf-amplitudes

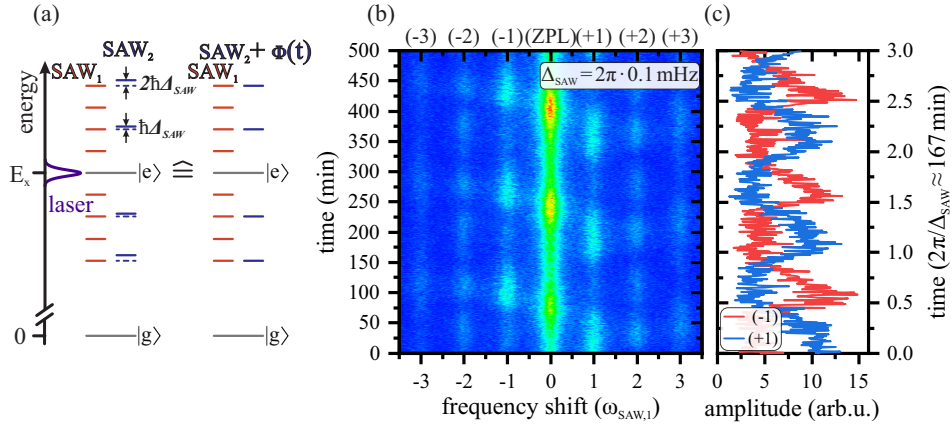


**Figure 8.10.:** (a) PSB alignment for small detunings  $\Delta_{\text{SAW}}$  from the criteria  $\omega_{\text{SAW},2} = 2 \cdot \omega_{\text{SAW},1}$  leads to a phase linearly depending on time  $\Phi(t)$ . (b) Measured RF spectra for a detuning of  $\Delta_{\text{SAW}} = 2\pi \cdot 0.1$  mHz as a function of time, showing clear intensity oscillations with a period of  $T_{\Delta} = \frac{2\pi}{\Delta_{\text{SAW}}}$ . (c) Extracted intensities for the  $(\pm 1)$  sidebands exhibit anti-correlated intensity oscillations with period  $T_{\Delta}$ .

were set to  $P_{\text{rf},1} = 12$  dBm and  $P_{\text{rf},2} = 17$  dBm. The detuning  $\Delta_{\text{SAW}}$  results in period of  $T_{\Delta} = 10^4 \text{ s} \approx 167$  min for the phase modulation. This period is large compared to the integration time of a single RF spectrum, which is in this case 1 min, making it possible to fully resolve the detuning induced dynamics in the time domain. It can clearly be seen that the intensity of the PSBs oscillates over time with an overall periodicity consistent with  $\frac{2\pi}{\Delta_{\text{SAW}}}$ . Within the time interval of 500 min ( $\approx 8$  h 20 min) covered by the experiment, three full oscillations can be observed. The underlying period becomes particularly clear when the intensity of the  $(\pm 1)$  sidebands is considered. The extracted PSB amplitudes are plotted in figure 8.10(c) as a function of time in units of  $T_{\Delta}$ . The two sidebands show pronounced anti-correlated intensity oscillations with the period  $T_{\Delta}$ . These oscillations are equivalent to the ones observed as a function of the relative phase  $\Phi_0$  for vanishing detuning  $\Delta_{\text{SAW}} = 0$ , shown in the previous section. This confirms, that a small detuning  $\Delta_{\text{SAW}}$  can be described by a linearly changing phase  $\Phi(t)$ .

Additional experimental data for a detuning of  $\Delta_{\text{SAW}} = 50 \mu\text{Hz}$ , and thus a beating period of  $T_{\Delta} = 2 \cdot 10^4 \text{ s} \approx 333$  min, is shown in Appendix B.3.

The fact that the intensity oscillations induced by the detuning  $\Delta_{\text{SAW}}$  can be observed over such long time intervals, without any external intervention, proves the high coherence of the two phonon fields exceeding several hours. This outstanding coherence is achieved by locking both of the used signal generators (*Stanford Research Systems*, SG384/SG382) to a common timebase, resulting in a phase-coherence between the two rf-signals used to excite the SAWs. The experimental data presented here confirms that this phase-coherence is transferred from the electrical signal to the mechanical SAW. Therefore, the coherence of the phonon fields is not limited by the sample itself but fully determined by the capabilities

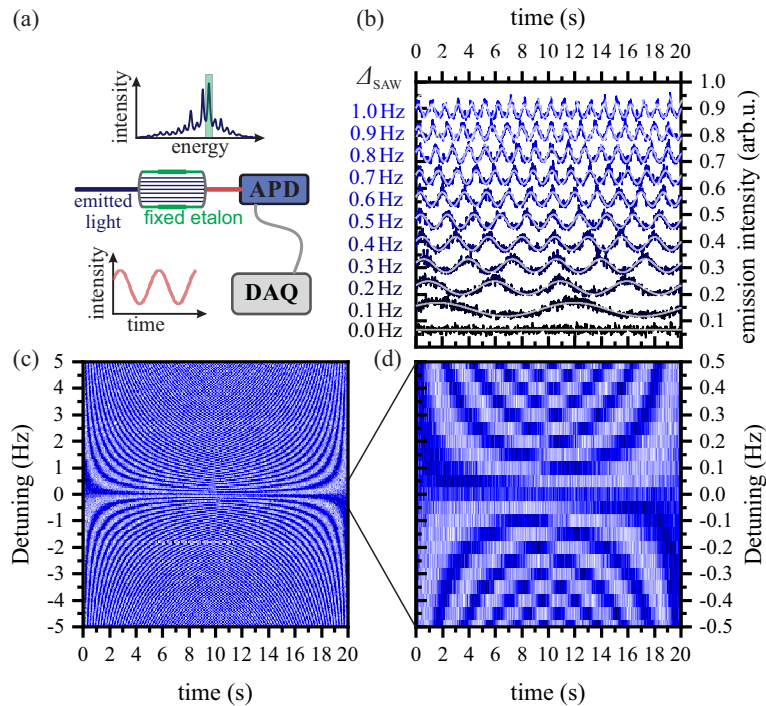


**Figure 8.11.:** (a) Experimental setup to monitor PSB oscillations in real time. The etalon is tuned to the (+1) PSB and the intensity of the sideband is detected by an APD and recorded by a data acquisition system. (b) (+1) sideband intensity as a function of time for detunings  $\Delta_{\text{SAW}}$  varying from 0 to 1 Hz in steps of 0.1 Hz. Transparent lines are best fits with a sine function. For clarity, the traces have a constant offset. (c) False colour representation of the RF intensity for the (+1) PSB as a function of time and  $\Delta_{\text{SAW}}$ . (d) Zoom-in on the detuning range  $\pm 0.5$  Hz.

of the signal generators which can maintain the phase coherence between the two signals for an indefinite period of time.

To evaluate the stability of the detuned non-linear frequency mixing scheme, the detuning  $\Delta_{\text{SAW}}/2\pi$  is tuned from  $-5$  Hz to  $5$  Hz in steps of  $0.05$  Hz. Since the beating periods  $T_{\Delta}$  for these detunings are smaller than typical integration times of a RF spectrum, it is not possible to observe the temporal evolution of all PSBs simultaneously. Instead, only the emission of a single PSB is considered as a function of time. The corresponding experimental setup is shown in figure 8.11(a). The collected RF signal is filtered by the etalon, whose transmission frequency is tuned to the (+1) PSB. The filtered emission of this sideband is then detected by an APD and recorded in real-time by a DAQ system. The measurements presented here were carried out continuously. This means that the intensity of (+1) sideband was recorded continuously and the detuning  $\Delta_{\text{SAW}}/2\pi$  was changed in discrete steps every 20 s. There was no further synchronisation between the detection and the SAW excitation.

In figure 8.11(b), the temporal evolutions of the (+1) PSB intensities are plotted as a

function of time for time intervals of 20 s. For each curve, the detuning  $\Delta_{\text{SAW}}$  increases from 0 (bottom) in discrete steps of 0.1 Hz to 1 Hz (top). While, for zero detuning, the intensity stays constant over time, clear modulations with a frequency of  $\Delta_{\text{SAW}}$  can be seen for the other curves. This means that the number of oscillations in the measuring range of 20 s increases by two for each curve. This is also confirmed by the sinusoidal fits, shown as transparent lines. The (+1) PSB intensity for detunings from  $-5$  Hz to  $5$  Hz is plotted in figure 8.11(c) in a false colour representation as a function of time. Again oscillations of the sideband intensities with a period of  $|2\pi/\Delta_{\text{SAW}}|$  defined by the detuning are observed. A zoom-in to the intensity pattern, covering the detuning range  $\pm 0.5$  Hz, is shown in figure 8.11(d). For all detunings  $\Delta_{\text{SAW}}$ , an integer number of intensity oscillations can be observed within the measurement range of 20 s, since the values for the detunings were chosen to fulfil  $\Delta_{\text{SAW}} = \frac{n}{20\text{s}} = n \cdot 0.05$  Hz. Furthermore, all intensity curves start with a constant phase, that only shifts by  $\pi$  going from negative to positive detunings. This means that switching the detuning maintains the phase of the intensity oscillations and thus the phase relation between the two phonon fields oscillating at  $\omega_{\text{SAW},1} = 2\pi \cdot 0.65$  GHz and  $\omega_{\text{SAW},2} = 2\pi \cdot 1.3$  GHz. This is remarkable, as the detection is not synchronised to the tuning of  $\Delta_{\text{SAW}}$  and shows again the high stability that can be achieved by this technique. As a result of the phase-continuous tuning of  $\Delta_{\text{SAW}}$ , the intensity patterns, shown in figure 8.11(c) and (d), are point symmetric with respect to the origin. Although the precise control over the phase and frequencies of the two phonon fields can be attributed to the capabilities of the used signal generators, the measurements show that these properties are transferred from electrical to the mechanical domain.

### 8.5.5. Further frequency ratios

The procedure introduced here for switching the emission between certain PSBs by varying the phase relation between two applied phonon fields is not limited to a frequency ratio of  $\frac{\omega_{\text{SAW},1}}{\omega_{\text{SAW},2}} = \frac{1}{2}$ , which was used so far. The method in general works for any two frequencies that have a stable phase relation to each other. This is the case for any two frequencies being a multiple integer  $m, n$  of a common frequency  $\omega_0$ :

$$\omega_{\text{SAW},1} = m \cdot \omega_0 \quad \omega_{\text{SAW},2} = n \cdot \omega_0 \quad m, n = 1, 2, 3, \dots \quad (8.12)$$

Phase dependent measurements for frequency ratios of  $\frac{\omega_{\text{SAW},1}}{\omega_{\text{SAW},2}} = \frac{2}{3}$  ( $m = 2, n = 3$ ) and  $\frac{\omega_{\text{SAW},1}}{\omega_{\text{SAW},2}} = \frac{3}{4}$  ( $m = 3, n = 4$ ) are shown in figure 8.12 (a) and (b) respectively. The phase averaged emission for the  $\frac{2}{3}$  frequency ratio was already presented in figure 8.7. The important SAW parameters for these two experiments are summarized in the following table:

figure 8.12	$m$	$n$	$\omega_0/2\pi$	$\omega_1/2\pi$	$\omega_2/2\pi$	$P_{\text{rf},1}$	$P_{\text{rf},2}$
(a)	2	3	460.00 MHz	920.00 MHz	1380 MHz	2 dBm	14 dBm
(b)	3	4	338.75 MHz	1016.25 MHz	1355 MHz	-2 dBm	2 dBm

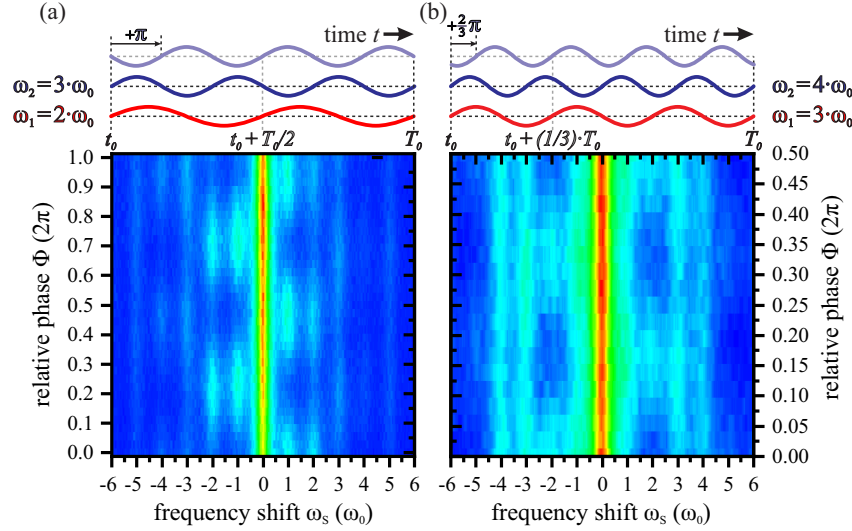


**Figure 8.12.:** Phase dependence of the RF of a QD, strained by two SAWs with a frequency ratio of  $\frac{\omega_{\text{SAW},1}}{\omega_{\text{SAW},2}} = \frac{2}{3}$  (a) and  $\frac{\omega_{\text{SAW},1}}{\omega_{\text{SAW},2}} = \frac{3}{4}$  (b). The top panel shows the respective alignments of the two phonon fields as a function of time. The light blue lines illustrate the periodicity of the RF emission. For the respective phase shifts, the same relative alignment as for the darkblue line is achieved but shifted in time.

To excite the two SAWs for measurement (a), two chirped IDTs, one for each frequency, were used, whereas for measurement (b) the third and fourth harmonic of a single non-chirped split-5-2 transducer was used. For both measurements, the relative phase  $\Phi$  was tuned via the signal generator delivering the higher frequency  $\omega_2$ .

Looking at the measurements presented in figure 8.12, for both frequency ratios, pronounced sideband intensity oscillations as a function of  $\Phi$  can be observed. However, they clearly differ from each other and from the oscillations observed for a frequency ratio of  $\frac{1}{2}$ . What remains the same is that, in both cases, the oscillations of negative and positive PSBs are clearly anti-correlated. For measurement (a), a correlated oscillation of the  $(\pm 1)$  and  $(\pm 2)$  sidebands can be observed, which is anti-correlated to the intensities of the  $(\pm 3)$  and  $(\pm 4)$  PSBs. In contrast to that, for measurement (b), a clear oscillation can only be observed for the  $(\pm 2)$  sidebands. The  $(\pm 1)$  PSBs cannot be clearly resolved but an asymmetry in the linewidth of the Rayleigh line (ZPL) seems to indicate an oscillation of the  $(\pm 1)$ , that is correlated to the  $(\pm 2)$  sidebands.

A qualitative description of the underlying processes leading to the intensity oscillations of certain PSBs on basis of the relative phonon field alignments, like it was done in figure 8.9 for a frequency ratio of  $\frac{1}{2}$ , is here no longer possible. The reason for that can be seen in

the two top panels of figure 8.12, where one possible alignment between the two respective phonon fields over one period is shown. The total period of the overall waveform, meaning the combination of the two fields  $\omega_{\text{SAW},1}$  and  $\omega_{\text{SAW},2}$ , is given by  $T_0 = \frac{2\pi}{\omega_0}$ . This in turn means that the number of oscillations per period  $T_0$  for the two phonon fields  $\omega_{\text{SAW},1}$  and  $\omega_{\text{SAW},2}$  are given by  $m$  and  $n$  (see equation 8.12) respectively. For increasing numbers  $m$  and  $n$ , this also means an increased number of possible phonon processes that can occur within one period for a given phase shift  $\Phi$ . Furthermore, for any frequency relations other than  $\frac{1}{2}$ , there exists no phase  $\Phi$  at which the extrema of the  $\omega_{\text{SAW},1}$  are correlated with the extrema of  $\omega_{\text{SAW},2}$ . In summary, this means that all processes occurring for a given phase shift  $\Phi$  can no longer be narrowed down to the four different fundamental phonon field alignments ( $\uparrow\uparrow, \downarrow\downarrow, \uparrow\downarrow, \downarrow\uparrow$ ), since these are no longer well separated in time and/or phase.

Another difference for the measurements shown in figure 8.12 concerns the overall periodicity of the intensity modulations. While for a frequency ratio of  $\frac{1}{2}$  the RF spectra showed a periodicity of  $2\pi$ , for  $\frac{2}{3}$  a  $\pi$ - and for  $\frac{3}{5}$  a  $\frac{2\pi}{3}$ -periodicity is observed. The origin for that is depicted in the top panels of figure 8.12. Although the combination of the two frequencies  $\omega_{\text{SAW},1}$  and  $\omega_{\text{SAW},2}$  is  $2\pi$  periodic in  $\Phi$ , for measurement (a) a phase shift of  $\pi$  leads to the same relative alignment of the two fields, only shifted in time by  $\frac{T_0}{2}$ . For measurement (b), a phase shift of  $\frac{3}{4}\pi$  leads to the same relative alignment of the two waveforms but shifted in time by  $\frac{1}{3}T_0$ . Since the measurements are time-integrated, these time-shifts do not affect the results of the measurement and a periodicity of  $\pi$  and  $\frac{2\pi}{3}$  for the measurements (a) and (b), respectively, are observed in the experimental data.

## 8.6. Conclusion of SAW driven resonance fluorescence

Photons of superior properties can be obtained by resonance fluorescence on single two-level systems in the limit of low Rabi frequencies. The bandwidth and coherence of the emitted single photons is fully tailored by the exciting laser. In this regime, inherent issues of solid state systems like spectral diffusion may alter the probability of resonant scattering but, due to the absence of exciton interaction with the environment, do not cause decoherence of the emitted photons. Furthermore, the stream of single photons that are emitted from a resonantly driven QD is phase-correlated with the driving laser field and thus the single photons are phase-correlated with each other. Therefore, using the same laser source to excite multiple QDs yields multiple single sources that are phase-correlated with each other [101].

Here, the concept of RF in the low Rabi limit was extended by a periodic frequency modulation of the excitonic transition. It was shown that the coherent optomechanical interaction between a QD and a SAW mixes optical frequencies at  $\omega_{\text{opt}}/2\pi \approx 330$  THz and

acoustic frequencies of phonons at  $\omega_{\text{SAW}}/2\pi \approx 1$  GHz. This results in the formation of phononic sidebands in the scattered light spectrum with a splitting of precisely  $\omega_{\text{SAW}}$ . The shape of this frequency comb depends on the modulation amplitude and frequency and thus on the properties of the driving SAW. Moving away from strictly resonant excitation by introducing a detuning  $\Delta_{\text{opt}}$  between laser and optical transition enables parametric transduction of energy between the optical and acoustic domains.

Furthermore, the non-linear interaction between different SAW fields leads to a mixing of both phonon fields and thus to the generation of sum and difference frequencies in the scattered light spectrum. For two mutually coherent SAW fields with  $\omega_{\text{SAW},2} = 2 \cdot \omega_{\text{SAW},1}$ , this enables the creation of a highly stable frequency comb, where the intensity of certain PSBs can be tuned by the relative phase relation between both phonon fields. When a small detuning between both phonon fields is deliberately introduced, intensity oscillations of the PSBs can be observed in the time domain. This was observed for detunings down to  $\Delta_{\text{SAW}} = 50$   $\mu\text{Hz}$  and over a time range exceeding eight hours, proving the high stability of this technique.

Higher modulation amplitudes can be achieved by transferring semiconductor QDs on substrates exhibiting a higher electromechanical coupling coefficient, like  $\text{LiNbO}_3$  [33,80,119]. Alternatively, the QDs can be embedded in photonic and/or phononic resonators to drastically enhance the interaction between the excitonic state of the QD and the light and/or phonon fields. Choosing a suitable platform even allows to achieve co-localised optical and mechanical resonator modes and thus the realisation of an optomechanical system exhibiting strong coupling between the optical and mechanical domain. Such systems have the additional advantage that they can directly be implemented on a GaAs substrate [120]. Such tailored photonic and phononic systems that are compatible with GaAs and the direct embedding of QDs are the scope the next chapter.



## 9. Quantum dots in tailored photonic and phononic environments

So far, mostly homogeneous samples have been considered, allowing a free propagation of both photons and phonons within the sample. However, a suitable structuring of a substrate can influence both the propagation of photons and phonons in the substrate. This can be realised by introducing a periodic variation of the refractive index  $n$  or the elastic parameters on the length scale of the respective photonic or phononic wavelengths. Such structures are depicted as photonic/phononic crystals and allow for the manipulation of the photonic and/or phononic band structure of a material and both photonic and phononic bandgaps can be realised. These structures are particularly interesting as their local phononic and photonic properties can be adjusted by locally changing the crystal structure. The introduction of a line defect, for instance, creates a waveguide and enables the guiding of photons and phonons on a chip. In contrast, a point defect can create a cavity that confines photons or phonons within a small volume, thus enabling a strong interaction between a quantum emitter placed in such a resonator and the confined photons or phonons.

In the first section of this chapter, a weakly coupled system consisting of a QD and a photonic cavity and the possibility to use SAWs to dynamically tune this system is considered. This dynamical spectral modulation influences the coupling of a cavity and a QD and thus the optical decay properties of the QD, enabling the realisation of a triggered single photon source. The photonic crystals used in these experiments were fabricated by Thorsten Reichert in the research group of Michael Kaniber and Jonathan Finley at the Walter Schottky Institut (WSI, TU Munich). IDTs were fabricated by Stephan Kapfinger at Augsburg University and the experiments were performed in close cooperation with S. Kapfinger. The presented experimental results were published in [83].

The second section gives an brief introduction on the emerging field of optomechanical crystals, where the focus lies in the mechanical properties of these crystals. The possibility to build such structures on GaAs and thus on a substrate in which QDs can be incorporated is shown by finite element simulations. Finally, first implementations of phononic crystals on a sample containing InGaAs-QDs are presented.

## 9.1. Photonic crystals nanocavity

A photonic crystal is created when the refractive index  $n$  varies periodically along one or more spatial dimensions. Along these directions, light is partially reflected at each interface and the resulting interference influences the propagation of light. Comparable to the electronic band-structure, which is caused by a periodic atom lattice and restricts the movement of charge carriers, the periodic variation of the refractive index results in the formation of a photonic bandgap, restricting the propagation of photons.

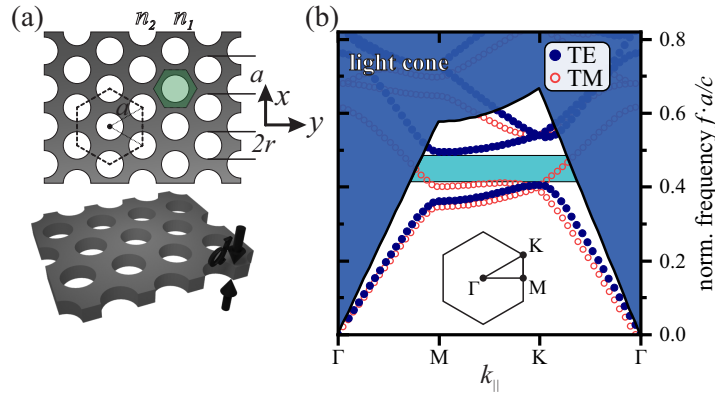


**Figure 9.1.:** (a) Schematic structure of a photonic crystal membrane (PCM). The PCM consists of triangular array of air holes with radius  $r$  and a lattice constant  $a$  in a membrane of thickness  $d$ . (b) Calculated photonic bandstructure for the structure presented in (a) with a hole radius of  $r = 0.4 \cdot a$ . A clear photonic bandgap can be seen for TE modes.

A schematic of the photonic crystal design used in this work is depicted in figure 9.1(a). It consists of a triangular array of cylinders with refractive index  $n_2$  oriented along the  $z$ -direction (perpendicular to the drawing plane) in a matrix material of refractive index  $n_1$ . The simplest realisation of such an array on a nano-scale is the drilling of holes in an existing material, in our case GaAs. The periodic variation of the refractive index between GaAs ( $n_1 \approx 3.6$ ) and the air holes ( $n_2 = 1$ ) results in the formation of a photonic band-structure for light with a non-zero wave vector in the  $xy$ -plane. Since there is no periodic variation of the refractive index in the  $z$ -direction, there is also no influence on the propagation of light in this direction. Introducing a variation in the  $z$ -direction, and thus creating a three dimensional (3D) photonic crystal, is in principle possible but cannot be realised with planar fabrication techniques [121, 122]. To achieve a full three dimensional confinement, the 2D photonic crystal is fabricated in a thin membrane, thus taking advantage of total internal reflection to realise a confinement in the  $z$ -direction. This confinement is retained only up to a frequency of  $\omega = ck_{||}$ , referred to as the light line. For higher frequencies  $\omega > ck_{||}$ , defining the so-called light cone, the light is no longer confined to the membrane, as it can couple to extended states propagating in air/vacuum.

The photonic band-structure of such a system can be determined numerically by the use of the finite-difference time domain (FDTD) method. The in-plane band-structure of a triangular array of air-holes in GaAs is shown in figure 9.1(b) and has been simulated using a commercial FDTD simulation software (*Lumerical*, FDTD). Below the light cone, indicated by the blue shaded area, several bands can be identified. Due to the mirror symmetry with respect to the  $x$ - $y$ -plane these bands can be divided into two distinct polarisations [123]. While for transverse electric (TE) bands the electric field is parallel and the magnetic field perpendicular to the  $xy$ -plane, for transverse magnetic (TM) it is the other way around, with the electric field being perpendicular and the magnetic field being parallel with respect to the  $xy$ -plane. Since solid state emitters like QDs in general emit TE polarised light, only the respective bands have to be considered here. For these bands, the band structure shows a photonic bandgap, indicated by the cyan region in figure 9.1(b). This means that the propagation of TE polarised light with frequencies lying in the bandgap is prohibited.

By introducing a defect in the photonic crystal array, energetic states can be created within the photonic bandgap. Such defects can confine photons within a small localised volume and are referred to as photonic cavities. One of the most common defects is the so-called L3-cavity, as it was the first design for which  $Q$ -factors exceeding  $10^4$  could be realised experimentally. The structure of a L3-cavity is shown in figure 9.2(a). It is implemented

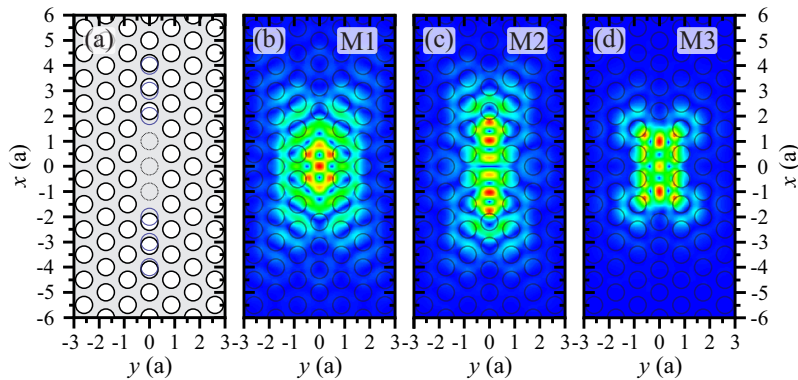


**Figure 9.2.:** (a) Structure of a L3 cavity created by omitting three holes in a row. To achieve higher  $Q$ -factor the three adjacent holes to the cavity are shifted away from the cavity by  $0.2 \cdot a$ ,  $0.15 \cdot a$  and  $0.1 \cdot a$ , respectively. (b-d) Electric mode profile  $|E|$  for the first three modes that are symmetric to the centre plane of the cavity, denoted M1 (b), M2 (c) and M3 (d). For the M1 mode, a pronounced anti-node of the electrical field can be observed at the centre of the cavity.

by omitting three holes of the photonic crystal in a row and shifting the holes at both ends of the so created cavity outwards to achieve a smoother confinement and thus lower losses. Figure 9.2(b-d) show the magnitude of the electrical field  $|E|$  at the centre of the membrane ( $z = 0$ ) for the fundamental mode of the cavity, denoted M1 and two higher orders, denoted M2 and M3 respectively. These mode profiles are obtained by FDTD

simulations and are in good agreement with the mode profiles reported in literature [124]. For most experiments in cavity quantum electrodynamics (cQED), as well as in this work, only the M1 mode is considered, as it exhibits an anti-node of the electric field at the centre of the cavity and has the highest  $Q$ -factor.

The photonic crystals which were considered in the following experiments were fabricated on a membrane containing a single layer of InAs-QDs, thus the interaction between a quantum emitter and the cavity can be investigated. A short summary of the respective fabrication process is presented in appendix C.1 and in reference [125].

The interaction between a QD transition and a cavity mode can be quantified by the coupling rate, depending on the alignment of the QD's transition dipole moment with respect to the cavity mode profile  $g_0$  [126]. Depending on the strength of the coupling rate  $g_0$ , two regimes can be distinguished. If the coupling rate is larger compared to the non-resonant decay rates of the emitter and the cavity, the system is in the strong coupling regime. On the other hand, if the coupling rate is smaller, the system is in the weak coupling regime. The coupling strength between a QD and a cavity depends, among other things, on the relative alignment of the two systems. The best coupling of an emitter to the M1 mode is for example achieved when the emitter is located in the centre of the cavity, thus at the antinode of the electric field. To enhance the probability of realising a strongly coupled QD-cavity system, the cavities can be aligned with respect to the already grown QDs, thus ensuring the presence of a QD at the anti-node of the cavity mode. This can be done by mapping the position of individual QDs by atomic force microscopy (AFM) [29] or by photoluminescence spectroscopy [127] and align the photonic cavities accordingly.

In the experiments presented here, however, only the weak coupling regime is considered. A QD, weakly coupled to a cavity, can either be in or out of spectral resonance with the cavity, which strongly affects the optical properties of the emitter. For an emitter being in resonance with a cavity resonance, the enhanced optical field results in an increase of the optical decay rate of the emitter. On the other hand, for an emitter being off resonance, the suppressed optical field also leads to the reduction of the decay rate. This effect is known as the Purcell effect [128] and its strength can be quantified by the Purcell-factor  $F_P$ :

$$F_P = \frac{\tau_{\text{free}}}{\tau_{\text{cavity}}} \quad (9.1)$$

Here,  $\tau_{\text{free}}$  and  $\tau_{\text{cavity}}$  denotes the spontaneous optical decay time of the QD in an isotropic optical medium and in the cavity, respectively. For  $F_P > 1$ , the decay time  $\tau$  of the emitter is reduced and, therefore, the decay rate is increased by the cavity. In this regime, the emission of the emitter is denoted as Purcell enhanced. On the contrast to that, for  $F_P < 1$ , the decay time  $\tau$  is increased by the cavity, meaning the emitter is Purcell suppressed. Under the assumption of a single mode cavity and using Fermi's Golden rule the Purcell

factor can be determined to be [126]:

$$F_P = \frac{3Q (\lambda/n)^3}{4\pi^2 V_0} \cdot \underbrace{\left( \frac{|\vec{p} \cdot \vec{\mathcal{E}}|}{|\vec{p}| \cdot |\vec{\mathcal{E}}|} \right)^2}_{\zeta^2} \cdot \frac{\delta E_{\text{cavity}}^2}{4(E_{\text{QD}} - E_{\text{cavity}})^2 + \delta E_{\text{cavity}}^2} \quad (9.2)$$

It depends on the cavity's quality factor  $Q = E_{\text{cavity}}/\delta E_{\text{cavity}}$  and its mode volume in units of cubic optical wavelengths  $V_0/(\lambda/n)^3$ . Furthermore,  $F_P$  depends on the normalized dipole orientation  $\zeta$  between the transition dipole of the cavity  $\vec{p}$  and of the emitter  $\vec{\mathcal{E}}$  and the detuning of the emission energies of the emitter  $E_{\text{QD}}$  and cavity  $E_{\text{cavity}}$ :

$$\Delta E_{\text{QD-cavity}} = E_{\text{QD}} - E_{\text{cavity}} \quad (9.3)$$

Since the quality factor  $Q$ , the mode volume  $V_0$  and dipole orientation  $\zeta$  depend on the structure of the emitter-cavity system, they can hardly be influenced, once the system has been fabricated. Thus, in order to influence the Purcell factor  $F_P$ , the spectral detuning  $\Delta E_{\text{QD-cavity}}$  between QD and cavity will be tuned in the following experiments.

The tuning of  $\Delta E_{\text{QD-cavity}}$  has been realised by two different approaches. First of all static temperature tuning is used to tune the QD and the cavity into or close to resonance and then dynamical tuning by a SAW is used to tune  $\Delta E_{\text{QD-cavity}}$  on a fast timescale.

### 9.1.1. Static temperature tuning

When fabricating a cavity-QD system, both the cavity and QD emission energies are subject to statistical variations. Therefore, a mechanism is needed which makes it possible to spectrally tune the QD and the cavity into resonance. The requirements for such a tuning mechanism are a precise tunability and a large tuning range. To tune the resonance frequency of a cavity, digital chemical wet etching [129] can be used, allowing for a large tuning range but being slow and especially non reversible. An alternative approach is the deposition of molecular layers [130], which is still a slow but reversible mechanism. In this work, static tuning is realised by changing the temperature of the sample, influencing both the cavity and the QD emission but at different rates [131] and thus allowing to influence the cavity-QD detuning  $\Delta E_{\text{QD-cavity}}$ .

For the latter experiments, the dynamic acoustic fields of a SAW are used to dynamically tune the QD-cavity system on a fast timescale. For this tuning, rather high acoustic powers are needed, resulting in the introduction of heat into the sample, which is generated by the conversion of electrical energy to mechanical energy at the IDT. This heat input can precisely be controlled by tuning the duty cycle of a pulsed SAW. Since, at first, only the quasi-static influence of the temperature and not the dynamic influence of the SAW is of interest, for the experiments presented in this section, an IDT was used, whose sound path

does not cross the investigated photonic cavity. While the rf-power  $P_{\text{rf}} = 25$  dBm and the length of the SAW pulses  $T_{\text{mod,SAW}} = 1$   $\mu\text{s}$  was kept constant, the modulation rate  $T_{\text{mod}}^{-1}$  and thus the duty cycle  $T_{\text{mod,SAW}}/T_{\text{mod}}$  was increased to increase the temperature of the sample. Details on the modulated SAW excitation were shown in section 5.1 (especially in figure 5.3). Time-integrated emission spectra as a function of the SAW duty cycle (temperature)

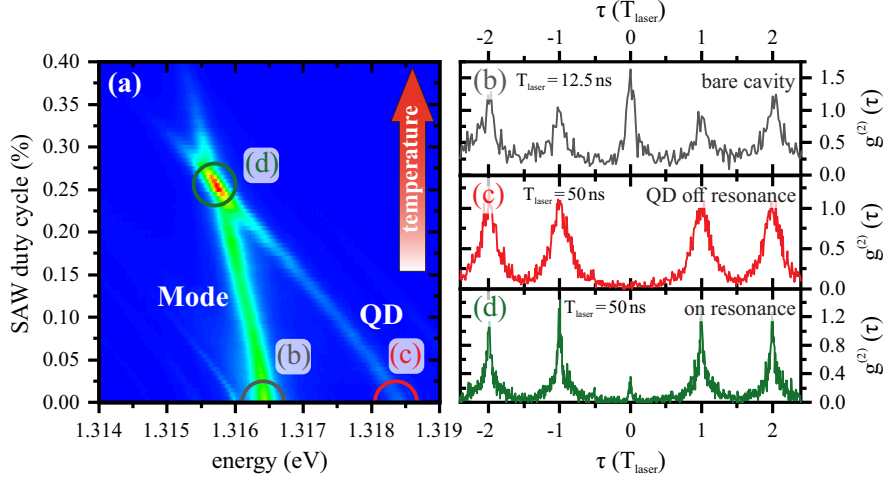


**Figure 9.3.:** (a) Static temperature tuning of a cavity-QD system. With increasing duty cycle and thus temperature, cavity and QD can be tuned into resonance. The generated SAW does not interact with the QD-cavity system. Therefore, only temperature tuning is observed here. (b)-(d) second order correlation function  $g^{(2)}$  of the detuned cavity mode (b), the bare QD (c) and the two systems in spectral resonance (d). Note the different laser periods  $T_{\text{laser}}$  for the pulsed excitation.

are presented in a false-colour representation in figure 9.3(a). For low SAW duty cycles, at a nominal temperature of  $T = 5$  K, two distinct emission peaks at  $E_{\text{cavity}} = 1.3164$  eV and  $E_{\text{QD}} = 1.3184$  eV can be resolved and associated to the emission of the cavity and the QD respectively. This assignment is confirmed by auto-correlation measurements presented in figure 9.3(b) for the cavity emission and (c) for the off-resonance QD. While the cavity emission shows bunching at  $\tau = 0$  as expected [132], the QD shows clear anti-bunching  $g^{(2)}(\tau = 0) \leq 0.1$ , proving single-photon emission. Looking at the correlation peaks for the QD, at multiple integers of the laser repetition rate  $T_{\text{laser}} = 50$  ns, it is noticeable that these have large temporal width, indicating a large radiative decay time of  $\tau_{\text{opt}} \approx 8.5$  ns. This large decay time is caused by the large spectral detuning between cavity and QD. The emission energy of the QD thus falls into the bandgap of the photonic crystal, leading to the Purcell-suppression of the emission.

For an increasing duty cycle/temperature, for both the QD and cavity emission, a clear red-shift can be observed. However, this shift is more pronounced for the QD, resulting in the two systems being in resonance at a duty cycle of about 25%. The second order correlation function at resonance, presented in figure 9.3(d), exhibits a clear anti-bunching

behaviour, again confirming single-photon emission and the coupling of the photonic cavity to a single QD. Compared to the off-resonance case shown in (c), the temporal width of the correlation peaks is greatly reduced, indicating a Purcell enhancement of the QD emission. Under closer examination a weak contribution of a slower process can be observed, which manifests itself by a broad base of the correlation peaks. This contribution can be explained by the emission of the opposite polarisation of the exciton transition that does not couple to the cavity mode.

### 9.1.2. Dynamic SAW tuning

For a dynamic modulation of the detuning between cavity mode and exciton transition, the acoustic field of SAW is used. Therefore, the propagation direction of the SAW is aligned with the long axis of the L3-cavity. Part of the Rayleigh SAW couples into the photonic crystal membrane. Since the thickness of the membrane is significantly smaller than the wavelength of the SAW, wave propagation in the membrane is described by Lamb-waves rather than Rayleigh-waves. Regardless of the wave mode, the QD-cavity system is periodically modulated with the frequency  $f_{\text{SAW}}$ .

As already discussed in the previous chapters, the QD responds to the local strain field and a sinusoidal modulation with a frequency  $f_{\text{SAW}}$  is expected for the QD's emission energy. The response of the cavity mode to the harmonic modulation can be understood by a simple model depicted in figure 9.4 [133]. The in-plane displacement  $u_x$  of the wave leads

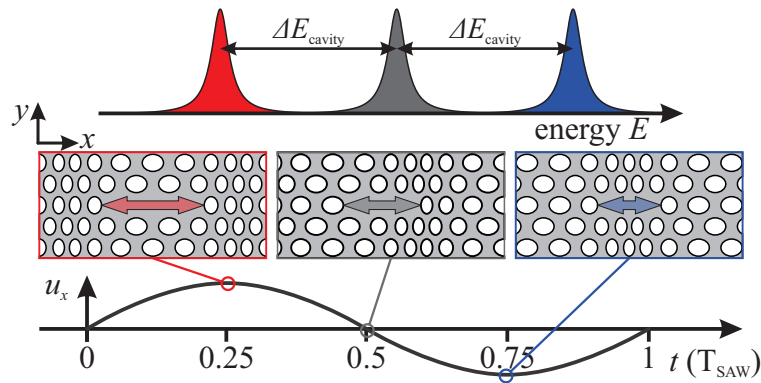


**Figure 9.4.:** Depending on the time during the acoustic cycle and the associated in plane displacement  $u_x$ , the effective length of the cavity is either increased, remains the same or is decreased with respect to the unperturbed cavity length. This geometric deformation then results in a periodic shift of the cavity's resonance frequency.

to a periodic deformation of the photonic cavity. When the maximum of this displacement is located at the centre of the cavity, the effective length of the resonator is increased, leading to a red-shift of the cavity mode. Half a SAW period  $T_{\text{SAW}}$  later the minimum of

the displacement is located in the centre of the cavity, decreasing the effective length of the resonator and resulting in a blue shift of the cavity mode. Between this two extrema, when the node of the displacement is in the centre of the cavity, one half of the resonator is compressed, while the other half is stretched, whereby the effective length of the cavity remains unchanged. Therefore, a periodic spectral modulation with frequency  $f_{\text{SAW}}$  is also expected for the cavity mode and has already been proven experimentally [133, 134].

Since the maximum compression/expansion of the resonator occurs at the same time as the maximal compressive/tensile strain in the centre of the cavity, the spectral oscillations for the cavity mode and QD emission are in-phase. However, the amplitudes of the two oscillations are not equal, so a dynamic modulation of the QD-cavity detuning  $\Delta E_{\text{QD-cavity}}$  is also expected when the system is under the influence of a SAW:

$$\Delta E_{\text{QD-cavity}}(t) = E_{\text{QD}}(t) - E_{\text{cavity}}(t) = \Delta_0 + \Delta \cdot \sin(\omega_{\text{SAW}}t) \quad (9.4)$$

where  $\Delta_0$  denotes the static detuning that can be adjusted by temperature tuning, and  $\Delta$  is the dynamic detuning that is caused by the different spectral tuning amplitudes for the QD and cavity emission.

$$\Delta = \Delta E_{\text{QD}} - \Delta E_{\text{cavity}} \quad (9.5)$$

The time-resolved PL emission for a dynamically strained QD-cavity system is presented in figure 9.5 as a function of time and emission energy relative to the unperturbed emission energy of the cavity  $E_{\text{cavity}}$ . The SAW was excited with a rf-amplitude of  $P_{\text{rf}} = 25$  dBm and a frequency of  $f_{\text{SAW}} = 796$  MHz in pulses of  $T_{\text{mod,SAW}} = 1$   $\mu\text{s}$ . The repetition rate of these pulses and thus the duty cycle of the SAW excitation was adjusted to achieve a static detuning of  $\Delta_0 = 0$  meV and  $\Delta_0 = 0.33$  meV for the measurements presented in figure 9.5(a) and (b) respectively. Laser excitation was strictly phase-locked to the SAW excitation with  $T_{\text{laser}} = 10 \cdot T_{\text{SAW}}$  ( $f_{\text{laser}} = f_{\text{SAW}}/10 = 79.6$  MHz) and set to occur at the falling edge of the spectral modulation. The dashed black and white lines are guides for the eye to the spectral modulations of the cavity and QD emission. For  $\Delta_0 = 0$ , an onset of the emission is observed around  $t \approx 250$  ps as the system is excited by the laser. After traversing the minimum of the spectral modulation, the emission strongly increases and reaches a maximum at  $t \approx 800$  ps when the two systems are in resonance. After that, the resonance is lifted again and the emission intensity strongly decreases. This intensity modulation is caused by the dynamic switching between the Purcell suppressed regime, when the two systems are out of resonance, and the Purcell enhanced regime, when the two systems are in resonance. After this global maximum two more local maxima can be observed one and two SAW periods later at  $t \approx 2$  ns and  $t \approx 3.3$  ns respectively, when both systems are in resonance again.

Next, the static detuning was set to  $\Delta_0 = 0.33$  meV, while the time of photoexcitation was kept constant. As indicated by the dashed lines in figure 9.5(b), this results in a

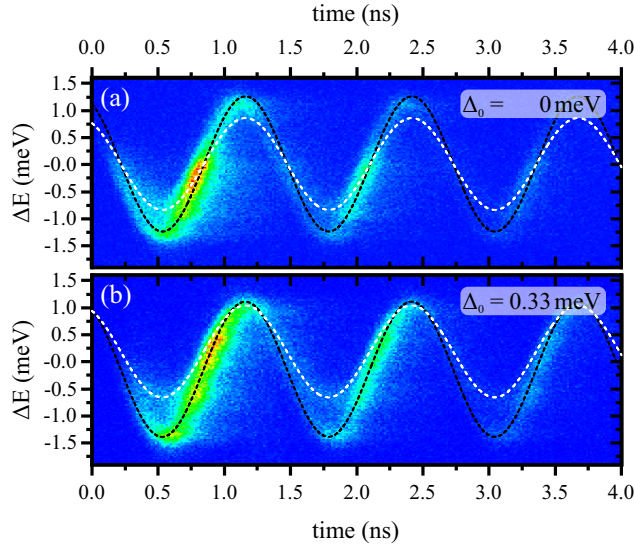


**Figure 9.5.:** Temporal modulation of the QD-cavity system for two different static detunings of  $\Delta_0 = 0$  (a) and  $\Delta_0 = 0.33$  meV (b). Dashed black and white lines are guides for the eye to the dynamic modulations of cavity and QD respectively.

shift of the QD modulation towards higher energies, while the amplitudes of the two modulations stay constant. As a result, the resonance is delayed by  $\approx 150$  ps and shifted to  $\Delta E = \Delta_0 = 0.33$  meV. The observed emission maxima nicely follow this shift both in time and energy, confirming that the emission indeed depends on the detuning  $\Delta E_{\text{QD-cavity}}$  and the associated Purcell enhancement/suppression.

A closer examination of the data presented in figure 9.4 reveals two deviations from the simple model where the QD emission is only influenced by Purcell enhancement and suppression. The first effect is the different coupling between cavity and QD depending on the slope of the spectral modulations. While the enhancement of the emission is clearly pronounced when the cavity is tuned into resonance with the QD from the low energy side, thus at the rising slopes of the respective spectral modulations, for the resonances at the falling edges of the modulation, an enhancement of the emission can barely be resolved. This effect, which cannot be observed in quasi-static experiments, points towards a so far unknown process and thus remains an area of active research. The second deviation is that the maximum emission intensity is not observed exactly at the expected resonance but slightly before and thus for a slightly blue-detuned QD. This effect can be attributed to a phonon-assisted coupling mechanism between QD and cavity, which indeed predicts an increased scattering rate for blue-detuned QDs [135].

Since the emission observed in the experiment steams from a single QD that is modulated by periodic Purcell suppression and enhancement, single photon emission and thus photon anti-bunching is expected for this system. To prove single photon emission,  $g^{(2)}$  measurements

were performed for the dynamically tuned QD-cavity system. For that purpose, the static detuning was set to  $\Delta_0 = 0$  by tuning the modulation rate to  $f_{\text{mod}} = 185$  kHz resulting in a SAW duty cycle of 18.5%<sup>1</sup>. The emission was collected at  $\Delta E = -0.2$  meV, where the maximum of the emission was observed, and  $g^{(2)}$  was measured by a HBT-interferometer. The such recorded  $g^{(2)}(\tau)$  function is plotted for a large and small range of  $\tau$  in figure 9.6(a)

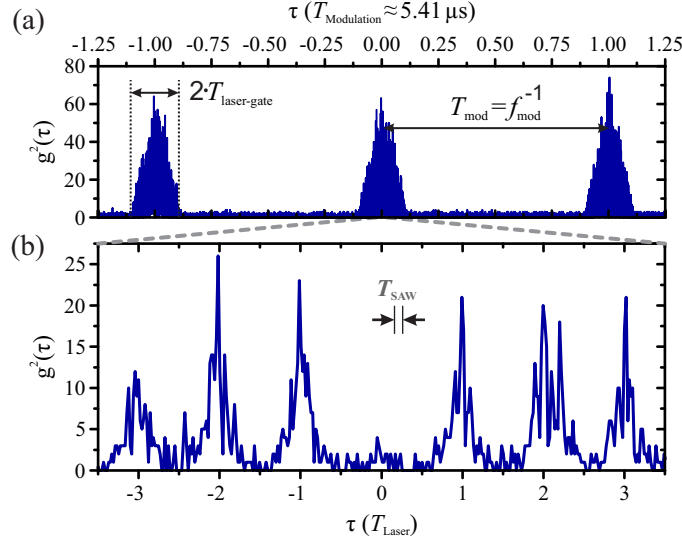


**Figure 9.6.:** (a) Measured  $g^{(2)}(\tau)$  for the dynamically tuned cavity-QD system, over a large range of  $\tau$ . Due to the modulated excitation scheme, correlations are only detected when the system is optically excited. (b) Zoom-in on the central region demonstrates single photon emission and clear modulations on the time scale of  $T_{\text{SAW}}$ .

and (b), respectively. In (a), the delay time  $\tau$  covers a range of  $\tau = \pm 1.25 \cdot T_{\text{mod}} (\approx \pm 6.76 \mu\text{s})$  and thus 2.5 modulation periods. As a consequence, three correlation peaks can be observed, which are separated by  $T_{\text{mod}}$  and are caused by the modulated excitation scheme. These correlation peaks have a triangular shape arising from the square modulation of the optical excitation and thus have a width of  $2 \cdot T_{\text{laser, gate}} = 1.2 \mu\text{s}$ . An enlargement of the central region covering a range of  $\tau = \pm 3 \cdot T_{\text{laser}} \approx \pm 43.97$  ns is shown in figure 9.6(b). Here, correlation peaks at multiple integers of the laser repetition rate ( $T_{\text{laser}} = f_{\text{laser}}^{-1} \approx 12.56$  ns) are observed, while the central peak at  $\tau = 0$  is missing, confirming single photon emission. Furthermore, the correlation peaks show a clear modulation on a timescale matching the SAW period  $T_{\text{SAW}} \approx 1.256$  ns. To further confirm this SAW triggered single-photon emission, a Fourier analysis of the  $g^{(2)}(\tau)$  function was performed. The full Fourier transform (FT) for the frequency range  $0 < f < 1$  GHz is presented in figure 9.7(a). This FT reveals all frequencies involved in the experiment, namely  $f_{\text{mod}} = 185$  kHz,  $f_{\text{laser}} = 79.6$  MHz and

<sup>1</sup>Note that this duty cycle is smaller compared to the one used for the static tuning experiment in figure 9.3, since the IDT used here is located closer to the investigated photonic cavity.

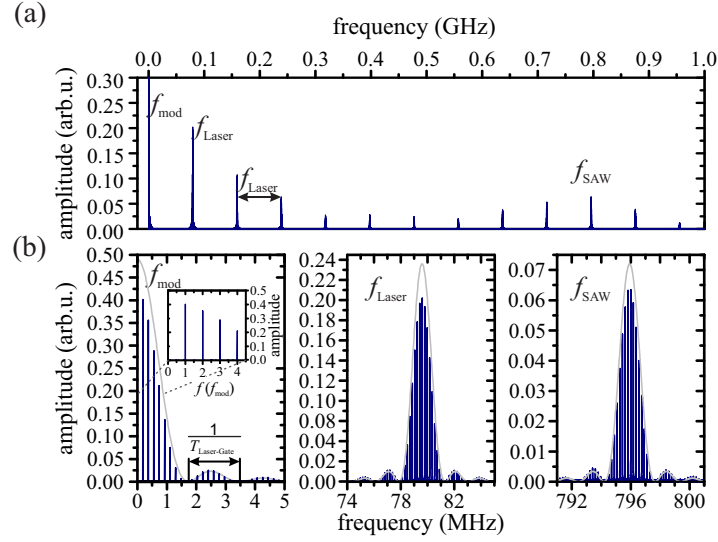


**Figure 9.7.:** (a) Fourier transform of the measured  $g^{(2)}$ , presented in figure 9.6, in the frequency range 0 – 1 GHz. (b) Zooms of the characteristic frequencies involved in the experiment  $f_{\text{mod}} = 185$  kHz,  $f_{\text{laser}} = 79.6$  MHz and  $f_{\text{SAW}} = 796$  MHz. The grey lines are the expected envelopes caused by the modulated laser excitation.

$f_{\text{SAW}} = 796$  MHz. Since the  $g^{(2)}(\tau)$  function is not harmonic, higher harmonics of  $f_{\text{laser}}$  can also be resolved over the entire presented frequency range. A closer examination of the three characteristic frequencies  $f_{\text{mod}}$ ,  $f_{\text{laser}}$  and  $f_{\text{SAW}}$ , presented in the three panels of figure 9.7(b), reveals that the respective FT peaks show a series of side peaks. These side peaks arise from the modulated laser excitation and thus are equidistantly separated by  $f_{\text{mod}}$ . For all three frequencies, the sidebands are limited by an envelope function that is depicted by the light grey lines and is proportional to:

$$\propto \text{sinc}^2(2\pi T_{\text{laser,gate}} \cdot f) = \frac{\sin^2(2\pi T_{\text{laser,gate}} \cdot f)}{(2\pi T_{\text{laser,gate}} \cdot f)^2} \quad (9.6)$$

This envelope function is caused by the square modulation of the laser excitation, with a gate length of  $T_{\text{laser,gate}}$ . Upon autocorrelation, this square modulation results in the triangular envelope that can be recognized in figure 9.6(a). The FT of this triangular envelope then results in the observed envelope function <sup>2</sup>.

<sup>2</sup>According to the convolution theorem, the FT of the convolution of two functions corresponds to the product of their FTs  $\mathcal{F}(f * g) = \mathcal{F}(f) \cdot \mathcal{F}(g)$ . As the FT of a square function is proportional to the sinc-function, the FT of a triangular function is proportional to the square of the sinc-function

## 9.2. Phononic crystals

Similar to photonic crystals, where a periodic modulation of the refractive index creates a photonic band structure, phononic crystals can be realised by a periodic variation of the mechanical properties. Like for photonic crystals, the simplest implementation of a phononic crystal is the patterning of a membrane with a two dimensional array of air-holes. As phonons cannot propagate in vacuum, they are confined within the membrane and their in-plane motion is affected by the periodic array, giving rise to the formation of a phononic band structure. For suitable arrangements, phononic bandgaps can be realised in such structures, meaning the propagation of phonons of certain frequencies is fully prohibited. Consequently, by introducing line or point defects in the crystal, phononic waveguides and cavities can be realised, allowing to control the propagation of phonons in the membrane. For certain geometries, simultaneous photonic and phononic bandgaps and thus co-localised photonic and phononic resonances can be realised. Such crystals are referred to as optomechanical crystals (OMC) and allow for the realisation of strongly coupled optical and mechanical modes.

A good overview of optomechanical crystals membranes can be found in the references [136] and [137]. While, in these references, optomechanical crystals made of silicon are considered, this section will focus on GaAs as a material system. This has the advantage that semiconductor QDs can directly be embedded within the membrane, thus enabling the investigation of acoustic wave propagation within the phononic crystal by measuring the optical response of the QD. Furthermore, GaAs allows for direct excitation of SAWs. In the following considerations, the focus is put on the phononic properties of the crystals. The first crystal to be considered here is the two dimensional "cross" crystal depicted in figure 9.8(a). It consists of a square array of cross shaped holes in a suspended membrane. The crystal is fully defined by the height  $2l$  and width  $w$  of the crosses, the lattice constant  $a$  of the square lattice and the thickness of the membrane  $d$ . For a better understanding of the phononic properties, this crystal can be considered as a quadratic arrangement of squares with a side length of  $(a - w)$ , connected by small bridges of length  $w$  and width  $(a - 2l)$ , rather than an array of cross shaped holes. The phononic band structure of the crystal is then determined by the size of the squares and the connectors. The low frequency (energy) phonons are mostly affected by the size of the connectors and can be shifted towards lower frequency by decreasing the size of the connectors, thus softening the crystal. The high frequency (energy) phonons are mostly dependent on the natural vibrations of the squares and are only slightly affected by the connectors. The complete band structure of such a crystal can be calculated numerically using FEM. For that purpose, a single unit cell is modelled and periodic Floquet (Bloch) boundary conditions are applied to the boundaries of the unit cell that are connected to the neighbouring unit cells. The wave vector is then varied along the high symmetry directions in reciprocal space. The calculated band structure of such a crystal (design parameters  $a = 2 \mu\text{m}$ ,  $w = 0.4 \mu\text{m}$ ,

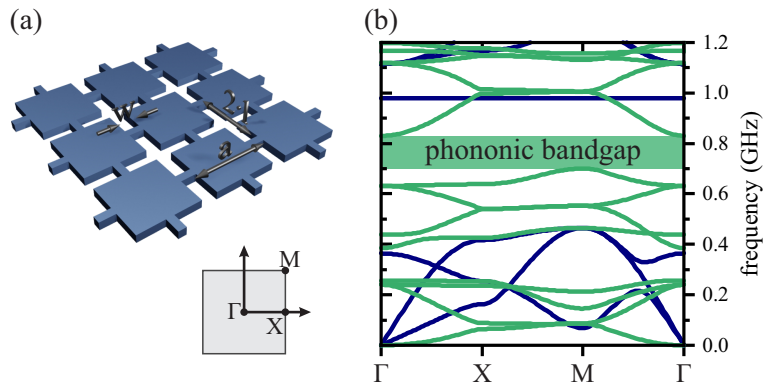


**Figure 9.8.:** (a) Schematic of the phononic "cross" crystal membrane. The inset shows the first Brillouin zone (FBZ) of the square lattice with its respective high symmetry points  $\Gamma = (0, 0)$ ,  $X = (\frac{\pi}{a}, 0)$ ,  $M = (\frac{\pi}{a}, \frac{\pi}{a})$ . (b) Calculated phononic band structure for the design parameters  $a = 2 \mu\text{m}$ ,  $w = 0.4 \mu\text{m}$ ,  $l = 0.9 \mu\text{m}$  and  $d = 0.22 \mu\text{m}$ . Depending on the symmetry with respect to the mirror plane through the centre of the membrane, phononic bands are divided in **antisymmetric** and **symmetric** modes.

$l = 0.9 \mu\text{m}$  and  $d = 0.22 \mu\text{m}$ ) consisting of GaAs is plotted in figure 9.8(b) along the  $\Gamma \rightarrow X \rightarrow M \rightarrow \Gamma$  path (see inset in Fig.9.8(a)). Due to the mirror symmetry of the membrane ( $(x, y, z) \rightarrow (x, y, -z)$ ), two different kinds of modes can be distinguished, depending on their respective symmetry. The modes are either symmetric (even) or antisymmetric (odd) with respect to the mirror plane and the two sets of modes are fully uncoupled.

In the field of optomechanics, the antisymmetric modes are typically neglected, since they do not substantially change the optical mode volume and, therefore, do not lead to a strong optomechanical coupling [138]. A similar argument can be made for the coupling of a QD to the mechanical modes of the crystal. Assuming that the QDs are located at the centre of the membrane  $a$ , pronounced coupling is only expected for the symmetric modes as, for the antisymmetric ones, the hydrostatic pressure in the centre plane of the membrane vanishes. However, recent experiments on QDs located in the centre of suspended string show a pronounced coupling to antisymmetric modes and thus to the off-diagonal components of the strain tensor [139]. Furthermore, imperfections in the fabrication of such phononic crystals, which result in an breaking of the mirror symmetry, cause a finite coupling between symmetric and antisymmetric bands. To avoid such unwanted couplings, it can be beneficial to engineer crystals that exhibit an overlap between symmetric and antisymmetric bandgaps.

As it can be seen in figure 9.8(b), the "cross" crystal allows for the realisation of a complete bandgap, meaning neither symmetric nor antisymmetric modes can propagate within the complete bandgap. For the design parameters used in figure 9.8, the complete bandgap ranges from 700 to 830 MHz. Due to this large complete bandgap that can be tuned over a wide range of frequencies by adapting the geometry, the phononic "cross" crystal can be

used to shield other structures from acoustic phonons of certain frequencies. Such phononic shields are, for example, used to suppress mechanical losses of optomechanical cavities, greatly increasing their respective mechanical quality factor [120, 140–143]. Furthermore, such a crystal could be used to confirm the coupling of QDs to antisymmetric membrane modes shown in [139] since, in certain frequency ranges, only symmetric or antisymmetric modes can propagate and, therefore, the two phonon polarisations can clearly be separated. Due to the comparatively low symmetry of the square lattice, the "cross" crystal does not support a complete photonic bandgap and is consequently not suitable for the realisation of an optomechanical crystal.

This limitation can be overcome by going over to structures of higher symmetry. The hexagonal analogue of the "cross" pattern is the so-called "snowflake" pattern, depicted in figures 9.9(a) and (b). This crystal can also be understood as a periodic array of triangles, where each triangle is connected to its respective three neighbours by small connectors. Again the geometry of the crystal is fully defined by the lattice constant  $a$ , the length ( $2r$ ) and width  $w$  of the air holes and the thickness of the membrane  $d$ . The photonic and

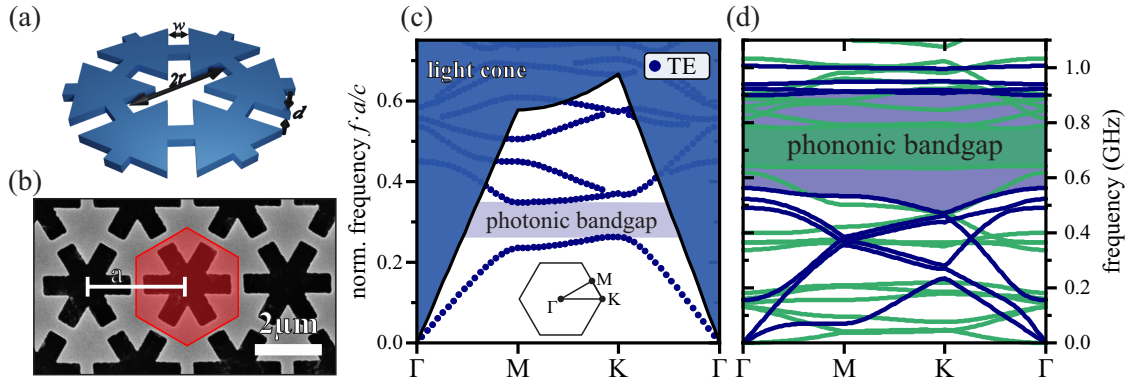


**Figure 9.9.:** (a) Schematic of the "snowflake" crystal membrane. (b) REM micrograph of a "snowflake" membrane fabricated on a GaAs substrate with design parameters of  $a = 3 \mu\text{m}$ ,  $r = 1.3 \mu\text{m}$ ,  $w = 0.55 \mu\text{m}$  and  $d = 0.22 \mu\text{m}$ . Red shaded area marks one possible unit cell. (c) Photonic band structure for TE modes for the crystal shown in (b), showing a photonic bandgap. The inset shows the first Brillouin zone (FBZ) of the hexagonal lattice with the high symmetry points  $\Gamma = (0, 0)$ ,  $M = \left(\frac{\pi}{a}, \frac{1}{\sqrt{3}}\frac{\pi}{a}\right)$ ,  $K = \left(\frac{4}{3}\frac{\pi}{a}, 0\right)$ . (d) Phononic band structure for the "snowflake" crystal, showing a bandgap for both **symmetric** and **antisymmetric** modes.

phononic band structures for such a crystal with  $a = 3 \mu\text{m}$ ,  $r = 1.3 \mu\text{m}$ ,  $w = 0.55 \mu\text{m}$  and  $d = 0.22 \mu\text{m}$ , obtained by FDTD and FEM calculations, are shown in figure 9.9(c) and (d), respectively. As it can be seen, the snowflake crystal exhibits both a photonic bandgap for TE modes and a complete phononic bandgap. Furthermore, the photonic band structure is more susceptible to the air-hole width  $w$ , while the phononic band structure is more susceptible to the width of the connectors ( $a - 2r$ ). This makes this system a promising candidate for optomechanical applications, as both photons and phonons can be controlled

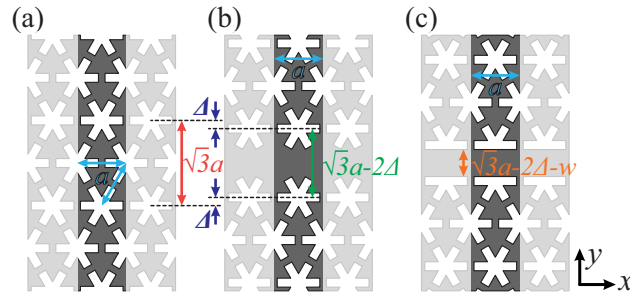


**Figure 9.10.:** (a) Schematic of a "snowflake" phononic crystal. (b) W1-like waveguide created by omitting one row of snowflakes along the  $x$ -direction and shifting the entire crystal structure above and below the waveguide towards each other by the value  $\Delta$ . (c) Proposed modified waveguide design, where the "snowflake arms" that extend into the waveguide region are omitted. The resulting waveguide is basically a straight beam that is connected to the adjacent phononic crystal by small connectors. The highlighted area shows a "super-cell" of the waveguides, where periodicity in the  $x$ -direction is maintained, while it is broken in the  $y$ -direction.

simultaneously and relatively independently [136, 137].

Moreover, due to the symmetry of the crystal, Dirac cones occur at the  $K$  and  $K'$  points of the phononic band structure. These Dirac cones can be shifted by distorting the geometry of the snowflakes, which is equivalent to the introduction of a pseudo-magnetic fields and allows for a helical transport of phonons [138]. This geometric tuning technique be further developed to create a phononic topological insulator, which allows for the realisation of topologically protected mechanical wave propagation on the nano-scale [144].

In the following, however, only the phononic properties of the crystal membranes are considered. For the geometry considered in figure 9.9, the complete phononic bandgap ranges from 640 to 780 MHz and the symmetric bandgap even extends from 560 to about 900 MHz.

By introducing a line defect in such a crystal, a waveguide can be realised. Such a defect causes the formation of waveguiding bands within the photonic and phononic band structures. These bands are localised at the defect and thus enables the steering of both photons and phonons along the waveguide. One of the most common types of waveguide, a so-called W1 waveguide, is depicted in figure 9.10(b). This WG is formed by omitting a row of snowflakes along the  $x$ -direction (corresponding to the  $\Gamma$ - $K$ -direction in reciprocal space). Additionally, the snowflake holes above and below the waveguide are each shifted by  $\Delta$  towards the waveguide, thus reducing the effective width of the WG by  $2\Delta$ . This type of waveguide is highly suitable in the field of optomechanics, as both phononic and photonic properties can be tuned simultaneously. Furthermore, by introducing an additional variation along the waveguide, for example by locally varying the waveguide width ( $\Delta$ ) or the radius  $r$  of the adjacent snowflakes, both photons and phonons can be confined in the same small volume. The spatial overlap of optical and mechanical modes result

in a strong coupling between the optical and mechanical resonances for such structures and optomechanical couplings of  $g_0/2\pi = 220$  kHz have been reported [145]. Introducing additional structures into the waveguide like c-shaped holes, the mechanical and optical modes can be confined further and thus the coupling rate can be further increased. [146] The mechanical modes and the band structure of this type of waveguide is shown in appendix D. There, it can be seen that the mechanical modes are predominately localised in the sharp corners of the waveguide. This makes the respective modes highly susceptible to disorder in fabrication and already small deviations in the crystal geometry can result in the localisation of photons and phonons [145].

Furthermore, the strong localisation in the corners complicates the study of the propagation of mechanical waves along the WG by measuring the optical response of QDs located within the waveguide, which is the preliminary goal of this project. Due to the strong spatial localisation of the strain fields within the waveguide, a single QD may only interact with certain modes, depending on its exact position, making conclusions about the corresponding modes difficult.

To overcome these limitations, a simplified waveguide design, depicted in figure 9.10(c), is proposed. Here, the snowflakes adjacent to the waveguide are additionally modified, by removing the respective two arms of the snowflakes that extend into the WG. The resulting WG can be considered as a straight beam of width  $t = (\sqrt{3}a - 2\Delta - w)$ , which is connected to the surrounding phononic crystal by bridges of length  $w$  and width  $(a - 2r)$ . The calculated phononic band structures and the mechanical WG modes are shown in figure 9.11 for the symmetric and antisymmetric modes. The parameters for the snowflake crystal are the same as for the band structure calculation shown in figure 9.9 ( $a = 3 \mu\text{m}$ ,  $r = 1.3 \mu\text{m}$ ,  $w = 0.55 \mu\text{m}$ ,  $d = 0.22 \mu\text{m}$ ) and  $\Delta$  was set to  $1.5 \mu\text{m}$ . This results in a WG beam width of  $t \approx 1.646 \mu\text{m}$  and a connector width of  $550 \times 400$  nm.

Compared to the mechanical modes for the not modified WG, presented in appendix D, the spatial mode profiles for this waveguide, presented in figures 9.11(a) and (c), extend much more uniformly over the entire waveguide structure. Therefore, a uniform optical response is expected for QDs located within the WG, largely independent of their respective exact position. Furthermore, a close look at the spatial mode profiles reveals that most of the modes are completely confined to the WG beam and barely extend to the adjacent phononic crystal. Comparing the spatial mode profiles to the modes of a suspended beam of width  $t$  and thickness  $d$ , shown in the lower panels of figure 9.11(b) and (d), show a very good agreement between the respective mode profiles. Furthermore, the bands of the suspended beam, plotted as dashed lines in figures 9.11(a) and (c), coincide largely with the corresponding waveguide bands for most modes. Only in the case of the symmetric bands labelled ① and ③ and the antisymmetric band labelled ⑥, larger deviations between the corresponding bands can be seen in the band structure. Looking at the mode profiles of these bands, it can be seen that these modes expand further in the adjacent phononic

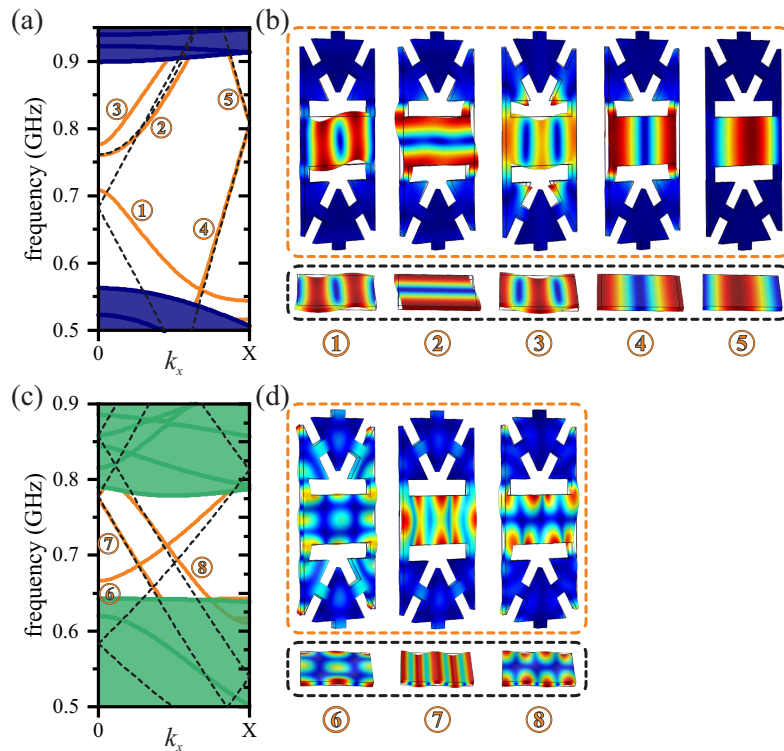


**Figure 9.11.:** (a),(b) Calculated phononic band structure of the WG geometry shown in figure 9.10(c) for the symmetric (a) and antisymmetric (c) modes respectively. The orange lines are WG bands and the dashed lines are the dispersion of a suspended beam with the corresponding size. (b),(d) Spatial mode profiles of the correspondingly labelled bands in (a) and (c) respectively. The top rows show the WG modes, while the bottom rows show the corresponding beam modes. The colour code indicates the normalized absolute displacement.

crystal and thus the approximation of a free beam is no longer valid.

In conclusion, the proposed waveguide design is expected to support the propagation of mechanical waves, which can be investigated by monitoring the optical response of QDs located in the waveguide membrane. Due to the simplified geometry of the waveguide, the supported modes can be described in good approximation by the modes of a suspended beam (see [139]). Finally, it should be noted that the simplified waveguide geometry is expected to be less suited for the manipulation of photon propagation, as the number of degrees of freedom is greatly reduced. As the focus is however on the phononic properties of the WG, no calculations of the photonic modes and band structures were carried out for these structures.

To investigate the propagation of mechanical waves in phononic crystal membranes, corresponding crystals with and without WG have been fabricated. These membranes, made of GaAs, contain a single layer of self-assembled InGaAs QDs right at its centre. The fabrication process is basically identical to the one used for the fabrication of photonic

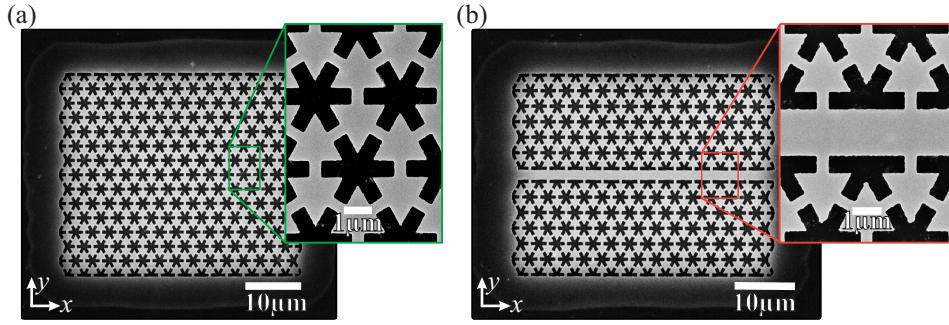


**Figure 9.12.:** SEM images of suspended phononic crystal membranes, consisting of GaAs and containing a single layer of InGaAs QDs at the centre. ( $a = 3 \mu\text{m}$ ,  $r = 1.3 \mu\text{m}$ ,  $w = 0.55 \mu\text{m}$ ,  $d = 0.22 \mu\text{m}$  and  $\Delta = 1.5 \mu\text{m}$ ) (a) Phononic crystal membrane with a size of about  $45 \times 35 \mu\text{m}$ . The inset nicely shows the structure of the crystal consisting of interconnecting triangles. (b) Phononic crystal membrane with a modified W1 waveguide in the centre, oriented along the long side of the crystal. IDTs fabricated on the same sample are oriented to excited SAWs propagating in the  $x$ -direction.

crystals and is shortly described in appendix C. Scanning electron micrographs of such phononic crystal membranes, with and without WG, are presented in figure 9.12(a) and (b) respectively. These membranes have roughly a size of  $45 \times 35 \mu\text{m}$  and the design parameters of the crystal were identical to the ones used for the simulations ( $a = 3 \mu\text{m}$ ,  $r = 1.3 \mu\text{m}$ ,  $w = 0.55 \mu\text{m}$ ,  $d = 0.22 \mu\text{m}$ ,  $\Delta = 1.5 \mu\text{m}$ ). In addition to the phononic membranes, chirped split-5-2 transducers with a fundamental frequencies ranging from 250 to 300 MHz, 300 to 350 MHz and 350 to 400 MHz were fabricated on the sample to excite mechanical waves. Identical phononic membranes were fabricated in the sound paths of each IDT, where the  $x$ -direction of the phononic crystal was aligned with respect of the SAW propagation direction. This enables the investigation of the mechanical wave propagation through the different phononic structures, by measuring the optical response of single QDs located in the membrane over a wide range of frequencies, similar to the experiments shown in [139]. In such experiments, single QDs can be used as localised strain sensors, thus allowing to determine the strain fields as a function of frequency and position within the crystal or waveguide. For example, the phononic bandgap or the propagation length of certain waves in the crystal/WG can be determined experimentally.

Although a sample was fabricated, the corresponding experiments have not been carried out until the completion of this work. Once these basic experiments are conducted, the considerations can be extended to more complex structures ranging from phononic cavities, beam splitters and interferometers up to fully integrated phononic circuits. Ultimately, the design demonstrated here can be extended to also support photonic modes, thus enabling the steering of both phonons and photons on a chip.

## 10. Conclusion and outlook

The main focus of this dissertation was set on the spectral modulation of single semiconductor QDs by propagating surface acoustic waves. The SAW dynamically modulates the transition energies of QDs, and thus the energy of the emitted single photons, via deformation potential coupling. Various experimental techniques were presented to monitor the spectral modulation both in time-integrated and time-resolved measurements. The use of multiharmonic frequency chirped transducers enables SAW generation over broad frequency bands and thus ultimately paves the way towards arbitrary nanomechanical wave generation. Furthermore, it was shown that such an IDT structure facilitates the stable phase-locking of a SAW to a second excitation of fixed repetition rate, as it was shown for a free running mode-locked laser.

In further experiments, the resonant optical excitation of single QDs was presented. Here, in the limit of low Rabi frequencies, the obtained single photons resonantly scattered at the QD possess superior properties in terms of coherence and bandwidth. Combining this optical excitation technique with the dynamical modulation of a SAW results in the formation of phononic sidebands. The formation of these PSBs was investigated in great detail as a function of the SAW's modulation amplitude and modulation frequency, both in time-integrated as well as in time-resolved measurements. Furthermore, parametric energy conversion between the phononic and photonic domain was demonstrated for detuned optical excitation. When modulating the QD with two SAWs, the QD mixes phonons of both SAW fields. This phenomenon manifests itself by the occurrence of sum and difference frequency PSBs in the RF signal. When these two SAW fields are mutually coherent, certain PSBs are enhanced, while others are suppressed. This phonon interference effect depends on the phase relation between the two phonon fields and can thus be precisely tuned. A slight frequency detuning between the two SAWs results in intensity oscillation of the PSBs in the time domain. These oscillations can be observed over time spans of several hours, proving the high coherence of this modulation technique.

In the last chapter of the thesis, the avenue to control coupling of a QD to photonic and/or phononic fields by placing it in an accordingly tailored environment is discussed. In the first part, a system consisting of a single QD coupled to a photonic crystal nanocavity is considered. Depending on whether the QD transition and the cavity mode are spectrally in resonance or not, the radiative decay rate of the QD is suppressed or enhanced respectively. Modulating the spectral detuning between the two systems with a SAW enables fast and dynamical switching between the Purcell enhanced and the Purcell suppressed regime and

ultimately allows to trigger single photon emission. Finally, phononic crystal membranes are discussed as a way to control and steer the propagation of phonons within a platform compatible to the implementation of semiconductor quantum dots.

Based on the experimental results presented here, various possibilities to continue this work exist.

One possibility would be to employ pulsed resonance fluorescence spectroscopy on a QD dynamically strained by a SAW. This would make it possible to employ the stroboscopic SAW excitation scheme introduced in section 5.3 of this thesis for PL spectroscopy. The required stable coupling between the SAW frequency  $f_{\text{SAW}}$  and the laser repetition rate  $f_{\text{laser}}$  can easily be realised with the frequency chirped transducer design presented in this work. Depending on the exact optical excitation time within an acoustic cycle, the appearance of red or blue PSBs can be controlled, resulting in an additional tuning mechanism.

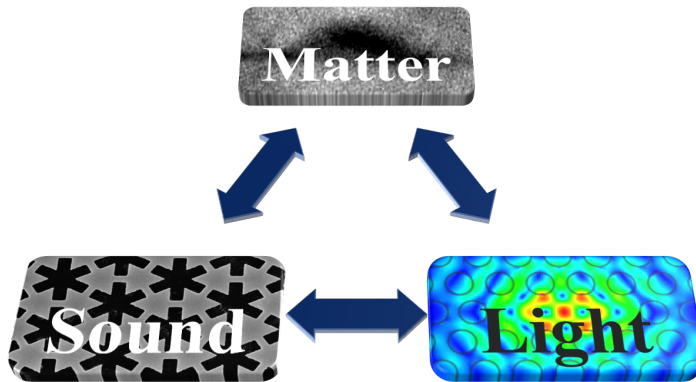


**Figure 10.1.:** Coupling between the three "elementary excitations" in condensed matter, phonons (sound), photons (light) and matter (excitons). Establishing all three interaction on a single platform paves the way towards hybrid optomechanics.

Another future task concerns further development of the photonic and phononic crystal membranes discussed in the last chapter of this thesis. The goal pursued in this project is the coupling between the three "elementary excitations" in condensed matter, excitons, photons and phonons on a single platform. The coupling between matter in the form of QD excitons and both sound (phonons) and light (photons) was demonstrated independently in this dissertation. On the one hand the coupling of a QD to a light field was demonstrated in the weak coupling regime. There, the radiative decay rate of a QD was influenced by the photonic environment of the QD via the Purcell effect. Strong coupling on the other hand,

---

was demonstrated by exciting the QD with a strong resonant laser field. The resulting Rabi oscillation manifested themselves by the appearance of Mollow triplets in the RF spectrum.

The coupling between phonons and excitons confined in a QD was the main focus of this work. This coupling leads to a spectral modulation of the QD's emission energy and was demonstrated throughout this work, even in the resolved sideband regime.

The coupling between photons and phonons is part the emerging field of optomechanics and the mutual coupling of coherent elastic and optical waves has already been shown in corresponding structures [120, 147].

By embedding single semiconductor QDs in such optomechanical cavities, the interaction between light (photons), sound (phonons) and matter (excitons) can deliberately be enhanced or suppressed. This ultimately enables the realisation of fully fledged coherent hybrid quantum optomechanics [148, 149].



# Appendices



# A. Remarks on elastic constants

In this chapter, some additional remarks concerning the elastic constants shall be provided. These remarks cover the Voigt notation, the rotation of the tensors to the needed reference system and the material parameters of  $\text{Al}_x\text{Ga}_{1-x}\text{As}$  used for the FEM simulations presented in the main text.

## A.1. Voigt Notation

The Voigt Notation is a notation that provides an abbreviate representation for symmetric tensors by reducing their order. It is often used in elasticity theory, as it reduces the complexity of the equations and, especially, makes it possible to write the fourth order elasticity tensor and the third order piezoelectric tensor as matrices (second order tensor). It works by combining two interchangeable indices and replacing them with a new one, according to the following mapping rule:

$$\begin{aligned} (1, 1) &\rightarrow 1 & (2, 2) &\rightarrow 2 & (3, 3) &\rightarrow 3 \\ (2, 3) &\rightarrow 4 & (1, 3) &\rightarrow 5 & (1, 2) &\rightarrow 6 \end{aligned} \quad (\text{A.1})$$

If this rule is applied to the stress tensor, the  $3 \times 3$  stress tensor can be transformed to a 6-element vector in the Voigt Notation:

$$T = \begin{pmatrix} T_{11} & T_{12} & T_{13} \\ \cdot & T_{22} & T_{23} \\ \cdot & \cdot & T_{33} \end{pmatrix} = \begin{pmatrix} T_1 & T_6 & T_5 \\ \cdot & T_2 & T_4 \\ \cdot & \cdot & T_3 \end{pmatrix} \Rightarrow T^{\mathbf{V}} = \begin{bmatrix} T_1 \\ T_2 \\ T_3 \\ T_4 \\ T_5 \\ T_6 \end{bmatrix} \quad (\text{A.2})$$

The superscript  $\mathbf{V}$  indicates the respective variable to be in the Voigt notation. The same simplification can be used for the strain tensor. However, care must be taken as, by convention, the elements with mixed indices are multiplied by a factor of 2. As it will be shown shortly, this factor ensures that the main equations of elasticity theory can be

written as matrix multiplications in the Voigt-Notation:

$$S = \begin{pmatrix} S_{11} & S_{12} & S_{13} \\ \cdot & S_{22} & S_{23} \\ \cdot & \cdot & S_{33} \end{pmatrix} = \begin{pmatrix} S_1 & S_6 & S_5 \\ \cdot & S_2 & S_4 \\ \cdot & \cdot & S_3 \end{pmatrix} \Rightarrow S^{\mathbf{V}} = \begin{bmatrix} S_1 \\ S_2 \\ S_3 \\ 2S_4 \\ 2S_5 \\ 2S_6 \end{bmatrix} \quad (\text{A.3})$$

For the elasticity tensor  $c_{ijkl}$ , the mapping rule A.1 is applied to first two ( $i, j$ ) indices and the last two indices ( $k, l$ ). So in Voigt-Notation, the elasticity tensor becomes a symmetric (due to major symmetry) ( $6 \times 6$ ) matrix:

$$c^{\mathbf{V}} = \begin{bmatrix} \mathbf{c}_{11} & \mathbf{c}_{12} & \mathbf{c}_{13} & c_{14} & c_{15} & c_{16} \\ \cdot & \mathbf{c}_{22} & \mathbf{c}_{23} & c_{24} & c_{25} & c_{26} \\ \cdot & \cdot & \mathbf{c}_{33} & c_{34} & c_{35} & c_{36} \\ \cdot & \cdot & \cdot & \mathbf{c}_{44} & c_{45} & c_{46} \\ \cdot & \cdot & \cdot & \cdot & \mathbf{c}_{55} & c_{56} \\ \cdot & \cdot & \cdot & \cdot & \cdot & \mathbf{c}_{66} \end{bmatrix} \quad (\text{A.4})$$

For the piezoelectric tensor  $e_{ijk}$ , the mapping rule A.1 is applied to the last two indices ( $j, k$ ), as the first index represents the electrical field, leading to a  $3 \times 6$  matrix:

$$e^{\mathbf{V}} = \begin{bmatrix} e_{11} & e_{12} & e_{13} & \mathbf{e}_{14} & e_{15} & e_{16} \\ e_{21} & e_{22} & e_{23} & e_{24} & \mathbf{e}_{25} & e_{26} \\ e_{31} & e_{32} & e_{33} & e_{34} & e_{35} & \mathbf{e}_{36} \end{bmatrix} \quad (\text{A.5})$$

Using these simplifications, the definition of the stress (see equation 3.6) and electric displacement (see equation 3.7) for a piezoelectric material can be written as a matrix multiplication in the Voigt-Notation:

$$\begin{aligned} T^{\mathbf{V}} &= c^{\mathbf{V}} \cdot S^{\mathbf{V}} - e^{\mathbf{V}\top} \cdot \mathcal{E} \\ D &= e^{\mathbf{V}} \cdot S^{\mathbf{V}} + \epsilon \mathcal{E} \end{aligned}$$

## A.2. Elastic constants of $\text{Al}_x\text{Ga}_{1-x}\text{As}$

For cubic systems like  $\text{Al}_x\text{Ga}_{1-x}\text{As}$ , the number of independent elements in the stiffness and piezoelectric tensor are significantly reduced so that the elasticity tensor has only three

and the piezoelectric tensor only one different value that is non zero:

$$c_{\text{GaAs}}^{\mathbf{V}} = \begin{bmatrix} c_{11} & c_{12} & c_{12} & 0 & 0 & 0 \\ c_{12} & c_{11} & c_{12} & 0 & 0 & 0 \\ c_{12} & c_{12} & c_{11} & 0 & 0 & 0 \\ \cdot & \cdot & \cdot & c_{44} & 0 & 0 \\ \cdot & \cdot & \cdot & \cdot & c_{44} & 0 \\ \cdot & \cdot & \cdot & \cdot & \cdot & c_{44} \end{bmatrix} \quad e_{\text{GaAs}}^{\mathbf{V}} = \begin{bmatrix} 0 & 0 & 0 & e_{14} & 0 & 0 \\ 0 & 0 & 0 & 0 & e_{14} & 0 \\ 0 & 0 & 0 & 0 & 0 & e_{14} \end{bmatrix}$$

The corresponding parameters for the elasticity tensor of GaAs as a function of temperature  $T$  are given by [150]:

$$\begin{aligned} c_{11} &= 12.17 \cdot 10^{10} \text{Pa} - 1.44 \cdot 10^7 \frac{\text{Pa}}{\text{K}} * T \\ c_{12} &= 5.46 \cdot 10^{10} \text{Pa} - 0.64 \cdot 10^7 \frac{\text{Pa}}{\text{K}} * T \\ c_{44} &= 6.16 \cdot 10^{10} \text{Pa} - 0.7 \cdot 10^7 \frac{\text{Pa}}{\text{K}} * T \end{aligned} \tag{A.6}$$

and the dielectric constant by [151]:

$$\epsilon = 12.35 + 2.01 \cdot 10^{-4} \frac{1}{\text{K}} * T$$

Finally, the density is given by [45]:

$$\rho(\text{GaAs}) = 5332 \frac{\text{kg}}{\text{m}^3} \tag{A.7}$$

and the piezoelectric tensor by [58]:

$$e_{14} = -0.16 \frac{\text{C}}{\text{m}^2} \tag{A.8}$$

For the simulations presented in the main text, a temperature of  $T = 10 \text{ K}$  was assumed, in accordance with the temperature prevailing in the optical measurements.

For  $\text{Al}_x\text{Ga}_{1-x}\text{As}$ , the corresponding parameters can be linearly interpolated between GaAs and AlAs [45, 152]:

$$\begin{aligned}
c_{11}(\text{Al}_x\text{Ga}_{1-x}\text{As}) &= c_{11}(\text{GaAs}) + 0.14 \cdot 10^{10} \text{Pa} \cdot x \\
c_{12}(\text{Al}_x\text{Ga}_{1-x}\text{As}) &= c_{12}(\text{GaAs}) + 0.32 \cdot 10^{10} \text{Pa} \cdot x \\
c_{44}(\text{Al}_x\text{Ga}_{1-x}\text{As}) &= c_{44}(\text{GaAs}) - 0.05 \cdot 10^{10} \text{Pa} \cdot x \\
\epsilon(\text{Al}_x\text{Ga}_{1-x}\text{As}) &= \epsilon(\text{GaAs}) - 2.84 \cdot x \\
e_{14}(\text{Al}_x\text{Ga}_{1-x}\text{As}) &= e_{14}(\text{GaAs}) - 0.065 \frac{\text{C}}{\text{m}^2} \cdot x
\end{aligned} \tag{A.9}$$

$$\rho(\text{Al}_x\text{Ga}_{1-x}\text{As}) = \rho(\text{GaAs}) - 1560 \frac{\text{kg}}{\text{m}^3} \cdot x \tag{A.10}$$

The change of the elasticity tensor is comparatively small and can usually be neglected compared to the change of the density, as it is described in the main text.

In order to describe the propagation of a SAW along the [110]-direction on a (001)-surface, the tensors have to be rotated by  $-\frac{\pi}{4}$  around the  $z$ -axis. Conventional rotation matrices cannot be applied to rotate a tensor in the Voigt notation. To avoid the elaborate back conversion to full subscripts, a technique proposed by Bond [153] can be used, allowing for the rotation in the Voigt notation by simple matrix multiplication with a matrix  $K$ . For a rotation by an angle of  $\alpha$  around the  $z$ -axis, this matrix is given by:

$$K_z = \begin{pmatrix} \cos(\alpha)^2 & \sin(\alpha)^2 & 0 & 0 & 0 & -2 \cos(\alpha) \sin(\alpha) \\ \sin(\alpha)^2 & \cos(\alpha)^2 & 0 & 0 & 0 & 2 \cos(\alpha) \sin(\alpha) \\ 0 & 0 & 1 & 0 & 0 & 0 \\ 0 & 0 & 0 & \cos(\alpha) & \sin(\alpha) & 0 \\ 0 & 0 & 0 & -\sin(\alpha) & \cos(\alpha) & 0 \\ \cos(\alpha) \sin(\alpha) & -\cos(\alpha) \sin(\alpha) & 0 & 0 & 0 & \cos(\alpha)^2 - \sin(\alpha)^2 \end{pmatrix} \tag{A.11}$$

Subsequently, the rotated elasticity tensor  $c_{\text{rot}}$  is given by:

$$c_{\text{rot}} = K_z \cdot c^{\mathbf{V}} \cdot K_z^{\text{T}} \tag{A.12}$$

For the piezoelectric tensor  $e$ , the conventional rotation matrix around the  $z$ -axis is needed:

$$R_z = \begin{pmatrix} \cos(\alpha) & -\sin(\alpha) & 0 \\ \sin(\alpha) & \cos(\alpha) & 0 \\ 0 & 0 & 1 \end{pmatrix} \tag{A.13}$$

and the rotated piezoelectric tensor  $e_{\text{rot}}$  can be calculated by:

$$e_{\text{rot}} = \left( K_z \cdot e^{\text{T}} \cdot R_z^{\text{T}} \right)^{\text{T}} \tag{A.14}$$

Consequently, for SAW propagation along the [110]-direction on a (001)-surface at  $T = 10\text{ K}$ , the elasticity tensor and the piezoelectric tensor for GaAs are given by:

$$c_{\text{GaAs}}^{\mathbf{V}} = \begin{bmatrix} 14.96 & 2.65 & 5.45 & 0 & 0 & 0 \\ 2.65 & 14.96 & 5.45 & 0 & 0 & 0 \\ 5.45 & 5.45 & 12.16 & 0 & 0 & 0 \\ 0 & 0 & 0 & 6.15 & 0 & 0 \\ 0 & 0 & 0 & 0 & 6.15 & 0 \\ 0 & 0 & 0 & 0 & 0 & 3.35 \end{bmatrix} \cdot 10^{10} \text{ Pa}$$

$$e_{\text{GaAs}}^{\mathbf{V}} = \begin{bmatrix} 0 & 0 & 0 & 0 & -0.16 & 0 \\ 0 & 0 & 0 & 0.16 & 0 & 0 \\ -0.16 & 0.16 & 0 & 0 & 0 & 0 \end{bmatrix} \cdot \frac{\text{C}}{\text{m}^2}$$



## B. Additional Resonance Fluorescence Measurements

In this chapter, some supplementary resonance fluorescence data of a dynamically strained QD shall be provided to allow a more detailed understanding of certain aspects covered in the main text.

### B.1. Time-resolved phononic sidebands

Figure B.1 shows time and energy resolved RF emission (a), time-integrated RF spectra (b) and time-dependent intensity oscillations for the ( $\pm 1$ ) sidebands (c) for three different SAW frequencies  $f_{\text{SAW}}$  of 677.5 MHz, 1016.25 MHz and 1355 MHz with rf-amplitudes  $P_{\text{rf}}$  of  $-10$  dBm,  $-6$  dBm and  $-3$  dBm, respectively. For the lowest frequency shown here (top panel), clear oscillations of the sideband intensities can be observed in time, as already considered in section 8.4. When increasing  $\omega_{\text{SAW}}$  to about 1 GHz (centre panel), intensity oscillations can barely be resolved in the time and energy resolved data shown in B.1(a). Only a closer examination of the extracted intensities for the ( $\pm 1$ ) PSBs reveals a clear, although much weaker, anti-correlated oscillation in time. In contrast, for the highest frequency of  $\omega_{\text{SAW}}/2\pi = 1.355$  GHz, no oscillations in time can be resolved. As already considered in the main text, the fact that intensity oscillations cannot be resolved at higher frequencies can be attributed to two effects. First of all the radiative decay time of the QD becomes comparable to the SAW period, thus phonons are both emitted and absorbed within one photon emission process. This limits the fundamental resolution limit of this measurement technique to the decay time  $\tau$  of the QD, similar to the stroboscopic excitation scheme introduced in 5.3.

Second of all, the absolute temporal resolution in units of  $T_{\text{SAW}}$  of the experimental setup itself decreases with increasing  $f_{\text{SAW}}$ . On the other hand, the spectral resolution in units of  $f_{\text{SAW}}$  increases with increasing  $f_{\text{SAW}}$ , which can clearly be recognized by the time-integrated spectra presented in figure B.1(b). Here, a clear increase of the spectral resolution with increasing frequency  $\omega_{\text{SAW}}$  and thus PSB splitting can be observed. While, for the two higher frequencies, neighbouring PSBs are clearly separated, for the lowest frequency already a clear overlap is recognizable.

These measurements illustrate the trade-off that must be made between spectral and temporal resolution. This is caused by the high spectral resolution of the etalon and limits

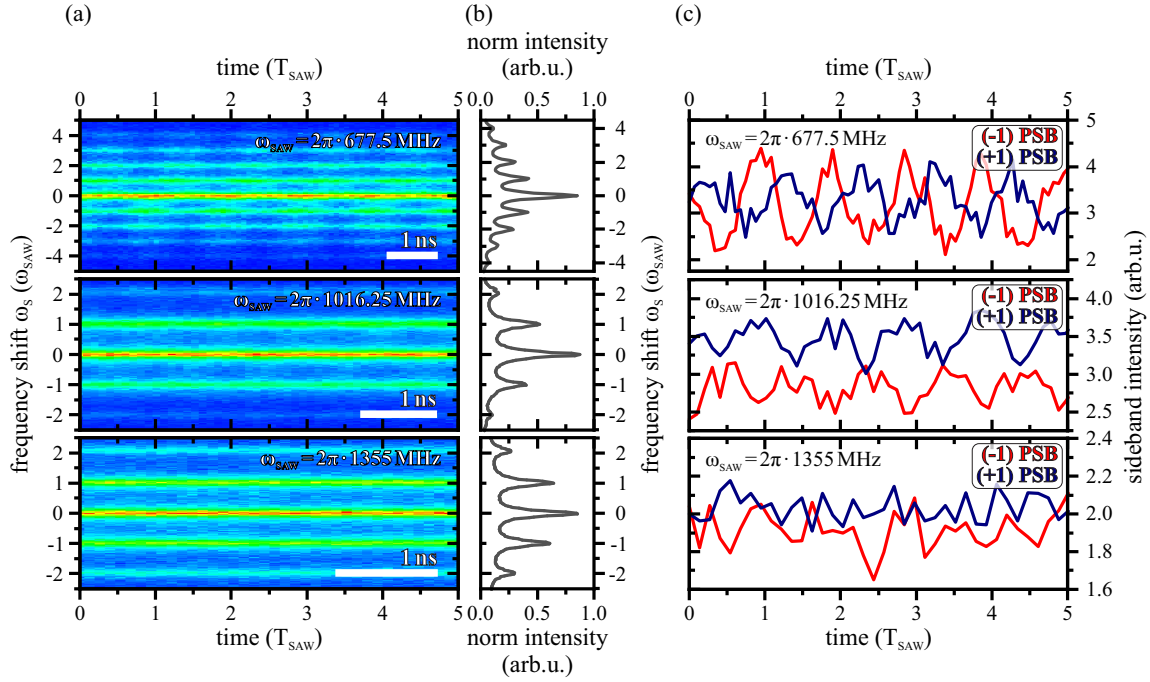


**Figure B.1.:** (a) Time and energy resolved resonance fluorescence intensity for a dynamically strained QD. (b) Time-integrated resonance fluorescence intensity, obtained by integrating the data shown in (a) over time. (c) Time dependent intensities for the  $(\pm 1)$  PSBs. Measurements are shown for three different SAW frequencies  $\omega_{\text{SAW}}/2\pi$  of 677.5 MHz (top panels), 1016.25 MHz (centre panels) and 1355 MHz (bottom panels).

the temporal resolution to about  $\Delta t = 0.35$  ns (see equation 8.5). Decreasing the SAW frequency  $\omega_{\text{SAW}}$  makes it possible to increase the relative temporal resolution  $\Delta t/T_{\text{SAW}}$ , while the sideband splitting, and thus the relative spectral resolution, is decreased. The exact opposite applies to an increase in the SAW frequency. Therefore the SAW frequency can be adjusted to match the requirements for a specific experiment.

Finally, it shall be noted that a tuning of the absolute resolution of the experimental setup is not possible, as the used etalon has spherical end mirrors. Thus, its resolution is determined by the respective mode that is formed inside the cavity and is not affected by the coupling of the light to the cavity. It just has to be ensured that light is only coupled to a single mode of the etalon. In contrast, for an etalon with planar mirrors the resolution can be influenced by the shape of the incoming beam and an increasing beam divergence leads to a decrease of the spectral resolution.

## B.2. Detuned optical excitation

In this section, the parametric excitation of a dynamically strained QD is expanded to stronger phonon fields and thus a higher number of PSBs. In contrast to the measurement shown in figure 8.4, a non-chirped transducer was used for the measurements presented in figure B.2. Therefore, the SAW frequency is shifted to  $\omega_{\text{SAW}}/2\pi = 1.355$  GHz and lower rf-amplitudes  $P_{\text{rf}}$  are necessary to achieve equally strong phonon fields. In all three cases

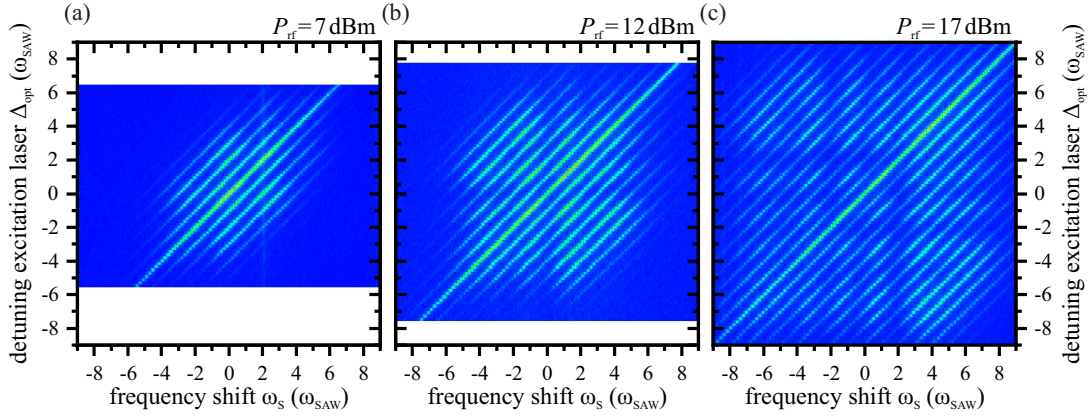


**Figure B.2.:** Resonance fluorescence spectra plotted in a false-colour representation as a function of detuning  $\Delta_{\text{opt}}$  of the driving optical field. Measurements were performed for different rf-amplitudes of  $P_{\text{rf}} = 7$  dBm (a)<sup>1</sup>,  $P_{\text{rf}} = 12$  dBm (b) and  $P_{\text{rf}} = 17$  dBm (c).

shown here, the ZPL follows the energy shift of the excitation laser and PSBs are formed on both sides of the ZPL, equally spaced by  $\omega_{\text{SAW}}$ . The number of observed sidebands, however, increases with the rf-amplitude. Whereas in figure 8.4 four PSBs can be observed on both sides of the ZPL, here five, nine and 14 PSBs can be observed for rf-amplitudes of 7 dBm, 12 dBm and 17 dBm, respectively. While the mirror symmetry of the intensity pattern with respect to the ZPL remains unchanged the structure itself becomes more complicated. With increasing SAW amplitude and thus modulation amplitude, the intensity of a sideband does not necessarily decrease linearly with the sideband index  $n$ . For that reason, a full theoretical consideration is inevitable, to fully describe the intensity pattern.

<sup>1</sup>The fade vertical line in figure B.2(a) at  $\omega_s = 2$  GHz stems from a higher mode of the laser that was used to provide a stable energy reference. This light is separated from the excitonic transition by multiple FSRs and thus does not interact with the QD.

### B.3. Detuned SAW frequency mixing

In this section, an additional measurement for the detuned frequency mixing:

$$\omega_{\text{SAW},2} = 2 \cdot \omega_{\text{SAW},1} + \Delta_{\text{SAW}} \quad (\text{B.1})$$

shall be provided. Except for the value of  $\Delta_{\text{SAW}}$ , the experimental conditions are identical to the measurement presented in figure 8.10 ( $\omega_{\text{SAW},1} = 650 \text{ MHz}$ ,  $P_{\text{rf},1} = 12 \text{ dBm}$  and  $P_{\text{rf},2} = 17 \text{ dBm}$ ). The detuning was increased by a factor of two to  $\Delta_{\text{SAW}} = 50 \mu\text{Hz}$ , resulting in a beat period of  $T_{\Delta} = 2 \cdot 10^4 \text{ s} = 333.\bar{3} \text{ min} = 5.5 \text{ h}$ . The resulting measurement is shown in figure B.3, covering a time range of 350 min and about one beating period. As expected, the PSBs intensities shown in figure B.3(a) exhibit pronounced oscillations

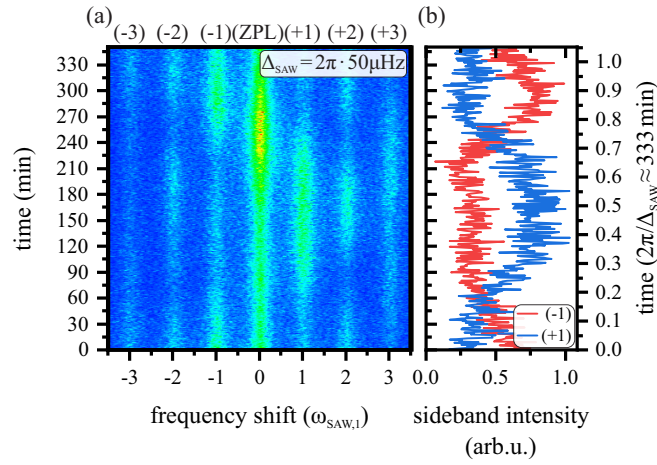


**Figure B.3.:** (a) Resonance fluorescence spectra for a detuning of  $\Delta_{\text{SAW}}/2\pi = 50 \mu\text{Hz}$ . PSBs show intensity oscillations with a period of  $T_{\Delta} = 2\pi/\Delta_{\text{SAW}} \approx 333 \text{ min}$ . (b) Extracted intensities of the  $(\pm 1)$  sidebands as a function of time in units of  $T_{\Delta} = 2\pi/\Delta_{\text{SAW}}$ .

with a period of  $T_{\Delta}$ . This becomes particularly clear when looking at the extracted  $(\pm 1)$  sideband intensities plotted as a function of time in figure B.3. This imprinted beating frequency  $\Delta_{\text{SAW}}$  is more than 13 orders of magnitude smaller than the applied phononic fields  $\omega_{\text{SAW}}$ , underlining the stability of this scheme.

The lowest possible detuning that can be achieved with the used experimental setup is  $\Delta_{\text{SAW}} = 1 \mu\text{Hz}$ , limited by the capabilities of the used signal generators. However, this would result in a beating period of  $T_{\Delta} = 10^6 \text{ s} = 277.\bar{7} \text{ h}$ , corresponding to over 11.2 days, making the experimental verification impractical.

## C. Fabrication of photonic and phononic crystals

The fabrication process of photonic and phononic crystal membranes are very similar and will be briefly sketched in this chapter. While the fabrication of the photonic cavities was performed by Thorsten Reichert<sup>1</sup> in the research group of M. Kaniber<sup>1</sup> and J. Finley<sup>1</sup> at the TU Munich, the snowflake phononic crystal structures presented in this work were fabricated at the University Augsburg.

As a starting point of the fabrication process, a sample with a specific layer sequence is

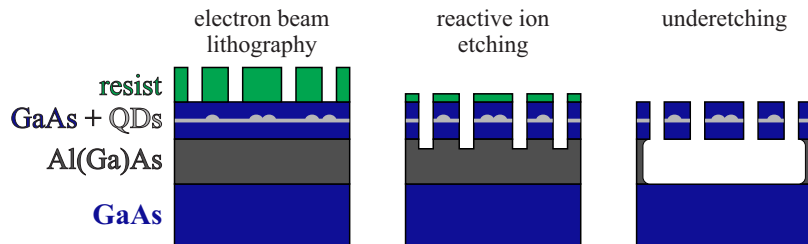


**Figure C.1.:** Main steps for the fabrication of suspended photonic/phononic crystal membranes. The geometry of the crystal is defined in a layer of resist by electron beam lithography and subsequent development (left panel). The pattern is transferred from the resist to the underlying substrate by reactive ion etching (middle panel). Finally, the sacrificial layer below the structure is removed by hydrofluoric acid and thus a suspended membrane is formed (right panel).

needed, depicted in figure C.1. The top layer of the substrate is GaAs, which will later form the free standing membrane and contains a layer of QDs at the centre. This layer is separated from the GaAs substrate by the so-called sacrificial layer, consisting of AlAs or  $\text{Al}_x\text{Ga}_{1-x}\text{As}$  with a high aluminium content. The three main steps of the fabrication are shown in figure C.1. In the first step, the sample is coated with a layer of positive electron beam resist (ZEP520A), the resist is patterned with the respective structure by electron beam lithography (EBL) and subsequently developed, removing the exposed resist. Since the used resist has a comparatively high resistance against dry etching and the membrane thickness is small ( $< 250$  nm), the pattern can directly be transferred from the resist to the sample using reactive ion etching (RIE). For both fabrication processes (photonic crystals at the TU Munich and phononic crystals at Augsburg University), a

<sup>1</sup>Walter Schottky Institut, Technische Universität München

chlorine based inductively coupled plasma (ICP) was used for dry etching the  $\text{Al}_x\text{Ga}_{1-x}\text{As}$  layers. While for the fabrication of photonic crystals, the plasma was composed of argon (Ar) and tetrachlorosilane ( $\text{SiCl}_4$ ), for the fabrication of phononic crystals, the plasma was composed of argon (Ar), chlorine ( $\text{Cl}_2$ ) and boron trichloride ( $\text{BCl}_3$ ). At this step, it must be ensured that the lithographically defined structure is etched all the way through the membrane and into the sacrificial layer. At the same time, it must be ensured that the resist is at least partly preserved to protect the membrane from etching. In the last step, the remaining resist is removed and the sacrificial layer beneath the etched substrate is selectively etched by hydrofluoric acid (HF), leaving behind a free standing membrane. Depending on the thickness of the airgap below the suspended membrane and the lateral expansion of the membrane, capillary forces can destroy the membrane when the sample is dried after under-etching. Thanks to their comparable small size, this was not an issue for the photonic crystals but, for the phononic crystals, critical point drying had to be applied to avoid surface tension and the consequent destruction of the membrane.

## D. Phononic snowflake waveguides

The band structures of the waveguide geometry introduced in 9.10(b) are presented in figures D.1(a) and (b) for the symmetric and antisymmetric modes, respectively. The design parameters of the waveguides are given by  $a = 3 \mu\text{m}$   $r = 1.3 \mu\text{m}$   $w = 0.55 \mu\text{m}$   $d = 0.22 \mu\text{m}$  and  $\Delta = 0.5 \mu\text{m}$ . Compared to the band structure of the modified waveguide design, shown in the main text (figure 9.11), a larger number of waveguiding bands with, in most cases, a flatter course can be seen for this WG geometry. This is attributed to the higher complexity of the lateral boundaries, resulting in an increased interaction with the material and a higher number of degrees of freedom. Looking at the spatial mode profiles in the right panel of figure D.1 reveals that a majority of the mechanical modes

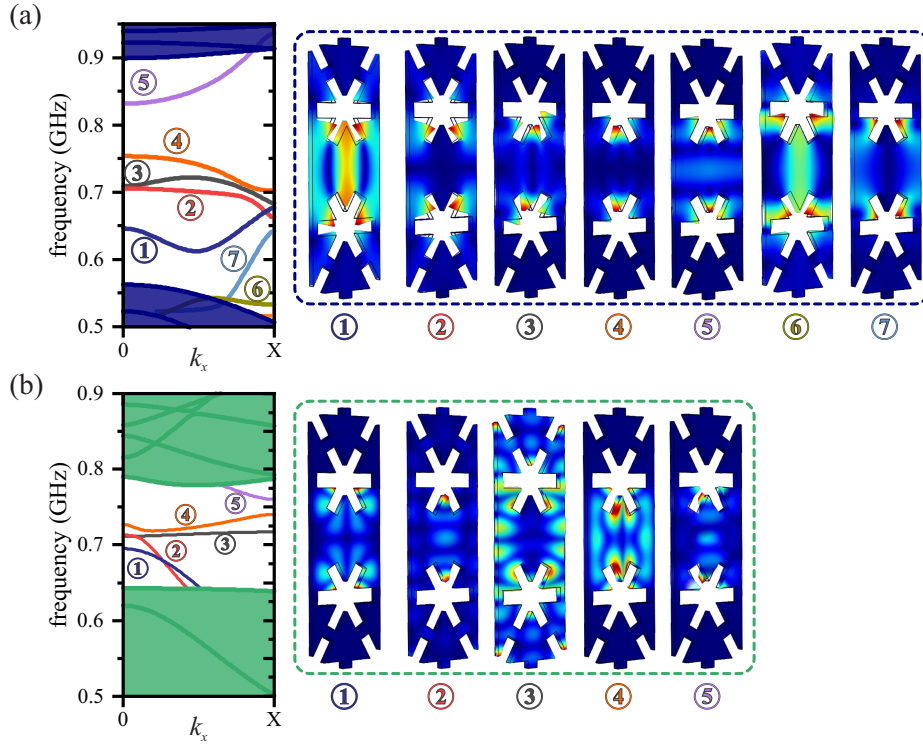


**Figure D.1.:** Band structure for the symmetric (a) and antisymmetric (b) waveguide modes. Right panels show the spatial mode profile of the respective bands labelled in the band structure. Colour code indicates the normalized total displacement.

are localised in the sharp corners at the boundary of the waveguide. On the one hand this allows for a precise tuning of the mechanical bands by adjusting the geometry of the WG. This enables, for example, to achieve co-localisation with an optical mode and thus optomechanical coupling, as it was shown for this type of structure [145]. On the other hand, it makes the waveguide highly susceptible to imperfections in the fabrication process. Furthermore, due to the strong localisation of the mechanical modes, only a weak interaction with quantum emitters at the WG centre can be expected.

The structure treated here is not only suitable for guiding the propagation of phonons but also photons. For more details on the properties of the optical waveguide, one is referred to [136].

## E. List of abbreviations

APD	avalanche photo diode
CCD	charge coupled device
DAQ	data acquisition
EBL	electron beam lithography
FEM	finite element method
FSR	free spectral range
HBT	Hanbury Brown and Twiss
IDT	interdigital transducer
LDE	liquid droplet etching
NIM	nuclear instrument module
OMC	optomechanical crystals
PL	photoluminescence
QCSE	quantum confined stark effect
QD	quantum dot
QW	quantum well
RF	resonance fluorescence
rf	radio frequency
SAW	surface acoustic wave
SEM	Scanning electron microscope
SPAD	single photon avalanche diode
STCD	spatio-temporal carrier dynamics
TCSPC	time-correlated single photon counting
TLS	two-level system



# Bibliography

- [1] Rincon, P. Google claims 'quantum supremacy' for computer. *BBC News website* (2019). URL [https://www.bbc.com/news/science-environment-50154993?intlink\\_from\\_url=https://www.bbc.com/news/topics/cyz9ex69xwlt/quantum-computing&#38;link\\_location=live-reporting-story](https://www.bbc.com/news/science-environment-50154993?intlink_from_url=https://www.bbc.com/news/topics/cyz9ex69xwlt/quantum-computing&#38;link_location=live-reporting-story).
- [2] Overbye, D. Quantum computing is coming, bit by qubit (2019). URL <https://www.nytimes.com/2019/10/21/science/quantum-computer-physics-qubits.html>.
- [3] Kremp, M. Google meldet Durchbruch mit Quantencomputer. *Spiegel online* (2019). URL <https://www.spiegel.de/netzwelt/gadgets/quantenueberlegenheit-google-meldet-durchbruch-beim-quantencomputing-a-1292901.html>.
- [4] Arute, F. *et al.* Quantum supremacy using a programmable superconducting processor. *Nature* **574**, 505–510 (2019).
- [5] Grover, L. K. Quantum Mechanics Helps in Searching for a Needle in a Haystack. *Physical Review Letters* **79**, 325–328 (1997).
- [6] Shor, P. W. Algorithms for quantum computation: discrete logarithms and factoring. In *Proceedings 35th Annual Symposium on Foundations of Computer Science* (IEEE Comput. Soc. Press).
- [7] Vandersypen, L. M. K. *et al.* Experimental realization of Shor's quantum factoring algorithm using nuclear magnetic resonance. *Nature* **414**, 883–887 (2001).
- [8] Lucero, E. *et al.* Computing prime factors with a Josephson phase qubit quantum processor. *Nature Physics* **8**, 719–723 (2012).
- [9] Martín-López, E. *et al.* Experimental realization of Shor's quantum factoring algorithm using qubit recycling. *Nature Photonics* **6**, 773–776 (2012).
- [10] Bennett, C. H. & Brassard, G. Quantum cryptography: Public key distribution and coin tossing. *Theoretical Computer Science* **560**, 7–11 (2014).
- [11] Park, J. L. The concept of transition in quantum mechanics. *Foundations of Physics* **1**, 23–33 (1970).

- [12] Wootters, W. K. & Zurek, W. H. A single quantum cannot be cloned. *Nature* **299**, 802–803 (1982).
- [13] Dieks, D. Communication by EPR devices. *Physics Letters A* **92**, 271–272 (1982).
- [14] Brassard, G., Lütkenhaus, N., Mor, T. & Sanders, B. C. Limitations on Practical Quantum Cryptography. *Physical Review Letters* **85**, 1330–1333 (2000).
- [15] Michler, P. A Quantum Dot Single-Photon Turnstile Device. *Science* **290**, 2282–2285 (2000).
- [16] Akopian, N. *et al.* Entangled Photon Pairs from Semiconductor Quantum Dots. *Physical Review Letters* **96** (2006).
- [17] Stevenson, R. M. *et al.* A semiconductor source of triggered entangled photon pairs. *Nature* **439**, 179–182 (2006).
- [18] Hafenbrak, R. *et al.* Triggered polarization-entangled photon pairs from a single quantum dot up to 30 K. *New Journal of Physics* **9**, 315–315 (2007).
- [19] Press, D., Ladd, T. D., Zhang, B. & Yamamoto, Y. Complete quantum control of a single quantum dot spin using ultrafast optical pulses. *Nature* **456**, 218–221 (2008).
- [20] Yuan, Z. Electrically Driven Single-Photon Source. *Science* **295**, 102–105 (2001).
- [21] Salter, C. L. *et al.* An entangled-light-emitting diode. *Nature* **465**, 594–597 (2010).
- [22] Zhang, J. *et al.* High yield and ultrafast sources of electrically triggered entangled-photon pairs based on strain-tunable quantum dots. *Nature Communications* **6** (2015).
- [23] Drexler, H., Leonard, D., Hansen, W., Kotthaus, J. P. & Petroff, P. M. Spectroscopy of Quantum Levels in Charge-Tunable InGaAs Quantum Dots. *Physical Review Letters* **73**, 2252–2255 (1994).
- [24] Warburton, R. J. *et al.* Optical emission from a charge-tunable quantum ring. *Nature* **405**, 926–929 (2000).
- [25] Finley, J. J. *et al.* Quantum-confined Stark shifts of charged exciton complexes in quantum dots. *Physical Review B* **70** (2004).
- [26] Gérard, J. *et al.* Enhanced Spontaneous Emission by Quantum Boxes in a Monolithic Optical Microcavity. *Physical Review Letters* **81**, 1110–1113 (1998).
- [27] Reithmaier, J. P. *et al.* Strong coupling in a single quantum dot–semiconductor microcavity system. *Nature* **432**, 197–200 (2004).

- 
- [28] Peter, E. *et al.* Exciton-Photon Strong-Coupling Regime for a Single Quantum Dot Embedded in a Microcavity. *Physical Review Letters* **95** (2005).
- [29] Hennessy, K. *et al.* Quantum nature of a strongly coupled single quantum dot-cavity system. *Nature* **445**, 896–899 (2007).
- [30] Völkl, S. *et al.* Enhanced Sequential Carrier Capture into Individual Quantum Dots and Quantum Posts Controlled by Surface Acoustic Waves. *Nano Letters* **10**, 3399–3407 (2010).
- [31] Couto, O. D. D. *et al.* Photon anti-bunching in acoustically pumped quantum dots. *Nature Photonics* **3**, 645–648 (2009).
- [32] Gell, J. R. *et al.* Modulation of single quantum dot energy levels by a surface-acoustic-wave. *Applied Physics Letters* **93**, 081115 (2008).
- [33] Pustowski, J. *et al.* Independent dynamic acousto-mechanical and electrostatic control of individual quantum dots in a LiNbO<sub>3</sub>-GaAs hybrid. *Applied Physics Letters* **106**, 013107 (2015).
- [34] Weiß, M. *et al.* Dynamic Acoustic Control of Individual Optically Active Quantum Dot-like Emission Centers in Heterostructure Nanowires. *Nano Letters* **14**, 2256–2264 (2014).
- [35] Weiß, M. & Krenner, H. J. Interfacing quantum emitters with propagating surface acoustic waves. *Journal of Physics D: Applied Physics* **51**, 373001 (2018).
- [36] NSM Archive - Physical Properties of Semiconductors. URL <http://www.ioffe.ru/SVA/NSM/Semicond/GaAs/bandstr.html>.
- [37] Nam, S. B. *et al.* Free-exciton energy spectrum in GaAs. *Physical Review B* **13**, 761–767 (1976).
- [38] Blakemore, J. S. Semiconducting and other major properties of gallium arsenide. *Journal of Applied Physics* **53**, R123–R181 (1982).
- [39] Aspnes, D. E. GaAs lower conduction-band minima: Ordering and properties. *Physical Review B* **14**, 5331–5343 (1976).
- [40] Vurgaftman, I., Meyer, J. R. & Ram-Mohan, L. R. Band parameters for III-V compound semiconductors and their alloys. *Journal of Applied Physics* **89**, 5815–5875 (2001).
- [41] Vehten, J. A. V. & Bergstresser, T. K. Electronic Structures of Semiconductor Alloys. *Physical Review B* **1**, 3351–3358 (1970).

- [42] Aspnes, D. E., Kelso, S. M., Logan, R. A. & Bhat, R. Optical properties of  $\text{Al}_x\text{Ga}_{1-x}\text{As}$ . *Journal of Applied Physics* **60**, 754–767 (1986).
- [43] Henning, J. C. M., Ansems, J. P. M. & Roksnoer, P. J. Spectroscopic determination of  $L_6$  conduction band minima in  $\text{Al}_x\text{Ga}_{1-x}\text{As}$ . *Journal of Physics C: Solid State Physics* **19**, L335–L338 (1986).
- [44] Guzzi, M. *et al.* Indirect-energy-gap dependence on Al concentration in  $\text{Al}_x\text{Ga}_{1-x}\text{As}$  alloys. *Physical Review B* **45**, 10951–10957 (1992).
- [45] Adachi, S. GaAs, AlAs, and  $\text{Al}_x\text{Ga}_{1-x}\text{As}$ : Material parameters for use in research and device applications. *Journal of Applied Physics* **58**, R1–R29 (1985).
- [46] Krenner, H. J. *et al.* Recent advances in exciton-based quantum information processing in quantum dot nanostructures. *New Journal of Physics* **7**, 184–184 (2005).
- [47] Gywat, O., Krenner, H. J. & Berezovsky, J. *Spins in Optically Active Quantum Dots: Concepts and Methods* (Wiley-VCH, 2010).
- [48] Brunner, K., Abstreiter, G., Böhm, G., Tränkle, G. & Weimann, G. Sharp-Line Photoluminescence and Two-Photon Absorption of Zero-Dimensional Biexcitons in a GaAs/AlGaAs Structure. *Physical Review Letters* **73**, 1138–1141 (1994).
- [49] Finley, J. J. *et al.* Charged and neutral exciton complexes in individual self-assembled In(Ga)As quantum dots. *Physical Review B* **63** (2001).
- [50] Benson, O., Santori, C., Pelton, M. & Yamamoto, Y. Regulated and Entangled Photons from a Single Quantum Dot. *Physical Review Letters* **84**, 2513–2516 (2000).
- [51] Bayer, M. *et al.* Fine structure of neutral and charged excitons in self-assembled In(Ga)As/(Al)GaAs quantum dots. *Physical Review B* **65** (2002).
- [52] Datta, S. *Surface acoustic wave devices* (Prentice-Hall, 1986).
- [53] D. Royer, E. D. *Elastic Waves in Solids I* (Springer Berlin Heidelberg, 1999).
- [54] D. Royer, E. D. *Elastic Waves in Solids II* (Springer-Verlag GmbH, 1999).
- [55] Morgan, D. *Surface Acoustic Wave Filters: With Applications to Electronic Communications and Signal Processing*. Studies in Electrical and Electronic Engineering (Elsevier Science, 2010).
- [56] Rayleigh, L. On Waves Propagated along the Plane Surface of an Elastic Solid. *Proceedings of the London Mathematical Society* **s1-17**, 4–11 (1885).

- 
- [57] Knuuttila, J. V., Tikka, P. T. & Salomaa, M. M. Scanning Michelson interferometer for imaging surface acoustic wave fields. *Optics Letters* **25**, 613–615 (2000).
- [58] Arlt, G. & Quadflieg, P. Piezoelectricity in III-Vs compounds with a phenomenological analysis of the piezoelectric effect. *Physica Status Solidi (b)* **25**, 323–330 (1968).
- [59] Campbell, C. *Surface Acoustic Wave Devices and Their Signal Processing Applications* (Academic Press, 2012).
- [60] Tancrrell, R. H. & Holland, M. G. Acoustic surface wave filters. *Proceedings of the IEEE* **59**, 393–409 (1971).
- [61] Matthews, H. (ed.) *Surface wave filters: Design, construction, and use* (1977).
- [62] Schüle, F. J. R. *Dynamische Kontrolle optisch aktiver Halbleiter-Quantenpunkte mittels akustischer Oberflächenwellen*. doctoralthesis, Universität Augsburg (2014).
- [63] Márquez, J., Geelhaar, L. & Jacobi, K. Atomically resolved structure of InAs quantum dots. *Applied Physics Letters* **78**, 2309–2311 (2001).
- [64] Stranski, J. & Krastanow, L. *Zur Theorie der orientierten Ausscheidung von Ionenkristallen aufeinander* (1938).
- [65] Goldstein, L., Glas, F., Marzin, J. Y., Charasse, M. N. & Roux, G. L. Growth by molecular beam epitaxy and characterization of InAs/GaAs strained-layer superlattices. *Applied Physics Letters* **47**, 1099–1101 (1985).
- [66] Leonard, D., Krishnamurthy, M., Reaves, C. M., Denbaars, S. P. & Petroff, P. M. Direct formation of quantum-sized dots from uniform coherent islands of InGaAs on GaAs surfaces. *Applied Physics Letters* **63**, 3203–3205 (1993).
- [67] Bauer, E. Phänomenologische Theorie der Kristallabscheidung an Oberflächen. I. *Zeitschrift für Kristallographie* **110**, 372–394 (1958).
- [68] Wang, Z. M., Liang, B. L., Sablon, K. A. & Salamo, G. J. Nanoholes fabricated by self-assembled gallium nanodrive on GaAs(100). *Applied Physics Letters* **90**, 113120 (2007).
- [69] Atkinson, P., Zallo, E. & Schmidt, O. G. Independent wavelength and density control of uniform GaAs/AlGaAs quantum dots grown by infilling self-assembled nanoholes. *Journal of Applied Physics* **112**, 054303 (2012).
- [70] Kumar, S. *et al.* Strain-induced tuning of the emission wavelength of high quality GaAs/AlGaAs quantum dots in the spectral range of the  $^{87}\text{Rb}$  D<sub>2</sub> lines. *Applied Physics Letters* **99**, 161118 (2011).

- [71] Rocke, C. *et al.* Acoustically Driven Storage of Light in a Quantum Well. *Physical Review Letters* **78**, 4099–4102 (1997).
- [72] Rocke, C., Govorov, A. O., Wixforth, A., Böhm, G. & Weimann, G. Exciton ionization in a quantum well studied by surface acoustic waves. *Physical Review B* **57**, R6850–R6853 (1998).
- [73] Völk, S. *et al.* Direct observation of dynamic surface acoustic wave controlled carrier injection into single quantum posts using phase-resolved optical spectroscopy. *Applied Physics Letters* **98**, 023109 (2011).
- [74] Krenner, H. J. *et al.* Surface acoustic wave controlled carrier injection into self-assembled quantum dots and quantum posts. *physica status solidi (c)* **9**, 407–410 (2011).
- [75] Schülein, F. J. R. *et al.* Acoustically regulated carrier injection into a single optically active quantum dot. *Physical Review B* **88** (2013).
- [76] Völk, S. *et al.* Surface acoustic wave mediated carrier injection into individual quantum post nano emitters. *Nanotechnology* **23**, 285201 (2012).
- [77] Hernández-Mínguez, A. *et al.* Acoustically Driven Photon Antibunching in Nanowires. *Nano Letters* **12**, 252–258 (2011).
- [78] Pollak, F. H. & Cardona, M. Piezo-Electroreflectance in Ge, GaAs, and Si. *Physical Review* **172**, 816–837 (1968).
- [79] Schülein, F. J. R. *et al.* Fourier synthesis of radiofrequency nanomechanical pulses with different shapes. *Nature Nanotechnology* **10**, 512–516 (2015).
- [80] Nysten, E. D. S. *et al.* Multi-harmonic quantum dot optomechanics in fused LiNbO<sub>3</sub>-GaAs hybrids. *Journal of Physics D: Applied Physics* **50**, 43LT01 (2017).
- [81] Miller, D. A. B. *et al.* Band-Edge Electroabsorption in Quantum Well Structures: The Quantum-Confined Stark Effect. *Physical Review Letters* **53**, 2173–2176 (1984).
- [82] Heller, W., Bockelmann, U. & Abstreiter, G. Electric-field effects on excitons in quantum dots. *Physical Review B* **57**, 6270–6273 (1998).
- [83] Weiß, M. *et al.* Surface acoustic wave regulated single photon emission from a coupled quantum dot–nanocavity system. *Applied Physics Letters* **109**, 033105 (2016).
- [84] Sauer, W. *et al.* X-ray imaging and diffraction from surface phonons on GaAs. *Applied Physics Letters* **75**, 1709–1711 (1999).

- 
- [85] Zolotoyabko, E. & Quintana, J. P. Time and phase control of X-rays in stroboscopic diffraction experiments. *Review of Scientific Instruments* **73**, 1643–1645 (2002).
- [86] Reusch, T. *et al.* Standing surface acoustic waves in LiNbO<sub>3</sub> studied by time resolved X-ray diffraction at Petra III. *AIP Advances* **3**, 072127 (2013).
- [87] van den Heuvel, A. Use of rotated electrodes for amplitude weighting in interdigital surface-wave transducers. *Applied Physics Letters* **21**, 280–282 (1972).
- [88] Tancrell, R. H., Schulz, M. B., Barrett, H. H., Davis, L. & Holland, M. G. Dispersive delay lines using ultrasonic surface waves. *Proceedings of the IEEE* **57**, 1211–1213 (1969).
- [89] Klauder, J. R., Price, A. C., Darlington, S. & Albersheim, W. J. The Theory and Design of Chirp Radars. *Bell System Technical Journal* **39**, 745–808 (1960).
- [90] Court, I. Microwave Acoustic Devices for Pulse Compression Filters. *IEEE Transactions on Microwave Theory and Techniques* **17**, 968–986 (1969).
- [91] Weiß, M. *et al.* Multiharmonic Frequency-Chirped Transducers for Surface-Acoustic-Wave Optomechanics. *Physical Review Applied* **9** (2018).
- [92] de Lima, M. M., Beck, M., Hey, R. & Santos, P. V. Compact Mach-Zehnder acousto-optic modulator. *Applied Physics Letters* **89**, 121104 (2006).
- [93] Blattmann, R., Krenner, H. J., Kohler, S. & Hänggi, P. Entanglement creation in a quantum-dot–nanocavity system by Fourier-synthesized acoustic pulses. *Physical Review A* **89** (2014).
- [94] Hong, C. K., Ou, Z. Y. & Mandel, L. Measurement of subpicosecond time intervals between two photons by interference. *Physical Review Letters* **59**, 2044–2046 (1987).
- [95] Portalupi, S. L. & Michler, P. Resonantly Excited Quantum Dots: Superior Non-classical Light Sources for Quantum Information. In *Quantum Dots for Quantum Information Technologies*, 77–121 (Springer International Publishing, 2017).
- [96] Scully, M. O. *Quantum Optics* (Cambridge University Press, 1997).
- [97] Walls, D. *Quantum Optics* (Springer, 2007).
- [98] Mollow, B. R. Power Spectrum of Light Scattered by Two-Level Systems. *Physical Review* **188**, 1969–1975 (1969).
- [99] Walls, D. F. *Quantum optics* (Springer, 1994).

- [100] Nguyen, H. S. *et al.* Ultra-coherent single photon source. *Applied Physics Letters* **99**, 261904 (2011).
- [101] Matthiesen, C., Vamivakas, A. N. & Atatüre, M. Subnatural Linewidth Single Photons from a Quantum Dot. *Physical Review Letters* **108** (2012).
- [102] Matthiesen, C. *et al.* Phase-locked indistinguishable photons with synthesized waveforms from a solid-state source. *Nature Communications* **4** (2013).
- [103] Schuda, F., Stroud, C. R. & Hercher, M. Observation of the resonant Stark effect at optical frequencies. *Journal of Physics B: Atomic and Molecular Physics* **7**, L198–L202 (1974).
- [104] Wu, F. Y., Grove, R. E. & Ezekiel, S. Investigation of the Spectrum of Resonance Fluorescence Induced by a Monochromatic Field. *Physical Review Letters* **35**, 1426–1429 (1975).
- [105] Muller, A. *et al.* Resonance Fluorescence from a Coherently Driven Semiconductor Quantum Dot in a Cavity. *Physical Review Letters* **99** (2007).
- [106] Vamivakas, A. N., Zhao, Y., Lu, C.-Y. & Atatüre, M. Spin-resolved quantum-dot resonance fluorescence. *Nature Physics* **5**, 198–202 (2009).
- [107] Jaynes, E. & Cummings, F. Comparison of quantum and semiclassical radiation theories with application to the beam maser. *Proceedings of the IEEE* **51**, 89–109 (1963).
- [108] Metcalfe, M., Carr, S. M., Muller, A., Solomon, G. S. & Lawall, J. Resolved Sideband Emission of InAs/GaAs Quantum Dots Strained by Surface Acoustic Waves. *Physical Review Letters* **105** (2010).
- [109] Nguyen, H. S. *et al.* Optically Gated Resonant Emission of Single Quantum Dots. *Physical Review Letters* **108** (2012).
- [110] Bennett, A. J. *et al.* Cavity-enhanced coherent light scattering from a quantum dot. *Science Advances* **2**, e1501256 (2016).
- [111] Lagoudakis, K. *et al.* Observation of Mollow Triplets with Tunable Interactions in Double Lambda Systems of Individual Hole Spins. *Physical Review Letters* **118** (2017).
- [112] Kuhlmann, A. V. *et al.* A dark-field microscope for background-free detection of resonance fluorescence from single semiconductor quantum dots operating in a set-and-forget mode. *Review of Scientific Instruments* **84**, 073905 (2013).

- 
- [113] Novotny, L. & Hecht, B. *Principles of Nano-Optics* (Cambridge University Press, 2006).
- [114] Schrama, C. A., Nienhuis, G., Dijkerman, H. A., Steijsiger, C. & Heideman, H. G. M. Intensity correlations between the components of the resonance fluorescence triplet. *Physical Review A* **45**, 8045–8055 (1992).
- [115] Ulhaq, A. *et al.* Detuning-dependent Mollow triplet of a coherently-driven single quantum dot. *Optics Express* **21**, 4382 (2013).
- [116] Weiler, S. *Mollow triplet emission properties and dephasing effects in semiconductor quantum dots*. Ph.D. thesis (2014).
- [117] Weiß, M. *et al.* Optomechanical single photon frequency division multiplexing <http://arxiv.org/abs/1910.12949v1>.
- [118] Villa, B. *et al.* Surface acoustic wave modulation of a coherently driven quantum dot in a pillar microcavity. *Applied Physics Letters* **111**, 011103 (2017).
- [119] Aghaeimeibodi, S. *et al.* Integration of quantum dots with lithium niobate photonics. *Applied Physics Letters* **113**, 221102 (2018).
- [120] Balram, K. C., Davanço, M. I., Song, J. D. & Srinivasan, K. Coherent coupling between radiofrequency, optical and acoustic waves in piezo-optomechanical circuits. *Nature Photonics* **10**, 346–352 (2016).
- [121] Noda, S., Fujita, M. & Asano, T. Spontaneous-emission control by photonic crystals and nanocavities. *Nature Photonics* **1**, 449–458 (2007).
- [122] Nelson, E. C. *et al.* Epitaxial growth of three-dimensionally architected optoelectronic devices. *Nature Materials* **10**, 676–681 (2011).
- [123] Joannopoulos, J. D., Johnson, S. G., Winn, J. N. & Meade, R. D. *Photonic Crystals: Molding the Flow of Light - Second Edition* (Princeton University Press, 2008).
- [124] Chalcraft, A. R. A. *et al.* Mode structure of the L3 photonic crystal cavity. *Applied Physics Letters* **90**, 241117 (2007).
- [125] Reichert, T. *et al.* Highly directed emission from self-assembled quantum dots into guided modes in disordered photonic-crystal waveguides. *Physical Review B* **90** (2014).
- [126] Fox, M. *Quantum Optics* (Oxford University Press, 2006).
- [127] Thon, S. M. *et al.* Strong coupling through optical positioning of a quantum dot in a photonic crystal cavity. *Applied Physics Letters* **94**, 111115 (2009).

- [128] Purcell, E. M. Proceedings of the American Physical Society. *Physical Review* **69**, 674–674 (1946).
- [129] Hennessy, K. *et al.* Tuning photonic crystal nanocavity modes by wet chemical digital etching. *Applied Physics Letters* **87**, 021108 (2005).
- [130] Strauf, S. *et al.* Frequency control of photonic crystal membrane resonators by monolayer deposition. *Applied Physics Letters* **88**, 043116 (2006).
- [131] Faraon, A. *et al.* Local quantum dot tuning on photonic crystal chips. *Applied Physics Letters* **90**, 213110 (2007).
- [132] Winger, M. *et al.* Explanation of Photon Correlations in the Far-Off-Resonance Optical Emission from a Quantum-Dot–Cavity System. *Physical Review Letters* **103** (2009).
- [133] Fuhrmann, D. A. *et al.* Dynamic modulation of photonic crystal nanocavities using gigahertz acoustic phonons. *Nature Photonics* **5**, 605–609 (2011).
- [134] Kapfinger, S. *et al.* Dynamic acousto-optic control of a strongly coupled photonic molecule. *Nature Communications* **6** (2015).
- [135] Hohenester, U. *et al.* Phonon-assisted transitions from quantum dot excitons to cavity photons. *Physical Review B* **80** (2009).
- [136] Safavi-Naeini, A. H. & Painter, O. Design of optomechanical cavities and waveguides on a simultaneous bandgap phononic-photonic crystal slab. *Optics Express* **18**, 14926 (2010).
- [137] Safavi-Naeini, A. H. & Painter, O. Optomechanical Crystal Devices. In *Cavity Optomechanics*, 195–231 (Springer Berlin Heidelberg, 2014).
- [138] Brendel, C., Peano, V., Painter, O. J. & Marquardt, F. Pseudomagnetic fields for sound at the nanoscale. *Proceedings of the National Academy of Sciences* **114**, E3390–E3395 (2017).
- [139] Vogeles, A. *et al.* Quantum Dot Optomechanics in Suspended Nanophononic Strings. *Advanced Quantum Technologies* 1900102 (2019).
- [140] Alegre, T. P. M., Safavi-Naeini, A., Winger, M. & Painter, O. Quasi-two-dimensional optomechanical crystals with a complete phononic bandgap. *Optics Express* **19**, 5658 (2011).
- [141] Chan, J., Safavi-Naeini, A. H., Hill, J. T., Meenehan, S. & Painter, O. Optimized optomechanical crystal cavity with acoustic radiation shield. *Applied Physics Letters* **101**, 081115 (2012).

- 
- [142] Safavi-Naeini, A. H. *et al.* Observation of Quantum Motion of a Nanomechanical Resonator. *Physical Review Letters* **108** (2012).
- [143] Yu, P.-L. *et al.* A phononic bandgap shield for high-Q membrane microresonators. *Applied Physics Letters* **104**, 023510 (2014).
- [144] Brendel, C., Peano, V., Painter, O. & Marquardt, F. Snowflake phononic topological insulator at the nanoscale. *Physical Review B* **97** (2018).
- [145] Safavi-Naeini, A. H. *et al.* Two-Dimensional Phononic-Photonic Band Gap Optomechanical Crystal Cavity. *Physical Review Letters* **112** (2014).
- [146] Ren, H. *et al.* Quasi-2D Optomechanical Crystal Cavity for Quantum Optomechanics. In *Conference on Lasers and Electro-Optics* (OSA, 2019).
- [147] Balram, K. C. *et al.* Acousto-Optic Modulation and Optoacoustic Gating in Piezo-Optomechanical Circuits. *Physical Review Applied* **7** (2017).
- [148] Restrepo, J., Ciuti, C. & Favero, I. Single-Polariton Optomechanics. *Physical Review Letters* **112** (2014).
- [149] Restrepo, J., Favero, I. & Ciuti, C. Fully coupled hybrid cavity optomechanics: Quantum interferences and correlations. *Physical Review A* **95** (2017).
- [150] Burenkov, Y. A., Burdukov, Y. M., Davidov, S. Y. & Nikanorov, S. P. Temperature dependences of the elastic constants of gallium arsenide. *Sov. Phys. Solid State* **15**, 1175–1177 (1973).
- [151] Strzalkowski, I., Joshi, S. & Crowell, C. R. Dielectric constant and its temperature dependence for GaAs, CdTe, and ZnSe. *Applied Physics Letters* **28**, 350–352 (1976).
- [152] Adachi, S. *GaAs and Related Materials* (WORLD SCIENTIFIC, 1994).
- [153] Bond, W. L. The Mathematics of the Physical Properties of Crystals. *Bell System Technical Journal* **22**, 1–72 (1943).



# List of Publications

## Published papers

- **”Li<sup>+</sup> Transport in Poly(Ethylene Oxide) Based Electrolytes: Neutron Scattering, Dielectric Spectroscopy, and Molecular Dynamics Simulations”**  
C. Do, P. Lunkenheimer, D. Diddens, M. Götz, M. Weiß, A. Loidl, X. Sun, J. Allgaier and M. Ohl  
Physical Review Letters 111 (2013), doi: 10.1103/PhysRevLett.111.018301
- **“Dynamic Acoustic Control of Individual Optically Active Quantum Dot-like Emission Centers in Heterostructure Nanowires”**  
M. Weiß, J. B. Kinzel, F. J. R. Schülein, M. Heigl, D. Rudolph, S. Morkötter, M. Döblinger, M. Bichler, G. Abstreiter, J. J. Finley, G. Koblmüller, A. Wixforth and H. J. Krenner  
Nano Letters 14 (2014), doi: 10.1021/nl4040434
- **“Radio frequency occupancy state control of a single nanowire quantum dot”**  
M. Weiß, F. J. R. Schülein, J. B. Kinzel, M. Heigl, D. Rudolph, M. Bichler, G. Abstreiter, J. J. Finley, A. Wixforth, G. Koblmüller and H. J. Krenner  
Journal of Physics D: Applied Physics 47 (2014), doi: 10.1088/0022-3727/47/39/394011
- **”Ultrafast Photodetection in the Quantum Wells of Single AlGaAs/GaAs-Based Nanowires”**  
N. Erhard, S. Zenger, S. Morkötter, D. Rudolph, M. Weiß, H. J. Krenner, H. Karl, G. Abstreiter, J. J. Finley, G. Koblmüller and A. W. Holleitner  
Nano Letters 15 (2015), doi: 10.1021/acs.nanolett.5b02766
- **”The Native Material Limit of Electron and Hole Mobilities in Semiconductor Nanowires”**  
J. B. Kinzel, F. J. R. Schülein, M. Weiß, L. Janker, D. D. Bühler, M. Heigl, D. Rudolph, S. Morkötter, M. Döblinger, M. Bichler, G. Abstreiter, J. J. Finley, A. Wixforth, G. Koblmüller and H. J. Krenner  
ACS Nano 10 (2016), doi: 10.1021/acsnano.5b07639

- **”Surface acoustic wave regulated single photon emission from a coupled quantum dot–nanocavity system”**  
M. Weiß, S. Kapfinger, T. Reichert, J. J. Finley, A. Wixforth, M. Kaniber and H. J. Krenner  
Applied Physics Letters 109 (2016), doi: 10.1063/1.4959079
- **”Dielectric study on mixtures of ionic liquids”**  
E. Thoms, P. Sippel, D. Reuter, M. Weiß, A. Loidl, S. Krohns  
Scientific Reports 7 (2017), doi: 10.1038/s41598-017-07982-3
- **”Multiharmonic Frequency-Chirped Transducers for Surface-Acoustic-Wave Optomechanics”**  
M. Weiß, A. L. Hörner, E. Zallo, P. Atkinson, A. Rastelli, O. G. Schmidt, A. Wixforth, and H. J. Krenner  
Physical Review Applied 9 (2018), doi: 10.1103/PhysRevApplied.9.014004
- **”Interfacing quantum emitters with propagating surface acoustic waves”**  
M. Weiß and H. J. Krenner  
Journal of Physics D: Applied Physics 51 (2018), doi: 10.1088/1361-6463/aace3c
- **”The 2019 surface acoustic waves roadmap”**  
P. Delsing, A. N. Cleland, M. J. A. Schuetz, J. Knörzer, G. Giedke, J. I. Cirac, K. Srinivasan, M. Wu, K. C. Balram, C. Bäuerle, T. Meunier, C. J. B. Ford, P. V. Santos, E. Cerda-Méndez, H. Wang, H. J. Krenner, E. D. S. Nysten, M. Weiß, G. R. Nash, L. Thevenard, C. Gourdon, P. Rovillain, M. Marangolo, J. Duquesne, G. Fischerauer, W. Ruile, A. Reiner, B. Paschke, D. Denysenko, D. Volkmer, A. Wixforth, H. Bruus, M. Wiklund, J. Reboud, J. M. Cooper, Y. Fu, M. S. Brugger, F. Rehfeldt and C. Westerhausen  
Journal of Physics D: Applied Physics 52 (2019), doi: 10.1088/1361-6463/ab1b04
- **”Quantum dot optomechanics in suspended nanophononic strings”**  
A. Vogegele, M. M. Sonner, B. Mayer, X. Yuan, M. Weiß, E. D. S. Nysten, S. F. Covre da Silva, A. Rastelli and H. J. Krenner  
Advanced Quantum Technologies 3 (2019), doi: 10.1002/qute.201900102

---

## Preprint

- **”Optomechanical single photon frequency division multiplexing”**  
M. Weiß, D. Wigger, M. Nägele, K. Müller, J. J. Finley, T. Kuhn, P. Machnikowski,  
H. J. Krenner  
arXiv: 1910.12949



# Danksagung

Zu guter Letzt möchte ich mich bei all denen bedanken die an dieser Arbeit auf die eine oder andere Art mitgewirkt haben:

- Allen voran natürlich Hubert Krenner, für die Betreuung dieser Arbeit und für die zahlreichen Ideen und Impulse, die diese Arbeit vorangebracht haben.
- Achim Wixforth, für die Möglichkeit diese Arbeit an seinem Lehrstuhl durchzuführen.
- Prof. Dr. Manfred Albrecht und Prof. Dr. Kai Mueller für die Erstellung der Gutachten zu dieser Arbeit
- Stephan Kapfinger und Jörg Kinzel, von denen ich viel über die Arbeit im Labor lernen konnte.  
Emeline Nysten für den Umgang mit Säuren, die mir zu gefährlich waren, die Rotation elastischer Konstanten, die mir zu verwirrend war und die Korrektur dieser Arbeit.  
Der gesamten Hoob-Group: Lisa Janker, Sebastian Hammer, Tobias Petzak, Maximilian Sonner, Moritz Mangold, Florian Schülein und Jens Pustiowski für die gute Zusammenarbeit und eine tolle Zeit sowohl im Labor, als auch weit darüber hinaus.
- Maximilian Nägele, Anja Vogele, Dominik Bühler, Michael Heigl und Lennart Kappl, deren Abschlussarbeiten ich (teilweise) betreuen durfte und denen ich hoffentlich ein, zwei Dinge beibringen konnte.
- Kai Müller, Thorsten Reichert, Michael Kaniber und Jonathan Finley vom Walter Schottky Institut für die Bereitstellung hervorragender Proben und unbezahlbaren Tipps zur Resonanzfluoreszenz
- Eugenio Zallo, Paola Atkinson, Armando Rastelli und Oliver Schmidt für die Bereitstellung weiterer Quantenpunktproben
- Daniel Wigger, Paweł Machnikowski und Tilmann Kuhn für die Entwicklung eines theoretischen Modells der resonanten Fluoreszenz eines dynamisch modulierten Zwei-Niveau-System, das maßgeblich zum Verständnis der Messungen beigetragen hat.

- Alexander Hupfer für die den gemeinsamen Laborbau und die Unterstützung bei unzähligen Computerproblemen  
Dem (Verwaltungs-)Technischen Personal, die den Lehrstuhl am Laufen halten: Sidonie Lieber, Andreas Hörner, Olga Ustinov, Andreas Spörhase, Adrian Mainka, Martina Mindt und Funda Cevik für die Hilfe bei vielen kleinen und großen Problemen
- Dem gesamten Lehrstuhl EP1 für ein tolles Arbeitsklima, viel Spaß und den fließenden Übergang sowohl zwischen Arbeit und Freizeit, als auch zwischen Kollegen und Freunden.
- Meiner Familie, für die anhaltende Unterstützung während dem Studium und der Promotion.